A) INTRODUCTION

B) THEORY OVERVIEW

C) APPARATUS OVERVIEW

D) EXPERIMENTS E288 AND E494

E) APPARATUS
1. BEAM
2. INCIDENT BEAM INTENSITY MONITOR
- TARGETS
- TARGET BOX
  COPPER FOILS AND LEAD PLUG
  SHIELDING PILE
  MAGNETS
  TRIGGER COUNTERS
  HODOSCOPES
  MULTIWIRE PROPORTIONAL CHAMBERS (MWPC)
  LEAD GLASS CALORIMETER

Guide post experimental details

F) ELECTRONICS
FAST TRIGGER LOGIC
D.C. LOGIC
DIGITIZERS AND DIGITIZER READOUT SYSTEM
MWPC ELECTRONICS
DATA AQUISITION

G) OFF-LINE ANALYSIS
OFF LINE ANALYSIS AND CUTS
PARTICLE TRACK DETERMINATION
MAGNETIC TRAJECTORY RECONSTRUCTION
EXPERIMENTAL RESOLUTION
LEAD GLASS CALIBRATION
LEAD GLASS ENERGY DETERMINATION
LEAD GLASS RESOLUTION
LONGITUDINAL SHOWER DEVELOPMENT
INTENSITY: LIMITATIONS AND CUTS
MONTE CARLO CALCULATION OF THE ACCEPTANCE
NORMALIZATION
ACCIDENTAL BACKGROUND DETERMINATION
DILECTRON BACKGROUND ABOVE 4 GeV

H) RESULTS

I) Conclusion - Summary

INTRODUCTION

This experiment was a search for dielectron pairs emitted near the proton-nucleus reaction:

$$p + Be \rightarrow e^+ + e^- + \text{ANYTHING}$$

close to a CMS rapidity y=0. In addition to other pair kinematical quantities. the effective mass of the observed dielectrons was calculated

$$M \doteq \sqrt{P_+ P_-} \sin(\theta_+ + \theta_-)$$

and the resultant mass spectrum revealed information on the continuum of produced dielectron pairs and resonant features superimposed on it.

The data presented here was taken during two periods of operation of the Fermilab accelerator between 9/6/75-2/23/76 (E288) and between / / - / / (E494). During these intervals. the Fermilab accelerator was operated at energies of 100, 200, 300, and 400 Gev. This thesis reports primarily on the 400 Gev dielectron sample.

While accelerator intensities were on the order of 10^{13} protons per pulse, this experiment was intensity limited to a few times (10^9 - 10^{10}), with 10-20% of these interacting in the target.

The history of the observation of high mass dilepton pairs began with the 1968 dimuon experiment of Christenson et al. (1) which observed muon pairs in the mass range from 1 to 6.7 GeV/c . Its purpose was to search for structures in the dimuon mass spectrum from the reaction:

$$p + \text{Nucleus} \rightarrow \mu^+ + \mu^- + X$$

Data were taken at BNL at four incident proton energies - 22, 25, 28.5 and 29.5 GeV. Horizontal (laboratory) angles extended over the range +-50 mr. to +-360 mr. with a 75 mr. vertical aperature. Mass resolution of the dimuon pairs was degraded by uranium and steel that served as the necessary hadron absorber. Multiple scattering effects limited the resolution to 15% at 2 GeV/c and 8% at 5 GeV/c . The experiment can be characterized as being one of high sensitivity but poor resolution.

Largely in retrospect, one now sees that the data of this experiment provided strong 'shoulder' evidence for the existence of the J/ψ, it served to first measure the predicted dilepton continuum, and its data showed consistency with dilepton 'scaling' over the s=45-60 GeV range.

As a logical continuation to this Brookhaven effort, a second series of dilepton experiments were proposed in June 1970 for the 200-500 GeV Fermilab accelerator. Both dilepton modes:

$$p + \text{Nucleus} \rightarrow \begin{Bmatrix} e^+ + e^- \\ \mu^+ + \mu^- \end{Bmatrix} + X$$

were to be studied. This was done, not simply as a check of μ-e universality, but to take full advantage of the complementary qualities of the muon and electron data sets. Electrons are sensitive to small amounts of matter in their path, and so one tries to minimize the material in the aperature for them. The electron experiment achieved its hadron rejection through use of a lead glass shower calorimeter; its experimental resolution was limited only by the finite counter resolution and multiple scattering in the apparatus downstream of the analysis magnets. The muon experiment, on the other hand, achieved its hadron rejection through use of an 'absorber' placed in the aperature. This absorber eliminated a large component of the hadronic background and permitted running at increased beam intensity relative to electrons, while its multiple scattering effects degraded the mass resolution.

Clearly both approaches have something to offer. Data taking began with the e+e- phase of E288.

THEORY OVERVIEW

WHY LEPTONS

In this century, the study of the structure of molecular, atomic, nuclear and subnuclear matter has been accomplished to a great extent, through experiments which employed electromagnetic interactions to probe the microworld (2). Presently the structure of the strongly interacting 'elementary' particles of physics - the hadrons - is being studied at particle accelerators around the world, using both the electromagnetic and weak interactions of high energy leptons.

The leptons (electrons, muons and neutrinos) have several exceptional qualities that recommend them for this purpose (3). They are not subject to the little understood 'nuclear' forces, behave as structureless point particles in their interactions and are all relatively stable. The leptons participate in the weak and the electromagnetic interaction, so first order approximate perturbation theory solutions normally suffice to describe their behavior. Hadrons, on the other hand, are subject to the strong nuclear forces, have radii of $(0.5 - 1.0)10^{-13}$ cm., may break up when probed by the pointlike leptons and are all unstable, except the proton and antiproton.

neutron is relatively stable

To the extent that the weak and electromagnetic interactions are understood, one can learn from the reactions of leptons with hadrons. The theory of Quantum Electrodynamics (QED), which has proved very successful in predicting the outcome of the electromagnetic pointlike particle interactions, is believed well understood up to the very high energies of present day accelerators. The properties of the weak force are not as well determined, but even so the available approximate theory has served as a fruitful guide in the interpretation and prediction of experimental results. Observed deviations from the theory will suggest avenues of improvement.

Today, hadrons are assumed to be composit particles, in one sense or another. As in the nuclear experiment of Rutherford (4), one can hope that any residual pointlike structure in the hadrons will manifest itself through 'large' cross sections, measured in high energy-momentum transfer experiments. One says 'hope' since it may be expected that the strong nuclear binding and confinement forces may cloud interpretation of the experimental results.

The study of hadrons is complicated by the fact that they are subject to strong forces of interaction and have a finite spacial extension. One can, in the case of electromagnetism, formally write an interaction hamiltonian as $J_\mu A^\mu$, but then one is faced with defining J_μ for an extended, perhaps composite particle. Quark/parton theories

(5) suggest that in a certain limit of high energy-momentum transfers, the charged currents in the hadrons behave as though made up of point charges of +2/3e and -1/3e. The unknown nature of the coupling between constituent quark/partons and of their 'mechanism of confinement' in the nucleus discourages, at present, a more complete treatment of this problem.

Happily it appears that some simple properties familiar from QED electromagnetic interactions may carry over into the study of hadrons. Charged hadrons do couple to the photon, and it was verified in electron-nuoleus elastic scattering that the interaction between scattering particles takes place primarily through one-photon-exchange (figure 1b). Observed two-photon-exchange effects are, at best, on the few percent level (6). For inelastic scattering, it is assumed that the smallness of the electromagnetic coupling constant (α) insures that reactions take place, primarily, through the exchange of one photon.

In what follows, a review will be made of some of the information learned about hadrons from 'lepton probe' experiments. These include experiments studying:

1. Lepton inelastic scattering on nucleons (figure 1a)

2. Electron-positron annihilation (figure 1d)

3. Dilepton production (figure 1e)

All three types of experiment probe the same object, but each in a different interaction mode and in a different kinematical region. So far the results from the three have proved very compatible, and in reasonably good agreement with simple quark/parton model (QPM) predictions for the hadrons.

In the sections that follow, the data results will be interpreted largely from the QPM point of view. Partons are pointlike nuclear constituents, which for high energy-momentum transfers, act individually to scatter leptons elastically and incoherently. At present, there are other theories that adequately account for certain features of the data, and in some cases, reproduce QPM results ('light cone' analysis, for example(7)). Nevertheless, the assumption of parton existence and the assignment of certain properties to them does account for major features of a broad range of data. It is probable that the theory represents an approximation, but it nonetheless provides physical insight, direction and a calculational approach where other methods may fail to do so. The partons' "simplicity and success are awesome considering that their theoretical basis is vaguely defined and perhaps not consistent" (8).

The case for identification of the pointlike partons with the Gell-Mann (9)', Zwieg (10) quarks is suggested by evidence that the partons have quantum numbers similar to the quarks. Measurements bear out that partons are also spin 1/2 particles, of fractional charge and that the net number of parton constituents in the nucleon is three, just as in the quark case. The concurrence of these two independent theories - of the quarks which seemed so successful in accounting for the spectrum of all known mesons and baryons in terms of 3 (4(?), 5(?)?,...) fractionally charged constituents - and of the pointlike partons whose well defined properties provided a calculational approach to hadronic interaction processes - makes the case for both theories stronger still.

Presently, the nucleon is viewed as being composed of 3 'valence' quarks, a 'sea' of low momentum quark-antiquark ($q\bar{q}$) pairs and neutral 'gluons' that interact through the strong force to bind quarks together in the nucleus. This scheme is, all in all, not far removed from that visualized in the highly successful theory of Quantum Electrodynamics. The 'valence' quarks give the hadron its quantum numbers and hadronic identity. The 'sea' of $q\bar{q}$ pairs is similar to the particle-antiparticle sea familiar from higher order QED calculations, with gluons playing the role of the strong force 'photon'.

While very successful in accounting for a broad range of data, there are existing 20-30% discrepancies and the simple model does not account for the large observed particle transverse momentum or for quark confinement in the nucleus. It is hoped that some of the QPM's problems can be remedied by establishing a more broadly based, deeply rooted theoretical framework that is consistent and capable of estimating higher order gluon and sea corrections to physical processes. At present, a theoretical effort is being made in the direction of developing the formalism of Quantum Chromodynamics - QCD - in which 'asymtotic freedom' (11) provides a calculational approach for treating strong force problems.

Apart from specific models, certain general predictions can be made about the 'scaling' of cross sections in high energy lepton probe experiments (12). The cross section for a given leptonic or semi-leptonic reaction, with constituent masses m_i, may be written:

$$d\sigma = F(s, q^2, m_i) \times \begin{cases} \alpha^2 & \text{LEPTONIC} \\ G^2 & \text{SEMI LEPTONIC} \end{cases}$$

where, for the case or reactions including hadrons, one must use the inclusive cross section and sum over all final hadronic states. A basic assumption of 'scaling' predictions for high energy reactions is that no masses will be observed above a certain mass M. This means that, for high enough energies (s, q^2) $(>>M)$, no parameter exists to determine

an absolute energy scale. In this limit (s, q^2 large), the m_i masses may be set equal to zero and:

$$d\sigma = F(s, q^2) \begin{cases} \alpha^2 \\ G^2 \end{cases}$$

With this formula, dimensional analysis predicts:

$$\left.\begin{array}{l} e^+ + e^- \to \mu^+ + \mu^- \\ e^+ + e^- \to \text{HADRONS} \end{array}\right\} \quad \sigma \propto \frac{\alpha^2}{s}$$

$$\left.\begin{array}{l} \nu_e + e \to \nu_e + e \\ \nu_\mu + N \to \mu + \text{HADRONS} \end{array}\right\} \quad \begin{array}{l} \text{a) } \dfrac{d\sigma}{dq^2} \propto G^2 F'\left(\dfrac{q^2}{s}\right) \\ \text{b) } \sigma \propto G^2 s \end{array}$$

$$\left.\begin{array}{l} e + \mu \to e + \mu \\ e + p \to e + \text{HADRONS} \end{array}\right\} \quad \begin{array}{l} \text{a) } \dfrac{d^2\sigma}{dq^2 d\omega} \propto \dfrac{\alpha^2}{q^4} F''\left(\dfrac{q^2}{s}, \omega\right) \\ \omega \equiv 1/x \\ \text{b) HADRONIC STRUCTURE FUNCTIONS DEPEND ONLY ON } x \end{array}$$

Any observed breakdown in these rather general relations is of great importance and may be attributed the existence of an absolute energy scale in physics, one's failure to reach high enough energies, the basic incorrectness of assuming the particle masses to be exactly zero or to a 'high energy' failure of some aspect of the QED and/or Fermi interaction viewpoint.

DEEP INELASTIC SCATTERING: Charged leptons (13)

First high energy attempts to probe the nuclear structure were made in experiments at SLAC[14] looking at the reaction (figure):

$$e + \text{NUCLEON} \rightarrow e + X$$

Due to large energy losses from synchrotron radiation, electrons are difficult to accelerate to ~100 GeV energies and later experiments probed nuclei with muons:[15]

$$\mu + \text{NUCLEON} \rightarrow \mu + X$$

A brief outline of some kinematical relations and cross section formulas pertaining to these reactions are presented in appendix I .

These scattering experiments yielded cross sections, exhibiting peaks due to elastic scattering, the excitation of discrete nuclear levels and a broad 'quasi elastic' peak due to leptons scattering off the constituent nuclei of the nucleus. What was surprising was the observed high probability for inelastic scattering - a large inclusive cross section was observed for deep inelastic scattering of leptons with the ~~nuclei~~ nucleon. For a relatively homogeneous ~~nucleus~~ target, one expected to observe inelastic events due to photon emission of the electron when accelerated near the ~~nucleus~~ nucleon, but estimates of this effect fell far short of accounting for the data. Integrated over ν, the cross section fell off slowly with q^2 and remained close to the

Mix up of nucleus & nucleon — the relevant expt'l. coeff. on protons + (nd) of the constituent.

order of magnitude of the (Mott) cross section for scattering off a pointlike proton (16).

The rather remarkable observations in charged lepton-nucleon scattering suggested the development of a theory of pointlike nuclear constituents confined within the finite sized hadrons. These particles were assigned certain properties, given the name of 'partons', and many features of deep inelastic scattering were analyzed in terms of their interactions. Tables 1+2 presents a short summary of some predictions and observations made in these scattering experiments. As one can see the data are supportive of nuolear, pointlike constituents, of spin 1/2 with fractional electric charge.

Assuming pointlike, spin 1/2 partons in the nucleons, one can use the QED elastic scattering formula from $e+\mu \rightarrow e+\mu$ to predict the scattering cross section for leptons on quarks:

$$\frac{d^2\sigma}{dq^2 dE'} = \frac{1}{2}\frac{4\pi\alpha^2}{q^4} 2m \left[\frac{E'^2}{E^2} + 1\right] \delta(2m(E-E') + q^2)$$

This scattering of the lepton off the nucleon is assumed to take place in incoherent and elastic interactions between the charged leptons and individual partons (figure 1c). The total cross section for the process is obtained by simply summing the cross sections for the individual parton constituent reactions. The resulting cross section obeys unbroken Bjorken scaling and relates the scaling structure

function. F_2, to parton momentum density distribution functions (17).

Lepton scattering data provides strong evidence for identifying the parton constituents of the nucleus with quarks, and it will be convenient now to adopt quark notation and assume 4 'flavors' or types of parton constituent: u, d, s and c. In terms of these, the deep inelastic scaling function F_2 becomes:

$$F_2^{ep}(x) = x\left(\tfrac{4}{9}(u+c) + \tfrac{1}{9}(d+s) + \text{ANTIQUARKS}\right)$$

$$F_2^{en}(x) = x\left(\tfrac{1}{9}(d+c) + \tfrac{4}{9}(u+s) + \text{ANTIQUARKS}\right)$$

The functions u, d, s, c are functions of x, and they measure the probability of finding a quark of type u, d, s or c in the proton, with momentum = x P(proton). 'x' is the fraction of nucleon momentum possesed by the scattered quark, and a simple kinematical argument shows that this definition agrees with the appendix definition: $x = q^2/2m\nu$. In writing the above equations, we have assumed isospin invarience of the nuclear forces:

$$u(\text{PROTON}) = d(\text{NEUTRON})$$

$$d(\text{PROTON}) = u(\text{NEUTRON})$$

and will adopt the assumed quark proton structure:

	u	d	s	c
PROTON	2	1	0	0
NEUTRON	1	2	0	0

So, for the proton:

$$\int_0^1 (u-\bar{u})\,dx = 2 \qquad \int_0^1 (s-\bar{s})\,dx = 0$$

$$\int_0^1 (d-\bar{d})\,dx = 1 \qquad \int_0^1 (c-\bar{c})\,dx = 0$$

One usually interprets the strangeness and charm relations as:

$$s = \bar{s}$$

$$c = \bar{c}$$

A zero isospin requirement on the $q\bar{q}$ sea leads to:

$$\bar{u} = \bar{d}$$

A common simplifying assumption, often made in literature, is then:

$$\bar{u} = \bar{d} = \bar{s} = \bar{c} = s = c$$

The nucleon charge is given by:

$$Q_A = \sum_i Q_i^A \int q_i^A(x)\,dx$$

where i = quark type or flavor, A=nucleon index, Q_i^A = charge of 'i' quark in nucleon 'A', q_i^A = u. d. s. $\bar{d}$. $\bar{u}$ etc. functions.

One advantage of electron scattering experiments over neutrino scattering experiments is that charged leptons scatter off strange and charmed quarks with no $\sin^2(\theta)$ Cabibbo angle suppression. This will prove very important in estimating the strange and charm quark contributions to the ~~nucleus.~~ lon

DEEP INELASTIC SCATTERING: Neutrinos ( )

Additional, complementary information regarding the constituents of the nucleus and their momentum distribution functions may be obtained from the data of deep inelastic scattering neutrino experiments (figure 1a). Some

kinematical formulas pertaining to the reactions:

$$\nu + \text{Nucleus} \rightarrow \mu^-(e^-) + \overline{X}$$

$$\bar{\nu} + \text{Nucleus} \rightarrow \mu^-(e^-) + \overline{X}$$

are presented in appendix 2. In terms of quark constituents (θ(Cabibbo) = 0):

$$\nu + \left\{\begin{matrix} d \\ \bar{u} \end{matrix}\right\} \rightarrow \mu^-(e^-) + \left\{\begin{matrix} u \\ \bar{d} \end{matrix}\right\}$$

As in the case of charged lepton-nucleon scattering, one can deduce the QPM cross section by first calculating the cross section for neutrino scattering off a single spin 1/2 parton and then summing this contribution, as before, over all nuclear partons.

As shown in Tables 3 through 5, neutrino reactions obey scaling over a wide range, and in conjunction with the charged lepton results:

1. reveal that the nucleon is made up of 3 net constituents over anticonstituents.
2. show that 50% of the nucleon momentum is carried by quarks (with the remainder attributed to gluons).
3. favor ~~predict~~ a fractional constituent charge.
4. demonstrate consistency with charged lepton structure functions.

Neutrino and antineutrino scattering on nucleons provides valuable relations between the measured structure functions and the to-be-determined quark distribution functions:

$$F_2^{\nu p} = 2x\,(d + \bar{u})$$

$$F_2^{\nu n} = 2x\,(u + \bar{d})$$

$$F_3^{\nu p} = 2\,(\bar{u} - d)$$

$$F_3^{\nu n} = 2\,(\bar{d} - u)$$

θ (Cabibbo) is assumed zero so the strange and charmed quark contributions do not appear (19). In principle, these relations can be solved for u, $\bar{u}$, ..., but in practice, the experimental measurements are not accurate enough to accomplish this. At present, there is no unique accepted set of quark and antiquark functions; several may be found in the literature (20). Typically, their determination requires use of not only the deep inelastic scattering results, but also certain theoretical constraints and simplifying assumptions.

The extension of the QPM to treat polarization problems is straightforward (21). One defines + and - helicity states for the quarks such that:

$$u = u_+ + u_-$$

$$d = d_+ + d_-$$

ETC.

In principle, the u#, u+, d#, ... can all be determined from scattering experiments off polarized targets and:

$$\langle S_z \rangle = \frac{1}{2} \int \left((u_+ - u_-) + (\bar{u}_+ - \bar{u}_-) + (d_+ - d_-) + (\bar{d}_+ - \bar{d}_-) \right) dx$$

$$\langle L_z \rangle = \frac{1}{2} - \langle S_z \rangle$$

For the proton, one expects $\langle S_z \rangle = 1/2$, $\langle L_z \rangle = 0$, while one finds, from available low energy data, $\langle S_z \rangle = 0.3$ and $\langle L_z \rangle = 0.2$. The naive QPM ignores the transverse momenta of nuclear constituents, so this discrepancy is not so surprizing. This example gives an indication of the calculational power in the QPM approach.

Observation of the reaction:

$$e^+ + e^- \rightarrow \text{HADRONS}$$

at colliding beam facilities at SLAC (23) and of its 'inverse' reaction:

$$p + p \rightarrow \mu^+ + \mu^- + X$$

at BNL (24) established the existence of the J/ψ particle, which so abruptly altered the course of present day physics. Here we shall be concerned with the first of these two reactions, e+, e- annihilation into hadrons. In the naive QPM, this reaction is visualized (figure 1F) as a process in which the electron positron pair annihilates to create a photon which converts to a $q\bar{q}$ pair; these quarks, before leaving the nucleus, become 'dressed' as physical hadrons. Since the photon has $J^{PC} = 1^{--}$, electron-positron spectroscopy is useful for the study of new and old vector mesons.

Of considerable theoretical and experimental interest is the ratio:

$$R = \frac{\sigma(e^+ + e^- \rightarrow \text{HADRONS})}{\sigma(e^+ + e^- \rightarrow \mu^+ + \mu^-)}$$

In the QPM, this ratio has a physical interpretation. To see this, we shall fall back on the QED spin 1/2 ($e^+e^- \rightarrow \mu^+\mu^-$) formula and apply it to the reaction ($e^+e^- \rightarrow q\bar{q}$):

$$\sigma(e^+ + e^- \rightarrow \mu^+ + \mu^-) = \frac{4\pi\alpha^2}{3s}$$

$$m_\mu << \sqrt{\frac{s}{4}}$$

$$s = 4E_1E_2$$

So for spin 1/2 partons of mass m and charge Qe:

$$\sigma(e^+ + e^- \to q + \bar{q}) = \frac{4\pi\alpha^2}{3s} Q^2 \qquad m_q \ll \sqrt{s/4}$$

If the parton/quark mass is close to $\sqrt{s/4}$ we expect threshold effects to yield a reduced cross section. To estimate the cross section for the e+e- going to all hadron states (one must do this to avoid folding in the probability that a quark will 'appear' in a specific hadronic state), one follows the QPM recipie of assuming incoherent, elastic scattering and one sums the quark cross section over all the ~~nuclear~~ hadron constituents. In general, if there are N partons in the ~~nucleus~~ hadron with charge Qe, all with mass $< \sqrt{s/4}$:

$$\sigma(e^+ + e^- \to \text{HADRONS}) = \frac{4\pi\alpha^2}{3s} \sum_1^N Q_i^2$$

In general for spin 0 and 1/2 partons (25):

$$R = \sum_{\substack{1 \\ \text{SPIN} \\ 1/2}} Q_i^2 + \frac{1}{4} \sum_{\substack{\text{SPIN} \\ 0}} Q_i^2$$

Spin 1 partons yield a rising value of R (26).

So one sees that in the QPM, R is the sum of the squares of the 'active' QP charges. This ratio of cross sections has been measured at SLAC and they find that R increases from 2.5 between 2-3 GeV to 4.5-5.0 between 4 and 5 GeV. The curve flattens out near 5.2 ~~from 5~~ and remains flat ~ to 8 GeV. (27). These observed values can be compared to some standard QPM predictions:

$$R(u,d,s) = 2/3$$
$$R(u,d,s,\text{color}) = 2$$
$$R(u,d,s,c,\text{color}) = 10/3$$
$$R(u,d,s,c,\text{color},\text{Heavy Lepton}) = 13/3$$

Observed values of R support the color hypothesis and are consistent with the excitation of charm in the 3-4 GeV region. To account for the large values of R observed above 3.5 GeV, an additional excited 'degree of freedom' may be needed to account for the data. The newly discovered heavy lepton (28) of charge +-e will add 1 unit to the value of R.

As one can see, this ratio of cross sections, R, provides yet another test of the QPM - this model should be able to account for the observed R values and predict the manner in which R will change as s and/or q^2 increase. In general, people will be rather surprized if R does not approach a constant in some sort of high energy limit. General scaling arguments and a large class of theories (including the QPM and 'light cone' analysis) agree that $R \rightarrow$ constant at large s and q^2. Efforts have been made to predict both its asymtotic value and the manner in which R will approach this limit (29).

How about a continued series of quarks + leptons?

If R does not tend towards a constant, then one may be forced into making some adjustments in our present understanding of the annihilation process. At one end of the spectrum, one is faced with admitting to an absolute energy scale in high energy physics; at the other, one may have to improve available theory to make accurate calculations of higher order corrections that may account for a variable R. Spin 1 partons yield rising R values -

perhaps the e+e- annihilation process is sensitive to constituents whose existence is not probed in lepton-nucleon scattering. "Striking a proton can only excite quarks present in the proton, whereas exciting the vacuum can give rise to the whole particle spectrum" (30). Alternatively, a non-constant value of R may be accounted for by various possible non-scaling corrections to present theory (quark size effects, gluon corrections etc.). At present the value of R has leveled at 5.2; it seems as though more data is needed, extending beyond 8 GeV, to decide asymtotic limit questions. The present status of R is clouded by the excitation of new degrees of freedom and new particle thresholds.

About the same time as the original deep inelastic scattering experiment at SLAC, experimenters at BNL ( ) were looking for dimuons produced in the reaction:

$$p + \text{NUCLEUS} \rightarrow \mu^+ + \mu^- + X$$

In a loose sense, this is the inverse reaction to e+e- annihilation (figure 1h). It is imagined in the QPM that the dileptons are produced as a result of quark-antiquark annihilation into a virtual photon, which later converts to lepton pairs (figure 1i). The differential cross section for producing a pair of invarient mass $m^2 = q^2$ is (32):

$$\frac{d^2\sigma}{dQ_0^2 d\xi} = \frac{4\pi\alpha^2}{3Q_0^4}\left(\sum_i \frac{e_i^2}{x_1+x_2} x_1 x_2 \left(q_i^1(x_1)\, q_i^2(x_2) + q_i^1(x_1)\, q_i^2(x_2)\right)\right)$$

$$x_{1(2)} = \frac{1}{2}\left(+(-)\xi - \sqrt{\xi - \frac{4Q_0^2}{s}}\right)$$

$$\xi = 2Q_3/\sqrt{s}$$

$$\tau = Q_0^2/s$$

$$s = 4p^2$$

Q = LEPTON PAIR 4 MOMENTUM ↙ q.so, $M^2 = Q_0^2$

$$x_1 - x_2 = x_F = \xi$$

$$s x_1 x_2 = m^2 \equiv Q_0^2$$

Also define Q_0^-

where the $q_a^{1,2}$ are the quark u, d, s, c... distribution functions ~~determined from deep inelastic scattering experiments~~ in the incident and struck hadron respectively. They reveal the momentum distribution of quarks of type a in hadron A. For the case of ~~this experiment~~ the experiment which is the subject of this thesis:

which?

$$x_F \cong 0$$

$$x_1 = x_2 = \sqrt{\tau}$$

$$\left.\frac{d^2\sigma}{dm\,dx_F}\right|_{x_F=0} = \frac{8\pi\alpha^2}{3\cdot 3\,Q^3} F(\tau)$$

where an extra '3' has been added in the denominator to account for the effects of the color degree of freedom. For ~~the~~ an incoming proton:

$$q' = q^p$$

For a nuclear target, ~~nucleons~~ (Z,A), one must weigh the neutron and proton contributions:

$$q^2 = \frac{Z}{A} q^p + \frac{A-Z}{A} q^n$$

One has the relation:

$$u^n = d^p \qquad d^n = u^p$$

which follows from the isospin invariance of nuclear forces. The sea will be assumed to have zero strangeness ($s = \bar{s}$), zero isospin ($\bar{u} = \bar{d}$), and the simplifying assumption will be made that ($\bar{u} = \bar{d} = \bar{s} = s$). Following the lead of Kuti and Weisskopf (33), we shall separate out the sea and valence quark contributions as:

$$u = u_v + S$$

$$d = d_v + S$$

So one arrives at the Drell and Yan (34) prediction for the dilepton continuum:

$$\frac{d^2\sigma}{dm\,dx_F}\Big|_{x_F=0} = \frac{4\pi\alpha^2}{9m^3}\tau\left(S(\tau)\left(\frac{8N_p+5N_n}{9A}u_v(\tau) + \frac{2N_p+5N_n}{9A}d_v(\tau)\right) + S(\tau)\,S(\tau)\right)$$

Many authors (35) have evaluated this cross section using

The u and d functions are obtained from deeply inelastic scattering

their own favorite quark distribution functions. A reasonable choice of distribution functions usually give QPM predictions which either straddle the data or are within a comfortable factor of 2 or 3 from the measured values.

Several comments can be made concerning the unique contribution that dilepton experiments made to our understanding of ~~nuclear~~ hadron structure! These comments provide the motivation for the research described below:

(1) Since lepton scattering cannot be easily done off hadrons other than neutrons and protons, dilepton pair production offers the opportunity to do π, K scattering off of nucleons to learn of their quark structure. A recent experiment (36), exploring the ~~small~~ y, large x region, measured cross section ratios for charge pions on carbon nuclei (equal number of protons and neutrons). A $\bar{d}$ in the π^+ annihilates with a d in the nucleons; an $\bar{u}$ in the π^- annihilates with a u in the target nucleons. Therefor one expects:

x & y measures the same thing

$$\frac{\sigma(\pi^+)}{\sigma(\pi^-)} = \frac{\left(\frac{1}{3}\right)^2}{\left(\frac{2}{3}\right)^2} = \frac{1}{4}$$

which agrees with observations. (2) From the above expression for the scattering cross section, one can readily see that:

$$m^3 \frac{d\sigma}{dm}$$

is a function of the ratio $\frac{m^2}{s}$ alone. Available data (37) support this prediction of a universal dilepton 'scaling'

function. Encouraging results were achieved by Peierls et. al. (38) to combine the results from various dilepton experiments, and show that scaling holds from BNL energies (20-30 GeV) up to Fermilab energies (400 GeV).

Since it is verified that Bjorken scaling is not exact in lepton-nuoleon scattering experiments one might suspect a violation of scaling in dilepton production experiments. So far, the available dilepton data has not been accurate enough to reveal 20-30% discrepancies that one might look for, has not been accurate enough to reveal any discrepancies on the 20-30% level. Light may be shed on this situation with the publication of 200-300-400 GeV data of S Herb et. al. (39).

(3) Yamagouchi (40) pointed out that the production cross section for the intermediate vector boson (W) in proton-nucleus collisins can be related (through the conserved vector current hypotesis) to the production cross section of virtual photons. Using CVC, assuming figure ( ) to be correct and taking the isoscaler contribution to dilepton production to be small, the production cross section for W's is predicted to be larger than :

$$0.11\ M_W^2 \left.\frac{d\sigma}{dm}\right|_{m_W}$$

Several current, detailed reviews of predictions deduced from Yamagouchi's idea have recently been published (41).

APPARATUS OVERVIEW

The dual experimental apertures in this experiment were symmetric about the incident beam line, and were of identical large solid angle (figures 2 and 3). The horizontal aperature opening was chosen so as to straddle 90 degrees in the CMS at various possible accelerator energies (67 mr. at 500 Gev., 96mr at 200 Gev).

A dipole magnet was placed in each arm downstream of the aperature defining collimators. These served to sweep low momentum particles oue of the aperature and select higher momentum particles of one sign, deflect them vertically out of the neutral beam and define their momentum. Typically, an inch separated the detectors from the +-3.5 mr. neutral beam envelope. A change of current in these magnets provided a means of improving the mass acceptance in either the high or low mass region, while maintaining a significant acceptance overlap from one current setting to the next (figures 4 and 5). The momentum acceptance of a spectrometer arm, for two magnet settings, is shown in figure 6.

Four planes of trigger counters downstream of each magnet served as a fast trigger for the experiment (figure 7). The voltages of the T0. T1. S2 and T2 counters were set so that they would efficiently detect minimum ionizing particles. The threshold of the T2 counter discriminator was set to require a pulse height of about 15 times minimum

APPARATUS OVERVIEW

The dual experimental aperatures in this experiment were symmetric about the incident beam line, and were of identical large solid angle (figures 2 and 3). The horizontal aperature opening was chosen so as to straddle 90 degrees in the CMS at various possible accelerator energies (67 mr. at 500 Gev., 96mr at 200 Gev).

A dipole magnet was placed in each arm downstream of the aperature defining collimators. These served to sweep low momentum particles oue of the aperature and select higher momentum particles of one sign, deflect them vertically out of the neutral beam and define their momentum. Typically, an inch separated the detectors from the +-3.5 mr. neutral beam envelope. A change of current in these magnets provided a means of improving the mass acceptance in either the high or low mass region, while maintaining a significant acceptance overlap from one current setting to the next (figures 4 and 5). The momentum acceptance of a spectrometer arm, for two magnet settings, is shown in figure 6.

Four planes of trigger counters downstream of each magnet served as a fast trigger for the experiment (figure 7). The voltages of the T0, T1, S2 and T2 counters were set so that they would efficiently detect minimum ionizing particles. The threshold of the T2 counter discriminator was set to require a pulse height of about 15 times minimum

ionizing. This requirement, made on this counter which was placed dirctly behind the first layer of lead glass, favored detection of particles showering early in the lead glass.

To do so would have limited the maximum proton flux severely.

~~Since~~ No particle detection was done before the vertical bending magnets. Thus the target origin of an event could be checked only in one dimension (the horizontal). The lack of redundancy in the vertical dimension was not considered serious. (Target out/target in) rates were low (1/250) and the projected horizontal target distribution for events was clean. Since electrons are sensitive to relatively small amounts of material in their path, inscattering does not represent as large a problem as in dimuon experiments. High energy electrons entering the large Z material of the collimator walls will quickly ~~begin to~~ loose energy through bremsstrahlung. Those few electrons that manage to rescatter into the aperature are of low energy and do not represent a background problem.

electron pairs

The particle hits in the wire chambers and hodoscopes downstream of the magnets served to ~~identify~~ define particle tracks, and each track served to measure the particle ~~magnet~~ momentum magnetic bend angle and so specified its momentum. A plot of the momentum and mass resolution of the apparatus is shown in figures 8 and 9, respectively.

To separate electrons from the 10^4 more copious hadrons, two identical total absorbtion lead glass calorimeters were employed. The characteristic shower

development of electrons in the 4 layers of lead glass served to distinguish them from other charged particles. On-line, a threshold requirement on the fanned in signal from the blocks of the first 2 lead glass layers served to reject both low energy particles and higher energy particles of 'late' shower development (hadrons, typically). Off-line cuts on an event's fractional energy deposit in each layer of lead glass ('shower' cuts) and on its total calorimeter deposit (Energy deposit=Particle momentum; E=P) further served to refine the sample of electron candidates. The trigger of the experiment provided a single arm rejection factor of $5\ 10^{-2}$, while off-line cuts improved the overall rejection to 10^{-3}.

Backgrounds in this experiment were due primarily to 'accidental' electron pairs, hadrons faking electrons and electrons due to hadron induced photons which convert via Dalitz process or ~~Dalitz or gamma conversions~~ in the material in the beam. These backgrounds can be of either an 'accidental' or 'correlated' nature. In an accidental pair event, the detected particles originate from unrelated interactions in the target and their mass spectrum can be simulated by the off-line pairing of single arm events. Correlated particles are those which originate in (or 'near') the same target interaction. An upper limit on the contribution of correlated pairs to the overall dielectron background was estimated using actual 'in time' pair data recorded during the course of the experiment.

As mentioned in this paper's introduction, the dielectron experiment reported on here ran during two separate periods, under 2 designations, E288 and E494. Table ( ) provides a list of the integrated intensities for both experiments. Modifications made to the apparatus for E494 include the addition, on each arm, of two threshold gas Cerenkov counters for hadron identification, and an 8 nuclear mean free path hadron calorimeter, placed behind the lead glass calorimeter. Two planes of MWPC's (a horizontal and a nearly vertical chamber) were added downstream of the analysis magnet on each arm to provide improved momentum resolution and hadron rejection. These chambers had 2 mm. wire spacing.

The Cerenkov and hadron calorimeter counters were to be used primarily for the study of the e494 dihadron data (ref. 49). A further description of these counters will not be presented here, since they, generally, did not play a major role in the dielectron data analysis. Information from the Cerenkov counters was used the improve an estimate of the dielectron hadronic background, and Table 7 provides some basic information on their running modes during E494.

The E288 and E494 dielectron experiments were very similar in most details, but differed in the following:

1. The additional planes of MWPC's, positioned just downstream of the magnets, improved the E288 mass resolution in the 3 Gev region by a factor of three and in the 6 Gev region by a factor of two.

2. In E494, less time was devoted to fine tuning the lead glass calibration. In E288, the lead glass and MWPC resolutions were comparable and one hoped to improve the overall mass resolution by folding together the energy and momentum measurements in the final mass calculation. This was desirable because the two resolutions were complementary. As the MWPC resolution worsens at high momenta, the lead glass resolution improves. In E494, however, the significant improvement in MWPC resolution made the need for fine lead glass resolution less important.

3. E494 used its improved J/ψ mass resolution to adjust the calibration of the analysis magnets in the difficult-to-map region near the magnet pole pieces. This will be discussed in a later section concerning the

analysis magnets.

4. The more complex hadronic trigger of E494 required a D.C. logic deadtime of 250 ns.

These points summarize some of the differences between E288 and E494. Both experiments had roughly equal sensitivity and were run under similar intensity conditions. Identical general analysis procedures and cuts were used for both data sets. The addition of wire chambers after the magnets added an important additional coordinate to the linear least squares fit done to particle trajectories, and the somewhat less carefully done lead glass calibration barely increased the E/P cut inefficiency (see below) for electrons.

Given the similarity of the two experiments and their modes of analysis, this paper will not provide a parallel discussion of both experiments at all points where they differ. It will concentrate on the earlier experiment, E288 and all studies will be done exclusively with E288 data, except where specified.

J. BEAM

The experiment reported on here utilized 100, 200, 300 and 400 Gev momentum protons provided by the Fermilab accelerator. The typical spill duration was 1 second, with an accelerator cycle time of 6-7 seconds. Incident intensities for this experiment ranged from a few 10^9 to a few 10^{10} protons per pulse. The beam particles were bunched in 1 ns. wide groups (RF buckets), separated by 20ns. Typically 3-4 10^7 filled bunches were in each spill, so the number of incident protons ranged from 70 to 700 per bucket. 10 - 20% of these protons interacted in the thin Be target used for data taking.

These accelerator 'buckets' were not always uniformly populated. Superbuckets of 5-10 times the average bucket size were monitored during the course of the experiment and eliminated when possible by judicious accelerator tuning. On a pulse-by-pulse basis, a cut was made on the final data sample on a quantity proportional to $\sum N_i^2$ where N_i measures the proton population of hte ith bucket and the sum is carried out over the full spill length (see ~~section~~ Appendix on 'Induty'). This cut served to eliminate events that were accompanied by grossly non-uniform spill structure. Figure 10 presents some sample photographs of this experiment's oscilloscope macro-spill monitor; figure 11 presents

photographs of a PHA display of bucket to bucket intensity variations.

* As previously stated, the experiment was extremely sensitive to time structure in the beam. Accidental rates were a prime source of background. The running conditions were a judicious choice between the desire for data and the fear of accidentals. This led to an observation of accelerator performance and the consequent "discovery" of "typebuckets".

2. INCIDENT BEAM INTENSITY MONITOR (SEM)

A secondary emission monitor (SEM) was used to measure the number of protons incident on target. Beam traversing the thin copper foils in the SEM knocked out secondary electrons and their integrated charge, collected over the spill, provided a measure of the incident number of protons. The SEM's relative calibration was checked once every 3-6 months during the course of the experiment. A sample of the foil calibration results from this experiment's SEM is presented in Table 8.

Predictions and measurements have been made regarding the dependence of SEM yield on various factors - time, incident energy, beam intensity, spot position, incident particle type etc (50). Some sample Fermilab SEM calibration data for 2 incident energies and 2 types of spill structure is presented in Table 8.

The absolute calibration of the SEM was based on information for the production of radionuclides in irradiated foils. For this purpose, the measured cross section for the production of ^{24}Na in Cu was used (with a cross check provided by ^{52}Mn production). ^{24}Na was chosen for its high threshold energy, its 15 hour half life and the ease in detecting its emitted gamma rays.

The cross section for ^{24}Na production was assumed to be 3.5 mb. This value was originally taken from a paper of Hudis (51), who for the case of incident protons, found the ^{24}Na production in Cu to be constant over a 7 - 30 Gev incident energy range. A Fermilab proton department measurement for 400 Gev protons supports the use of 3.5mb. at this higher energy.

Since the SEM was 2.5" in diameter, unfocused particles in a beam halo or random spray down the beampipe from upstream could give rise to spuriously high SEM counting rates. Beam displacement studies and defocusing tests indicated that these potential problems were a minor concern.

As determined from horizontal and vertical target sweeps, the beam spot size on target was 20 mils horizontally and 25 mils vertically. During running, the vertical and horizontal beam position was monitored on a television display of the vertical and horizontal wires of a split wire ionization chamber (SWIC), with 1/2 mm. wire spacing. This was positioned after the SEM, 69cm. upstream of the target.

3. TARGETS

One target was used for the main data aquisition of this experiment. It was made of Beryllium, 4" long, 1" high and .0088" thick. Along its length, it provided 0.27 interaction lengths of material; 1.3% of a radiation length was seen by particles exiting at 50 mr., and 0.7% of a radiation length at 95 mr.

The choice of such a target represents a compromise among several desires. One needed a target substantial enough to provide a large target in/out ratio, without being so long as to create collimator wall illumination problems. It was to be narrow and of material with long radiation length to reduce as far as possible the opportunity for gamma rays to convert into background electron-positron pairs (the pi zero lifetime is $8.3\ 10^{-17}$ sec or $2.5\ 10^{-6}$ cm.).

In addition to this main target, three wider targets (0.063" thick) were available, and could be easily moved into the beam under remote control. A wide Be target (which intercepted the entire beam) was used to measure the targeting efficiency (65%) of the standard thinner Be target. The second wide target was of copper and was utilized when special studies or electron calibration required an increase in the fraction of gamma conversion

electrons in the beam. The final target was of aluminum and consisted of a .063" square bar suspended from above and below. This was used in cross checking the vertical beam position and in measuring the vertical spot size.

Targeting was monitored by a three fold coincidence scintillation counter telescope (referred to as NDN). It was positioned in the neutral beam, at station 1 on the 'down' arm of the spectrometer, near 83 mr. The target in/out rates for this counter were 250/1. On the 10% level, NDN's counting rate was unaffected by changes of magnet current and only a slight correction was required for its non-linearity at high intensities:

$$NDN \times \frac{1}{(1 + A \times NDN^2)}$$

$$A = (1.0 \pm 0.25) \times 10^{-11}$$

The rates of this counter were monitored both with and without various vetoes and/or gates (beam gate, electronic's busy etc.), and its counting rate was used to provide the overall normalization of the pair cross section.

TARGET BOX

1.52 meters downstream of the target was a symmetrid. tungsten lined precision collimator (figure 12). This defined the 50 mr. edge of the horizontal aperature and allowed vertical production angles in the +-4 mr. range. The collimator was 0.61 m. ? long and was lined with tungsten to maximize the number of radiation lengths seen by particles that were out of the aperature and might rescatter in from the shielding walls. Downstream of this, also centered on 0 degrees was a water cooled beam dump which served to attenuate the primary beam that did not interact in the target. The experimental horizontal aperatures on both sides of the dump were lined with steel to provide semi-precision collimation and to increase shielding around the dump. No vertical tapering of shielding in the target box was done downstream of the precision collimator (+-1.13" was allowed).

A continuous flow of helium to the target box was maintained in an effort to minimize the number of radiation lengths of material in the aperature before the magnet bend.

COPPER FOILS AND LEAD PLUG

The air gap of 0.86 m., shown in figure 12, provided room for positioning a compressed air driven mechanism for inserting, into the aperature, thin copper foils (0.036,0.076,0.114 cm. thick) or a 5.08 cm. thick block of lead. The copper foils served to increase material in the aperature by 2-4 times and this facilitated further study of gamma ray conversion backgrounds. The 5.08 cm. block of lead provided a sufficient number of radiation lengths to eliminate electrons and gammas from the beam; this data sample was useful in studying hadronic backgrounds. Lead was chosen so as not to introduce an excessive number of interaction lengths of material into the beam for inducing appreciable hadronic showers or charge exchange conversions.

Typically, during a run in which 'foil' data was taken, the foil control mechanism would be set into a fixed cycle of foil and no foil states, moving the foils in and out of the beam between accelerator pulses. The pulse by pulse state of these foils was read out as a bit pattern into the computer. These bits were set by microswitches on the moving foil assembly. It was considered desirable to include in the same run both standard (no foil) and 'foil' data to best sample beam under average data conditions. The fraction of integrated intensity for each foil state is

given in Table 9 .

Positioned after the foils, in this same area, was a rectangular aperature made from ½" thick bars of tungsten, whose opening defined the +-3.5 mr. vertical aperature.

The shielding pile (figure 12) was of steel and 2.22 m. thick, along the beam direction. Its aperature was oversize and untapered in the vertical (+-3.8cm.); horizontally, its edges provided collimation at 46 and 96 mr. The symmetric aperatures in the shielding in both arms were vacuum sealed, connected to the vacuum boxes in each of the analyzing magnets and evacuated to 0-4 mm. Hg. The pressure in each magnet-shielding pile aperature was monitored on a pressure gauge viewed by a close circuit television camera.

MAGNETS

The purpose of the two analysis dipole magnets in this experiment has been described in the introduction. Briefly, they deflect charged particles from the neutral beam, sweep low momentum partioles out of the aperature and define the momenta of particles leaving tracks in the MWPC - hodoscope system downstream. Particles were swept up into the aperature of one arm and down into the aperature of the other. Earlier Monte Carlo studies showed this arrangement to have greater acceptance for symmetric decays than up-up bending (for example) and one less dependent on pair transverse momentum.

Magnet power and cost considerations plus the need for a long lever arm to bend particles out of the neutral beam suggested that the magnets should be placed as far upstream as possible. The center of the 3.05 m. long magnets was situated 11.3 m. from the target (figure 12). Using tapered pole pieces, the magnet's horizontal aperature opened from 18 to 24". to subtend 47mr. in the laboratory system (figure 13). Vertically, the magnet gap was an untapered 10". This large gap height allowed for a possible vertical production angle aperature increase to +-10mr., instead of the chosen +-3.5 mr. The requirement that charged partioles be free and clear of the neutral beam

before detection, the limited bend power of the magnets and the finite size of the lead glass array set limits to the usable vertical aperature. Increasing the vertical production angle acceptance increased the size of the neutral beam envelope and forced detectors farther from the region of high momentum particles.

A horizontally tapered aluminum vacuum box was inserted inside of each magnet. Its gap height was 7.75". These boxes were coupled to the shielding pile collimators and evacuated during running.

Momentum and mass acceptance curves for the magnetic spectrometer are shown in figures 6, 4 and 5. Changes in magnet current provided a means of more efficiently exploring lower or higher mass regions, while maintaining a large acceptance overlap with other current settings.

The 4 magnet coils (0.105 Ohms each) were powered in series and so carried identical currents. Early Monte Carlo studies indicated that J/ψ acceptance was not improved by running assymmetric currents. In addition, power load and supply requirements for two separate current systems were seen as considerable. Voltage limitations of the power supplies and substation load limits set the maximum magnetic field at 11.7 kg., which corresponded to a magnet current of 1430 amp. The magnet settings used during the course of this experiment were 400, 600, 800, 960, 1100 and 1300 amp.

The current in the magnets was monitored by a Hall probe in each magnet, a shunt and a Fermilab transductor readback from the power supply. These four values were recorded on a run check sheet during every run. Using their measured values from the data runs, one can calculate each monitor's average value and standard deviation for a given magnet setting. The observed fluctuations in the monitors were independent of magnet setting and were small. The fluctuations had the following values: transductor, 0.098%; shunt, 0.32%; Hall probes, 0.13%. Added in quadrature, these fluctuations contribute an error of 0.12% to the overall momentum resolution. Compared to the resolution of the remainder of the spectrometer, this source of error is negligible.

In calculating the transverse momentum kick due to each magnet, all the available monitors were checked for 1% consistency, and they were weighed equally in the final transverse momentum kick calculation. If one value failed the consistency check, it was eliminated and the two remaining values were compared. If these two were inconsistent, no momentum kick value was provided for the off line analysis program (no runs were found in this catagory).

The Hall probes were mounted inside the vacuum box of each magnet to separately monitor their fields. The calibration of the Hall probes was done against an NMR

calibrated gaussmeter and, in operation, the probes provided reproducible values with 0.1 to 0.2% fluctuations observed over a month's time. Hysterisis on the negligible 0.1% level was observed in them. No measurable magnet hysterisis was found.

The magnetic field of the analyzing magnets was mapped parallel (z) and transverse (x,y) to the beam direction. The measured data points were fitted to first order solutions for the magnetic field shape (appendix 3) and agreement to 0.2% was achieved. To this same accuracy, the central field values of the magnets were identical, and the magnetic field shapes in the four magnet (x,y) quadrants were the same. Because of the tapered horizontal aperature, the magnetic field was not constant along the beam direction (z). This shifted the effective magnetic bend plane 2.7" upstream of the magnet center line.

Given the finite size of the probe used for magnet calibration, determination of the field shape near the magnet pole pieces was difficult to achieve. Higher power terms in the field expansion of appendix 3 could not be well determined. These terms predict relatively large corrections to the momentum near the magnet pole pieces.

In E494, the magnet calibration was redone and adjusted using the E494 J/ψ signal with its improved resolution. A study of the magnet field map showed that the field in the magnets could be adequately described, ignoring high order

terms of the magnetic field expansion:

$$B_x = B_x(0,0)\left(1 + a\left(x^2 - y^2\right)\right)$$

$$B_y = B_y(0,0)\left(-2a\,xy\right)$$

$$a = 0.00015$$

A proper magnetic measurement determination of 'a' was made difficult by systematic fringe field effects and an inability to measure the field near the magnet pole pieces. Magnet 'calibration' with E494 J/ψ data revealed that a best fit required a=0.0007. Applying this magnet calibration to the E288 data caused mass shifts on the order of 0 to 50 Mev. A summary of E288 J/ψ mass values using both the E288 and E494 magnet calibrations is presented in Table 10. Some of the magnet current dependence of the E288 J/ψ mass is removed when the E494 magnet calibration is used. Figures 54 and 56 show the overall E288 cross section plots using the E288 and E494 magnet calibrations, respectively.

TRIGGER COUNTERS

After allowing sufficient drift space for separation of charged from neutral particles, there followed 4 planes of scintillation counters - T0, T1, S2, T2 - making up a trigger telescope pointing towards the target.

The three counters T0, T1, S2 were located at stations 1, 2 and 3 respectively (figure 7). Each was ~~set to fire~~ adjusted so that would provide 100mv pulses, sufficient to fire the associated discriminator (set to 30mv threshold) on minimum ionizing particles and their purpose was to provide for unbiased detection of charged particles passing through the aperature. T0·T1·S2 is referred to as the T trigger: TU refers to a T trigger on the up arm. TD refers to a T trigger on the down arm (TUD=TU·TD).

Some details of counter construction are shown in figure 14 and details are specified in Table II. T0 was made up of 5 strips of NE110 scintillator and used Amperex 56AVP tubes, which were current boosted to prevent sagging in high rate running. The individual T0 signals were cabled to the trailer on disc loaded coaxial cable (hard line). T1 consisted of 8 counters. made similarly to those of T0, with only the small angle (high rate) counters boosted. Pairs of T1 counters at the same height were passively fanned in and cabled on hard line to the trailer.

S2 was a counter situated behind a sheet of 2.3 radiation lengths of lead placed before the lead glass array It used RCA 6342A photomultiplier tubes which had been tested and were found to be tubes of good long term stability and desirable rate independent behavior. The uniformity of pulse height response of S2 to minimum ionizing partioles over its length was improved by the use of a yellow photographic filter (Kodak Wrattan #4) and a 8-10" sheet of black construction paper placed just below the light pipe scintillator junction. This filter was sandwiched between two 1/8" discs of lucite, sealed around the edge with epoxy and glued between the photomultiplier tube and the lightpipe. The filter served to absorb blue light, whose absorbtion length in scintillator is shortest. A 35% change in pulseheight over the scintillator length was thus reduced to 10%.

On each arm, the S2 dynode signals were fanned in, amplified and cabled to the trailer on hard line. Their individual anode signals were sent up on RG8 cable and digitized.

T2 was nearly identical to S2 in construction and cabling (there were 13 T2 counters covering the same aperature as S2 but they were slightly overlapped). As shown in figure , T2 was placed between the first and second layers of lead glass at station 3. Large pulseheight in T2 meant that an entering particle had initiated its

shower in 2.3 radiation lengths of lead and 6.5 radiation lengths of lead glass, a signature of electron like behavior. The T2 discriminator threshold set the pulse height requirement on the fanned in T2 signal at 15 times minimum ionizing. This signal was referred to as T2(HIGH). When 'anded' with the T trigger (T0·T1·S2·T2(HIGH)), this provided the fast logic 'E' trigger.

A second (not independent) trigger was used to crudely monitor the EUD pair trigger. The 'F' trigger was made up of T1 and T2(HIGH) (T1UD·T2UD(HIGH)). This trigger did not include S2 and the 48" long, high rate T0 counter.

Some typical trigger rates for various currents are given in tables 12 through 16, in various intensity bins (1-8). The 'T' to 'E' rejection is illustrated in the histogram of figure 15. Typical trigger counter efficiencies are presented in table 17.

Wow! Neuer in fahrer Anglisch

HODOSCOPES

Table .11 presents information concerning the construction of the V1, V2 hodoscope planes at stations 1 and 3 (figure). These were made up of vertical strips of NE110 scintillator with UVT light pipes and individual RCA 6655A tubes. The scintillator strip widths were varied to adjust for the changing rates across the horizontal aperature. Each hodoscope signal was amplified by 10 in the experimental area and the individual signals were cabled to the experimental trailer. All hodoscope channels were available to be read into the computer. A typical efficiency per hodoscope plane was 97%.

did we do any tricks to equalize top to bottom pulse height? or did we just think about it?

MULTIWIRE PROPORTIONAL CHAMBERS (MWPC)

The 7 MWPC's on each arm of the spectrometer (figure) were primarily responsible for the momentum and target resolution achieved in this experiment. Table 18 provides a summary of chamber construction information and Table 19 provides a resolution summary. The chambers were of two types - 'Y' chambers (horizontal wires) and 'P','Q' chambers (slanted wires, 7.125 from the horizontal. The entire readout system for the chambers (to be described later) was designed and built by Columbia's Nevis Laboratories.

Mounted on the chambers were amplifier-discriminator cards, each of which provided for the readout of 8 wires. Electron drift time to the wires was estimated to be 15 ns./mm.; electronics deadtime per wire was 500 ns. External voltage adjustments allowed one to vary the discriminator threshold and/or output pulse width on all channels of a particular chamber.

The discriminated outputs of the cards were cabled to the experimental trailer on stripline (ribbon) cable* of 32 wires per cable. In addition to the individual wire readouts, each chamber was provided with an output which was an 'OR' of all chamber signals. This would have allowed the chambers to be used in a fast trigger.

* Manufactured by —

The gas mixture used for the chambers was 0.097% freon. 17.2% CO2 and the balance was argon. Individual chamber efficiencies were in the range of 98-99%.

LEAD GLASS CALORIMETER

Electron identification in this experiment was provided by identical lead glass calorimeter and magnetic spectrometer apparatus on each arm. An entering particle's longitudinal shower development and total energy deposit in the lead glass provided information which served to identify it as an electron or non-electron event.

The lead glass calorimeter in this experiment served as a total absorbtion Cerenkov counter for containing the cascade showers initiated by incident electrons. Many descriptions exist in literature relating how the passage of a single electron through matter can give birth to observed large numbers of electrons and positrons. Both analytic calculations (52) and Monte Carlo simulations (53) have been used to test the assumed physical model.

On entering matter, electrons typically undergo bremsstrahlung to produce one or more photons, the photons convert to e+e- pairs, and the process starts over again, but with an increased number of electrons of decreased average energy. The growth of the shower will continue until pair production is no longer the dominant mode of photon interaction, and the shower will die out as electrons fall in energy and loose larger fractions of their energy to the medium in small, relatively continuous ionization energy

transfers. Heitler (54) points out that such cascade showers were first observed in Wilson Chamber experiments, and that the most direct evidence for their physical nature comes from photographic plates that record the actual shower particle tracks (figure 17).

Figure 18 presents some formulas of Cerenkov and bremsstrahlung radiation. When integrating the Cerenkov formulas over frequency, it is important to note that the condition $n>1/\beta$ bounds the available range of integration. A schematic plot of the index of refraction (n) for a typical optical medium is shown in figure 19a. The restricted range of integration at high frequencies usually insures that Cerenkov energy losses will be small compared to losses due to other available radiative mechanisms.

Electrons and positrons will generate Cerenkov light in lead glass until they reach kinetic energies near 0.13 MeV. Monte Carlo simulation programs which trace electron showers down to energies close to this lower limit energy indicate that the total track length traversed by the e+e- particles in an electromagnetic shower is proportional to the energy of the original, initiating electron. Since the energy loss to Cerenkov radiation is independent of electron energy over a wide energy range (see figure 18b), the total Cerenkov light emitted in a cascade shower will be proportional to the total track length of the e+e- particles, and thus proportional to the initiating electron's (or positron's)

energy. This suggests the use of a transparent medium, of preferably short radiation length, to serve as an energy calorimeter. Lead glass was chosen for this experiment.

While bremsstrahlung energy losses are greater than those due to Cerenkov radiation in lead glass (bremsstrahlung photons range in energy from 0 up to the maximum allowed by the radiating electron), energy losses to Cerenkov radiation in a band near the visible region of the spectrum (400-800nm.) are typically orders of magnitude larger than bremsstrahlung losses in the same restricted frequency range. Given the frequency dependence of glass transmission, and a photocatode's sensitivity to radiation near the visible region of the spectrum, a phototube can be used to sample emitted radiation in lead glass near the visible region. The system's limited sensitivity to frequencies removed from the visible range makes it insensitive to the more prevalent bremsstrahlung radiation.

The digitized pulse area measured from each lead glass block's photomultiplier tube will be proportional to the block's shower energy deposit; the constant of proportionality is referred to as the lead glass block's 'calibration' constant. The determination of a set of these constants for all lead glass blocks, and the monitoring of their variation with time will be discussed in the section on lead glass calibration.

The configuration of lead glass blocks for one arm is shown in figure 20 . Each array consisted of 24 (15×15×35)cm^3 blocks and 72(15.25×15.25×45)cm^3 blocks. Some properties of the lead glass are summarized in figure 21 . Many details pertaining to this calorimeter are described adequately elsewhere (55) and will not be reconsidered here.

An RCA 8055 photomultiplier tube was glued to the small face of each lead glass block with Kodak HE10 assembly cement (n=1.58). Aluminum foil (1 mil thick) was wrapped about the glass up to the tube base, and this foil was put at cathode potential (through a 1.5M resistor) to limit leakage currents flowing across the photocathode. The block sides and remaining small face were covered with mylar (5 mil) to mechanically protect the aluminum foil surface and provide electrical insulation for the ungrounded foil. To light tight each block, black polyethylene (6 mil) was used. A cylindrical mu metal shield was placed around the phototube, and soft iron foil was wrapped about the upper portion of the lead glass block to extend the magnetic shielding beyond the photocathode about one tube diameter.

Blocks in each lead glass layer were stacked tightly together with no significant gaps. The layers themselves were separated by 2-3 inches. RG-8 cable (low dispersion) was used to transmit the anode signals from each block to the experiment's trailer.

The epsilon (ε) signals of the D.C. logic were derived on each arm, from the dynode signals of blocks in the first two lead glass layers. These dynode signals were passively fanned-in, inverted, amplified and cabled to the trailer on disc loaded coaxial cable. There this signal's pulse height was discriminated; the threshold setting of the discriminator on each arm determined the minimum energy deposit in the first two lead glass layers necessary for the D.C. logic ε bit to be set.

Both lead glass arrays were maintained in temperature and humidity controlled huts. A lead sheet (2.3 radiation lengths) was placed directly in front of the first layer of lead glass to increase the observable differences between hadrons and electrons. Lead was chosen for its small ratio of ~~absorption~~ nuclear interaction to radiation length.

FAST TRIGGER LOGIC

A sketch of the fast trigger logic is shown in figure 22. The T trigger, made up of (T0, T1, S2) combinations was meant to serve as an unbiased trigger on the charged particles passing through the aperature; the E trigger, with its additional T2 pulse height requirement (T2(HIGH)) was biased towards particles initiating showers in the previous 2.3 + 6.5 radiation lengths of material (E/T= 0.25)

T0, T1, S2 signals were fanned in, in combinations designated in Table 20. Timing was set by T1, the shortest counter with the least time jitter.

Lead glass pulse height information was not included in the fast trigger logic decision. Due primarily to the 'slowness' of the RCA 8055 photomultiplier tubes, the summed energy from the first two lead glass layers (referred to as $\mathcal{E}$) arrived rather late for the fast trigger. Time jitter and pulse height slewing problems associated with such a trigger would have complicated, but not excluded, the inclusion in the fast logic decision. This '$\mathcal{E}$' pulseheight was present in the D.C. logic and provided an important component in the overall electron trigger ($\mathcal{E}$/E=.2). Typical efficiency curves for the epsilon bit of the slow logic are shown in figure 23.

The D.C. logic (figure 24) provided a second (and final) stage of decision after the fast trigger. The fast trigger output (TGI) served to gate hodoscope , trigger counter and lead glass calorimeter information into coincidence registers (CR's) in the D.C. logic, where the information was stored as DC level 'bits'. At D.C. logic decision time, information derived from this stored data would be tested to see if it satisfied certain logical conditions, before initiating a computer readout. At the expense of an increased deadtime (typically ns), this system allowed for the making of complex logical decisions without requiring the careful timing of fast pulse electronics. Each fast trigger accepted by the logic generated a 105 ns. deadtime (adjustable) to cover its operations. A tight fast trigger served to minimize the overall logic deadtime of the experiment.

The operation of the D.C. Logic can be described as follows. After the initiating fast trigger, the input information stored in the CR's was logically processed('or'ed, 'and'ed, 'matrix'ed etc.) in the available deadtime and synthesized into resultant outputs that were used to set master bits for the upcoming logical decision.

Each one of the requirements to be logically tested in the final trigger decision was represented as a D.C. level on one of the 16 data bus lines in a pin logic module crate. The configuration of 16 jumper pins in each pin logic module would determine whether a particular data bus level ('bit') was to be required, vetoed on or simply ignored.

The sequence of 'pin' requirements of each logic module usually corresponded to the signature of a particle type in the apparatus (hadron, electron, muon). Each module would output only if the data bus information, at decision time, satisfied the logical 'and' of all its jumper pin requirements. The modules were strobed for their final decision 105 ns. after initiation of the process. Their outputs were fanned together into a 'TGO' module and its output initiated a computer readout.

A further level of complexity could be achieved in this system by the use of an external cable connecting the output of one logic module to the 'L' input of another. This served to 'and' the modules together.

This experiment used one pin logic module crate for each spectrometer arm (there were about 20 modules and 16 data bus lines per crate). Arm to arm coincidences were made by the use of jumper cables between pin logic modules in separate crates. The triggers for this experiment are specified in table .

As system inputs, the D.C. logic was provided with hodoscope, trigger counter and lead glass calorimeter information and it required a trigger to strobe this pulse information into coincidence registers. As system outputs, the TGO module provided strobe signals for transfer of hodoscope and logic bus information to Camac level data buffers; it generated gates for the ADC's; and after an appropriate delay (12 microseconds) to cover digitizing action and settling, it provided a trigger to the computer for initiating the event readout. In addition to these outputs, the individual pin logic modules generated a pulse suitable for scaling, so that their rates could be conveniently monitored.

After the hodoscope, trigger counter and logic bus bit information had been stored in Camac level buffers, the D.C. logic could be cleared and made 'live' once again, so that the scalers of the pin logic modules could continue to monitor rates. The MWPC electronics could not be regated at this time, since no second level buffer was provided for storage of its information. It would have to await completion of the computer readout before being regated.

Digitizers and Digitizer Readout System

This section will describe the readout system for the Nevis ADC's and its various options.

We have in the system 256 channels of ADC's. The digitizers and scalers in their normal operation will digitize 500 pC full scale. Full scale being 1024 channels as the scalers are 10 bit scalers. Of the 256 channels, 192 are for the lead glass. These 192 digitizers are the quad types. Each unit has a common gate, four BNC signal inputs and four NIM level pulse train outputs in the rear. The scalers for the new digitizers are slightly different from those of the previous experiment.[62] There is a line in the dataway which, if enabled, will allow the scaler to overflow 1024, resetting it to 0. This option would have given us an effective 2048 channels if used in conjunction with the variable format module (VFM). The other 64 channels are the ones used in the previous experiment. All scalers were placed in NEVAC crates 3 and 4, so as not to use up valuable space in the master crate (crate 1). (NEVAC is the Nevis version of a CAMAC crate made with ECL (Emitter Coupled Logic) but compatible with CAMAC on the branch highway level.) For calibration purposes, the slope voltage of the ADC's is set to 1.2 V (instead of 24.0 V) to give us 20 times greater gain. A bias voltage is also changed to balance the circuit. This

high gain setting was used for muon straight-through calibration (see ~~Appendix III~~ SECTION ON LEAD GLASS CALIBRATION)

Other features of our ADC's are:

1. Base line restoration: an electronic servo clamps the input stage base line to its value for the last few μs. Thus only signal above the base line is digitized. This allows us to filter 60 cycle and other low frequency noise.

2. Pedestal injection into linear range of ADC: pedestals were normally in channels 30-40 with a standard deviation of about 1%.

3. Ground isolation: the ADC's have only one ground, that of the DC coupled input. The pulse train outputs are transformer coupled. We are able to minimize ground loop problems.

We now discuss the readout system itself. The Nevis CAMAC dataway is 16 bit for the read lines. To use computer core space efficiently and reduce readout time, the data for each octal scaler is packed from eight 10 bit words into five 16 bit words. This is accomplished by the scaler packer module and the branch driver. Crates 3 and 4 are not connected to the branch highway directly, but through crate 1's dataway. In crate 1, we have two master crate links (MCL) which connect to slave crate links (SCL) in crates 3 and 4. This eliminates the need for two additional complicated crate controllers. The crate controller in crate 1 acts as the crate controller

for crates 3 and 4. To a branch driver, it would appear as if crates 3 and 4 were normal crates on the branch highway.

As 256 ADC's are a large number to read out (when most of them will be pedestal anyway), we designed the crate linkage so as to allow the hardware (i.e. hodoscopes) to determine the groups of lead glass blocks to be read out. This is accomplished by addressing the MCL directly, which activates the dataway variable line (V). This is a signal for the variable format module to take over all dataway addressing operations. When an ADC read is executed, the status of the 16 individual inputs to the VFM determine the groups of octal scalers to be read. The bit pattern of header words sent out initially by the VFM informs us as to which octal scalers are to follow the header word. Using the VFM, we were able to cut down event size by about 50%.

The digitizers were calibrated for their high gain setting. The slope of the linear response of the ADC was measured by changing the pedestal injection voltage. This was done for both the normal and high gain settings. The ratio of the slopes was the relative gain of the two settings. This was then incorporated into the muon straight-through calibration. In addition, tests of digitzer linearity and stability were made. The non-linear term in the quadratic fit to the pedestal data indicates a 1/2 (digitizer) scale error of 0.6% and a full scale error of 1.3%. Digitizer gains fluctuate with time on the level of σ = 0.4% over a period of 2 months.

MWPC ELECTRONICS

The MWPC electronics, designed and built at Nevis Laboratory, provided a system for reading out the chamber hits as encoded addresses. Signals from the amplifier-discriminator cards (8 wires/card) on each chamber were transmitted on 32 wire stripline (ribbon) cable to the experimental trailer, where each set of 32 was connected to a coincidence register (CR) card. Each MWPC bin could contain 23 of these cards, in addition to a bin 'encoder' card.

Wire information was strobed into the CR's following the MWPC gate, and the subsequent encoding of the 'hit' wires into addresses was performed by the bin's 'encoder' card. These encoder cards (one per MWPC bin) were daisy chained together and connected to a Camac level master module, the MWPC interface, which served to multiplex the MWPC data from various crates through to the computer. This interface unit was provided with an LED display of addressing and data information and could be controlled in an off-line mode for debugging purposes. D/A converters in the unit served to generate an x,y oscilloscope display of all active channels in an addressed MWPC crate.

Wire addresses were encoded into a 3 bit wire number (0-2), a 2 bit group of 8 count (3,4), a CR card address (5-9), an encoder card crate address (10-13) and adjacency bit information (14-15). The encoder cards checked for up to 4 adjacent wires that might have fired in the system. The address of the last wire that fired was encoded into an address and the presence of up to 3 neighboring active wires was indicated by bits 14-15.

DATA AQUISITION

A DEC Unichannel 15 computer system was used for the data aquisition of this experiment. It consisted of a PDP-15 attached to a small PDP-11, which served primarily as a peripherals controller. The PDP-15 was equipped with a fixed head disc, 32 K of 18 bit memory, 2 tape drives, a line printer, a storage display scope and a special Nevis designed and built interface (assembled from standard cards) connecting the PDP-15 to a Nevis branch driver. The PDP-15 operated under DOS. The PDP-11 used DEC Pack discs and was equipped with 8K of 16 bit memory, a Versatec line printer and a DEC TU10 tape drive. It operated under PIREX.

In standard operation, the on line program initialized the PDP-15 interface by loading it with addressing information, which specified the locations of data buffers in memory, and by storing in the Nevis branch driver a series of Camac-like commands that selected the modules to be included in the event readout. Having done this, the computer awaited a start of spill pulse. At start of spill, it cleared the blind scalers and enabled the branch driver to accept triggers. Accepted event triggers caused the driver to begin executing its series of prestored commands in sequential order. This would accomplish a read out of the available event information:

1. Digitized lead glass pulse areas
   (approx. 40 words)

2. Digitized T2, S2 pulse areas
   Digitized sum of T2's and S2's
   Digitized Σ pulse height
   Digitized Cerenkov bucket monitor
   (35 words)

3. Encoded hodoscope information
   (approx. 6 words)

4. Encoded MWPC information
   (approx. 50 words)

5. Logic bus bit information
   (2 words)

6. TDC's monitoring Trigger timing
   (24 words)

7. Additional data buffer information
   (5 words)

Events were transfered to 2 memory buffers (1500K words each) in the PDP-15. Since their starting locations had been prestored in the PDP-15 half of the interface, data transmission proceeded without program intervention. When the event buffers became nearly full, they were written out to the PDP-15 disc. Per word, about 4 microseconds were

lost to memory and processing operations and 16 microseconds were lost to disc writing.

Events were accumulated on disc until the end of spill. At this time, a separate trigger was sent to the interface initiating the readout of fifty six 24 bit blind scalers. These recorded the rates of counters over each spill. After this information had been read, all the data that had been written to disc was transferred to magnetic tape. At completion of tape writing, requests made of the on-line program were honored and events were read from disc and analyzed on-line.

A typical data run lasted 1 hour. The on-line program automatically provided information monitoring the state of the apparatus during each run:

1. the number of times the energy in each lead glass block exceeded 1 Gev
2. the accumulated logic bus bit count
3. MWPC hit multiplicity and adjacency information
4. blind scaler accumulated sums
5. MWPC readout error statistics
6. hit multiplicities in hodoscope and trigger counters

In addition, a series of rates were tabulated and checked for run to run consistency. These rates monitored beam intensity, targeting efficiency, the symmetry of trigger counters between arms, the trigger stability, 'dead' times, on-line electron rates and 'accidental' (out of time coincidence) rates.

The dielectron running schedule was dominated by pair data runs taken at various magnet settings. Occasionally 'copper foil' and 'lead plug' data would be taken during the same runs as standard data (Table 9). Muon lead glass calibration runs (of 1-2 hours duration) were made once every two days and electron calibration (2-3 hours) was done every week. The remainder of the running time was devoted to miscellaneous special study runs. These included special runs taken to measure targeting and trigger counter efficiencies.

OFF LINE ANALYSIS AND CUTS

The dielectron data written to tape in this experiment was analysed using a single off line analysis package on the CDC 6600 at the Fermi National Accelerator Laboratory. Typically, the data underwent several stages of compression (filtering) before large scale analysis was attempted. Without the use of the standard off line track reconstruction, the dielectron data was compressed (in essentially its original data format) from 210 tapes to 3 using the lead glass cuts specified in Table 21. Over the mass range for which this experiment had adequate acceptance, these cuts passed dielectrons with close to 100% efficiency.

The final level of compression is referred to as the data summary tape level (DST). For this, events taken from the 3 'DDT' level tapes were completely processed by the off line analysis program and information regarding 'good' events was written out to disc in summary form. In passing to this level, loose cuts were made on the event's reconstructed E/P, the particle's lead glass shower development, the particle's position at the target and middle of magnet and the total number of MWPC hits (NHIT<81).

Final data plots were made using the DST file and they included the following cuts:

1. FIDUCIAL CUTS: (Table 23) Essentially these were made to insure that an event originated from the target (+- 3" tolerance), that it had not passed near the collimating edges of the apparatus and that its shower was well contained within the lead glass.

2. E/P CUTS: These are specified in table 22 and are discussed in the sections on lead glass calibration. See p. —

3. SHOWER CUTS: These are presented in Table 22 and are discussed in the section on lead glass shower cuts.

4. TOF CUTS: These cuts were made on the timing of the epsilon (ε) lead glass signal, in each arm, to insure that the particle's energy deposit had come from the proper accelerator bucket. Figures 25 and 26 present scatter plots of the E12 lead glass energy deposit vs. the TOF channel reading. The well defined bands shown in the figures occur because of the bunched accelerator spill structure (23 ns. peak to peak separation).

5. SCALER CUTS: These are specified in Table 22 and are discussed in the section entitled 'Intensity: limitations and cuts'. These cuts were intended to eliminate data taken under 'unfavorable' beam conditions.

6. RAPIDITY CUT: This cut was made in the acceptance Monte Carlo to improve its efficiency, and so the same cut must be made on the data itself.

Provided in Table 9 is information on the raw numbers of events affected by some of these cuts.

This important feature ~~is no~~ is apparently hidden — I can't find it! Correction p. 7

PARTICLE TRACK DETERMINATION

Information from hits in the proportional wire chamber-hodoscope system was used to reconstruct particle trajectories through the apparatus. Results from the least squares fit to the particle's trajectory were used in calculating the particle's momentum , in specifying its position at the target and for selecting lead glass blocks whose energies were to be summed in the event off line energy determination.

As a first step, the off-line reconstruction program sought candidate (x,y) coordinates at stations 1 and 3 (figure 7). It accepted all unique wire chamber triplets consistent to 0.2" and also all chamber doublets unless one (or more) of the members was already included in a valid triplet. Each (x,y) coordinate was checked to be in the aperature and screened fo agreement with the nearest hodoscope (0.75" tolerance).

Track coordinate candidates were created using all pairs of station 1 and 3 coordinates that passed certain screening tests with station 2 counters. All pairs were first screened for agreement with T1 (1.5" tolerance). Those found agreeing with a Y2 coordinate (0.4" tolerance) were then accepted. All other possible coordinate pairs were accepted as long as neither of them already

participated in a track with a Y2 ordinate.

Using these rough track coordinates, loose fiducial cuts were made on the particle's estimated vertical position at the center of the magnet (+-2.3") and on the particle's x coordinate at the target (+-5.0"). This was done to eliminate, as early as possible, uninteresting track candidates. Given coordinates at stations 1 and 3 that passed these tests, a linear least square fit was done to determine the best fit track parameters and their errors. The error matrix used in this calculation included the effects of multiple scattering in material between stations 1 and 3.

To check the efficiency of the standard reconstruction routine, this experiment relied on the scan of many events and on the comparison of the standard reconstruction's track selection with that of an almost separate reconstruction routine (both relied on the same survey file data).

A measure of the overall track finding efficiency would be provided by using a simple overly efficient reconstruction routine to 'recover' events failing the standard reconstruction on either or both arms. If the mass spectra of these recovered events shows an enhancement in the J/ψ region, this provides a rough measure of the standard reconstruction's track finding inefficiency in the region of the apparatus illuminated by J/ψ events. At the 600A setting of the magnets, J/ψ events illuminate a large

fraction of the aperature; at 1300 amps. they illuminate only a small (high rate) corner of it.

Table 24 presents a series of definitions that will be useful in describing the results of this reconstruction inefficiency study. One should become familiar with them before continuing.

The simple reconstruction routine (referred to in Table as 'RØ') used only pairs of 'Y' chamber hits to determine a particle's trajectory. Pairs of Y chamber hits were matched together, extrapolated to the magnet midplane and the event's momentum was calculated. If , on each arm, the particle's vertical position at the magnet midplane was within 2.5" of center and its E/P was between 0.9 and 1.12, the pair was considered reconstructed as a dielectron event. These cuts referred to as the 'CØ' cuts - the cuts based on the RØ reconstruction. To determine an approximate effective mass for the 'recovered' pair event, a calculation was done of the pair opening angle, assuming target origin of the event and using detailed information from the lateral shower spread in the lead glass.

The J/ψ mass resolution achieved with such a simple reconstruction routine is compared with that of the standard reconstruction in figure 27 ('MPØPØ' plot as compared to the 'MPP' plot).

A comparison of the effects of the 'C0' and 'C' cuts is made in figure 28, C and D. In both plots the mass was calculated using the standard reconstruction routine; they differ in that 'C0' cuts were applied to obtain spectrum C, and 'C' cuts for D. The two mass spectra do not differ greatly; this gives a measure of confidence in the effectiveness of the 'C0' cuts.

The spectra, relevant to the study of track finding inefficiencies, are shown in figure 28, A and B. These plots compare the 'recovered' event mass spectrum to that of the standard reconstructed events. (A) contains events in the 'XT' catagory, those for which a standard reconstructed track was not found on one arm. (B) contains 'TT' events, those for which standard tracks were found on both arms. In these sample 'recovered' event plots, as in others made for this study, an enhancement in the J/ψ region was discernable.

Not presented here is the spectrum of recovered 'XX' events, those with no standard track found on either arm. The number of recovered 'XX' events was down by a large factor from 'XT' and no measure of the track finding inefficiency could be extracted from so few events.

From this study, estimates of the number of J/ψ events above background in XT and TT mass spectra yielded the following efficiency values (1-(XT/TT)): 95% (600 amp.), 88% (800 amp.), 81% (960 amp.), 86% (1100 amp.). These

inefficiencies in the track reconstruction can, by and large, be accounted for by the inefficiencies in the individual counters required by the track selection procedure.

Assuming an MWPC plane efficiency of 98.5%. one has for the probability of a particle registering as a chamber triplet:

$$P(\text{TRIPLET}) = \frac{3!}{3!\,0!}(.985)^3 = .956$$

whereas the probability of it registering as a doublet is given by:

$$P(\text{DOUBLET}) = \frac{3!}{2!\,1!}(.985)^2(.015) = .044$$

Both doublets and triplets were acceptable to the standard reconstruction so the probability of an (x,y) coordinate being found at a station is then equal to:

$$P(\text{COORDINATE}) = (P(\text{TRIPLET}) + P(\text{DOUBLET}) \times 0.97 = 0.97$$

where a hodoscope efficiency of 97% has been assumed. For a track, 2 coordinates and the correct T1 (in the trigger) were required so:

$$P(\text{TRACK}) = P^2(\text{COORDINATE}) = 0.94$$

Using the value of 94% for the single arm track finding efficiency, one has for the probability of a TT event:

$$\frac{2!}{2!\,0!}(0.94)^2 = 0.88$$

and for an XT event:

$$\frac{2!}{1!\,1!}\ (.94)\,(.06) = 0.11$$

while for an XX event:

$$\frac{2!}{0!\,2!}\ (.06)^2 = 0.0036$$

From these numbers one can see that (1-(XT/TT)) is equal to 88%; Given the statistical uncertainties of this analysis, this value is in agreement with the numbers obtained from the J/ψ efficiency study. One concludes that the inefficiency of the off-line reconstruction was due, almost entirely, to the inefficiency of individual counter planes. In addition, XX events are predicted from this analysis to be down from XT events by a factor of 30, which was roughly seen in the 'recovered' XX mass spectrum.

Observed track multiplicities (after fiducial cuts) are presented in Table 25. There are so few events with truly different multiple tracks that track selection criteria are of minor importance.

MAGNETIC TRAJECTORY RECONSTRUCTION

Two iterations were made in the reconstruction of particle trajectories through the magnet. The initial pass was done using a simplified magnetic field shape and a simple magnet bend plane approximation. For the second iteration, a better estimate was made of the particle's average vertical position in the two halves of the magnet, and the full magnetic field shape was used in calculating the each magnet's transverse magnetic kick. Typically, this second iteration had the effect of increasing particle momenta by about 1%.

Using the downstream reconstructed track information, (Figure 29) first order calculations were done of the particle's vertical production angle (THY), its magnet bend angle (THB) and its horizontal production angle (THX). These calculations were done in the single magnet bend plane approximation , assuming a magnetic field shape independent of x and y. Since no particle detection is done before the magnets, all particle trajectories were assumed to originate from y=0 at the target.

Based on these THY, THB and THX starting values and using the knowledge of the magnetic field variation along the beam direction (z), one can do an analytic calculation of the particle's average y position value in the upstream

and downstream halves of the magnet. These y values were then used, along with the full (x,y) transverse magnetic field shape, to evaluate particle momentum kicks in x and y for the two magnet halves. A new effective bend plane, THY, THB and THX were recalculated and the particle momentum was evaluated. The horizontal (x) momentum kicks were used to correct for the slight horizontal bend of the particle trajectories in the magnets (+-0.5 mr.).

In the off line analysis, the multiple scattering and measurement errors made in the downstream reconstructed track were propagated through the reconstruction in the analysis magnets. This was done to provide a consistent overall event-by-event error analysis for the data.

EXPERIMENTAL RESOLUTION

As discussed earlier, the off line reconstruction routine used hit ordinates 'decoded' from the MWPC and hodoscope information to determine particle trajectories through the apparatus. It is the purpose of this section to outline, in some detail, the method for doing the least squares fit to the track coordinates and for calculating the errors on the fitted track parameters. After this, figures are shown which present the calculated momentum and mass resolution calculated through such a procedure.

The momentum is calculated through use of the following equation:

$$P = \frac{C \times I}{THB}$$

where

$$THB = \frac{Z3 \cdot Y1 - Z1 \cdot Y3 - (Z3 - Z1)\, Y\emptyset}{Zm\,(Z3 - Z1)}$$

Figure 29 defines the terms appearing in both equations. Knowing the error in 'C', the magnet constant (0.3%), in 'I', the magnet current (0.3%) and in 'THB', the particle bend angle, one can estimate this experiment's momentum resolution.

The error in THB is due primarily to errors in the fitted Y1 and Y3 values. These errors include both finite resolution and multiple scattering effects. Since there is little material in the beam before station 1, much of the (TABLE 26) multiple scattering error enters through the Y3 term in the above expression for THB (NOTE: not shown in the drawing of figure 3 is a helium bag, placed downstream of the magnets, covering the aperature from the magnet exit to station 1).

A proper determination of a particle's trajectory should weigh each track coordinate with its appropriate error, in performing the fit. Multiple scattering effects introduce into the error analysis important correlation terms that should be treated in a systematic way. To provide a general framework for this study, an appendix has been included in this paper to outline the general method of least squares analysis when correlation error terms are no longer negligible.

As one can see from the appendix, a knowledge of the form of the error matrix, E, for the problem at hand, is of fundamental importance. Ignoring the multiple scattering in material before station 1, the multiple scattering part of the error matrix E will have the following approximate form:

$$E_{ms} = \begin{array}{c} \\ Y1 \\ P1 \\ Q1 \\ Y2 \\ Y3 \\ P3 \\ Q3 \end{array} \begin{array}{c} \begin{array}{ccccccc} Y1 & P1 & Q1 & Y2 & Y3 & P3 & Q3 \end{array} \\ \begin{pmatrix} 0 & & & & & & \\ & 0 & & & & & \\ & & 0 & & & & \\ & & & I & K & K & K \\ & & & K & J & L & L \\ & & & K & L & J & L \\ & & & K & L & L & J \end{pmatrix} \end{array}$$

where

$$I = \sigma_{ms}^2(Y2)$$

$$J = \sigma_{ms}^2(Y3) \cong \sigma_{ms}^2(P3) \cong \sigma_{ms}(Q3)$$

$$K = \sigma_{ms}(Y2,Y3) \cong \sigma_{ms}(Y2,P3) \cong \sigma_{ms}(Y2,Q3)$$

$$L = \sigma_{ms}(Y3,P3) \cong \sigma_{ms}(Y3,Q3) \cong \sigma_{ms}(P3,Q3)$$

$\sigma_{ms} \cong \sigma$ (MULTIPLE SCATTERING)

The full error matrix includes all these terms, plus additional diagonal terms to take into account the finite chamber resolution:

$$E_{Res} = \begin{array}{c} \\ Y1 \\ P1 \\ Q1 \\ Y2 \\ \vdots \end{array} \begin{array}{c} \begin{array}{ccccccc} Y1 & P1 & Q1 & Y2 & Y3 & P3 & Q3 \end{array} \\ \begin{pmatrix} \sigma_R^2(Y1) & & & & & & \\ & \sigma_R^2(P1) & & & \bigcirc & & \\ & & \sigma_R^2(Q1) & & & & \\ & \bigcirc & & & & \ddots & \end{pmatrix} \end{array}$$

where '$\sigma_R(cs)$' is the finite resolution error of chamber 'c' at station 's' (see Table 19).

The multiple scattering sigmas are defined as follows: for the material in the beam at station s (either station 1 or 2):

$$\sigma_{ms}(YA,YB) = \left(\frac{0.015}{p}\right)^2 \frac{L}{L_R} (ZA - ZS)(ZB - ZS)$$

and for the air gaps between positions Zs and Zt (between stations 1 and 2, 2 and 3):

$$\sigma_{ms}(YA,YB) = \left(\frac{0.015}{p}\right)^2 \frac{L}{L_R} \frac{1}{L} \int_{ZS}^{ZT} dz\, (ZA - z)(ZB - z)$$

[redacted]

where

$$L \equiv z_T - z_S$$

$$\sigma_{ms}(y_A, y_A) \equiv \sigma_{ms}^2(y_A)$$

The E matrix elements must be evaluated for the material at both stations 1 and 2 and for the air separating stations 1 and 2, 2 and 3. After this is done, all contributions to E are summed. The calculation of the multiple scattering terms is a bit tedious and the results are as follows:

$$I = \frac{F}{p^2}\left(t_1/4 + t_{12}/12\right)$$

$$J = \frac{F}{p^2}\left(t_1 + 7t_{12}/12 + t_2/4 + t_{23}/12\right)$$

$$K = \frac{F}{p^2}\left(t_1/2 + 5t_{12}/24\right)$$

$$L = \frac{F}{p^2}\left(t_1 + 7t_{12}/12 + t_2/4 + t_{23}/12\right)$$

where:

$t_{AB} \equiv$ MATERIAL BETWEEN STATIONS A AND B (IN FRAC. OF R.L.)

$t_A \equiv$ MATERIAL AT STATION A

$$F \equiv (0.015)^2 (z_3 - z_1)^2$$

The unusual fractional values are due, in large part, to the common factor 'F' extracted from each term.

The knowledge of E permits one to evaluate the best fit track parameters ('A' of appendix 4) and their errors (Cov(A) of the same appendix). Knowing these best fit track parameters and their errors allows one to calculate track related quantities (such as the momentum) and their associated errors.

As a matter of course, the standard off line reconstruction performed a track fit and calculated the fit parameter errors, essentially as outlined above. Figures 8 and 9, respectively, present this reconstruction routine's estimate of the momentum and mass resolution achieved in E288 and E494, for events of the dielectron sample.

LEAD GLASS CALIBRATION

Two types of special data were used for calibration of the lead glass arrays. Muon calibration (done once every two days) provided information used to equalize the gain of each lead glass block with respect to those directly in front or in back of it. A relatively pure muon sample was obtained by removing the target and allowing the incident beam to interact completely in a tungsten beam dump 2.1 meters downstream of the target position.

Electron calibration (done once every week) provided data used to absolutely calibrate the lead glass arrays. For this calibration, the sample of electrons in the beam was increased by use of a wider copper target and by the insertion of copper foils (15-45 mils thick) into the aperature, 7 feet downstream of the target. The thicker target and thin foils served to increase the amount of material in the aperature, to convert more gamma rays into e+e- pairs.

MUON CALIBRATION: For a fixed incident trajectory with respect to lead glass, a muon will deposit a constant amount of energy in the block, regardless of the muon incident energy. 135 MeV was assumed to be the muon energy deposit in 15 cm. of lead glass (block sizes were uniform to 1/2 %)

In muon calibration, the trigger was set to illuminate the half of the lead glass block most distant from the photocathode; histograms of digitized pulse area were made for each block. Analysis of these histograms, on-line, provided a means of adjusting high voltages to equalize lead glass block gains (to +-10%). This same data served to provide finer individual block gain corrections off-line. Repetition of one muon calibration after another served to check reproducibility of muon gain values measured by this procedure. Muon median channel values were reproducible with a measured σ of 1.2%.

To measure the muon energy deposit, lead glass digitizer gains were increased by a factor of 20 above normal. The linearity and gain of each digitizer was measured for both the normal and high gain settings. +-0.5% fluctuations in gain were measured over a one month time period.

ELECTRON CALIBRATION: Contrasted with muons, electrons deposit all their energy in the 25.8 radiation lengths of lead glass, and so their measured shower energy should equal their incident momentum (E=P). Plots of E/P, which were made using data with enhanced electron beam, showed a prominent peak near 1.0 (figure 30). Each set of four blocks (in a row, along the beam direction) was calibrated by multiplying their calibration constants by a factor that would center the set's electron peak at 1.0. These

corrections typically amounted to a few percent and varied by 2-4% over the experiment's lifetime. The weekly electron calibration runs provided data for adjustment of these corrections with time. In addition to providing absolute energy calibration, this adjustment roughly corrects for the small amount of energy lost by electrons in the 2.3 radiation lengths of lead before the arrays.

In using lead glass to measure the energy of showering particles, corrections must be made for light attenuation effects. The closer the entering particle is to the photocathode, the greater the measured light output. The correction factor used to adjust for this effect is plotted in figure 31 . This curve describes an average behavior of the lead glass in the arrays. Individual sets of 4 blocks typically deviate from this average behavior by less than 0.5%.

Even with this correction, the lead glass resolution degraded significantly when the entering particle passed within 5-7 cm. of the photocathode. This was probably due to energy leakages out of the glass. For this reason, a fiducial cut was made on the data 6.35 cm. from the outer edges of the array. Monte Carlo results (56) from the simulation of 20 GeV electron initiated showers indicate that 97% of the electron shower energy is contained within a 6.35 cm. radius.

LEAD GLASS ENERGY DETERMINATION

To accomodate the long rise time of the RCA 8055 photomultiplier tube, the lead glass digitizer gate was set at 270 ns. and so it extended over 13 accelerator RF buckets. During this time, the lead glass was 'open' to secondary events that could shower (pile up) in the lead glass after the triggering particle. This possibility made it undesirable to simply sum the energy deposited in all lead glass blocks to calculate an event's calorimeter deposit. In the off-line analysis, the reconstructed track (as determined from wire chamber and hodoscope information) was used to select those blocks to be included in the event energy determination. Circles were traced around the track at the rear of each lead glass layer, and the overlap of these circles with lead glass blocks selected those blocks included in the energy summation.

For these circles, radii of 3.0,3.5,3.75 and 4.0 inches were chosen (for layers 1,2,3 and 4 respectively). These radii gradually increase to accomodate the expanding particle shower and will be referred to as defining a 'cone' about the particle trajectory. Comparison of this radii set with others was done and the results are shown in figures 32 and 33, for two different momentum ranges.

Figure 34 provides information on the lateral spread of electron showers in the lead glass. The curves present the fraction of layer energy deposited in a single lead glass block as a function of the entering particle's distance from block center (the center of the distributions corresponds to block center; the 50% point appears at the edge of the block). The change in shape of the curves, going from momenta of 20 to 40 GeV is slight and did not merit the use of momentum-dependent radii.

The chosen set of radii included (99+-1.4%) of the electron shower energy. A study was made to determine the fraction of energy deposited outside this cone as a function of E/P. Results of this study are shown in figure 35 . They indicate that as E/P approaches 1.0, more of the total event energy is included in the electron shower cone. The hadrons close to E/P=1.0, passing electron longitudinal shower cuts, seem rather similar to electrons in their transverse shower dimensions. One concludes that, using the present radii set, this experiment's hadron rejection would not be improved by cuts on the transverse size of a particle's lead glass shower.

As intensity increases and spill quality worsens, one expects an increase in lead glass energy pile up due to secondary events showering in the glass within 270 nanoseconds after the triggering particle. The effect of this on the dielectron data can be judged from the values of

Table 27 . Presented are average E/P values for 400 GeV dielectrons, where the data has been divided into 4 bins of NDN and INDUTY x NDN. Severe pile up problems in the data would be reflected in a shift of the average E/P upward, going from low to high intensity, or from good to bad beam quality. No such shift is observed. The actual plots from which these numbers were taken are shown in figures 36 and 37 . The percentage of energy found outside the event cone, in the remainder of the lead glass blocks, is plotted in figure 38 , for the 400 GeV dielectrons (this percentage was calculated relative to the event's cone energy). At each current setting, lead glass background levels are low.

A check on the absolute energy calibration of the lead glass, and on the energy determination procedure can be made using the clear signal of the J/ψ particle. Presented in table 28 are average E/P values for J/ψ events, for each arm of the spectrometer and for magnet settings at which J/ψ acceptance was adequate. Provided also are J/ψ mass values, calculated using the events lead glass energy and the reconstructed pair opening angle.

LEAD GLASS RESOLUTION

Test beam data taken over a range of energies from 3 to 75 GeV, was used to determine the validity of the following lead glass resolution formula (55):

$$\%\ \text{FWHM} = 1.5 + \frac{10}{\sqrt{E}}$$

Of particular interest are the data points for 50 and 75 GeV, which were measured using this experiment's large lead glass blocks, stacked as in the spectrometer arrays.

In practice, all the benefits of this lead glass resolution will not be realized due to random errors inherent in the calibration procedure. Using estimates of calibration errors given in the section on lead glass calibration, one can calculate a predicted resolution of the lead glass by folding known errors in with the published resolution formula. Values for this predicted resolution, along with values calculated from the publisned formula are shown in Table 29 . One sees a 20-30% resolution shift over the 20-30 GeV momentum range.

A measurement of the actual lead glass resolution was made, using an electron enhanced beam and studying the variation of the electron peak width in E/P histograms with energy. The results are shown in the same table. There is good agreement with the predicted resolution in the high momentum region, but not in the low.

Longitudinal Shower Development

One of the handles we have in identifying electrons is that they show a characteristic longitudinal shower development. We make use of this by sampling the shower four times in the four layers of lead glass. This section will discuss how cuts were arrived at to discriminate between electrons and hadrons. We will also discuss whether we have made the optimal cut or not.

To look at electron shower development, we must first isolate a sample of electrons. This is accomplished by a subtraction technique. We take a run in which we enhance the number of electrons by using a wide high Z target (Cu) and inserting a 0.015 in. foil in the secondary beam. This results in conversion of γ's from π^o decay into e^+e^- pairs. During this run, half the time we insert 2 in. of lead in the secondary beam. This would absorb all electrons in the beam leaving only hadrons. We then histogram for each event the ratio of energy in the lead glass and the momentum in the magnetic spectrometer (E/p), and the various fractional energies E_i/E (where E_i is the energy in the i^{th} layer, and E = total energy). Histograms were divided into lead and no lead and into momentum bins. For each momentum bin, we subtract the lead from the no-lead distributions. We normalize the subtraction using the E/p region away from 1 since the shape of the hadron distributions in E/p would not

be affected by the lead. This same normalization is used to subtract the E_i/E distributions. What is left after the subtraction are the various electron shower distributions for each momentum bin. See Fig. 31 + 40 for an example of the subtraction. Note that the E_i/E distributions all have a E/p cut applied to enhance the electron sample. The subtracted E/p distribution shows how good is the subtraction method given sufficient statistics.

Our first set of cuts was determined by cutting 5, 10, 20% into tails of the distributions. These cuts were then plotted as a function of momentum. A linear fit was used:

cut E_i/E: $C_i = A_i p + B_i$.

Due to the way electrons shower, E_1/E, E_{12}/E cuts were lower limit cuts and E_2/E, E_3/E, E_4/E were upper limit cuts.

Since cutting at the tails of distributions involves large statistical fluctuations, we developed a second set of cuts to determine the coefficient A_i better. This involves plotting the median of the distributions as a function of momentum. B_i is then allowed to float depending upon the efficiency desired.

The cuts that were in fact used were E_1/E, E_{12}/E, E_4/E. A look at the E_3/E distribution shows that the background is flat even under the electrons. To maintain high efficiency, the E_3/E cut would not gain much in background rejection since it has a relatively long tail. The E_2/E cut was not used since the information is carried by the E_1/E and E_{12}/E cut.

For a given set of cuts, we calculate the efficiency for electrons. Here again we use a subtraction technique on the E/p plots. The number of electrons is determined by subtracting E/p histograms with and without the lead filter in. The electrons are defined as the number of events in the region $0.90 < E/p < 1.10$ left after subtraction. We do the same thing again but this time apply the shower cuts. The number of events remaining after cuts allows us to calculate the efficiency. The efficiencies were calculated for several momentum bins 20-25, 25-30, > 30 GeV. There was no momentum dependence to the level of $\sigma = \pm$ 3%.

A study on the question of whether we have the optimal signal to background ratio for a given efficiency was made. The background was defined in a region below E/p = 1 but above any software or hardware thresholds: $0.60 < E/p < 0.88$. The results of the study were that for a given efficiency the signal to background ratio was a fairly flat function of the various shower cuts. A gain in signal to background of about 10 $\pm$ 5% could have been gotten if our cuts had been optimized. A minimal gain at best.

The efficiencies and definition of the various cuts used are given in Table 22.

INTENSITY: LIMITATIONS AND CUTS

Several monitors were used during the course of this experiment to measure beam intensity and check the quality of the accelerator spill structure. The SEM measured the number of protons incident on target. NDN was a three fold coincidence of scintillation counters that monitored the relative number of target interactions per spill and was used for this experiment's overall normalization. T refers to the T trigger (either TU or TD). Its pair rate (TUD=TU TD) was dominated by accidentals. Scatter plots of the ratio (TUD/NDN) for TUD in and out of time showed TUD to be more than 90% accidentals at all magnet settings. INDUTY (see appendix on Induty) was calculated using the T trigger rates (TUD×N/TU×TD) and provided a pulse by pulse monitor of spill quality.

In addition to these pulse by pulse monitors, a time of flight module, which was started and stopped by independent counters viewing the beam, provided a visual display of bucket to bucket spill uniformity on a PHA (figure 11). A storage oscilloscope (whose input came from a T0 counter) was used to monitor the spill macro structure (figure 10). In cases of poor beam quality, accelerator controls people were notified, and major problems were usually remedied by judicious tuning. In E494, an air Cerenkov counter was

installed in the beamline, before the target, to measure, event by event, the relative number of protons per bucket. An Amperex 56AVP photomultiplier tube was used and a special voltage divider was designed for it to provide low gain, fast risetime operation. Since this counter's information was not available for a significant fraction of the dielectron running, no cut were made on this counter's pulse height in the final analysis.

A desirable running intensity for this experiment would be one at which accidental pair backgrounds are not overwhelming, the boosted trigger counters do not sag, MWPC and D.C. logic deadtimes are small, the number of secondary showers in the lead glass is low and the off-line reconstruction of events is relatively unambiguous. Consideration of these factors, along with a off-line scan of many events yielded the following practical rule of thumb: at each magnet setting, increase the incident intensity until T=1.0M counts/second.

This general rule of thumb was not always followed, neither by the experimenters nor by the Fermilab accelerator. The intensity did fluctuate during the course of the dielectron running, and this section will discuss the effects of this on the data. A summary of an intensity study is presented in tables 12 through 16. All the data has been divided into 8 intensity bins, determined as follows. For each magnet setting, a histogram of NDN was

made using all the scaler events of the 400 Gev E288 data. Each histogram (one for each current) had its own average NDN value (AVG) and standard deviation (SD). The 8 intensity bins were made up, using these average values and cutting on multiples of the standard deviation. The bins go from #1 (NDN < AVG-2×SD) up to #8 (NDN > AVG+4×SD). The use of a current dependent average and standard deviation was done in a crude attempt to normalize the current settings, one with respect to another. It was hoped that doing this would make general trends in the data more obvious.

Some typical counter rates and track multiplicities (no fiducial cuts) are shown in Tables 12 through 16, for various currents. The E12 T/E12 entries give the fraction of the time there was more than 17 Gev in the first two lead glass layers (E12) and an associated track (T) was found by the off-line reconstruction program. XX, X1, 11, ... are track multiplicity designations:

1. XX=no track on either arm
2. X1=1 track found
3. 11=1 track found on each arm
4. etc.

These track multiplicity entries are percentages calculated relative to the total number of events found with good pair logic bus bits. The %NDNBY entries give the fraction of the E288 400 Gev dielectron integrated intensity in each of the Table's intensity catagories (E494 intensities were, on the average, lower than those of E286). Events used for this track study were taken from compressed electron data tapes, which means that all events have already passed certain loose electron shower cuts on both arms (Table 21).

One can use the values in the tables to estimate inefficiencies that may have arisen during high intensity running. One first notes that above TUD=100K, the fraction of (XX) and (X1) events seems to increase. The numbers suggest a track finding efficiency dropoff of 10% above TUD=100K, increasing to 20% above 300K TUD. For all magnet settings (except 1300 amp.) the fraction of data affected by these inefficiencies is less than 10%.

Verification that dielectron yields remain constant at various intensities is difficult to achieve because an increase in accidental pairs at high intensity may mask charged particle detection inefficiencies. An E494 intensity study (960 amp.) of <u>single arm</u> electron yields showed that this yield decreased by 20% above 200K TUD and that it had fallen off by 30% above 550K TUD. This is in rough agreement with the track finding data commented on

from Table .

J/ψ events provide a data samole dominated by correlated pairs. so a plot of J/ψ yield vs. intensity should provide a monitor of this experiment's efficiency. Such a study is statistically limited; at each magnet setting there are not enough J/ψ events to adequately explore the high intensity regions. Indeed at 1300 amp. (the setting at which this experiment covered its greatest range of intensities). J/ψ acceptance was so low that no study of this type could be done.

All of this notwithstanding, the 400 Gev J/ψ yield data for 600, 800 and 1100 amp. is shown in figure 41. Note that each magnet current corresponds to a different average intensity and a different region of J/ψ illumination of the apparatus. For these reasons. the division of the data according to magnet current is desirable. Plotted are the number of J/ψ events per NDNAY vs. $A/\bar{A}$ were A represents one of several beam quality monitors (NDN (=N). INDUTY (=I), NDN INDUTY (=I N)). 1.0 on the horizontal scale represents the point of average NDN, INDUTY or NDN*INDUTY for a particular magnet setting. Each point in the plot represents 20-30 J/ψ events and so has 20% statistical error.

While the scatter of data points in this plot is too great to draw firm conclusions about efficiency changes on the 20-30% level, the rather random scatter of data points

about 1.0 suggests a relatively uniform J/ψ efficiency over the limited range of beam intensity and spill quality displayed.

Given the previous indication of a slight dropoff in electron yield at high intensities, loose scaler cuts were made on NDN, INDUTY and NDN*INDUTY. Their cut levels were determined by histogramming N, I and N*I for the entire 400 Gev data sample, for the various magnet settings, and bins for the data were made up using the averages and standard deviations measured from these histograms. These average and standard deviation values are given in Table 27. The final 'scaler' cut was done by eliminating data falling beyond the average plus a certain fixed multiple of the standard deviation (Table 22). The number of events eliminated by these 'SCALER' cuts is given in Table 9.

Monte Carlo Calculation of Acceptances

In the calculation of cross sections, one must correct the data for the finite probability that an event will be seen by the apparatus. This probability is commonly called the acceptance probability of the apparatus or just the acceptance. We begin with a general discussion before we discuss the specific case of this experiment.

Let

$\frac{dN}{dx_j}$ = number of events observed in the interval x_j to $x_j + dx_j$,

$\frac{d\sigma}{dx_i}$ = differential cross section for process in question ,

$\frac{d\theta}{dx_j}(x_i,x_j)$ = differential probability for various apparatus effects not related to geometry. It is the probability for a particle to be produced with parameters x_i and be observed with parameters x_j to $x_j + dx_j$. x_i and x_j constitute a complete description of an event.

$A(x_i,x_j) = 1$ if event is observed ,

$= 0$ if event is not observed ,

n = normalization factor (i.e., flux) .

Then

$$\frac{dN}{dx_j} = n \int \frac{d\sigma}{dx_i} \frac{d\theta}{dx_j} (x_i,x_j) \cdot A(x_i,x_j) \cdot dx_i \quad ,$$

where the integral is over the production variables to take into account the various uninteresting apparatus effects (i.e., multiple scattering, axial symmetry, resolution effects, etc.). If there are no apparatus effects, then $\frac{d\theta}{dx_j} = \delta(x_i - x_j)$.

$$\frac{dN}{dx_j} = n \quad A(x_j) \frac{d\sigma}{dx_j} \quad ,$$

where the last equality defines the acceptance $A(x_j)$ $(0 < A(x_j) < 1)$ and n is a flux factor.

$A(x_j)$ is the probability that an event will be observed at x_j if we integrate over the x_i. In general, the integration to obtain $A(x_j)$ is difficult if not impossible to do analytically. A Monte Carlo technique is used.

$n \frac{d\sigma}{dx_i}$ particles are thrown in the phase space x_i and we ask how many are accepted: dN/dx_j . The acceptance is then the ratio of accepted to thrown.

The models used throughout in this experiment have been various J/ψ production models. As in most models, we assume that the invariant cross section factorizes into a p_t and x or y distribution. An event is thrown with p_t and x or y and is weighted according to the cross section. The J/ψ is then allowed to decay. Various models of the production and decay of the J/ψ have been looked at: the helicity and the Gottfried-Jackson frame with flat and $1 + \cos^2\theta$ distributions.

The decay products are then traced through the apparatus. The target interaction point is thrown to allow the interaction to be anywhere along the 4 in. target. Bremsstrahlung loss of the decay electrons in the target is included. About 10% of the J/ψ is irrecoverably lost due to this. The apparent mass is shifted well below 3.1 GeV so that the event would not be recognized as a J/ψ. The particles are then bent into the

detector apparatus. At the 80 ft station, we include an effective multiple scattering as the lepton passes through the detector.

If the lepton pair is still in the apparatus as far as the lead glass, we then reconstruct the event exactly as we would with real data. The resolution of the hodoscopes and wire chambers is included in a constrained fit of the track. The track is then traced back through the bending magnet with the constraint that the track pass through the center of the target. Various quantities are calculated for the tracks: momentum, mass, p_t, y, x, etc.

Fiducial cuts are then applied to each track. If the event passes, it is histogrammed as a function of p_t, y weighted by $d\sigma/dp_t dy$. The ratio of the accepted histogram and the thrown histogram gives the acceptance as a function of p_t and y.

For the mass acceptance, we throw J/ψ with various masses and integrate over p_t. The distribution of thrown events is given by

$$n \frac{d^2\sigma}{dmdy} .$$

The accepted events by

$$\frac{d^2N}{dmdy} .$$

The acceptance is then given by

$$A(m,y) = \frac{d^2N/dmdy}{nd^2\sigma/dmdy} .$$

NORMALIZATION

The following proportionality is assumed to hold:

$$\frac{\sigma(R)}{NUMEVTS} = \frac{\sigma(N)}{I \times f}$$

Where:

1. $\sigma(R)$ = cross section for the reaction (R): $p + Be \rightarrow e^+ + e^- + X$

2. NUMEVTS = Total number of events in 4π solid angle. This is the total number of observed events, multiplied by correction factors for acceptance, trigger and track finding efficiencies, off line cut efficiencies and electronic's dead time.

3. $\sigma(N)$ = nuclear (or nucleon) cross section.

4. I = Total integrated intensity on target.

5. f = fraction of beam that interacted in the target.

Several elements are involved in the calculation of the final cross section and it would be best to discuss them one at a time. The estimated error in this experiment's overall normalization is +-25%. A large fraction of this uncertainty is due to model dependence in the acceptance Monte Carlo.

ACCEPTANCE: The acceptance is a model dependent correction (see section on Monte Carlo) applied to the data, which allows one to estimate the number of events that would have been observed by an experiment subtending the full 4π solid angle around the target. Since cross sections are usually steeply falling in behavior, significant bremsstrahlung, multiple scattering and apparatus resolution effects should be included in the acceptance estimate. Bremsstrahlung effects tend to steepen mass spectra, while the 'smearing' effects of a finite experimental resolution tend to make them more gentle.

TRIGGER EFFICIENCIES: Special runs taken with loose trigger requirements were made to measure the efficiency of each trigger counter. The results are presented in Table

TRACK FINDING EFFICENCIES: The off line algorithm for track reconstruction has already been described and its efficiency estimated. It will be assumed to be 100% efficient, since the fraction of lost tracks is well explained by the inefficiencies of individual counter and

chamber planes.

OFF LINE CUT EFFICENCIES: The electron yield observed in this experiment must be corrected for electrons lost to cuts in the off-line analysis. These cuts were made to improve hadron rejection (E/P and shower cuts), to eliminate events near the outer edges of the apparatus (fiducial cuts), to eliminate out of time triggers (TOF information), to compress data off line (Table 21), to eliminate data taken under bad beam conditions(scaler cuts) and to duplicate cuts made in the acceptance Monte Carlo (rapidity cut). The efficiency of the shower cuts is presented in Table 22. The E/P cuts are close to 100% efficient (see figure 36 for dielectron E/P plots). The number of events eliminated by the scaler, TOF and rapidity cuts are given in table 9. Information on the fraction of events eliminated by fiducial cuts (for event passing loose electron criteria) is presented in Table 23.

ELECTRONICS BUSY TIME: This was monitored by scaling NDN with and without a 'system busy' veto. Typically the overall experimental deadtimes were kept below 10-15%. The system busy came from 3 possible sources. The electronics could be 'dead' either because it was processing an event or because it was shut off by a spill 'spike killer' or an SCR noise killer. The 'spike killer' gated off the experiment during high intensity spill periods. It was slow and required on the order of 100 accelerator RF buckets to turn

on.

NUMBER OF INCIDENT PROTONS: This was measured by this experiment's SEM. The reliability and stability of such a device and the validity of its absolute calibration are discussed in an earlier section.

FRACTION OF BEAM INTERACTING IN TARGET: The incident intensity measurement (SEM) must be corrected for the fraction of beam that does not intercept the thin Be target and for the fraction of the beam that traverses the target and does not interact. The fraction of beam that does intercept the target was measured by using a wider Be target (0.063"), and measuring the ratio of thin/thick target rates as determined by NDN. This counter rate ratio was typically 65%.

The second target related factor corrects for the fraction of beam that passes through the finite length target and does not interact. In the case of a target of length L, width W, particle exit angle A and absorbtion length d, the interacting fraction is:

$$\left(1 - Exp\left(-\left(L + \frac{W}{2}\right)/d\right)\right) Exp\left(-WA/2d\right) + \left(W/2d\right) Exp\left(-L/d\right)$$

For narrow targets, this reduces to:

$$\left(1 - Exp\left(-L/d\right)\right)$$

or 24.2% for a 4" long Be target.

Surveys of the target position included a visual check for target skewness along the beam direction.

Accidental Background Determination

This section will describe how we have determined the accidental background in our data. We first define what we mean by accidentals. An accidental event occurs when two protons in the same time resolution bin of the apparatus (in our experiment this is determined by the rf structure of the accelerator: 18.9 ns) interact. One interaction sends a particle into one arm and the other into the other arm of the spectrometer. Our background arises when these two uncorrelated particles are identified as electrons. There is no way to distinguish this from two particles from the same interacting proton on an event by event basis. We must resort to determining the background integrated over the entire data set.

The shape of the accidental background is obtained from pairing uncorrelated single arm events (i.e., events which trigger one arm of the spectrometer). This "pair" event is required to pass the exact same cuts that the normal pair data must pass. The number of events gotten this way goes as the number of single arm events squared so statistics are not a problem. This spectrum must now be normalized.

Let n_U, n_D = counting rate of counters U and D in time interval T. U and D are uncorrelated.

t = time resolution.

Then $n_i t/T$ = probability of i counting in time interval T_0 to T_0+t.

n_{UD} = coincidence rate of counters U and D

$= n_U t/T \cdot n_D t/T \cdot T/t$

if uniform counting rate throughout time interval T

T/t is the number of period t.

If the counting rate is not uniform (dn/dt not a constant), the effective counting time T' is given by

$$T' = n_U n_D t/n_{UD} \ .$$

Define duty factor

$$D = T'/T.$$

The electron accidental pair rate is then given by

$$e_{UD} = e_U e_D t/T'$$
$$= t/T \cdot e_U e_D/D$$

for time interval T (i.e., beam pulse). The single arm electron yield e_i was calibrated per NDNBY (= N) which is a measure of the number of interacting protons. The duty factor D was calculated from the coincidence T_U, T_D, T_{UD}. T_{UD} was mostly accidental since there were a great number of uncorrelated hadrons going through the spectrometer. The rate constants found are given in Table XXII[30]. e_{UD} was summed pulse by pulse for the data set presented

$$E_{UD} = \Sigma\ e_{UD} \ .$$

The spectrum of pair events is then normalized to E_{UD} events. The number of events is given in Table XXII[30]. We note that most of the events will be in the low mass region of the spectrometer. This normalized spectrum is then corrected

for acceptance and flux just as the normal pair data. As explained in Appendix IX, the model used is the J/ψ production model.

The differential cross sections for the two energies are given in Figs. 25-26, where the smooth curve is the accidental spectrum. The figures show that ~~at~~ IN the J/ψ and ψ' region, except for the resonances, everything is dominated by accidentals. Table XI gives the number of accidental events expected in the J/ψ and ψ' region.

We note that the accidentals go up with current. This is due to our running at higher intensity for the higher currents. The accidentals go as the square of the intensity but it is dominated by the low mass region. Except for 1100 A, the accidental background is very low. If we assume everything away from the J/ψ and ψ' is accidental, we get a second normalization of the accidental spectrum. The results of this are shown in Table 31.

DIELECTRON BACKGROUND ABOVE 4 GEV

Shown in figure 42 is an E/P histogram obtained after applying lead glass shower cuts to a small sample of the E288 data. Events classified as electrons are those of the 'e' region near E/P =1.0. This selection of events includes not only target produced electrons (E) but also Dalitz pair electrons (N), electrons from gamma ray conversions in matter in the aperature (N) and hadrons (H). Events recorded in this pair experiment can be classified as being of an 'accidental' or 'correlated' nature. 'Correlated' particles were produced in (or 'near') the same nuclear interaction; 'accidental' pairs were produced in separate particle interactions. Background in this experiment consists of all correlated and accidental pair combinations of N, H and E events, excluding only correlated E:E pairs. These correlated E:E pairs are signal. The purpose of this section will be to estimate the level of background from these particles above a mass of 4 Gev. Below this mass value. hardware thresholds and software tape compression cuts bias a sample of the data used for the background studies (the 'h' sample of events). It will be convenient to define a few terms before starting. To specify a pair event, the notation 'C:D' will be used to indicate a pair with a 'C' particle on one arm and a 'D' particle on the other. The notation is meant to include both correlated and

accidental pairs. In addition, the following definition will be convenient to use:

$$[C:D] = C:D + D:C$$

In this notation, the dielectron background is written as follows:

$$B = H:H + N:N + E:E(\text{accid.}) + [H:N] + [N:E] + [H:E]$$

To specify the 'foil' state of the apparatus when necessary, '0' will be used to indicate no foil in the aperature, 'c' to indicate the 45 mil foil in the aperature. So one has, for example, C(0):D(0), C(c):D(0), C(c):D(c) etc. C:D will be considered a shorthand for C(0):D(0).

THE HADRONIC BACKGROUND: Let us define as the hadronic background:

$$B(H) = H:H + [H:N] + [H:E]$$

The study of this component of the background is facilitated by the fact that both 'e' and 'h' events pass normal trigger requirements and are both recorded on tape during data runs. From this sample of 'e' and 'h' events on both arms, one can extract reconstructed 'h:e', 'e:h', 'h:h' pairs, calculate their cross section and scale the resultant plots, using the single arm H/h ratio. This will yield an estimate of the hadronic ('accidental' and 'correlated') background under the E/P=1.0 peak.

Before making use of events below E/P=1 for study purposes, one must be sure that trigger and data tape compression efficiencies have not introduced momentum biases into the data sample. It will be shown that choosing a lower E/P bound of 0.66-0.68 for the 'h' sample, and using the standard shower cuts, ensures a 90-100% bias free hadron sample above masses of 4 CeV.

Biases due to the lead glass trigger will be considered first. Hadrons 'low' in E/P deposit a smaller fraction of their energy in the first two lead glass layers (E12) than electrons and so are more susceptible to failing this experiment's trigger requirements. The 'E' trigger requirements were looser than than those of epsilon (figure 15), so it suffices to study the effect of the $\mathcal{E}$ trigger on the hadronic sample.

Using the expression for the E12/E lead glass shower cut ($E12/\mathcal{E} > -0.0024\ P + 0.92$) and assuming adequate (>90%) epsilon trigger efficiency to be reached by E12=12 Gev, one can easily show that worst case hadrons (at 0.66 on E/P, barely passing the standard shower cuts) would pass this experiment's hardware trigger if they have momenta greater than 21 GeV.

Of primary concern for this study, is the data of the 'higher' mass magnet settings of 960, 1100 and 1300 amp. All were taken with the same epsilon threshold, and all have momentum acceptance which turns on near the 21 Gev level

(Table 32). The case of greatest concern is that of the 960 amp. setting, where the momentum acceptance turns on near 17 GeV and is not fully on until 24 GeV. So the 'worst' case hadrons of 960 amp. would be a cause for some concern, in the lowest mass bins. Given that all hadrons do not fall into the 'worst' case category and that a background study mass cut will be made at 4 GeV, a simple calculation convinces one that even the 960 amp. setting offers a hadron sample relatively unaffected by the lead glass trigger requirements.

A second possible source for bias in the hadron sample may be due to the cuts used to 'compress' the dielectron data onto a small number of tapes. This compression was done for convenience of analysis and the cuts used to accomplish it are specified in Table 21. Progressing from one level of compression to the next, tighter cuts were made to filter out non-electron events from the data sample. The case for which the hadron sample was most likely to be biased by these cuts is that of 'H:H' pair events at 1300 amp.

To study this question in sufficient detail, 26 raw data tapes from 1300 amp. running were analyzed and mass spectra of h:h, [h:e] and e:e pair events were made. Standard shower cuts were applied to all samples and a lower bound of E/P=0.68 was used to define the 'h' sample for the study. A subroutine was used to simulate the tightest tape

compression cuts and these were applied to the raw data to study their effects. It was found that [h:e] events passed compression cuts with 100% efficiency, h:h with 95% efficiency. Because of their high 100% efficiency, the E/P bound of 0.68 was lowered to 0.66 to define the 'h' sample of [h:e] events.

Returning to the task of background estimation then, the hadronic component of the background is given by:

$$B(H) = H:H + [H:E] + [H:N]$$

Its magnitude can be estimated by combining h:h and [h:e] mass spectra in the following manner (e=E+N+H):

$$B(H) \leq a\,[h:e] - a^2\,h:h$$

where 'a' is the hadronic scaling factor:

$$a = H/h \qquad \text{(SINGLE ARM)}$$

A complication to this analysis arises because several types of hadrons are intermingled in the data sample. If one wishes to arrive at a worst case background estimate, one must choose the largest possible value of 'a'. Then, regardless of 2 arm correlations, the right hand side of the above inequality will be an upper limit for B(H).

To study this hadronic background in more detail, the E494 Cerenkov counters were employed for distinguishing pions, kaons and protons. Overall E/P plots for each type

of particle are shown in figure 43. This data was taken with the T trigger which makes no pulse height requirements other than minimum ionizing. The figures suggest that pions contribute the most to background in the electron (E/P=1) region, protons the least.

A measurement of the H/h ratio, for the various hadron types, was performed, using single arm data taken in E494. The 5.08 cm. lead plug was placed in the aperature, 21 feet downstream of the target, to eliminate the N and E components from the beam. The remaining particles in the beam were studied and identified as pion, kaon or proton by the E494 Cerenkov counters. Presented in Table . are the 'a' cross section scaling factors for the [h:e] (lower bound E/P=0.66) and h:h (L.B.=0.68) spectra. One can see that pions have the largest 'a' value, protons the smallest. A scan of the 'a' values in this table shows that 'a' may have slight momentum and magnet polarity dependances.

To arrive at a worst case estimate of the hadronic background one should use the largest observed 'a' value to scale the [h:e] and h:h cross sections. Since the larger 'a' values belong to pions. this is equivalent to assuming that all hadrons are pions. This is not a bad assumption, as one can see from the available hadron data (57).

An important fact to note is that the [h:e] and h:h cross sections are self normalizing to the e:e cross section data. This is true since all these types of pair events

were recorded simultaneously in standard data runs. In addition it is important to emphasize that these spectra are made up of 'in time' pair events, and so include both accidental and correlated hadron contributions to the background.

GAMMA CONVERSION BACKGROUND: An estimate of the upper bound contribution of conversion gamma rays to the dielectron background is made using data taken with thin copper foils (45 mil) inserted in the aperature, 21 feet downstream of the target. These copper foils served to convert gamma rays and bremsstrahl electrons, while leaving hadrons unaffected. These 'conversion' and 'bremsstrahlung' effects will change the character of the data and must be studied with some care.

CONVERSIONS: Of interest for calculating the number of gamma conversion electrons is the amount of material in the beam before the bend in the analyzing magnets. Gammas converting after this point will yield electrons whose E/P (as measured by the magnetic spectrometer and lead glass) will be below 1.0. These events will fail standard electron cuts and so do not represent a background problem. A list of the material in the beam before the bend is summarized in Table 34.

One entry in this Table that deserves some comment concerns the air contamination of the helium in the target box. Helium was provided from bottles in a service building, where its outflow, its return flow and the gas purity of the return flow could be measured. In principle, this system was identical to that used in a previous experiment, during which a 0.2% air contamination (by weight) of the target box helium was measured. Compared to the previous experiment, however, the outflow of helium measured at the service building was low. Though visible on the meter, the outflow was not substantial enough to permit a measurement of the helium gas purity. Efforts were made to track down the source of this problem but no solution was found. It was felt that maintaining an overpressure of helium in the box was sufficient to insure adequate helium purity.

In a straightforward manner, one can estimate the flux of conversion electrons, F(e,d), exiting a foil of thickness d, given that F(γ) gamma rays are incident. This can be done utilizing the gamma conversion factor of exp(-z/Lc) and allowing the converted electrons to be attenuated in the remaining (d-z) of material following exp(-(d-z)/Lr). One finds that:

$$\frac{F(e,d)}{F(\gamma)} = \frac{\alpha}{1-\alpha}\left(e^{-\alpha t} - e^{-t}\right) \qquad (1)$$

$$t = d/L_R$$

$$\alpha = L_R/L_c = 7/9$$

For small radiation lengths, this formula yields an easy to remember result for the ratio of conversion electrons due to foils of different thicknesses (for example d and D):

$$\frac{F(c,d)}{F(c,D)} \cong \frac{t_d - t_d^2(\alpha-1)/2}{t_D - t_D^2(\alpha-1)/2} \cong \frac{t_d}{t_D}$$

Equation 1 is an approximate relation and its deduction leaves something to be desired. The use of the gamma attenuation factor exp(-z/Lc) seems physically proper, but the treatment of bremsstrahlung as an all or nothing attenuation process is not realistic. Particles typically loose small fractions of their energy when they bremsstrahl and this causes events to shift 'leftwards' on the energy scale to lower bins. While equation 1 may be correct in an average sense for a flat energy spectrum, one could suspect that it requires a correction when applied to particles with a steeply falling spectrum of energies.

BREMSSTRAHLUNG: The effects of bremsstrahlung on a pair cross section could, in general, depend on the momentum and opening angle distribution of the particles contributing to the spectrum. To study this, a Monte Carlo was used to generate events to simulate a pair cross section falling according to exp(-k M), where 'k' was chosen to take on sample values of 0.5, 1.0, 2.0, and 4.0. Events were thrown according to several 'models' with different momentum and opening angle distributions, and then 'bremsstrahled' to learn the effect of the models on the exponentially falling

cross section. The ratio of the bremsstrahled to un bremsstrahled mass spectra will be referred to as the 'bremsstrahlung correction' to the data. It will always be less than 1.0.

To simulate bremsstrahlung, one needs to start with a bremsstrahlung formula. Three formulas (ref. 57, 58, and 59). were selected, checked against each other and found to give similar predictions. The three formulas predict similar values for the integrated probability of energy loss over segments of the energy range and application of the formulas to artificially 'bremsstrahl' actual pair data yielded similar mass spectra. In the study that follows, the formula taken from Mibler's work has been used.

In this study then, a pair mass was thrown according to exp(-k M), and the particle momenta, P1 and P2, and opening angle (THX) were calculated for 4 extreme models:

1. THX=0.12; P1=P2=M/THX
2. THX=0.16; P1=P2=M/THX
3. THX=0.12; P1=1.3*M/THX, P2=M/(1.3*THX)
4. THX=0.16; P1=1.3*M/THX, P2=M/(1.3*THX)

(M = Mass)

The above four 'models' were selected to study the effect of bremsstrahlung on pair events of symmetric or assymetric momenta, at small or large angles. Having calculated these momenta and opening angle, both momenta were 'bremsstrahled', the pair mass recalculated and the 'bremsstrahled' mass spectrum was histogrammed.

The bremsstrahlung program assumed that 8% of a radiation length of copper had been placed in each aperature. Results of the study are presented in Table 35. No change in the bremsstrahlung correction was observed in going from case 1 to 4. The bremsstrahlung correction seems to depend primarily on the spectrum slope and not on many of the fine details of particle production. This slope dependence is not unexpected. In comparison with a shallow sloped spectrum, a steep sloped spectrum has fewer events on the 'high' side of the scale that can 'bremsstrahl' to lower values. This will affect the slope of the resultant spectra.

To give an example of this 'slope' effect, one can look at a simple case in which the effect of bremsstrahlung on a spectrum can be calculated analytically (61). The following simple input spectrum will be used:

$$\frac{dN}{dE}\Big|_0 = \alpha E^{-n} \equiv I$$

In this case the Heitler bremsstrahlung formula can be integrated to evaluate the effect of bremsstrahlung on the

input spectrum:

$$\frac{dN}{dE}\Big|_x = \int_E^\infty W(E_0, E, x)\,\frac{dN}{dE_0}\,dE_0 = \alpha E^{-m} x^{-x} \equiv J$$

$$x = \frac{\Delta x}{\ell_{rad}}$$

$$\Delta x = \frac{d}{L_R}$$

Under bremsstrahlung, E shifts to E + ΔE and:

$$-\frac{\Delta E}{E} = \left(1 - \frac{I}{J}\right)/m \cong x \ln m / m$$

which explicitly displays a slope correction to be made to the well known relation:

$$-\frac{\Delta E}{E} = \Delta t$$

It is unfortunate that one cannot solve many problems of this type in such a straightforward manner. Bremsstrahlung functions do not always come in simple to integrate forms and input particle spectra are not always well known. The previous calculation suggests that one can correct the simple bremsstrahlung attenuation formula by including a corrective 'b' factor:

$$-\frac{dE}{dt} = bE$$

or similarly, one can show for the mass:

$$-\frac{dM}{dt} = bM$$

The following expressions then result for describing electron attenuation effects due to bremsstrahlung and the electron flux increase due to gamma conversions.

respectively:

$$F'(e,d) = F'(e,0)\exp(-bd/L_R)$$

$$F(e,d) = F(\gamma)\frac{a}{b-a}\left(\exp(-at) - \exp(-bt)\right)$$

The above argument can be improved (appendix 6) and a rather general proof can be made for these formulas. assuming a thin radiator (small value of 't'). One learns that:

$$b = \frac{4}{3}\ln(\ln E_0/E) \qquad (2)$$

For steep spectra, only nearby bins have enough events to significantly contribute, through bremsstrahlung, to the population of lower bins. This means that, for steep spectra E0/E is close to 1.0 and equation 2 predicts a large value of 'b'. For flat spectra, E0/E can be larger and 'b' will be closer to 1.0. So the equation is in rough accord with one's expectations.

BACKGROUND ESTIMATE: In what follows, various mass spectra will be combined to yield an upper limit on the dielectron background. Table 36 presents, in entries S1-S7, a list of the various pair data sets available from the dielectron running. All these have been expanded in terms of their constituent particles. The multiplicative factors B and G, respectively, represent the effects of bremsstrahlung and gamma conversions on the data.

The various cross section plots corresponding to e(0):e(0), e(c):e(c) etc. are shown in figures 44 through 46. For the sake of clarity, error bars have been left out of these plots. Figures 47 through 52 present the individual mass plots with error bars (statistical errors only).

By substituting the proper expressions from table 36, one can easily demonstrate that an upper limit on the dielectron background is given by:

$$B = \text{BACKGROUND} \leq \frac{(57-55) - B^2(56-53)}{B(G-B)} + 54 \quad (3)$$

UNITS of This - 54 what?

excluding E:E accidentals. This formula overestimates the N:N contribution by a factor of ((B+G)/B) and so provides an upper limit on the background. The final upper limit curve is shown as a dashed line in the cross section plot of figure 53.

To treat the case of E:E accidentals, one can use results from single arm electron data (references 62 and). One learns that direct electrons and pi zeroes have similar spectral slopes and that:

Conversion/Direct/Dalitz = 2/1/2

for an experiment with 0.74% of a radiation length of matter in the aperature, before the magnet bend. In E288 and E494,

there was more material in the aperature and this implies that:

N:N(accidentals) > E:E(accidentals)

In EXPRESSION 3, the N:N contribution to the background is overestimated by a factor of about 6; this includes both accidentals and correlateds. So the dashed line in figure 53 covers also the E:E accidental spectrum.

As noted previously, there is some uncertainty in this experiment's estimate of the air contamination of helium in the target box. While the helium outflow from the box was visible on a flow gauge, its flow rate was not sufficient to allow a purity measurement. The contamination of the helium must be known in order to make an accurate determination of the 'B' and 'G' values. 'B' is not affected greatly by filling the target box with all air , but B(G-B) shifts from 3.5 for pure helium, to 1.6 for pure air in the target box. The background estimate in figure 53 assumes a conservative value of 3 for B(G-B).

RESULTS: DIELECTRONS FROM 4 TO 11 GeV

Provided in figures 54 through 61 are various cross section plots based on the E288, E494 dielectron data samples:

Fig 54 1. E288

52 2. E494

3. E288 using E494 magnet calibration.

4. (1)+(2)

5. (3)+(2)

6. (4) with tight 'scaler' (incident beam quality) cuts

7. (4) with medium lead glass longitudinal shower cuts

8. (4) with 'loose' cuts

DILEPTON CONTINUUM

As has been shown in the section concerning backgrounds above M=4 GeV, hadronic and gamma conversion backgrounds are of minor importance above a mass of 5.5 GeV. The observed events above this mass are background free, target

originating dielectrons, and their observation in E288 yielded the first measurement of the theoretically predicted dielectron continuum.

Adequate fits to dimuon cross section data (M>5.0 GeV) are given by:

$$\frac{d^2\sigma}{dm\,dy}\Big|_{y=0} = A\,\frac{\left(1-\frac{M}{\sqrt{s}}\right)^B}{M^3} \qquad A \simeq 0.13\times10^{-31} \quad B = 10$$

Reference (63)

$$\frac{d^2\sigma}{dm\,dy}\Big|_{y=0} = C\,\exp(-DM) \qquad C \simeq 1.2\times10^{-33} \quad D = 0.95$$

Reference (64)

Change to correspond to Kaplan data

Ideally, one would like to fit these functional forms to the dielectron data, arrive at optimal values for A, B, C and D and compare these results directly with the dimuon cross section. Unfortunately, because of a low number of events, accurate determination of both a slope and an exponent in the fitting functions is impossible. While this is true, one can show consistency with the previously mentioned dimuon results. If one uses the above functional forms and allows only the overall normalizations (A and C) to vary, one arrives at the following fit normalization: A=0.124 ± 0.072; C=1.30 ± 0.26. Both results are in good agreement with the dimuon cross section results. A cross section plot of the region above M=5.5 GeV is provided in figure 62. Also shown is a dashed line to indicate the level of the dimuon cross section data of Herb et. al. (64).

THE 3.5 TO 5.5 GeV MASS REGION

In this region of the spectrum, significant background is present, and several components make up the observed data: 'accidental' pairs, 'correlated' hadronic and gamma conversion electron pairs and 'correlated' dielectrons.

The shape of the accidental background was determined by pairing single arm events and histograming their resultant mass spectrum. The relative normalization of the accidental cross section is known to better than 25%.

The cross sections of the correlated H:E, H:H, N:N and E:N components of the background (figure 42) are, for the most part, unknown. Cross section results from the correlated dihadron analysis of E494 (49) were found to be fit in the 4 - 10 GeV mass region by the single functional form $C/M^{11.25}$. When extrapolated to M=3 GeV, this formula predicts a cross section slope in good agreement with a prior dihadron experiment (65), and so may have some validity in the lower mass region.

Use of this single dihadron function to approximate all the correlated backgrounds is, of course, unjustified. Attempts were made to replace it with the more complex form of an (exponential + a mass power) function, but no significant fit improvement was achieved. The resultant 'fit subtracted' data plots were nearly identical. One of

these subtracted plots is shown in figure 63. It is, perhaps, mainly in the lower mass regions where one might suspect inadequacy of the employed fitting functions.

To estimate the magnitude of the dielectron cross section at low mass, formulas 4 and 5 were used. Both functional forms yield nearly identical overall fits to the cross section data and so will not be distinguished further. The applicability of these formulas to the M>5 GeV region is established by existing dimuon data, but their extrapolation to lower masses is presently in dispute (63).

All objections notwithstanding. a fit to the observed cross section of figure 57 was performed by combining the cross sections for the accidental background, the 'dihadron' background and the dilepton continuum. The fit was done in two stages. First, the overall normalization of the dilepton contribution was determined a fit to the data above 5.5 GeV; secondly, the fit to the lower mass regions was done, maintaining this measured dielectron normalization, and allowing the accidental and correlated 'dihadron' normalizations to vary. This fit was done over the 3.5 to 11.0 mass range, and excluded all suspected enhancement and known resonance regions. Typically, in each fit, the dielectron normalization remained close to its dimuon predicted value. the accidental normalization was shifted down 30%, and the magnitude of the 'dihadron' contribution varied, depending on the functional form of the dilepton

continuum function.

Where are the results of this fit?

ENHANCEMENT STUDY

The enhancement regions selected for study were near the mass values of 4.2, 4.9, 6.0 and 9.4 GeV. The number of events appearing in the 6.0 and 9.4 GeV regions can be read from the cross section plot of figure 57. For the 4.2 and 4.9 GeV mass regions, a detailed raw data plot is provided in figure 64. Regarding the actual number of events, 20-25 events are found within resolution near 4.2, 15-20 near 4.9, 10-15 near 6.0 and 6 near 9.4.

To decide questions of an enhancement's significance, one would like to measure the number of standard deviations each enhancement represents over a smooth background, insisting that the enhancement's width be consistent with one's experimental resolution. Clearly, when one deals with few events, the 'background' may not appear smooth, the estimate of the enhancement's statistical significance may not be very reliable, and the measured enhancement width may not be well defined. Nonetheless, one can perform the calculations. Estimates of statistical significance, mass values, cross sections and widths are presented in Table 38.

The subtracted data plot on which the Gaussian peak fit and the statistical significance calculations are based is shown in figure 63. In estimating the significance of enhancements, 'negative event' bins have been set to zero, so as not to increase the statistical significance estimates. ~~The treatment of these bins is of minor importance.~~

The fitting program minimized the negative log likelihood for each fit, assuming a Poissonian distribution function. Errors were combined using the log likelihood result from Poisson statistics:

$$a_i = N_i - N_i'$$

$$\Delta a = \left(-\sum \frac{\partial^2 w}{\partial a_i^2}\right)^{1/2} = \sqrt{\sum \frac{a_i^2}{N_i}}$$

N_i = NUMBER OF OBSERVED EVENTS IN iTH BIN

N_i' = ESTIMATED NUMBER OF 'CONTINUUM' EVENTS IN iTH BIN (REFERENCE 66)

This 'classical' treatment of the statistical significance question yields unambiguous results when applied to large numbers of events, but such is not the case in the data sample of this paper. One knows that fluctuations of small numbers of events in the 'background' can give rise to spurious clusterings of events. To attempt to answer some questions regarding the statistical significance of small numbers of events, a second, quite different approach was used to study the enhancement problem

- a series of Monte Carlo simulations of the experiment were made. Ideally, one would like to answer the the following question: If this dielectron experiment were repeated 100 times, in how many experiments would random 'background' fluctuations yield spectra with enhancements equal to or better than those observed in E288+E494. Expressed as a percentage, this number will be referred to as the random cluster probability for a given event configuration.

One can simulate the non-resonant data spectrum of this experiment by generating random number 'events' and sorting them out into bins, whose width is proportional to the product, at each mass value, of this experiment's sensitivity and observed cross section. Having thrown all events, the resultant event spectrum can be scanned for clusters of N events. To qualify as an enhancement, the events must be required to fall within some multiple of the experimental mass resolution (figure 65), at the mass value where the cluster is centered.

For the study of the combined E288+E494 data samples, 262 events (ψ' subtracted) were thrown in the mass region from 3.5 to 11 GeV. and a search was made for enhancements falling within 4 or 5 times the σ of the experimental mass resolution. The cross section distribution, used for determining the width of the 'event' bins was estimated using a wide binned (1 GeV) cross section plot of the dielectron data, excluding only the ψ' region. No

functional form was sought to approximate the cross section curve; an interpolation program was used to calculate cross section values between data points.

Results are shown in Table 38. The 'cluster probability' program evaluated cluster probabilities for 'N' events within resolution, at mass values from 3.5 to 11 GeV. A few smple cluster probability values for the number of events observed at other masses. A few sample cluster probability values for the number of events observed at other masses are as follows: 4.5 GeV - 83.4%, 5.5 GeV - 49.2%, 6.5 GeV - 65.6%, 7.5 GeV - 66.3%. 8.5 GeV - 2.9%.

It is instructive, in addition to this, to compare results from E288 and E494 separately to see whether both data sets yield similar cluster probability values at the same masses. For this study. 138 (E494) and 124 (E288) events were thrown into the 3.5 to 11 GeV mass region, using each experiment's sensitivity and each experiment's measured cross section. A search for clusters within 4 σ (mass resolution) was done as before, adjusting the mass resolution for each experiment following figure 65. Results are presented in an easy-to-compare form in Table 39.

A few comments are in order about each enhancement region. While none of the lower mass enhancements are very strong each does have its characteristic features.

<u>M=4.2 GeV</u>: A glance at figure 63 reveals that, of all the

mass regions under study. the 4.2 GeV region has the most uncertain functional fit. While the 'accidental's' mass spectrum shape is not well known at low masses. The dilepton continuum function is not well verified below M=5.0 GeV. The 'classical' statistical significance estimates cannot be simply taken at face value. The interesting fact about this enhancement is not not that it is associated with a relatively low cluster probability, but that the enhancement is see by two experiments of widly differing resolution. The cluster probability values for the enhancement are too large to permit further conclusions.

M=4.9 GeV: The significance of this enhancement is weakened by the lack of agreement between E288 and E494.

M=6.0 GeV: This enhancement, unlike those already considered, appears in a region where the nature of the 'continuum' is completely known. This is an important fact. A calculation of the enhancements statistical significance can be made with some confidence. Referring to figure , the level of the dielectron continuum, in the 5.8 to 6.1 region, is 1.2 to 0.8 events per bin (50 MeV). All events above this are excess. A glance at figures 59, 60 and 61 convinces one that the cluster is not easily 'dispersed' by tighter or looser cuts. The fitting program estimates that the enhancement has a standard deviation of 110 MeV, which is beyond resolution. An additional study was made to

investigate the significance of a possible wide enhancement. The cluster probability for 17 events in eight 5% MeV bins was 2.5%. Assuming that the M=6.8 enhancement is wide, the apparently serious inconsistency between E288 and E494 cluster mass values disappears.

M=9.4 GeV: This is, of course, a resonance region. It has been treated as an enhancement so far to learn what the dielectron data, alone, would say about the Υ (9.4). Its measured cluster probability is low, and its measured cross section is +- .

Table 39

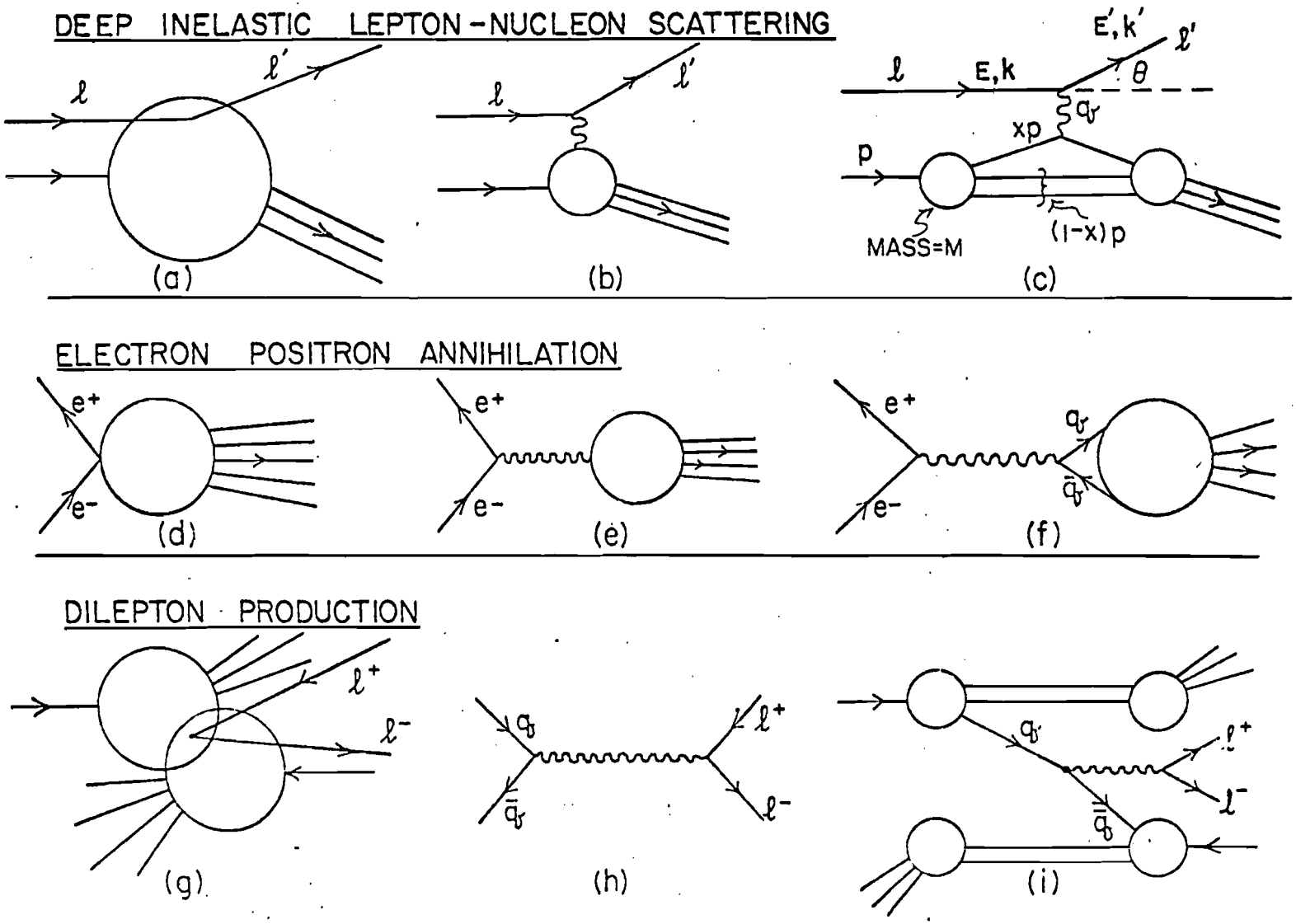
DEEP INELASTIC LEPTON-NUCLEON SCATTERING
ℓ
ℓ′
(a)
ℓ
ℓ′
(b)
E′,k′
ℓ′
ℓ
E,k
θ
q_γ
xp
p
MASS=M
(1-x)p
(c)
ELECTRON POSITRON ANNIHILATION
e+
e-
(d)
e+
e-
(e)
e+
e-
q_γ
$\bar{q}_\gamma$
(f)
DILEPTON PRODUCTION
ℓ+
ℓ-
(g)
q_γ
$\bar{q}_\gamma$
ℓ+
ℓ-
(h)
q_γ
ℓ+
ℓ-
$\bar{q}_\gamma$
(i)

FIGURE 1

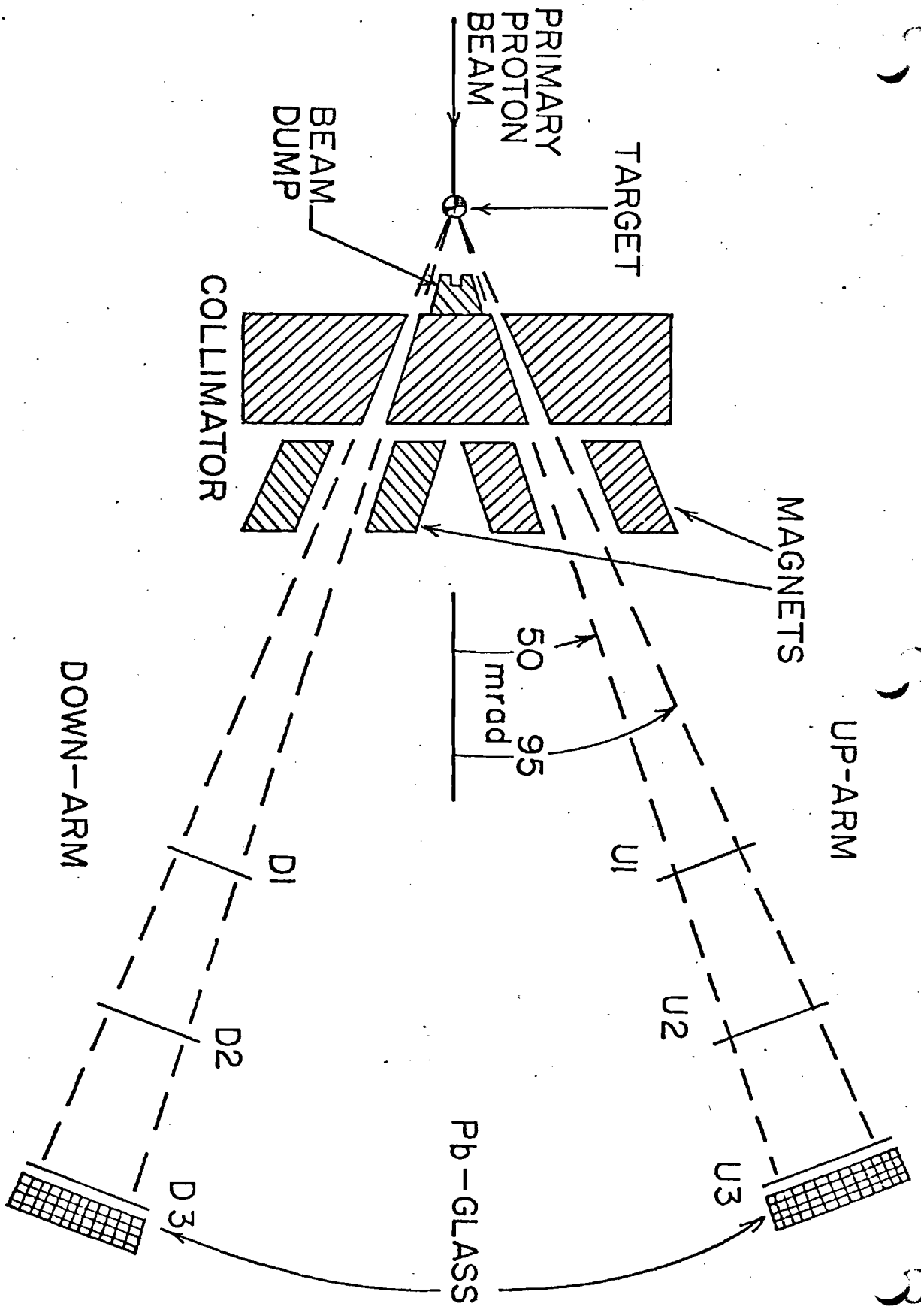
PRIMARY PROTON BEAM
TARGET
BEAM DUMP
COLLIMATOR
MAGNETS
50 mrad 95
UP-ARM
DOWN-ARM
U1
U2
U3
D1
D2
D3
Pb-GLASS
0
10
20
30
40
meters

FIGURE 2

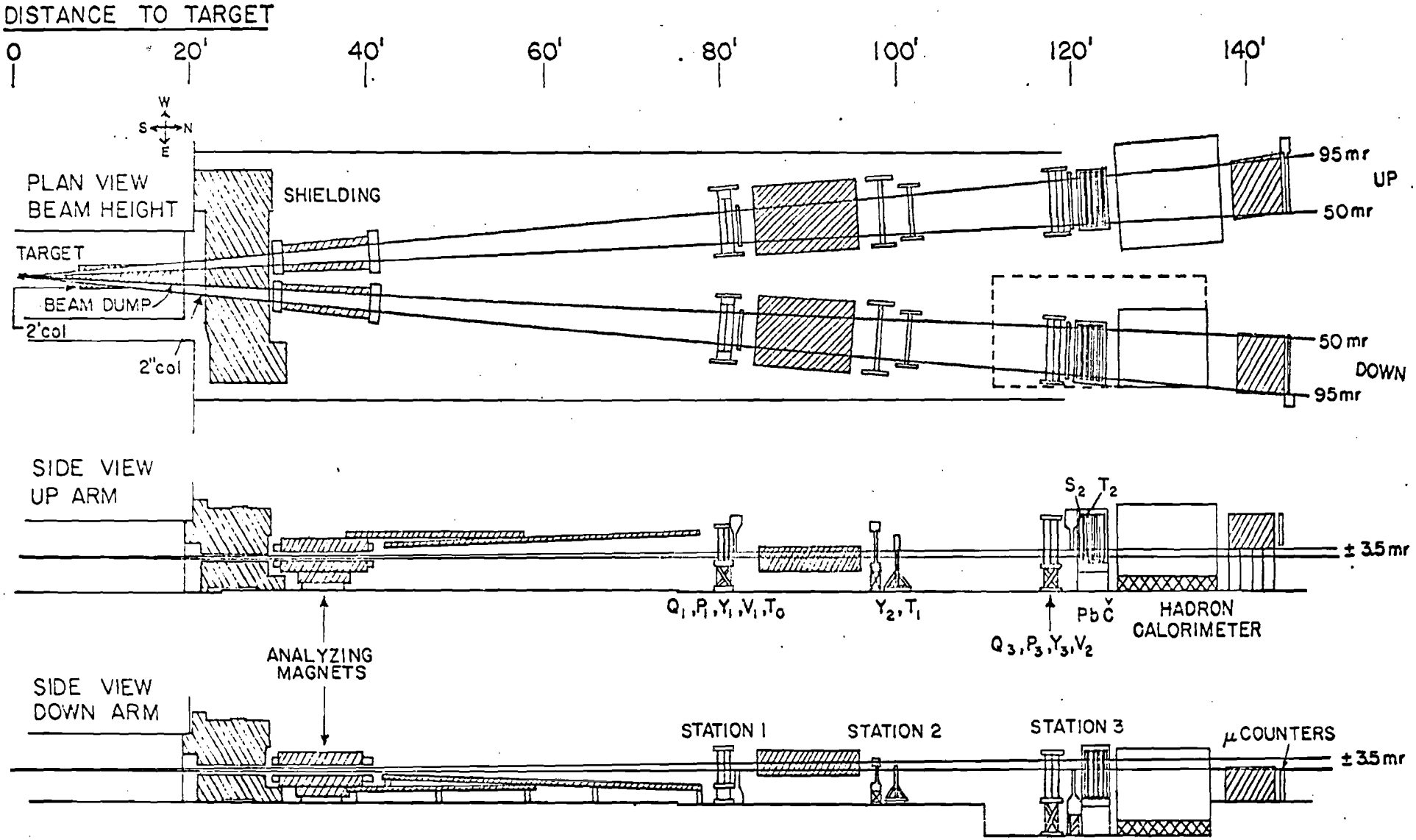
DISTANCE TO TARGET
0
20'
40'
60'
80'
100'
120'
140'
W
S
N
E
PLAN VIEW
BEAM HEIGHT
SHIELDING
TARGET
BEAM DUMP
2'col
2"col
95mr
UP
50mr
50 mr
DOWN
95mr
SIDE VIEW
UP ARM
S_2 T_2
± 3.5mr
Q_1, P_1, Y_1, V_1, T_0
Y_2, T_1
Q_3, P_3, Y_3, V_2
PbČ
HADRON
CALORIMETER
ANALYZING
MAGNETS
SIDE VIEW
DOWN ARM
STATION 1
STATION 2
STATION 3
μ COUNTERS
± 3.5mr

FIGURE 3

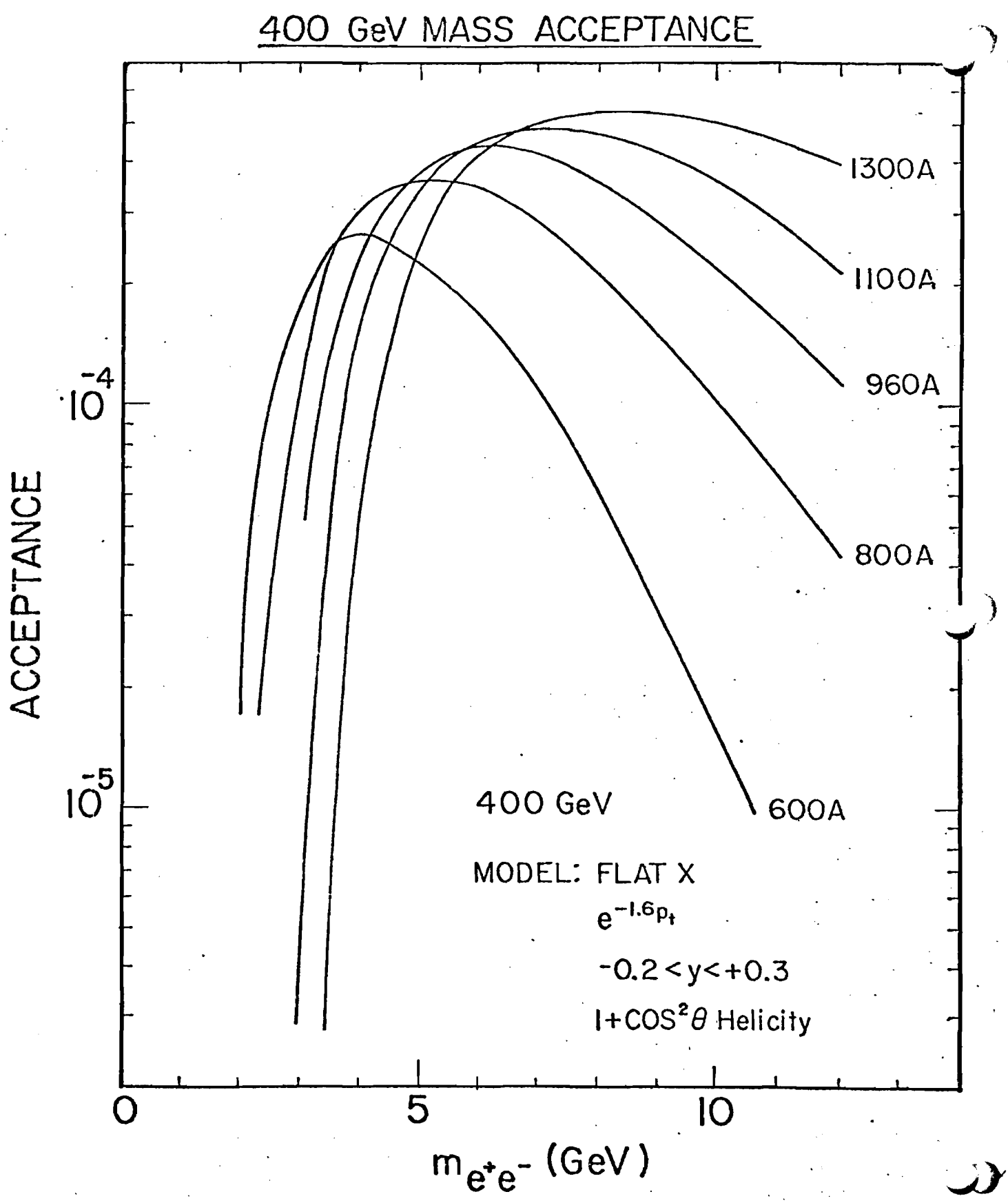
400 GeV MASS ACCEPTANCE
ACCEPTANCE
10^{-4}
10^{-5}
1300A
1100A
960A
800A
600A
400 GeV
MODEL: FLAT X
$e^{-1.6p_t}$
$-0.2<y<+0.3$
$1+\cos^2\theta$ Helicity
0
5
10
$m_{e^+e^-}$ (GeV)

FIGURE 4

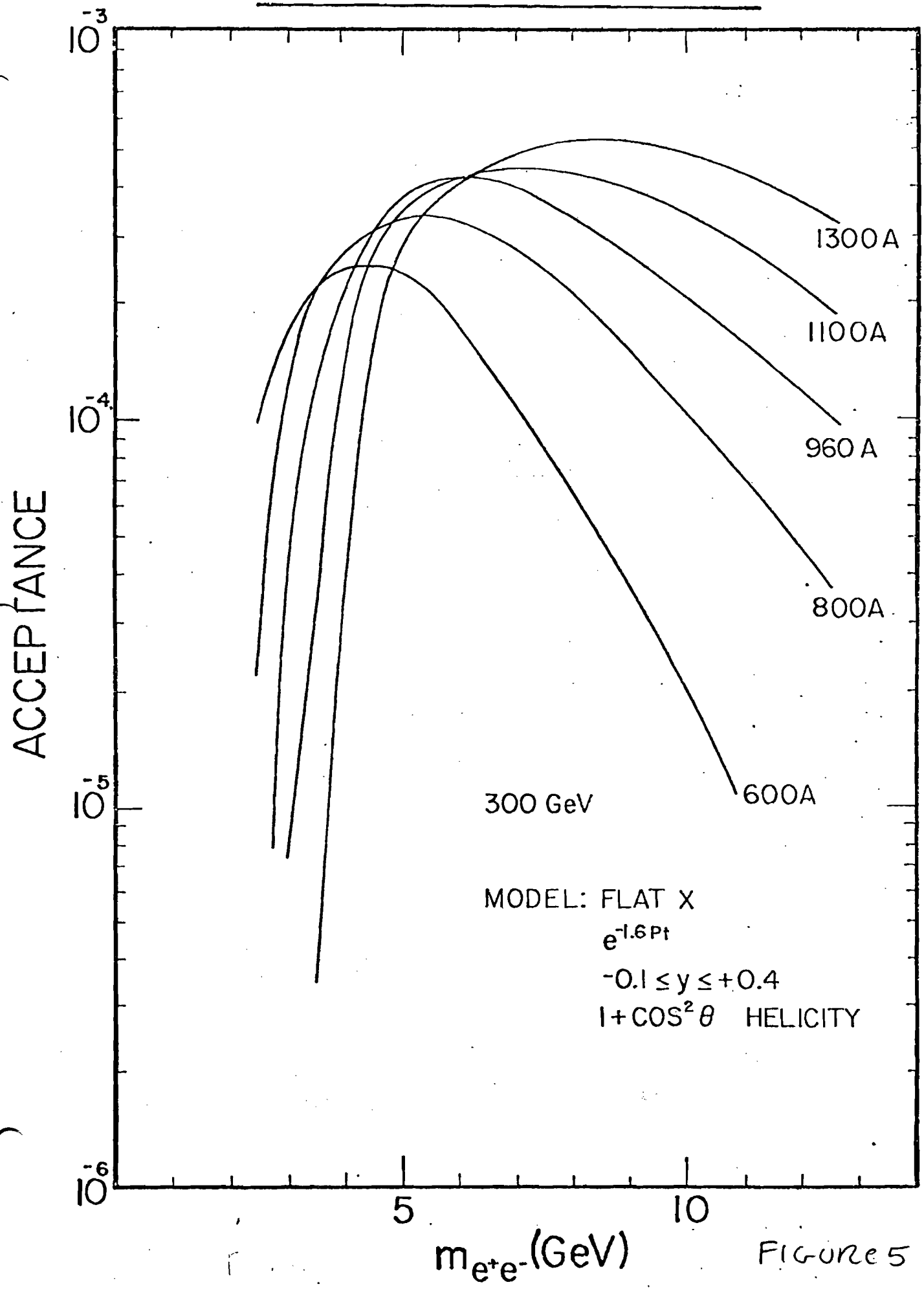
300 GeV MASS ACCEPTANCE
ACCEPTANCE
10^{-3}
10^{-4}
10^{-5}
10^{-6}
1300A
1100A
960A
800A
600A
300 GeV
MODEL: FLAT X
$e^{-1.6Pt}$
$-0.1 \leq y \leq +0.4$
$1+\cos^2\theta$ HELICITY
5
10
$m_{e^+e^-}$(GeV)

FIGURE 5

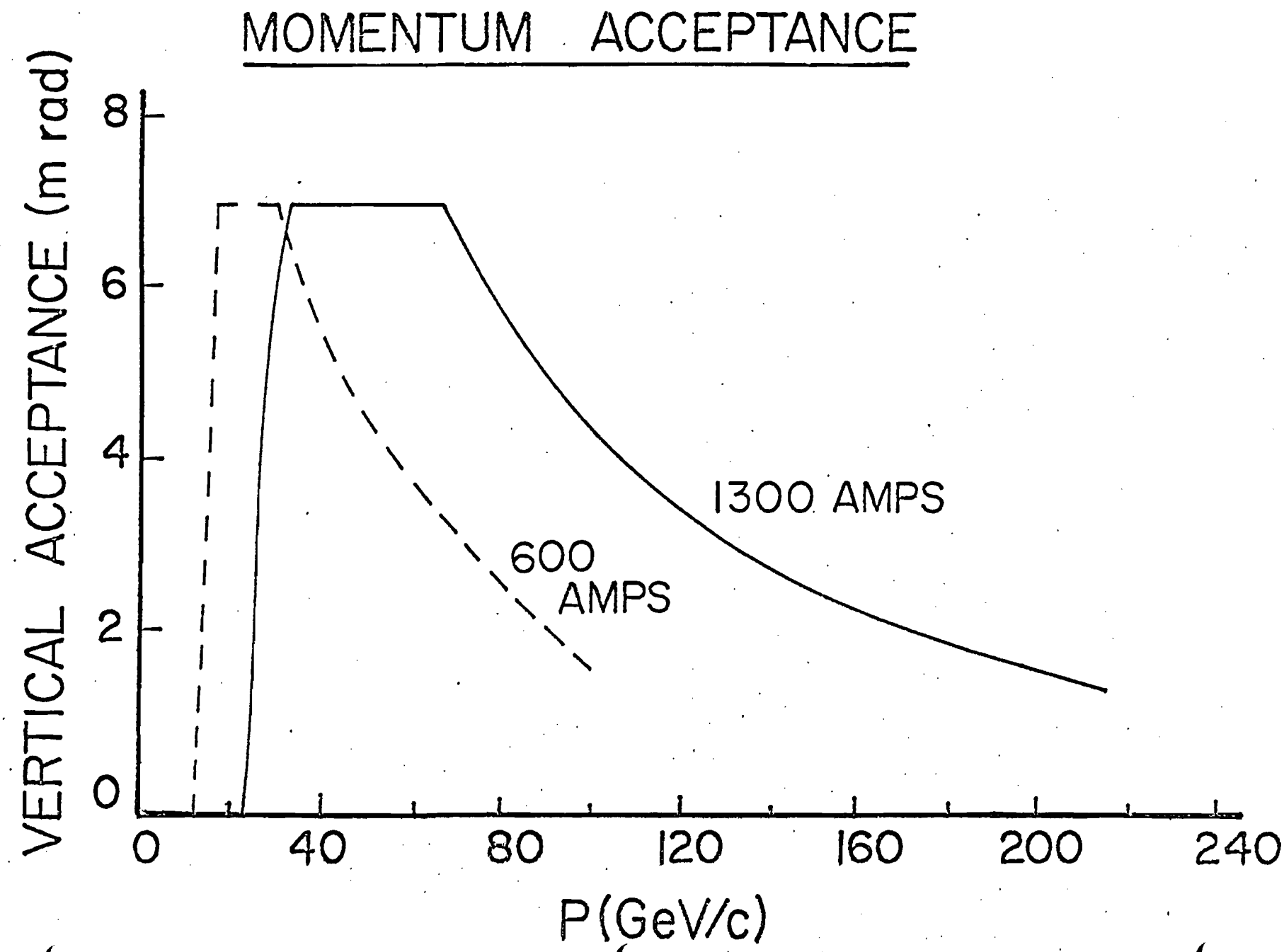
MOMENTUM ACCEPTANCE
VERTICAL ACCEPTANCE (m rad)
0
2
4
6
8
0
40
80
120
160
200
240
P(GeV/c)
1300 AMPS
600
AMPS

Figure 6

TRIGGER COUNTERS: TØ, TI, S2, T2
MWPC: IQ, IP, IY, 2Y, 3Q, 3P, 3Y
HODOSCOPES: VI, V2

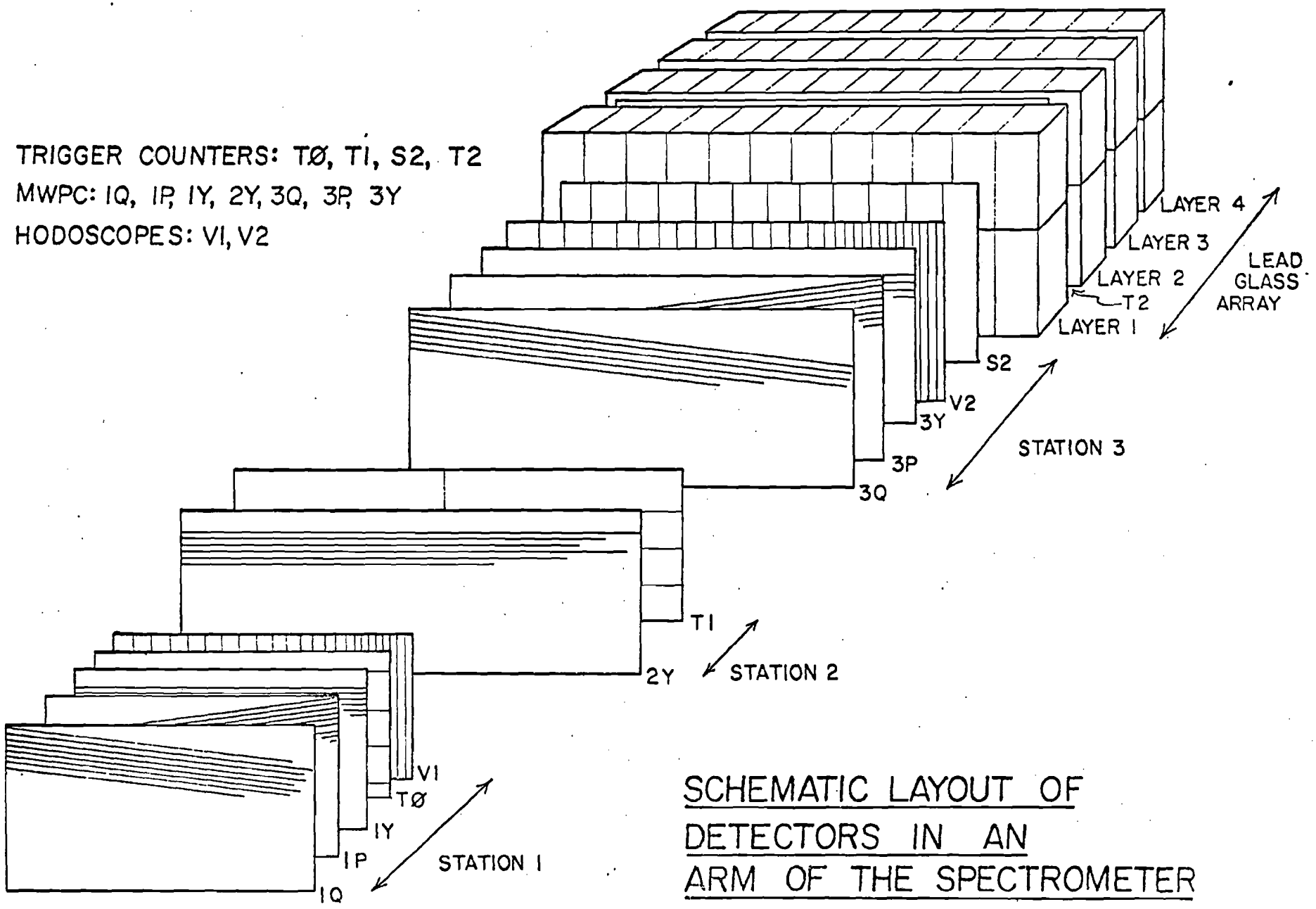

SCHEMATIC LAYOUT OF DETECTORS IN AN ARM OF THE SPECTROMETER

Figure 7

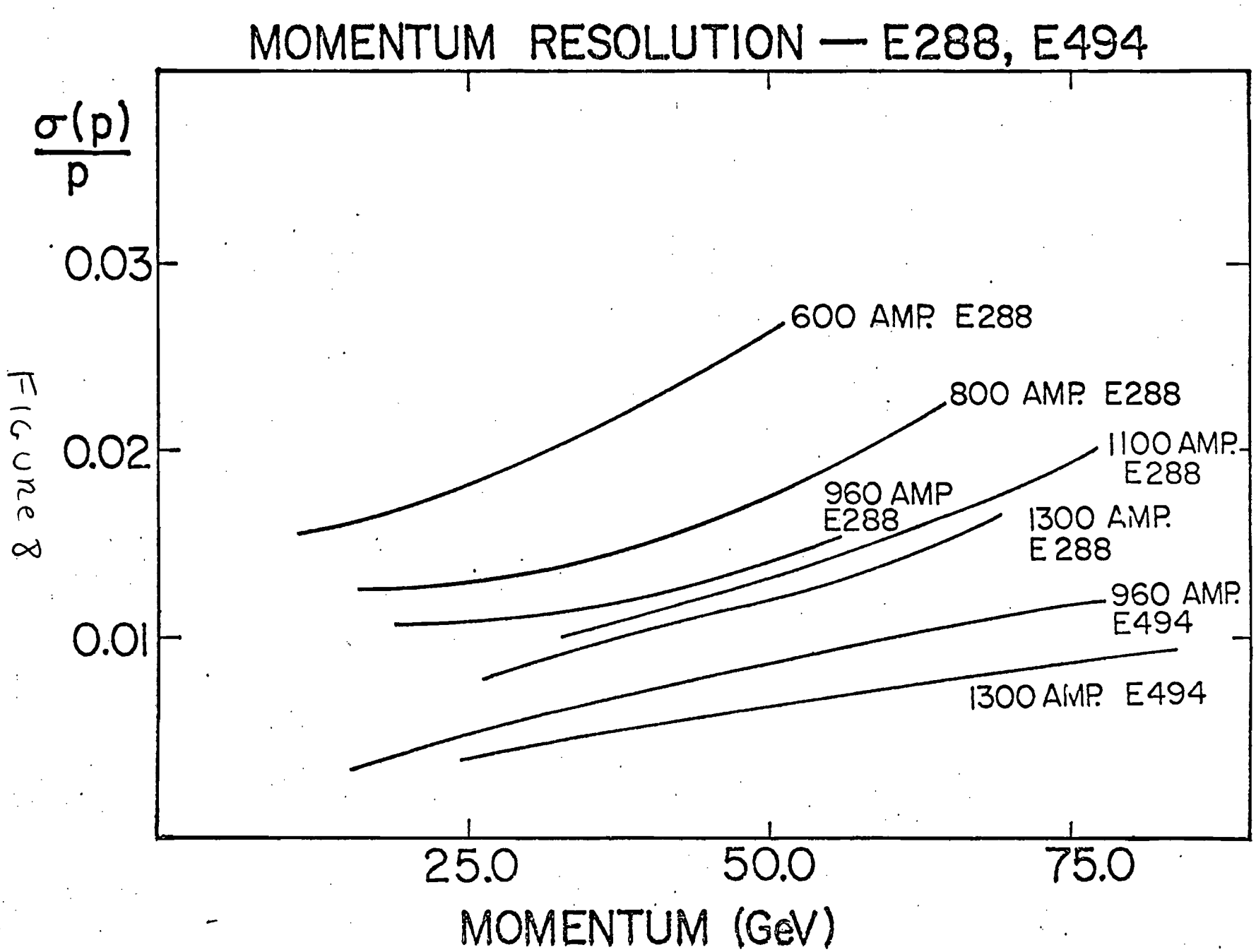
MOMENTUM RESOLUTION — E288, E494
σ(p)/p
0.03
0.02
0.01
600 AMP. E288
800 AMP. E288
1100 AMP. E288
960 AMP E288
1300 AMP. E288
960 AMP. E494
1300 AMP. E494
25.0
50.0
75.0
MOMENTUM (GeV)

Figure 8

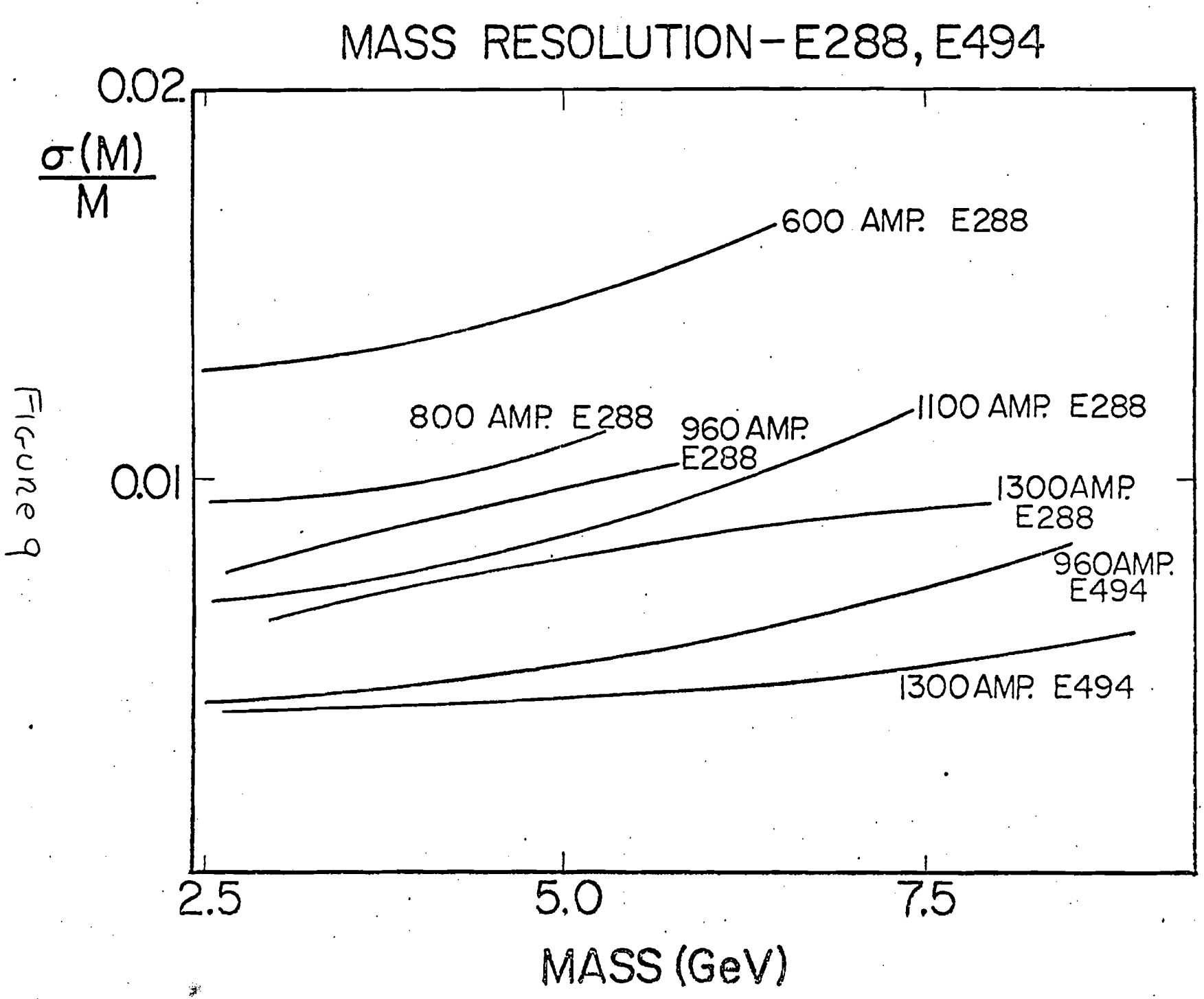
MASS RESOLUTION – E288, E494
0.02
σ(M)/M
0.01
600 AMP. E288
800 AMP. E288
960 AMP. E288
1100 AMP. E288
1300AMP. E288
960AMP. E494
1300AMP. E494
2.5
5.0
7.5
MASS (GeV)

Figure 9

SAMPLE PHOTOGRAPHS OF OSCILLOSCOPE SPILL MACROSTRUCTURE MONITOR

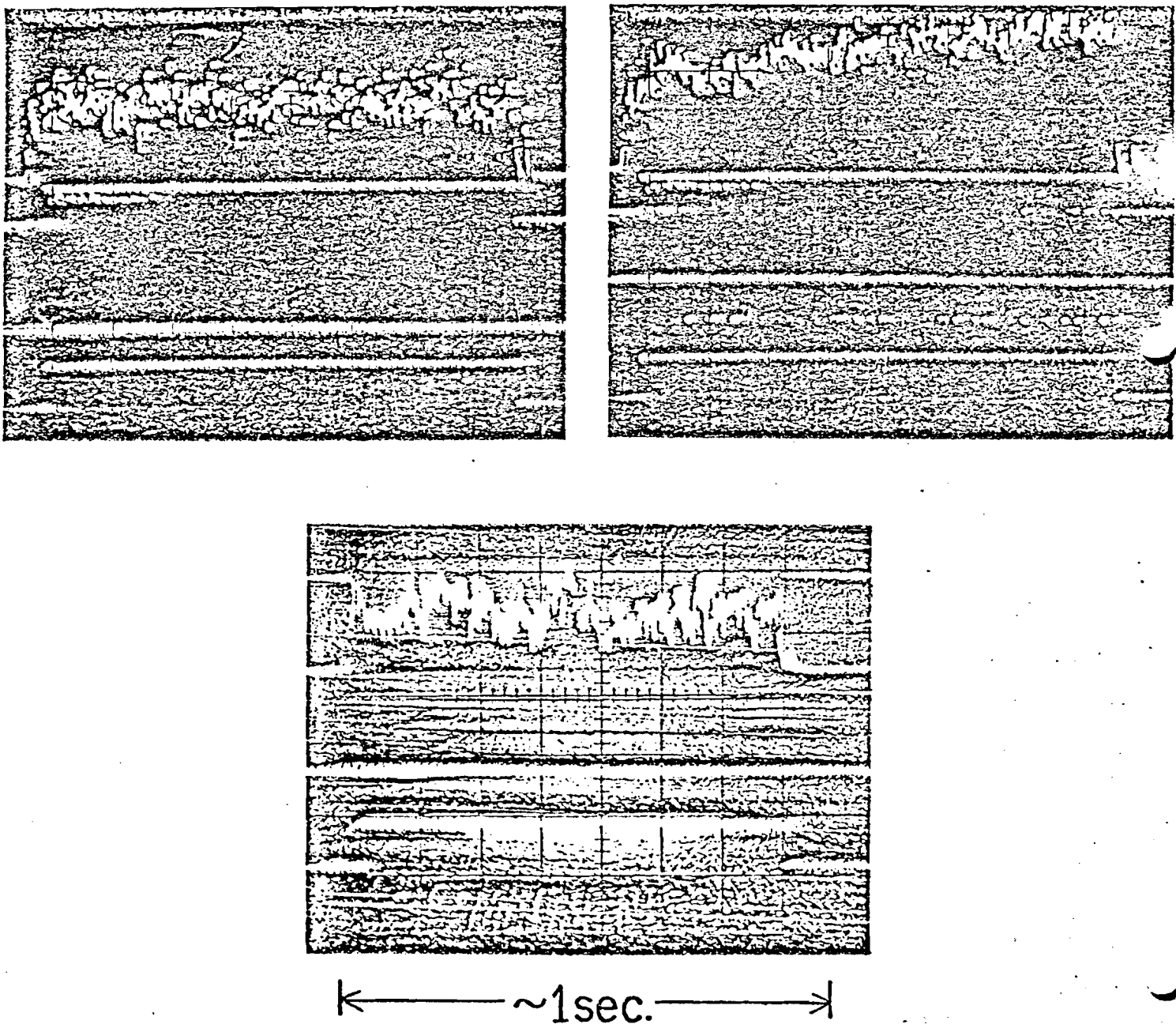

FIGURE 10

SAMPLE PHOTOGRAPHS OF PHA BUCKET MONITOR

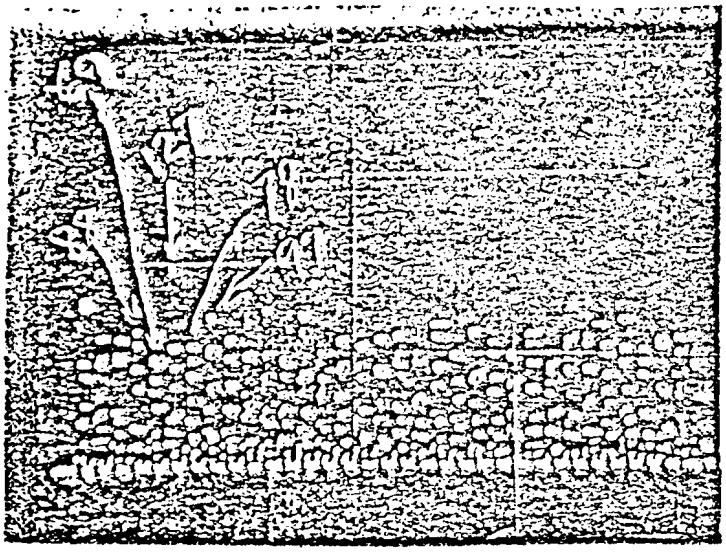

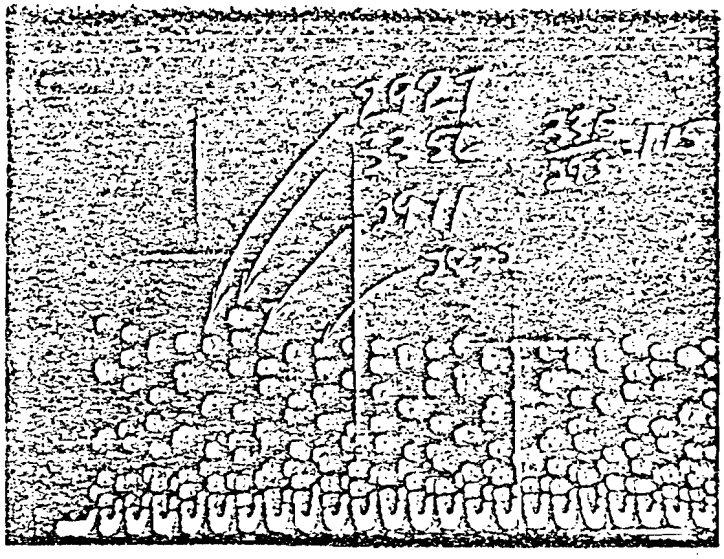

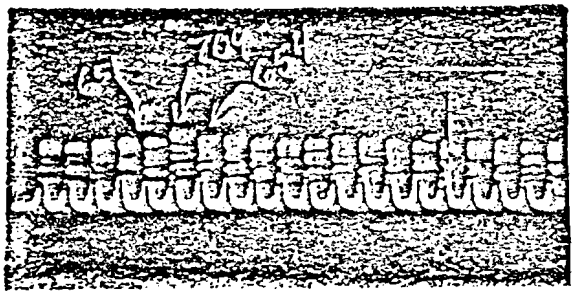

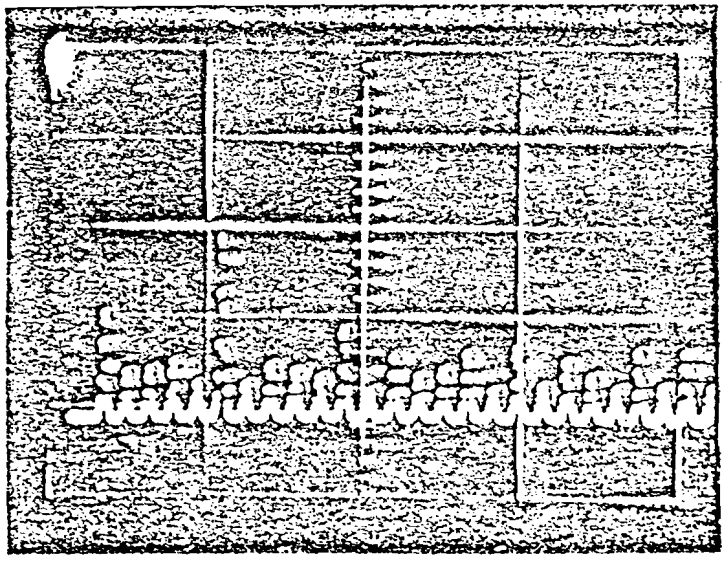

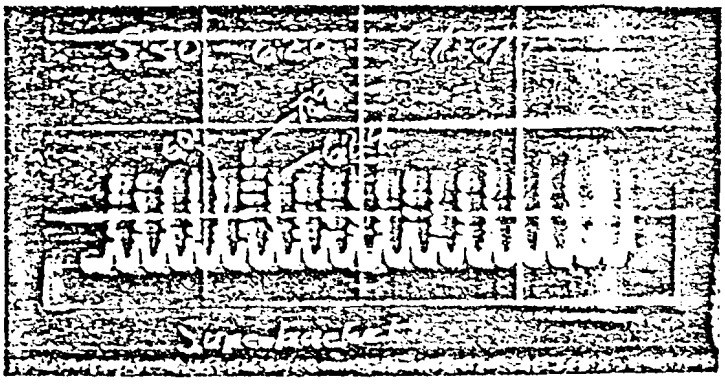

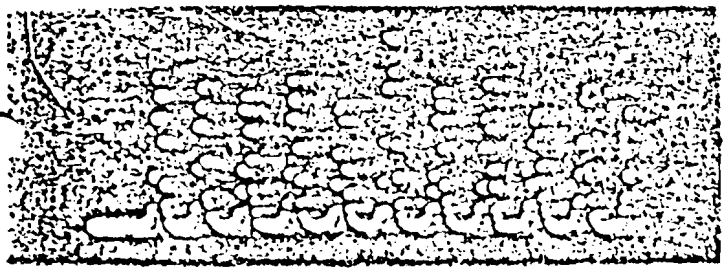

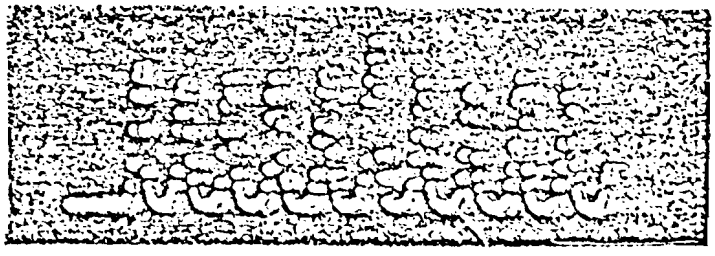

Figure 11

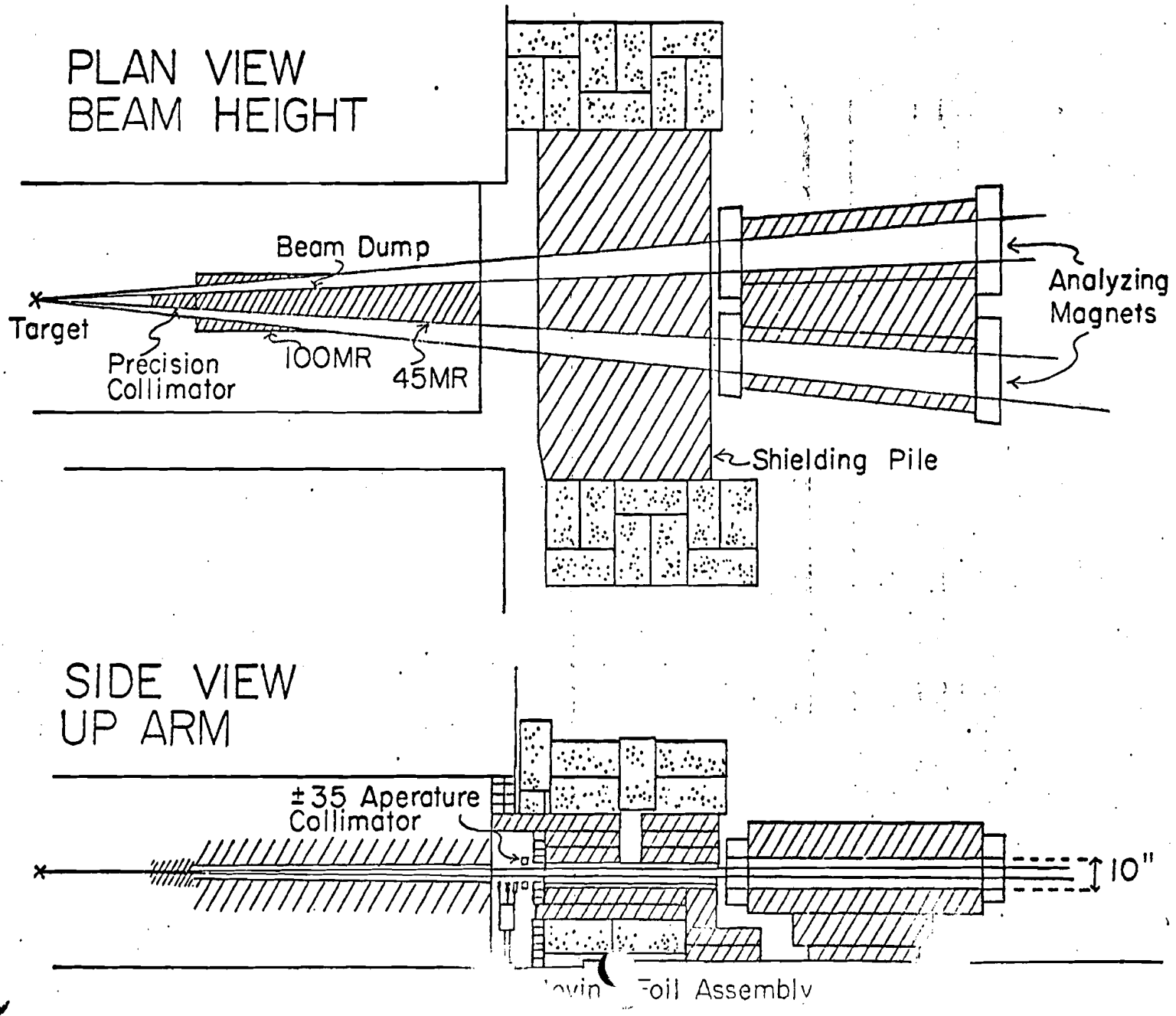
PLAN VIEW
BEAM HEIGHT
Beam Dump
Target
Precision
Collimator
100MR
45MR
Analyzing
Magnets
Shielding Pile
SIDE VIEW
UP ARM
±35 Aperature
Collimator
10"
Foil Assembly

Figure 12

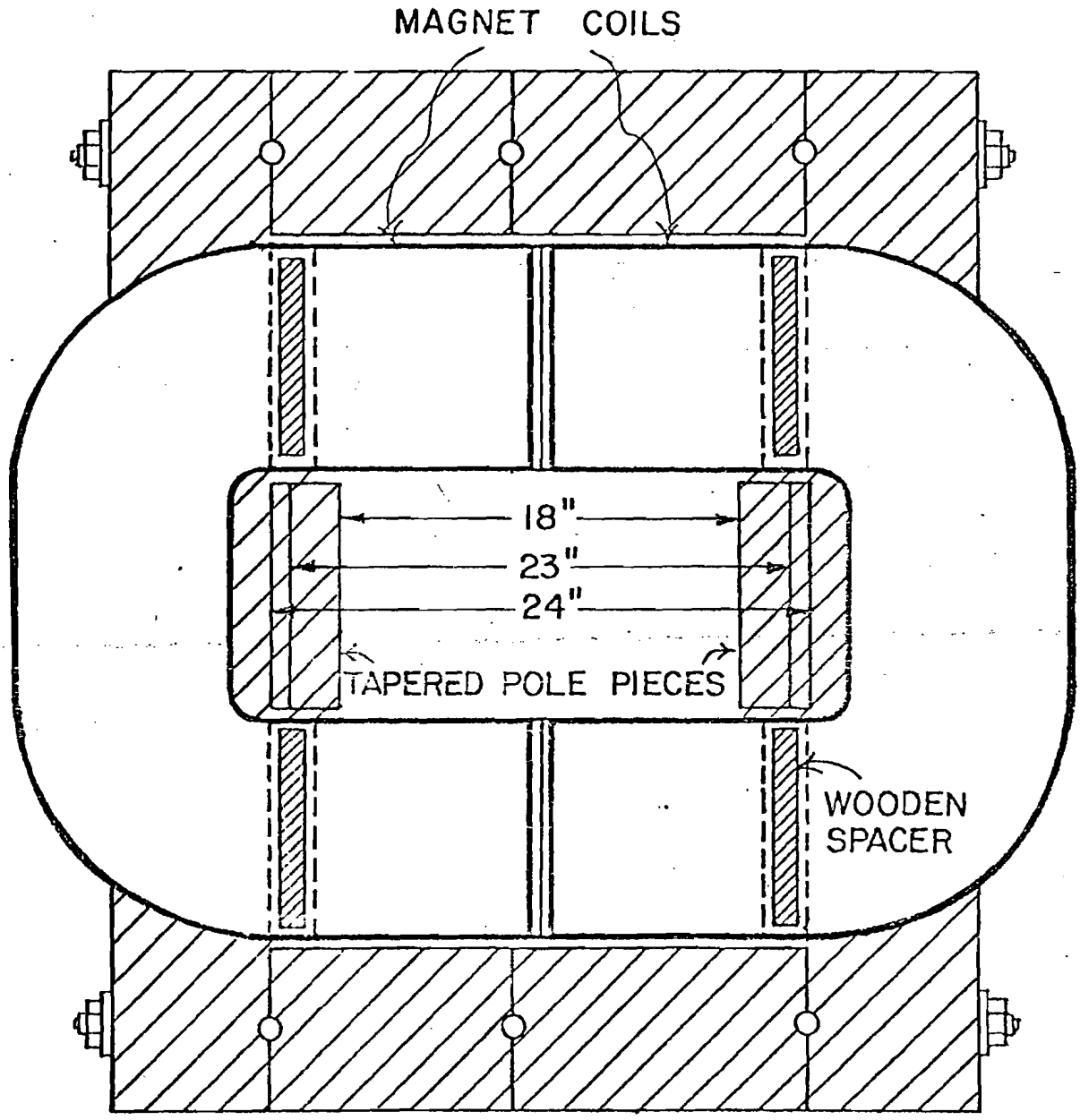

MAGNET VIEWED FROM DOWNSTREAM

Figure 13

TRIGGER COUNTER GEOMETRY

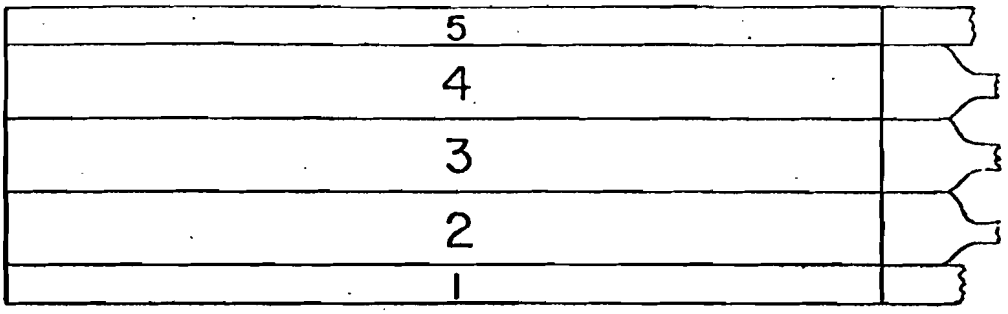

TØ

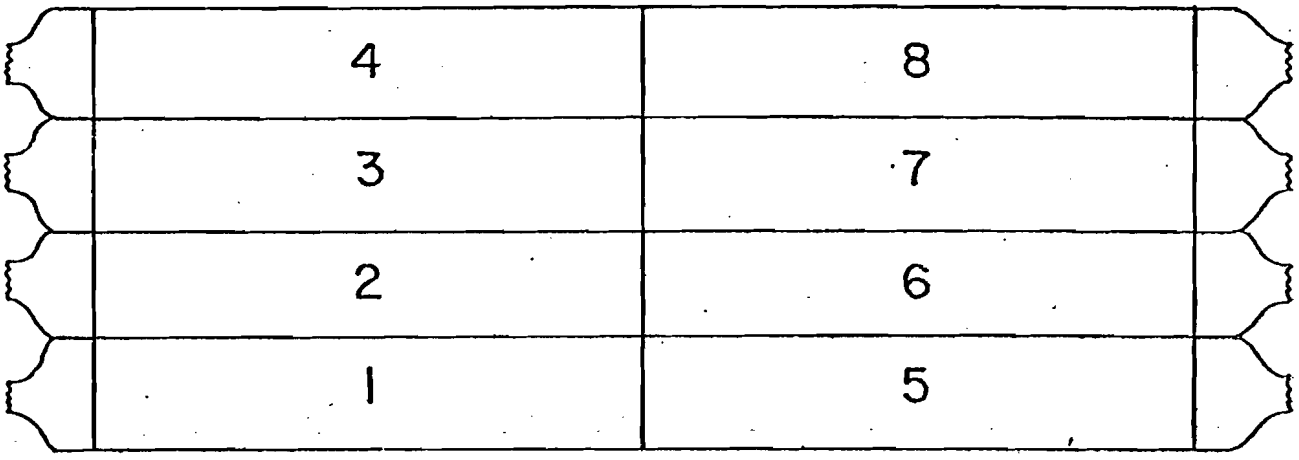

T1

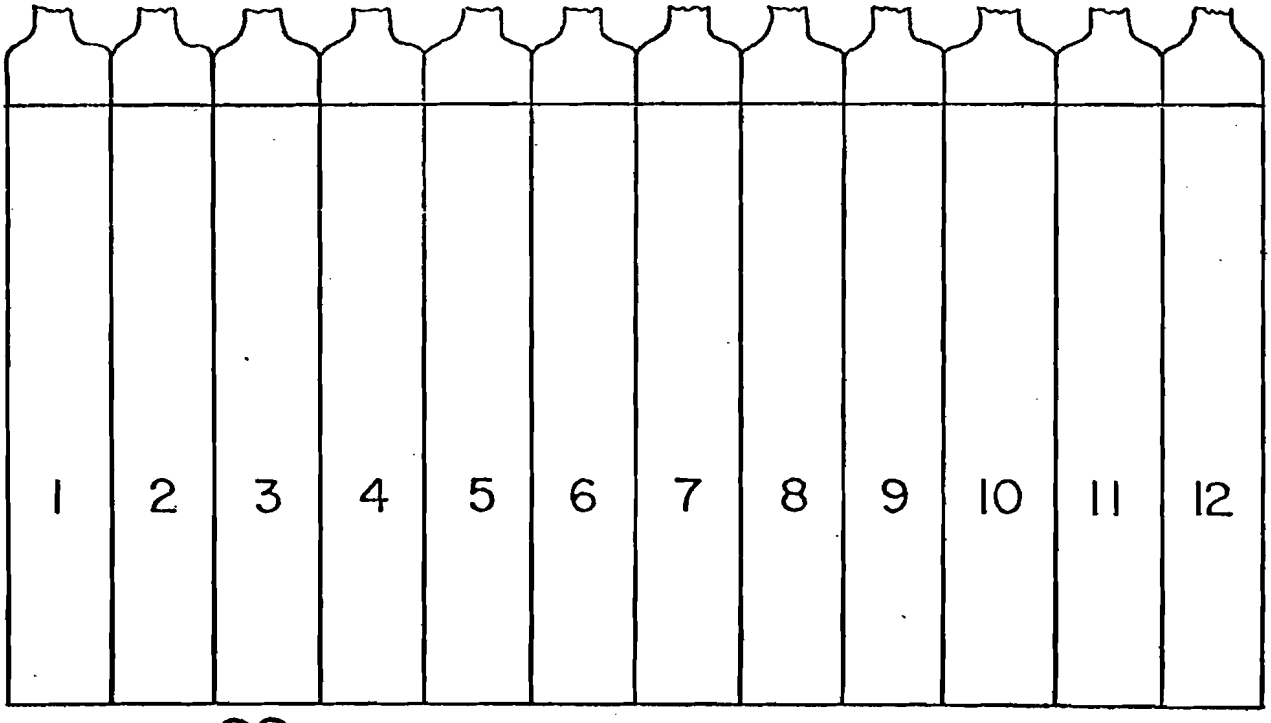

S2

12"

FIGURE 14

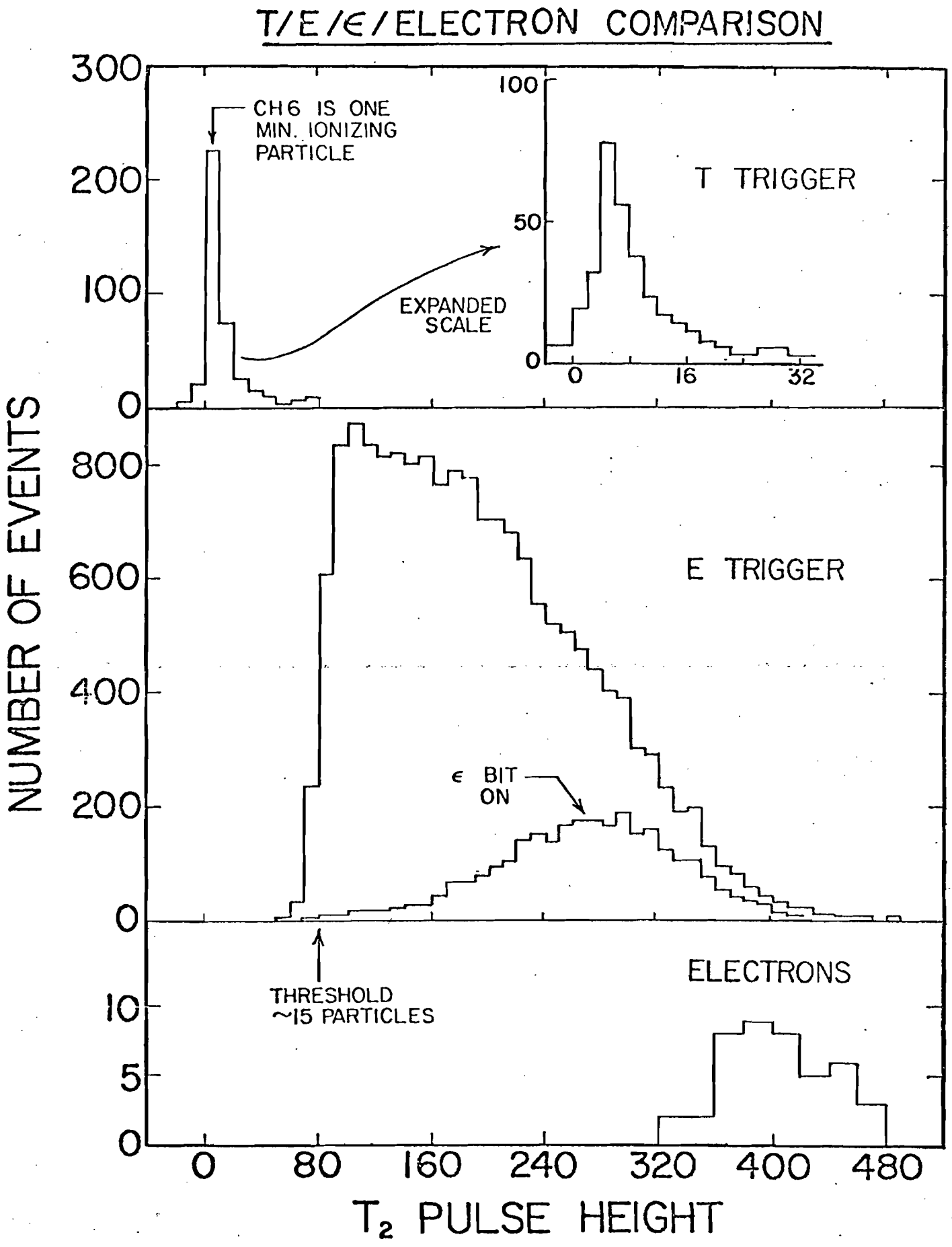
T/E/ϵ/ELECTRON COMPARISON
CH6 IS ONE MIN. IONIZING PARTICLE
EXPANDED SCALE
T TRIGGER
E TRIGGER
ϵ BIT ON
ELECTRONS
THRESHOLD ~15 PARTICLES
NUMBER OF EVENTS
T2 PULSE HEIGHT
300
200
100
0
100
50
0
0
16
32
800
600
400
200
0
10
5
0
0
80
160
240
320
400
480

Figure 15

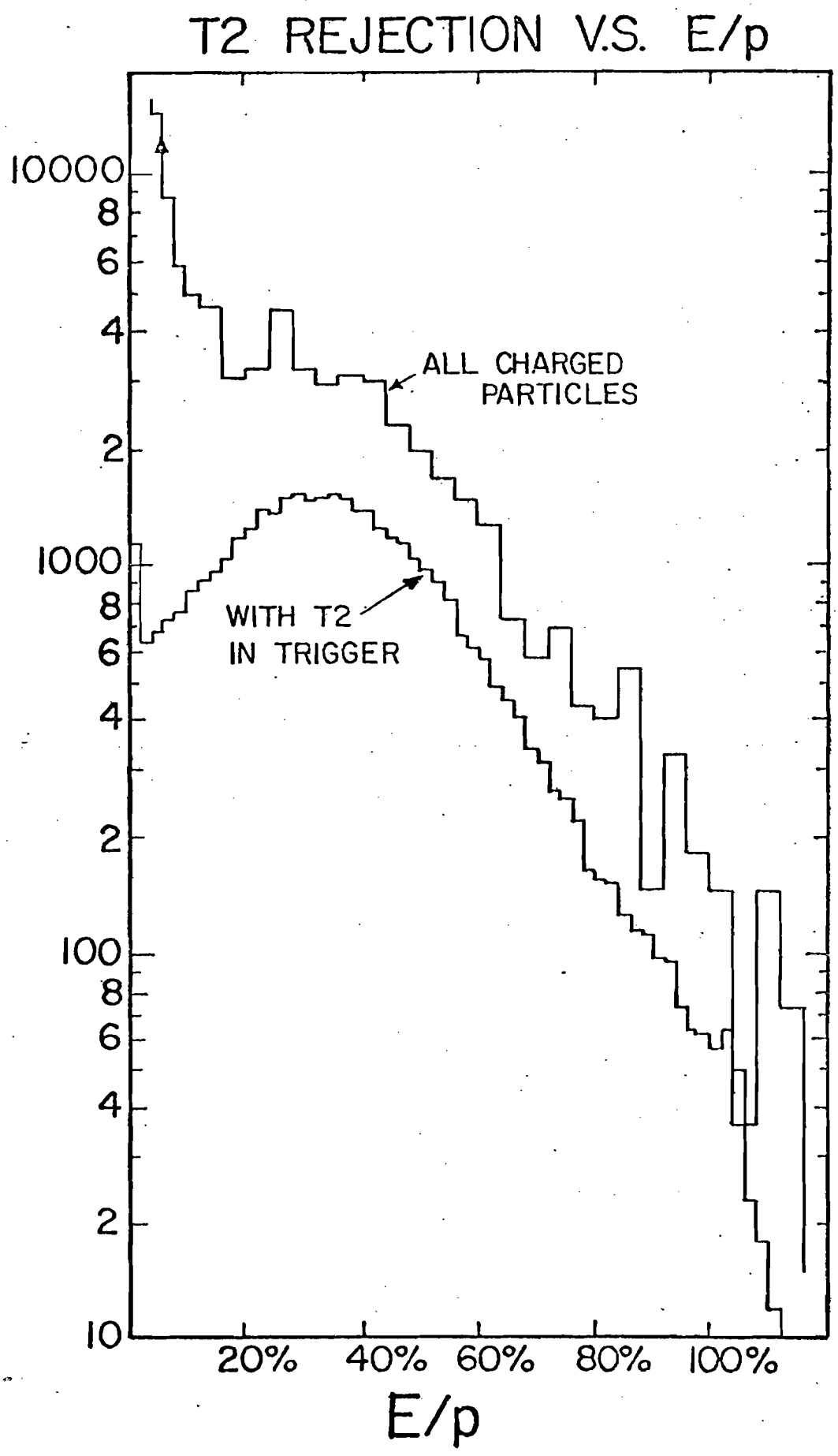
T2 REJECTION V.S. E/p
10000
8
6
4
2
1000
8
6
4
2
100
8
6
4
2
10
ALL CHARGED PARTICLES
WITH T2 IN TRIGGER
20%
40%
60%
80%
100%
E/p

Figure 16

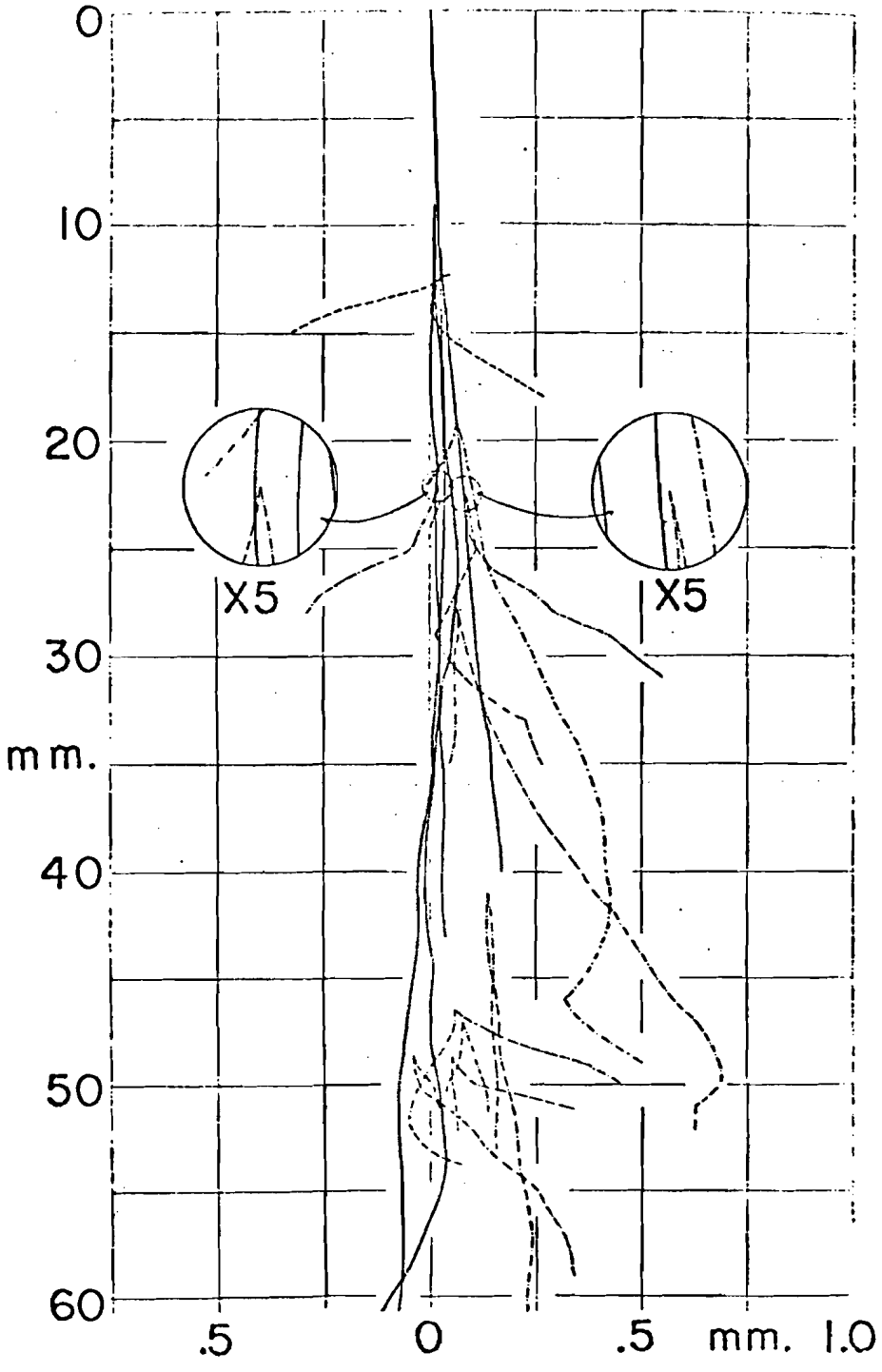

Tracing drawing of the tracks in a cascade shower, initiated by an 18 MeV photon. Two radiation lengths of the shower development are shown. Note the factor of 20 difference in the horizontal and vertical scales. Particle tracks eventually disappear as they pass out of the plane of the photographic emulsion. (After J. H. Hooper, D. T. King, A. H. Morrish, Canadian Journal of Physics, 29, 550 (1951))

FIGURE 17

CERENKOV RADIATION

(a)

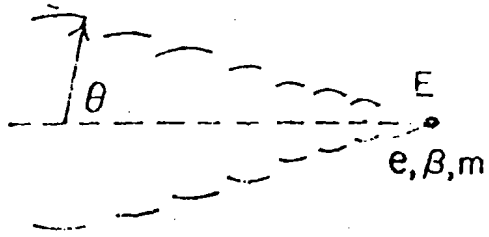

N = # OF PHOTONS

$$\cos\theta = (\beta n)^{-1}$$

$$\frac{d^2E}{dx\,d\omega} = \frac{e^2}{c^2}\left(1 - \frac{1}{n^2(\omega)\beta^2}\right)\omega \qquad \left[\beta n(\omega) > 1\right]$$

$$\frac{d^2N}{dx\,d\omega} = \frac{\alpha}{c}\left(1 - \frac{1}{n^2(\omega)\beta^2}\right)$$

$$\frac{dN}{dx} = 2\pi\alpha\left(\frac{1}{\lambda_1} - \frac{1}{\lambda_2}\right)\left(1 - \frac{1}{n^2\beta^2}\right)$$

(b)

CERENKOV FACTOR vs ELECTRON ENERGY

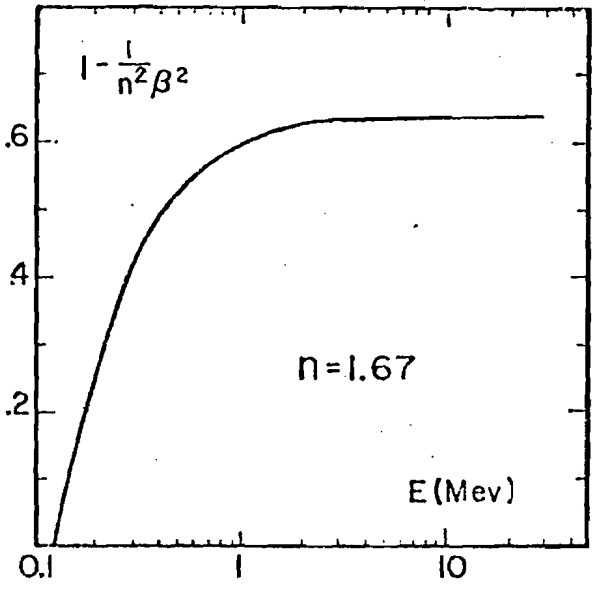

REF. E. LONGO, I. SESTILI, NIM, 128, 283 (1975)

MINIMUM ELECTRON E for $\hat{C}$ EMISSION $= m\left(\frac{1}{\sqrt{1-n^2}} - 1\right) \simeq .13$ MeV

BREMSSTRAHLUNG

(c)

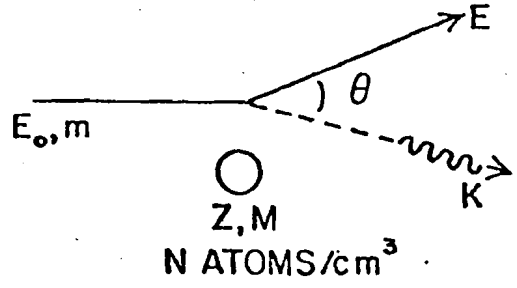

$\theta(\text{RMS}) \simeq 8.0\, \ln(E_0/mc^2)/(E_0/mc^2)$ RADIANS

ϕ_K = CROSS SECTION FOR PHOTON EMISSION IN $dK/(E_0 - mc^2)$

$$-\frac{dE}{dx} = N\int_0^1 K\phi_K\, d\left(\frac{K}{E - mc^2}\right)$$

$$-\frac{dE}{dx} = \frac{E}{\text{R.L.}}\left(\frac{E_0 E}{mc^2 K} \gg 137\, Z^{-1/3}\right)$$

Figure 18

(a)

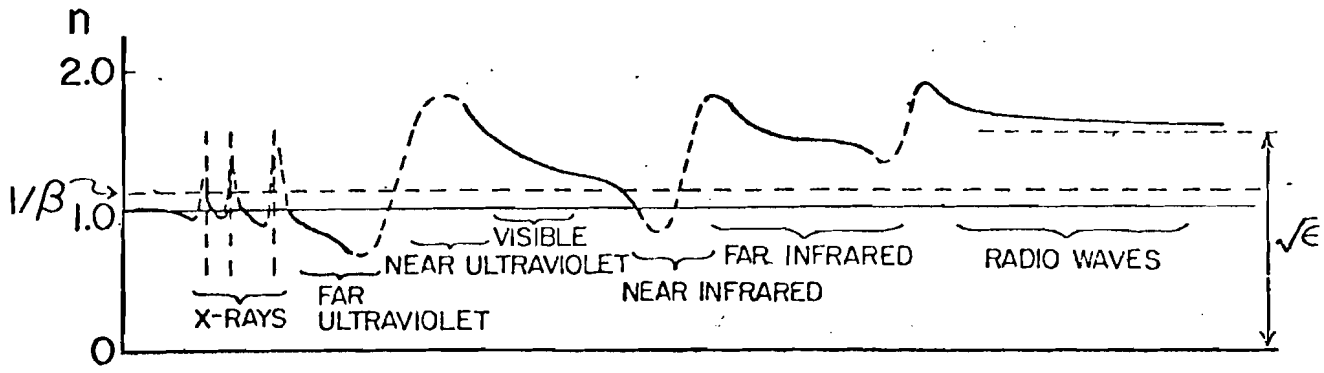

SCHEMATIC DISPERSION CURVE FOR OPTICAL MEDIA

(after Jenkins and White, Fundamentals of Optics, p487 (3rd. Ed)).

(b)

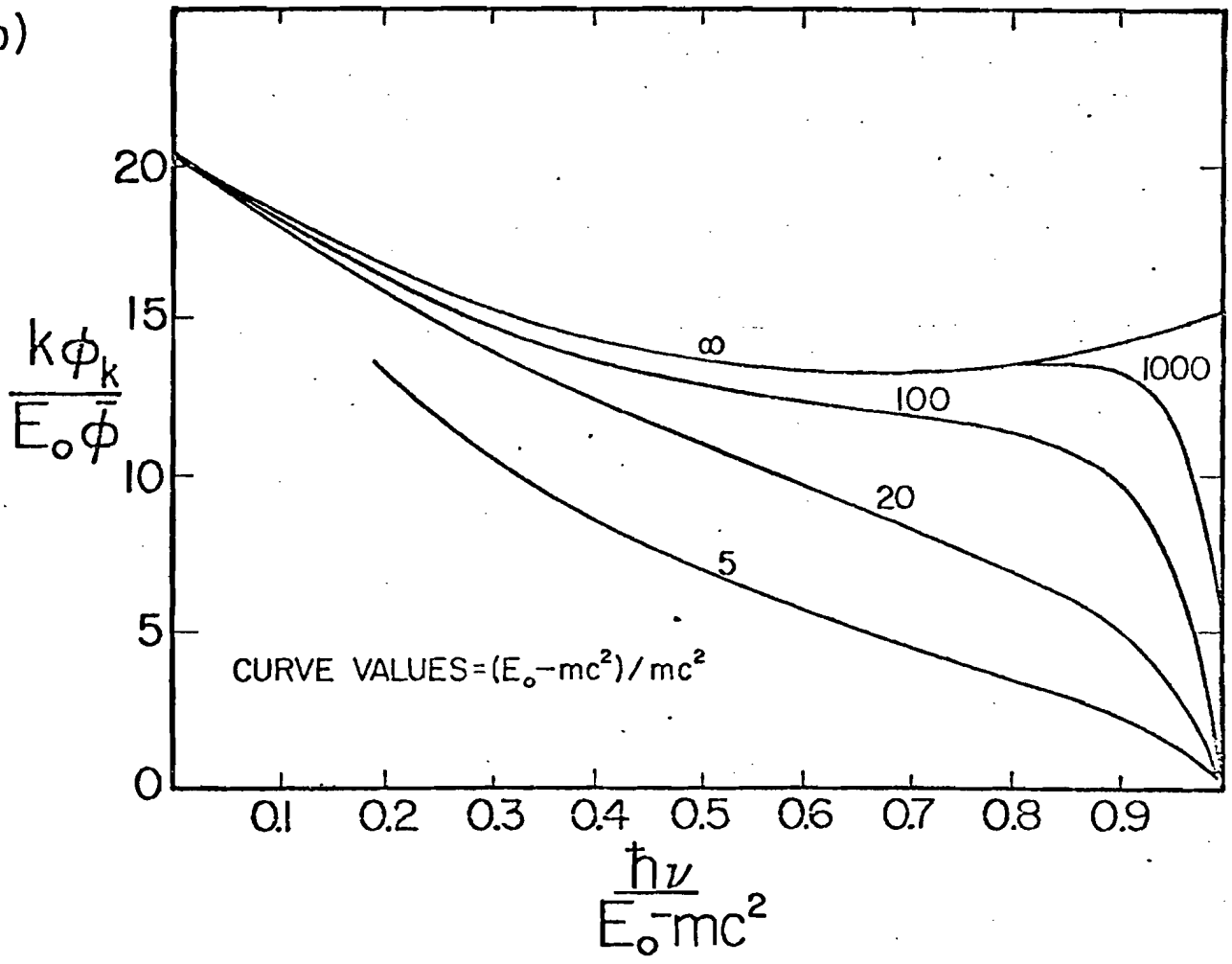

CALCULATED BREMSSTRAHLUNG INTENSITY AS A FUNCTION OF $\hbar\nu/(E_0-mc^2)$ FOR LEAD

(after W. Heitler, Quantum Theory of Radiation, Oxford, (3rd Ed.), V,25)

$\bar{\phi} = Z^2 e^4/(137 m^2 c^4)$

Figure 19

LEAD GLASS ARRAY

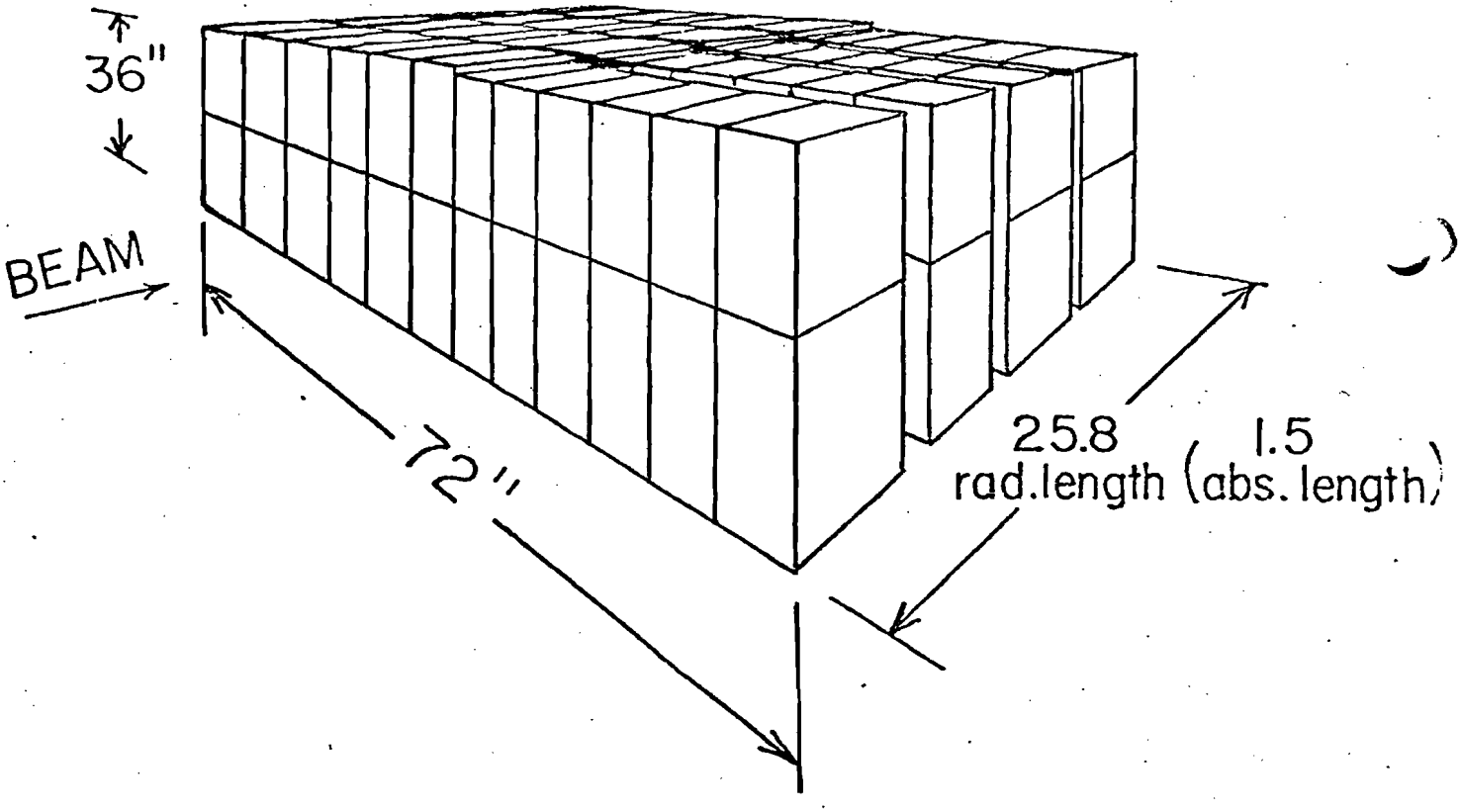

72 LARGE, 24 SMALL BLOCKS PER ARM

LEAD GLASS BLOCK SIZES:

$15\frac{1}{4} \times 15\frac{1}{4} \times 45\,cm^3$ (Large)

$15 \times 15 \times 35\,cm^3$ (Small)

Figure 20

LEAD GLASS PROPERTIES

Manufacturer	Ohara, Inc. Tokyo
Type	SF 5
Radiation Length (R.L.)	2.36 cm.
Interaction Length	25.6 cm.
Specific Gravity	4.08 gm/cm.^{3}
Critical Energy	15.8 MeV
Composition	.55 PbO
	.38 SiO_2
	.05 K_2O
	.01 Na_2O

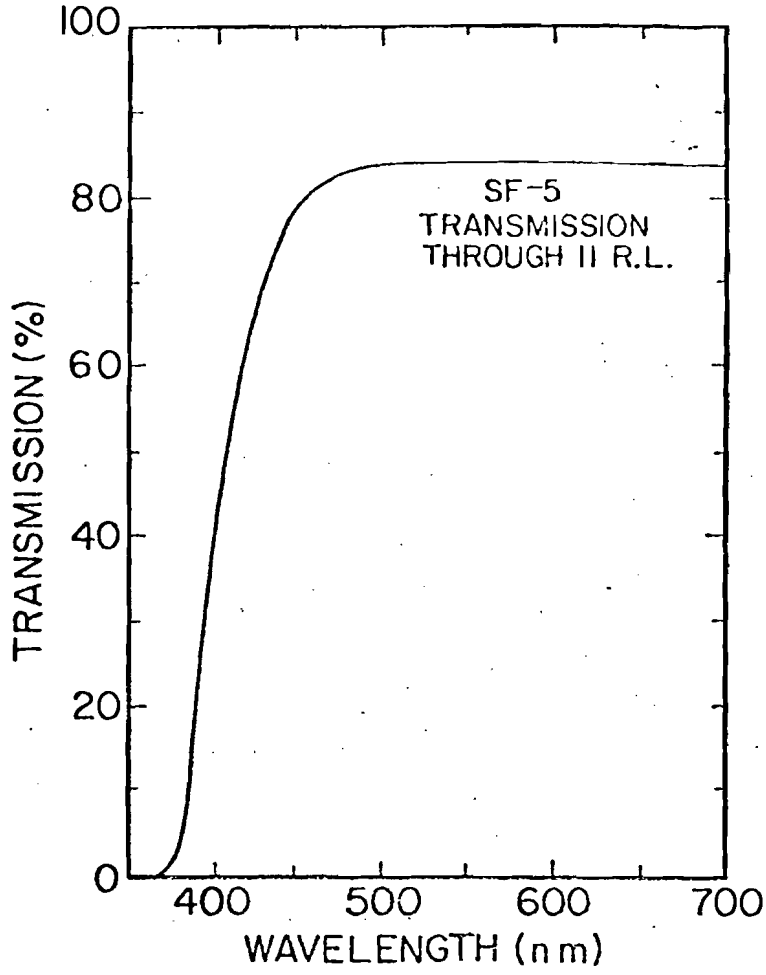

(REF. W.B. ATWOOD, SLAC REPORT 185 (JUNE 1975), APPENDIX B

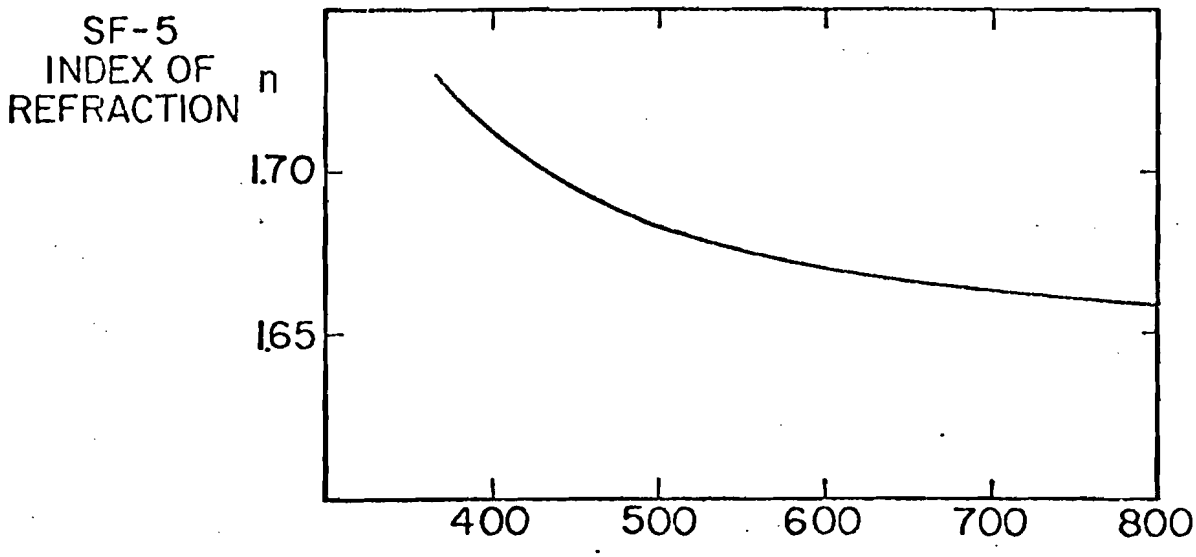

(REF. 1971 OHARA OPTICAL GLASS CATALOG)

Figure 21

FAST TRIGGER LOGIC DIAGRAM

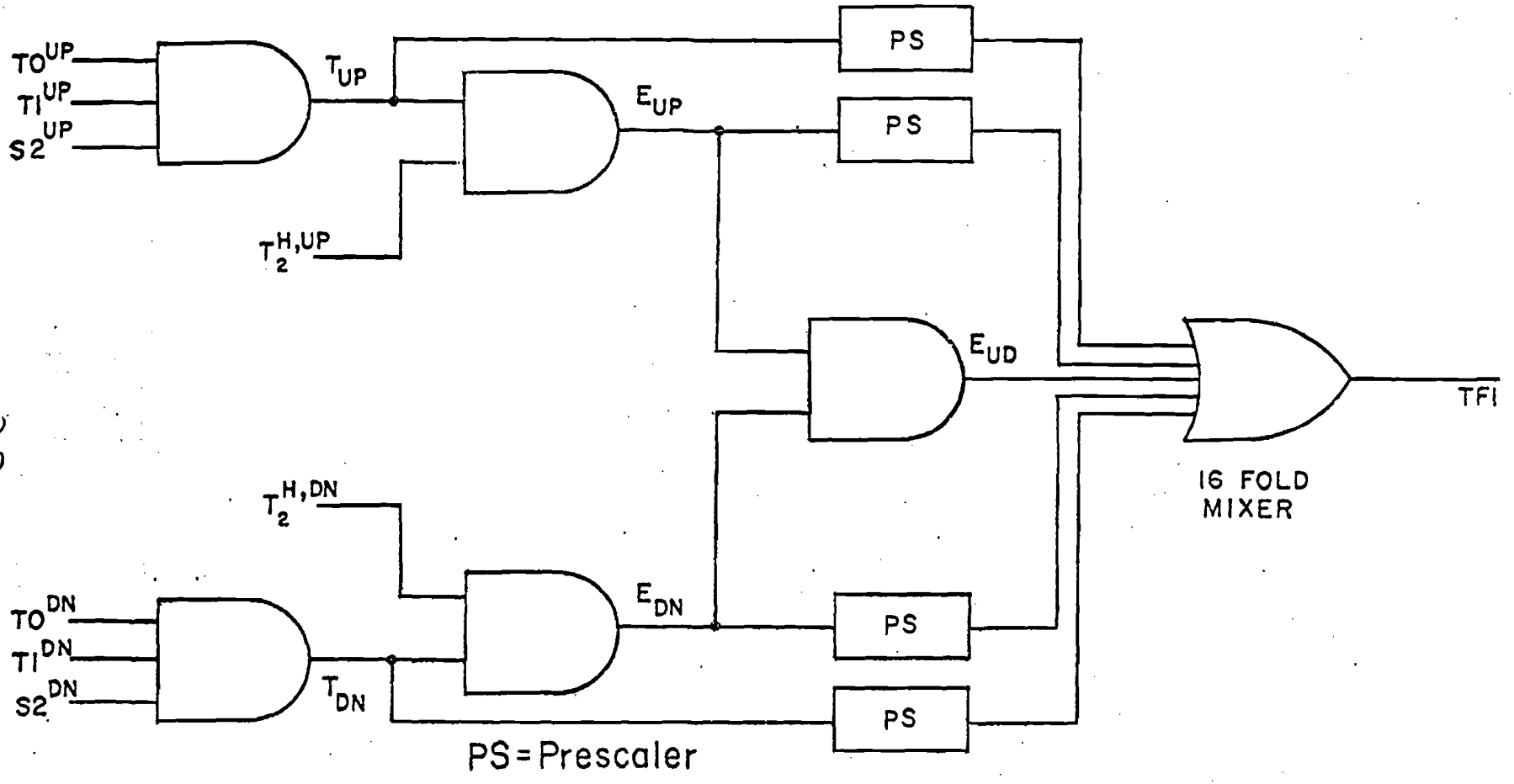

FIGURE 22

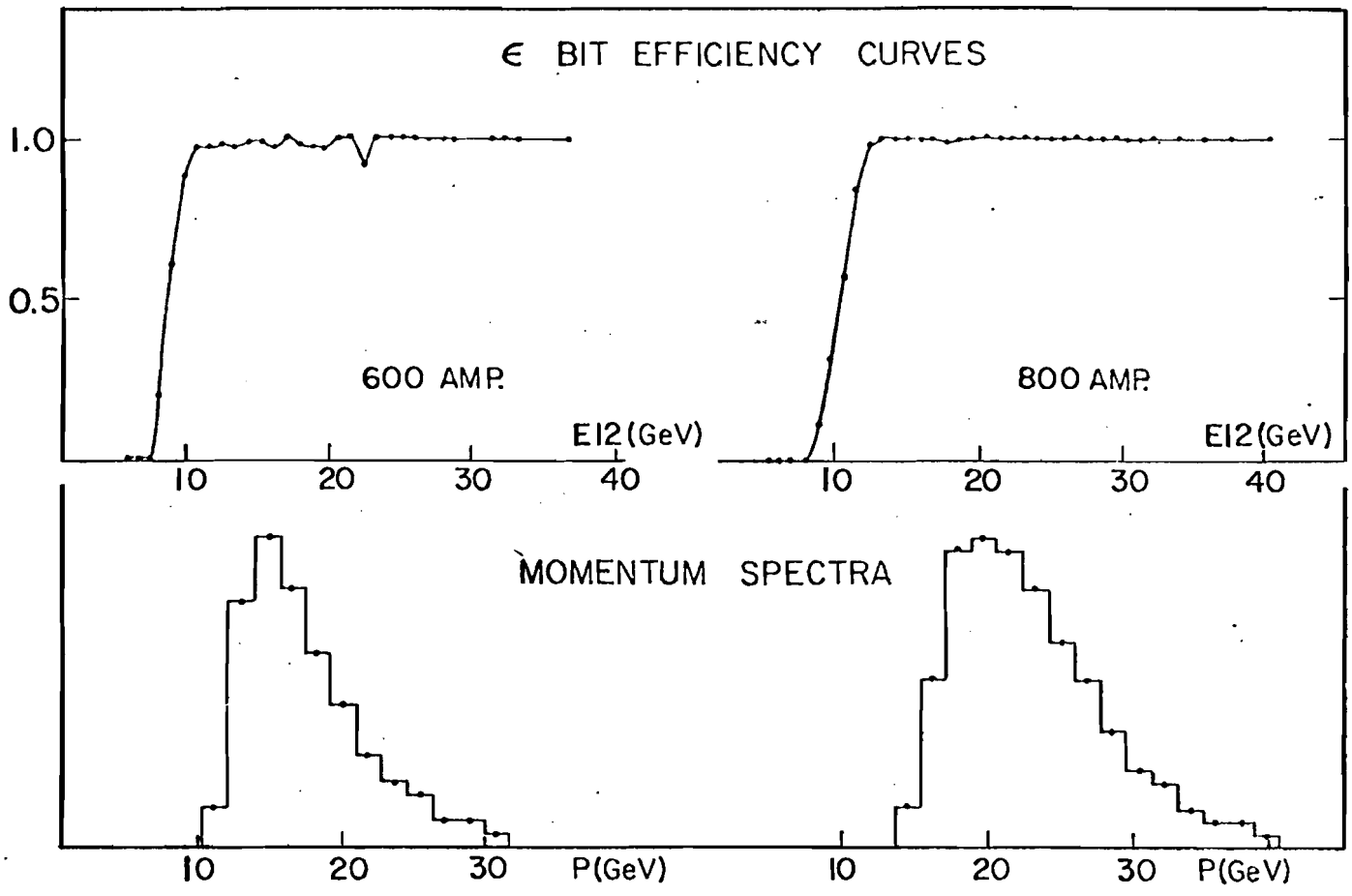
ϵ BIT EFFICIENCY CURVES
1.0
0.5
600 AMP.
E12(GeV)
10
20
30
40
800 AMP.
E12(GeV)
10
20
30
40
MOMENTUM SPECTRA
10
20
30
P(GeV)
10
20
30
P(GeV)

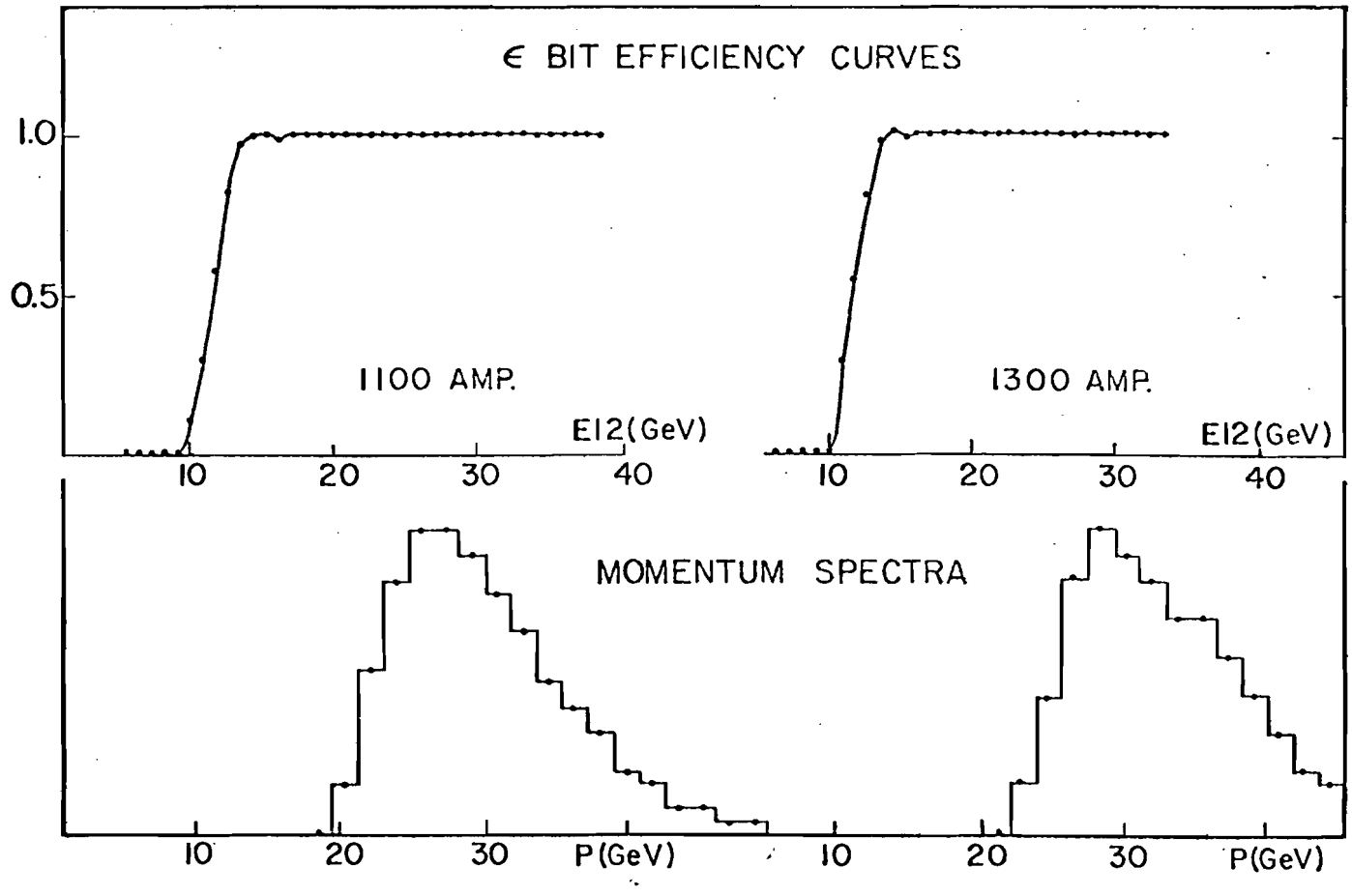
ϵ BIT EFFICIENCY CURVES
1.0
0.5
1100 AMP.
E12(GeV)
10
20
30
40
1300 AMP.
E12(GeV)
10
20
30
40
MOMENTUM SPECTRA
10
20
30
P(GeV)
10
20
30
P(GeV)

Figure 23

D.C. LOGIC DIAGRAM

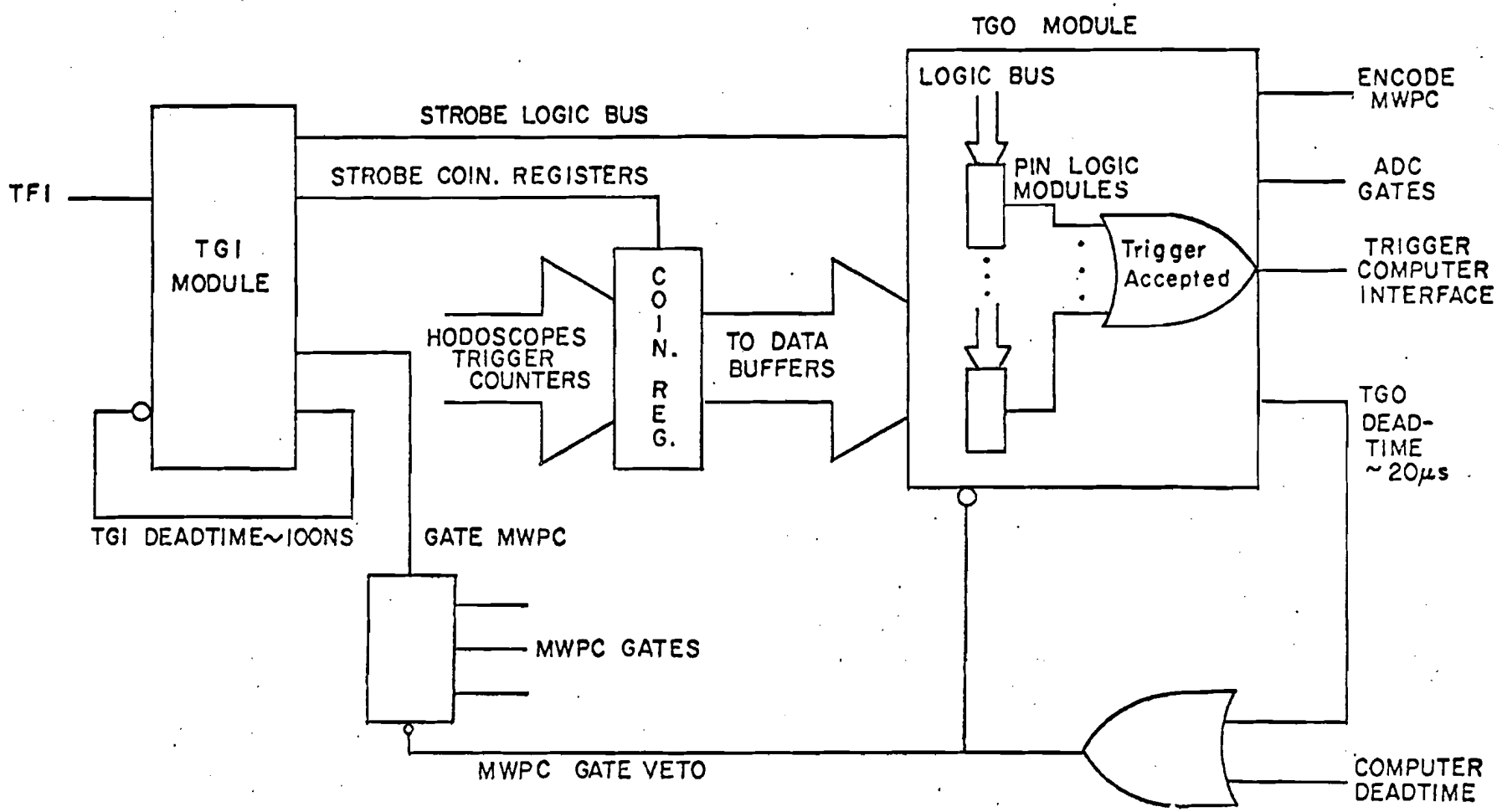

Figure 24

EPSILON (ϵ) TIME OF FLIGHT FOR 400 GeV DIELECTRON EVENTS

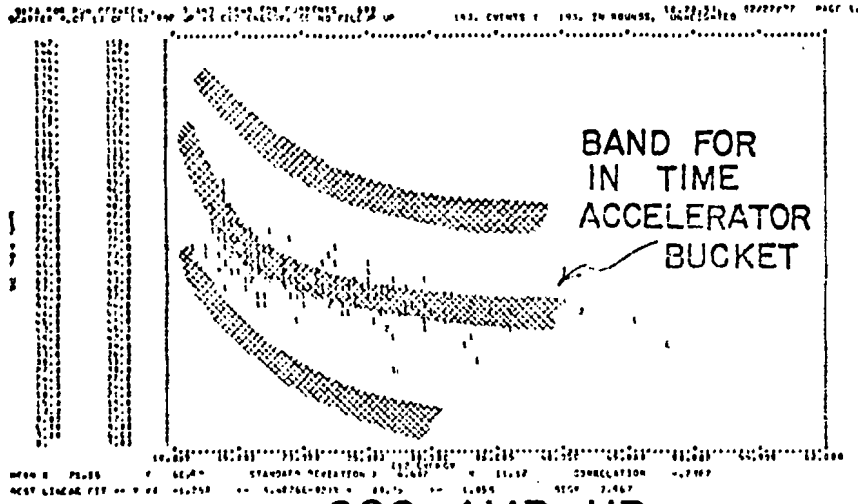

600 AMP. UP

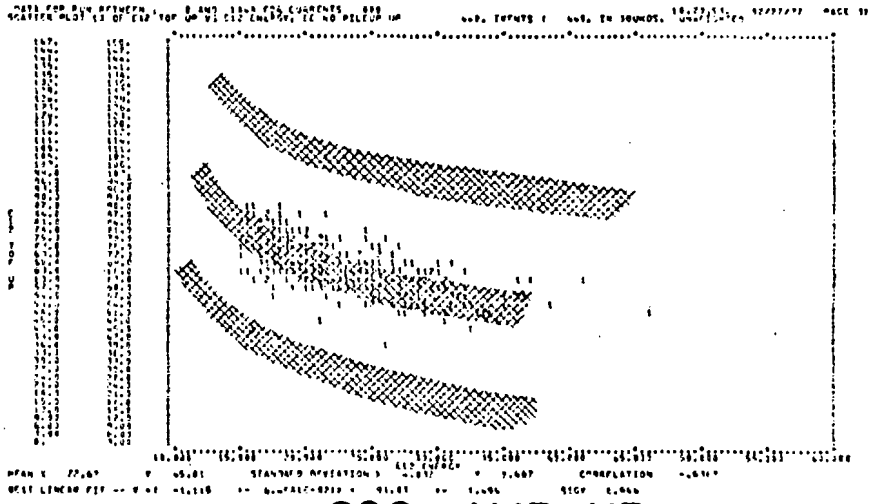

800 AMP. UP

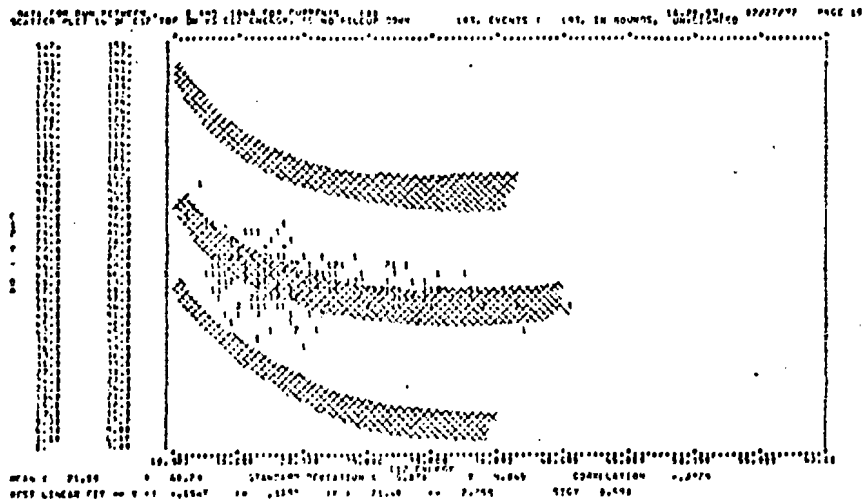

600 AMP. DOWN

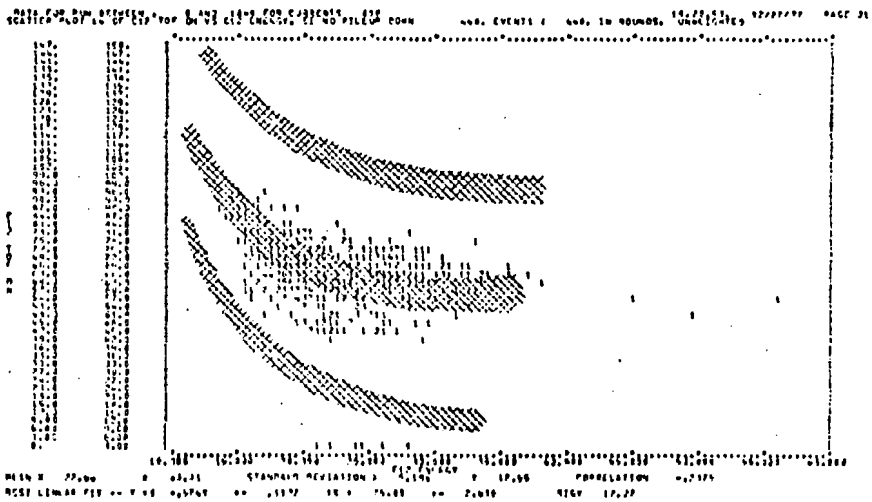

800 AMP. DOWN

Figure 25

EPSILON (ϵ) TIME OF FLIGHT FOR 400 GeV DIELECTRON EVENTS

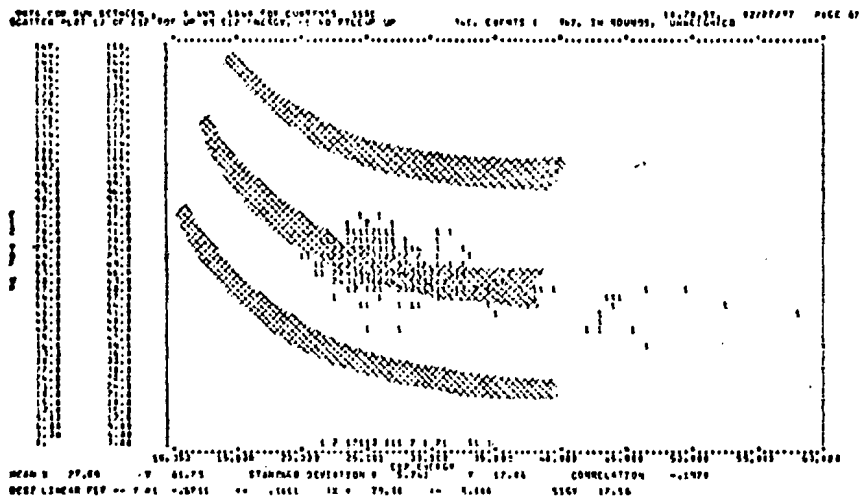

1100 AMP. UP

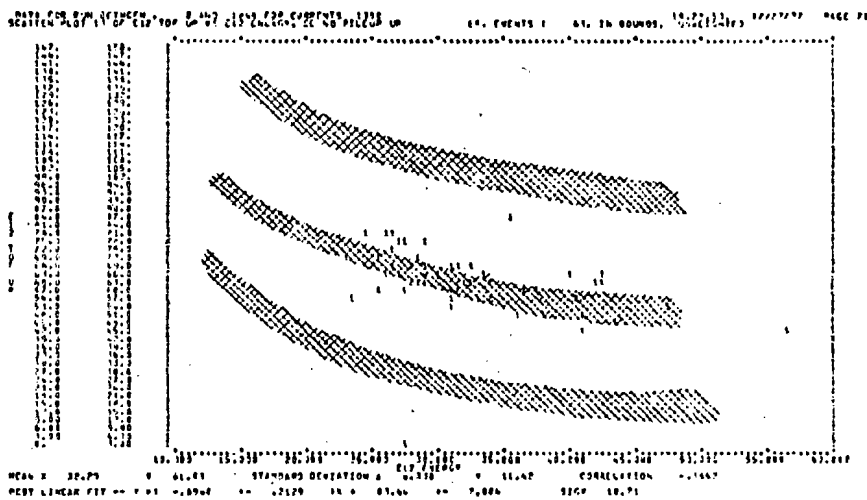

1300 AMP. UP

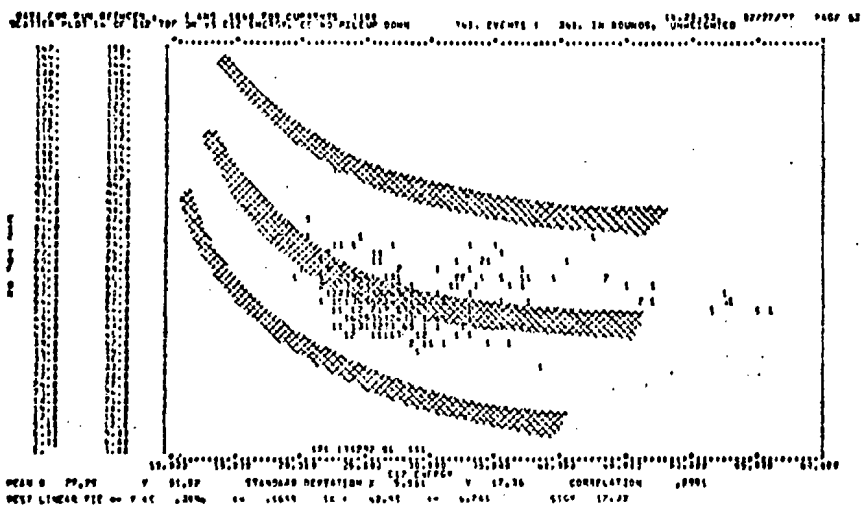

1100 AMP. DOWN

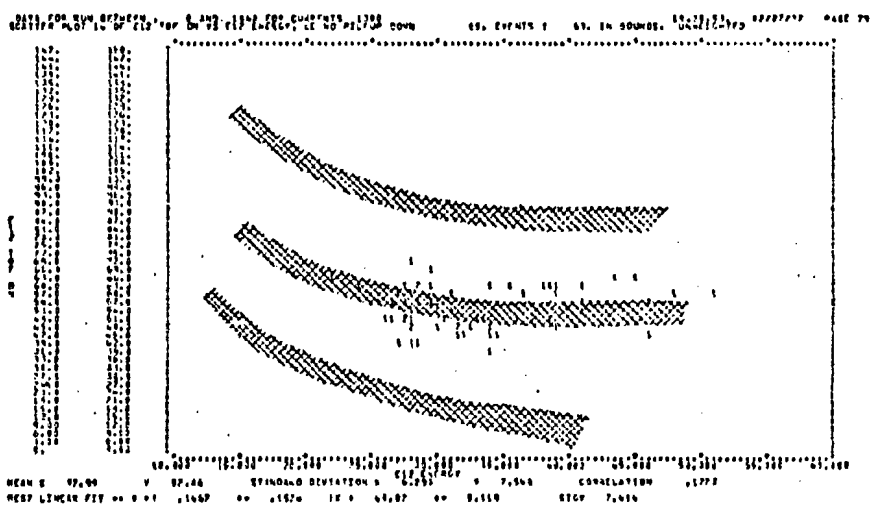

1300 AMP. DOWN

Figure 26

MASS SPECTRA-MEE, MPØPØ, MPP (800A)

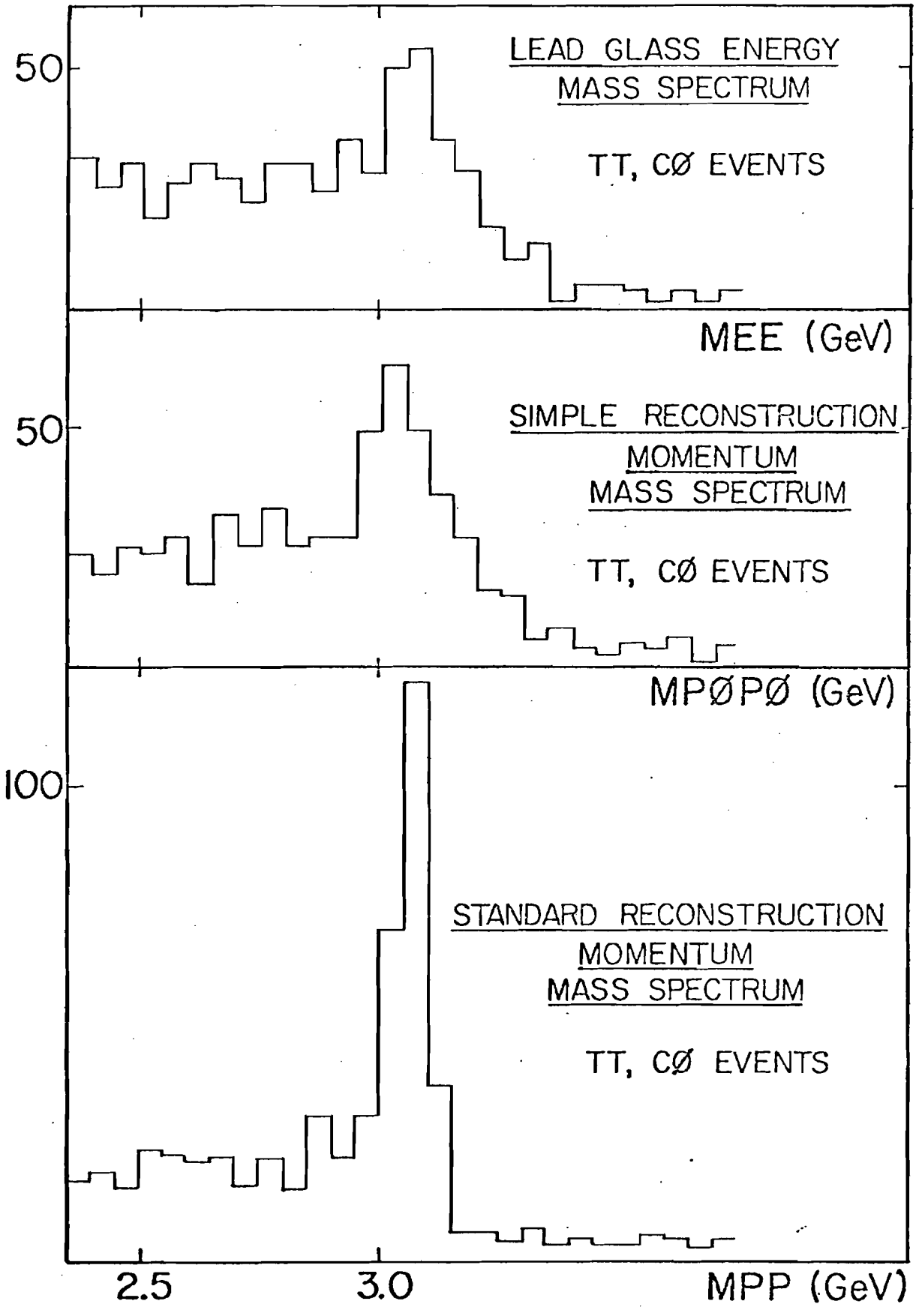

Figure 27

TRACK RECONSTRUCTION EFFICIENCY STUDY

MASS SPECTRA FROM SAMPLE OF 600, 800, 1100 AMP. DATA

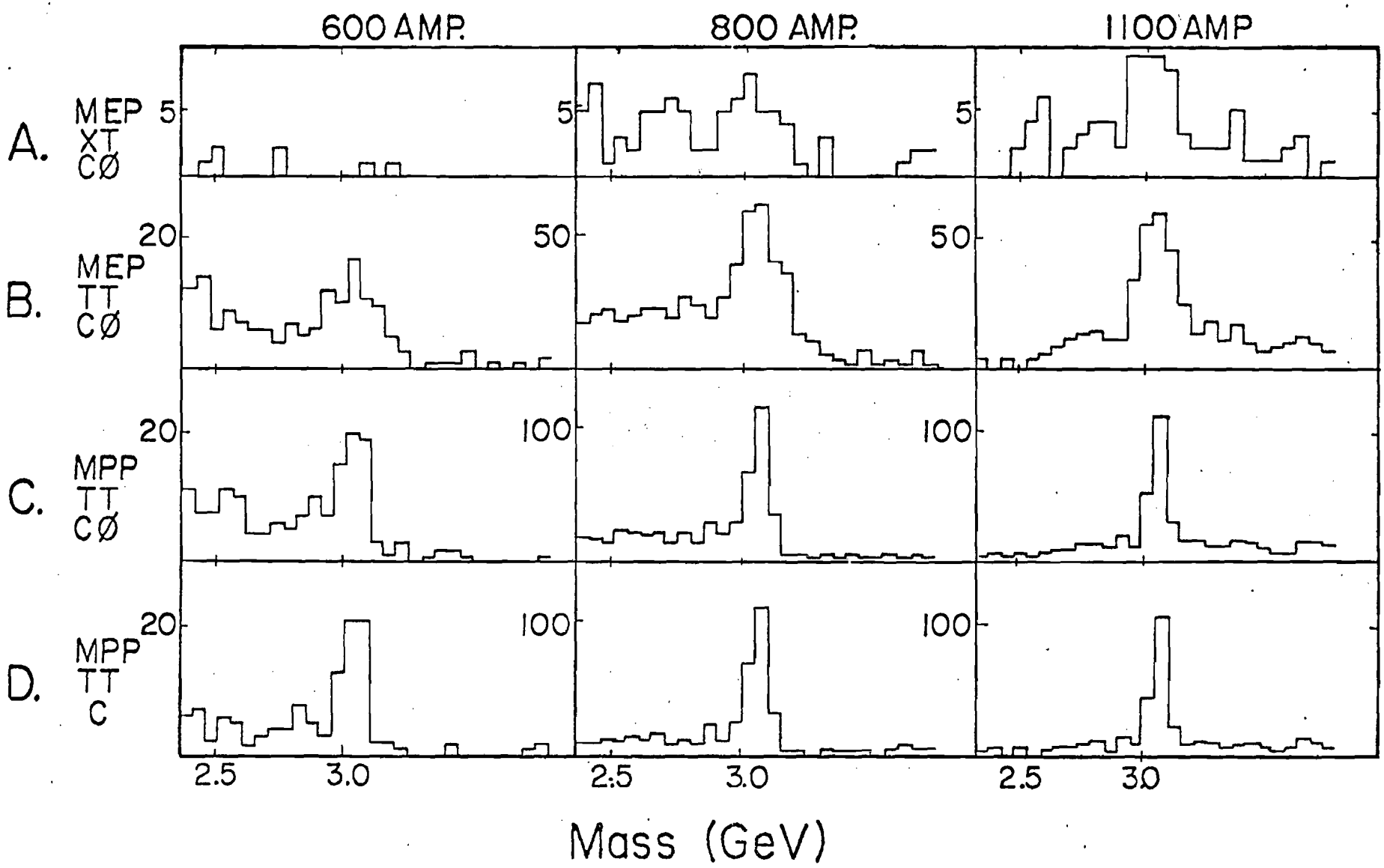

Figure 28

SCHEMATIC SIDE VIEW OF SPECTROMETER ARM

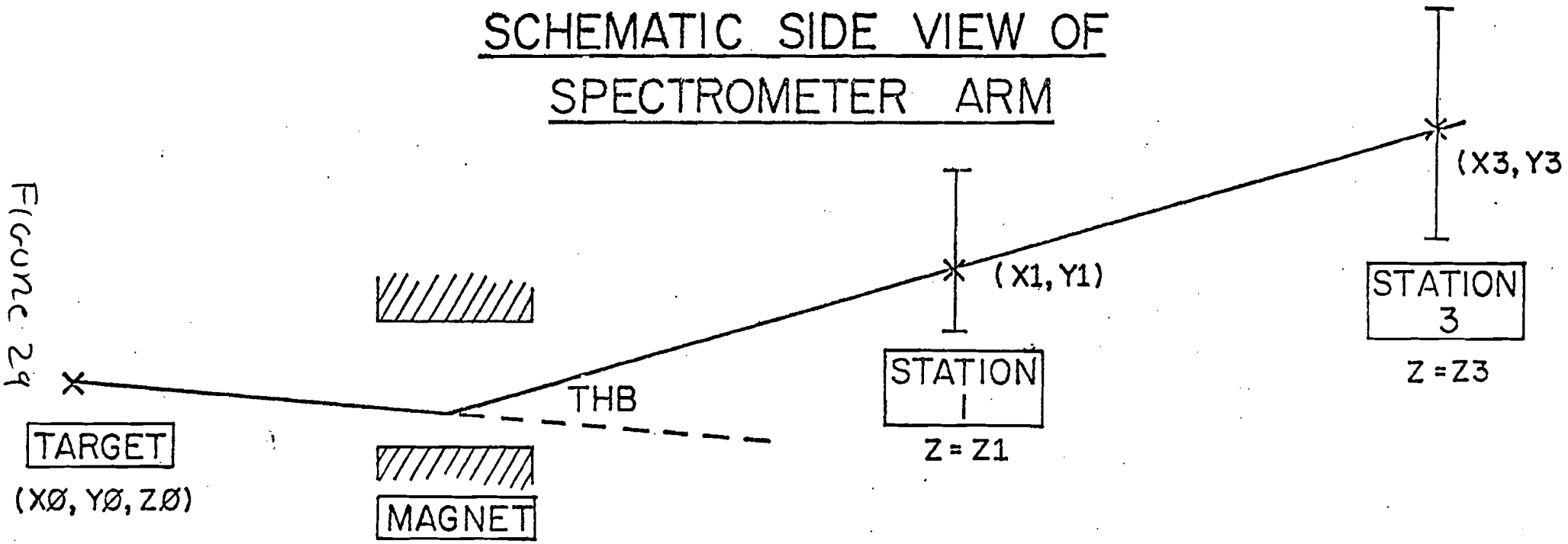

Figure 24

P = MOMENTUM (GeV) $= \frac{IC}{THB}$

C = MAGNET CONSTANT $= 8.1 \times 10^{-4}$

I = MAGNET CURRENT (AMP.)

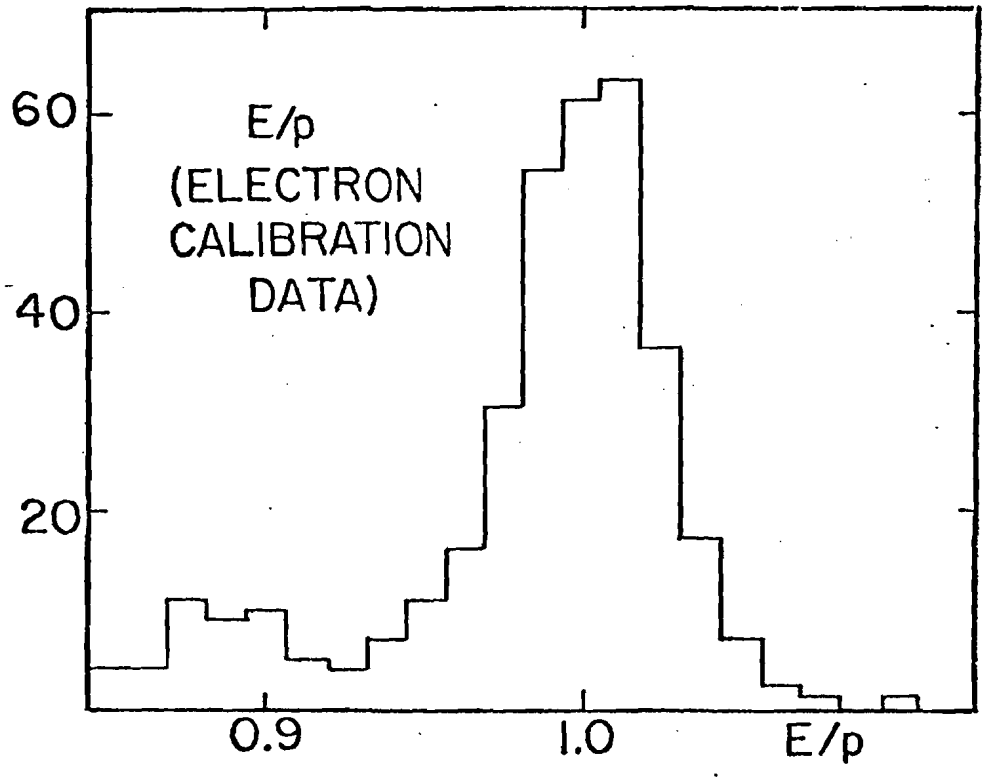

Figure 30

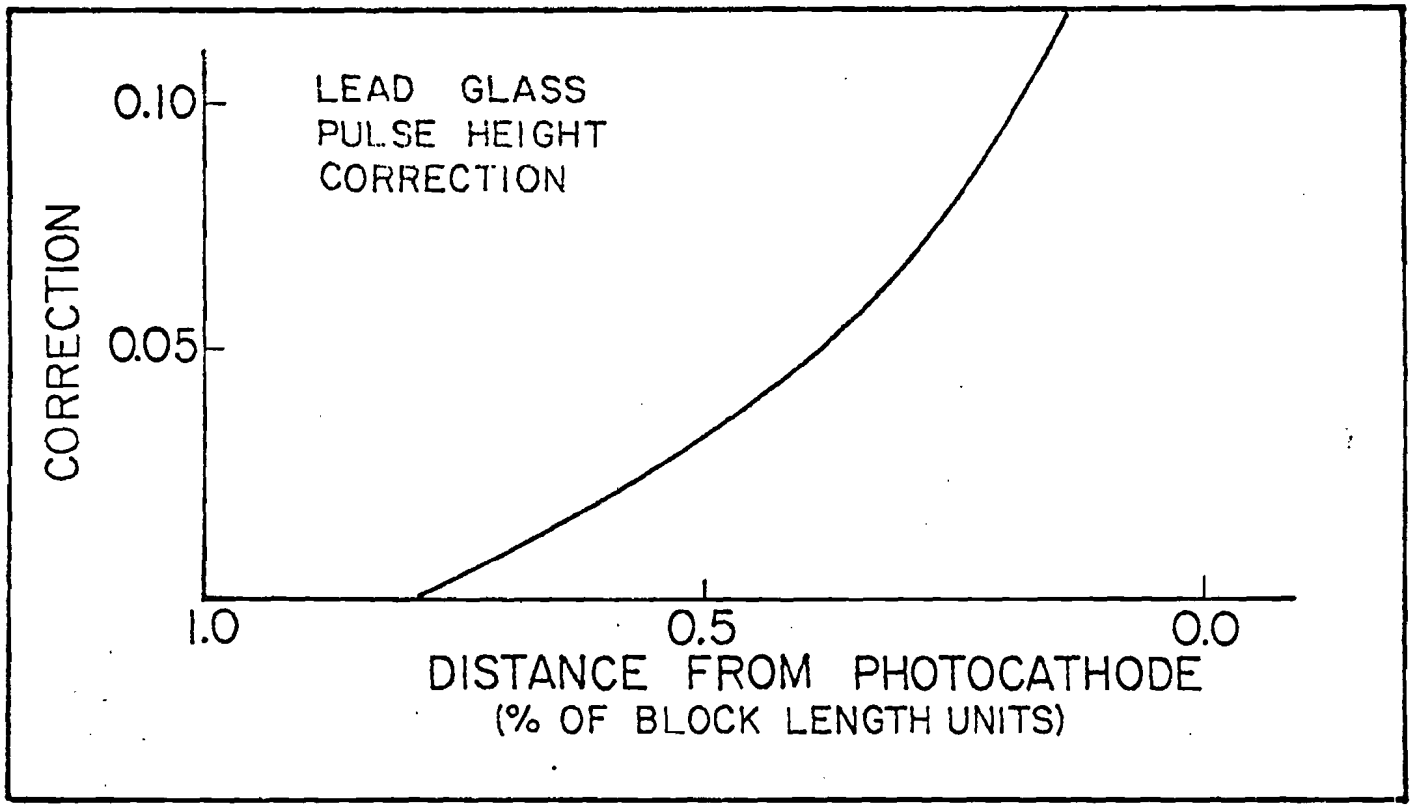
LEAD GLASS
PULSE HEIGHT
CORRECTION
0.10
0.05
CORRECTION
1.0
0.5
0.0
DISTANCE FROM PHOTOCATHODE
(% OF BLOCK LENGTH UNITS)

Figure 31

% OF TOTAL LEAD GLASS LAYER ENERGY IN SHOWER 'CONE' VS. 'CONE' RADII

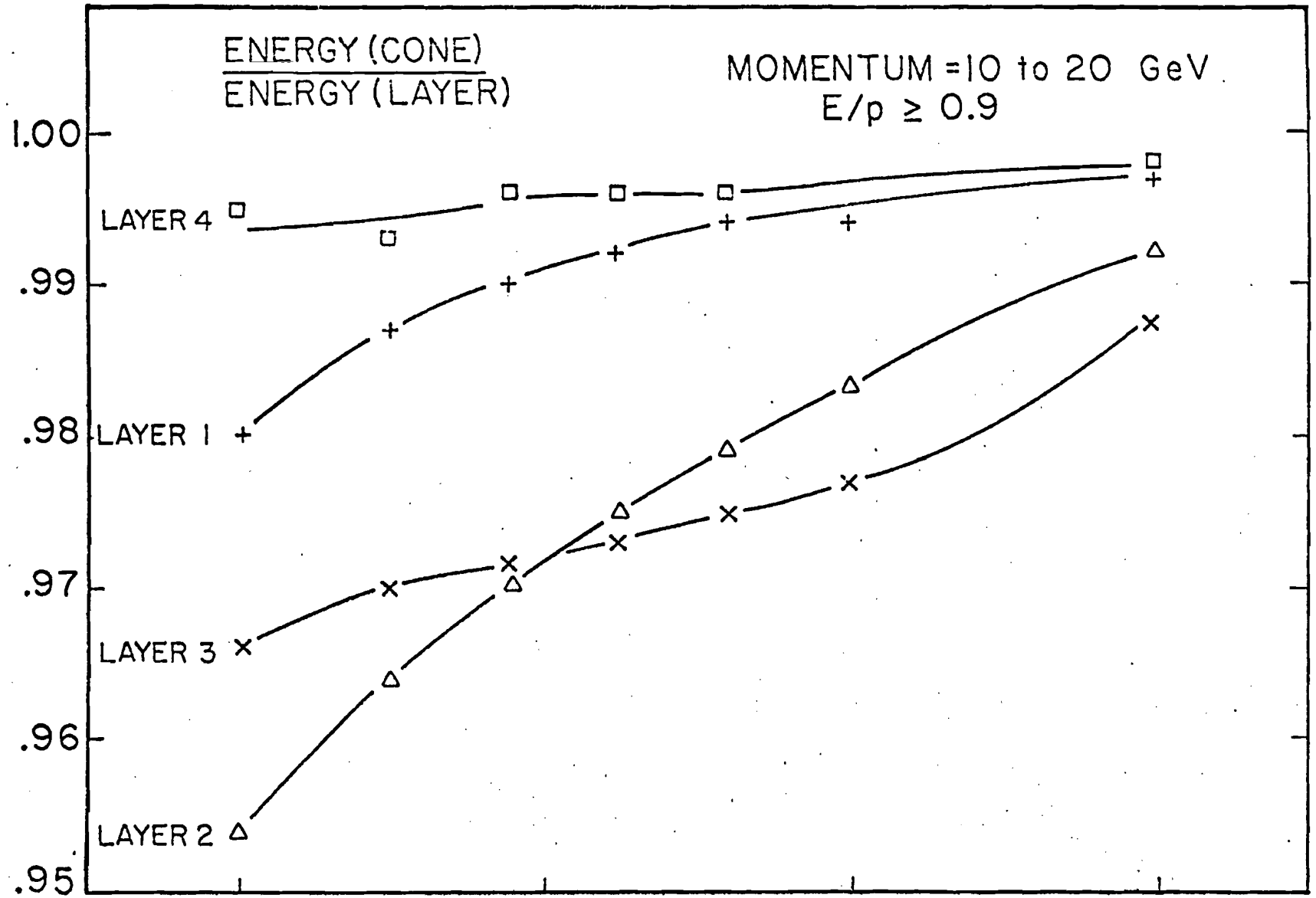

Figure 32

% OF TOTAL LEAD GLASS LAYER ENERGY IN SHOWER 'CONE' VS. 'CONE' RADII

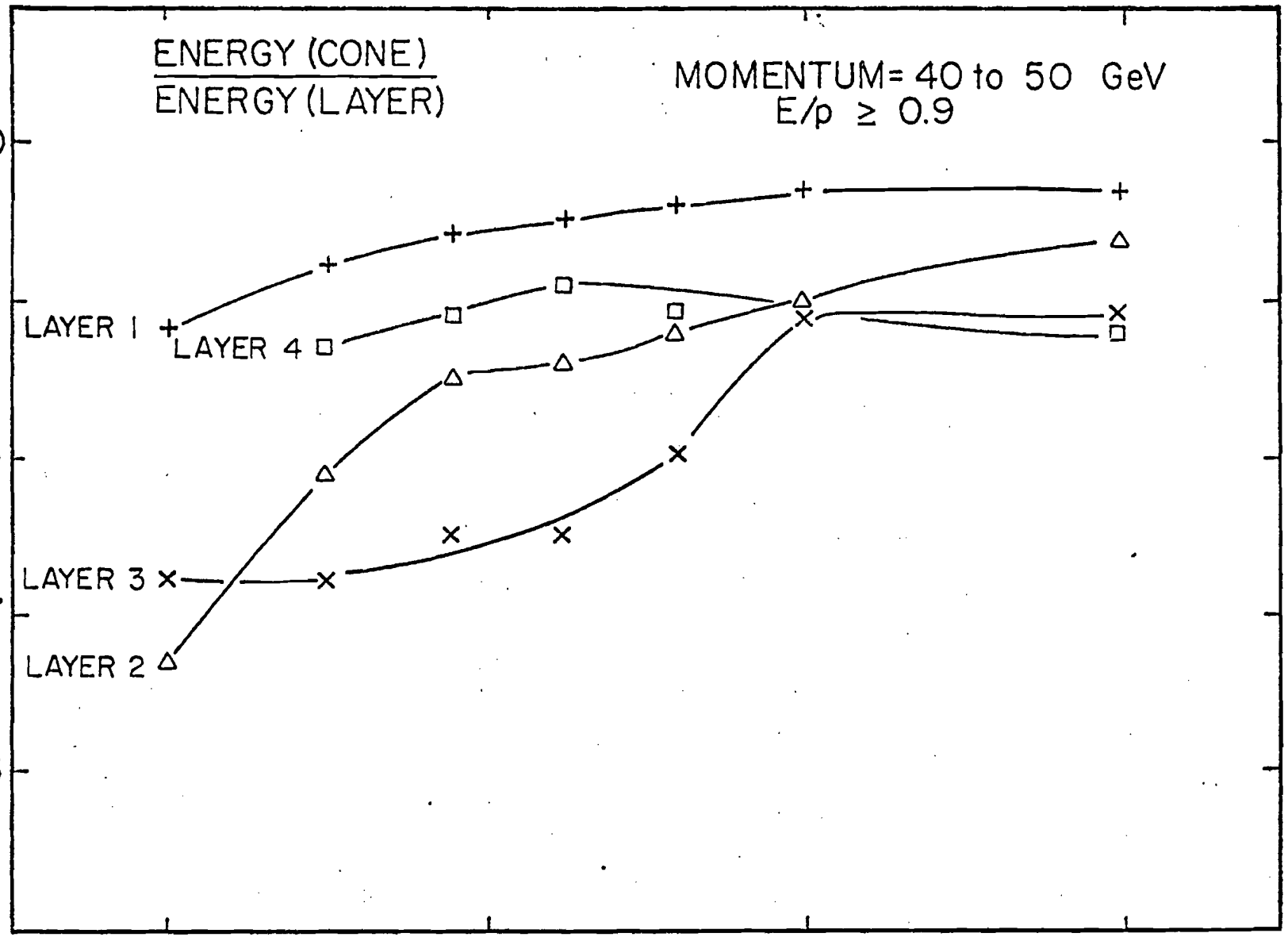

Figure 33

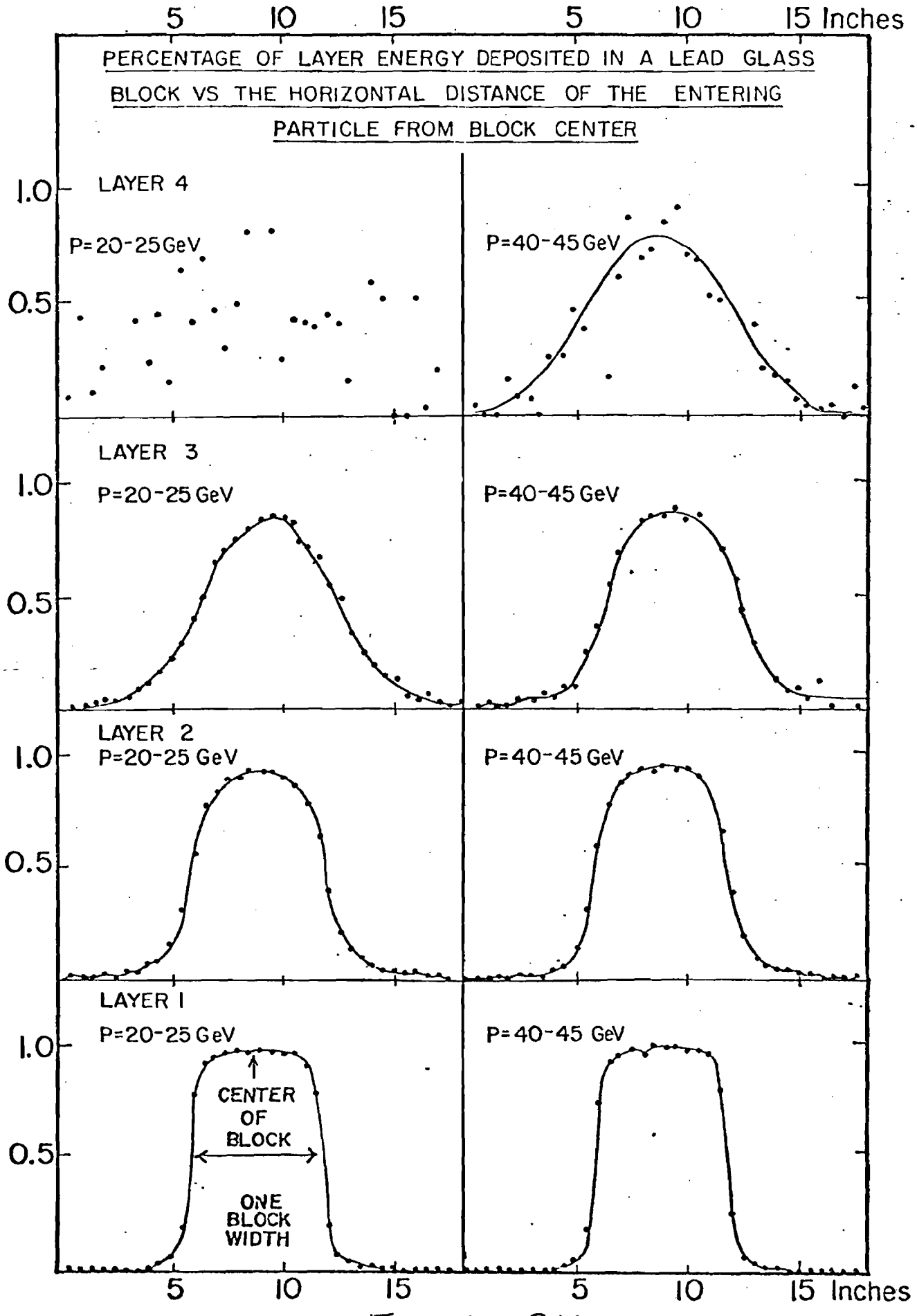
5 10 15 5 10 15 Inches
PERCENTAGE OF LAYER ENERGY DEPOSITED IN A LEAD GLASS BLOCK VS THE HORIZONTAL DISTANCE OF THE ENTERING PARTICLE FROM BLOCK CENTER
LAYER 4
P=20-25GeV
P=40-45GeV
LAYER 3
P=20-25 GeV
P=40-45 GeV
LAYER 2
P=20-25 GeV
P=40-45 GeV
LAYER 1
P=20-25 GeV
P=40-45 GeV
1.0
0.5
CENTER OF BLOCK
ONE BLOCK WIDTH
5 10 15 5 10 15 Inches

FIGURE 34

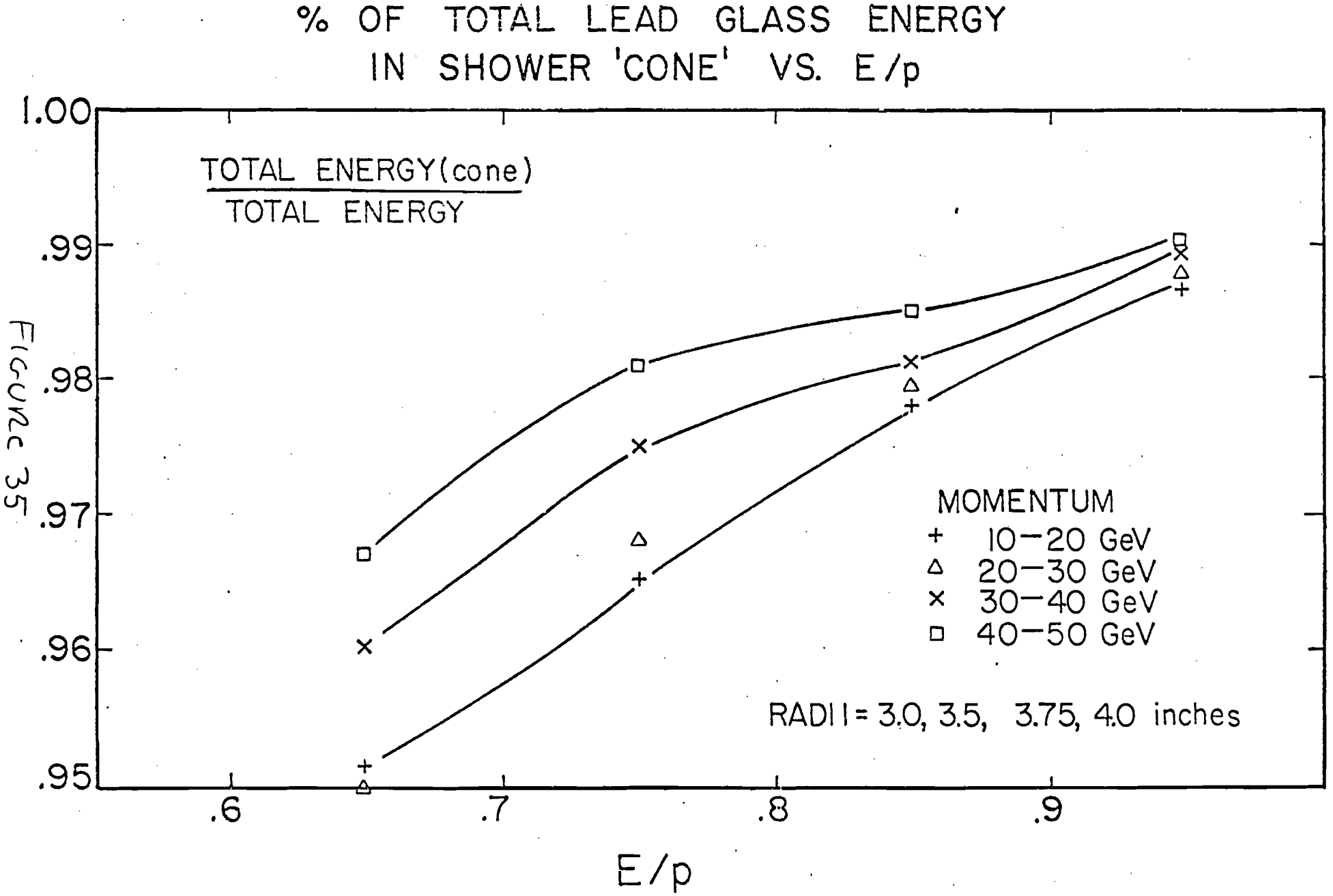
% OF TOTAL LEAD GLASS ENERGY
IN SHOWER 'CONE' VS. E/p
TOTAL ENERGY(cone)
TOTAL ENERGY
1.00
.99
.98
.97
.96
.95
.6
.7
.8
.9
E/p
MOMENTUM
+ 10–20 GeV
△ 20–30 GeV
× 30–40 GeV
□ 40–50 GeV
RADII = 3.0, 3.5, 3.75, 4.0 inches

Figure 35

DIELECTRON E/p PLOTS

a.) EVENTS OF $E/p \geq 0.9$ (PAIRS ONLY)
b.) PASSING MEDIUM LEAD GLASS LONGITUDINAL SHOWER CUTS.
c.) 400 GeV DATA
d.) DIVIDED INTO 4 BINS OF NDN

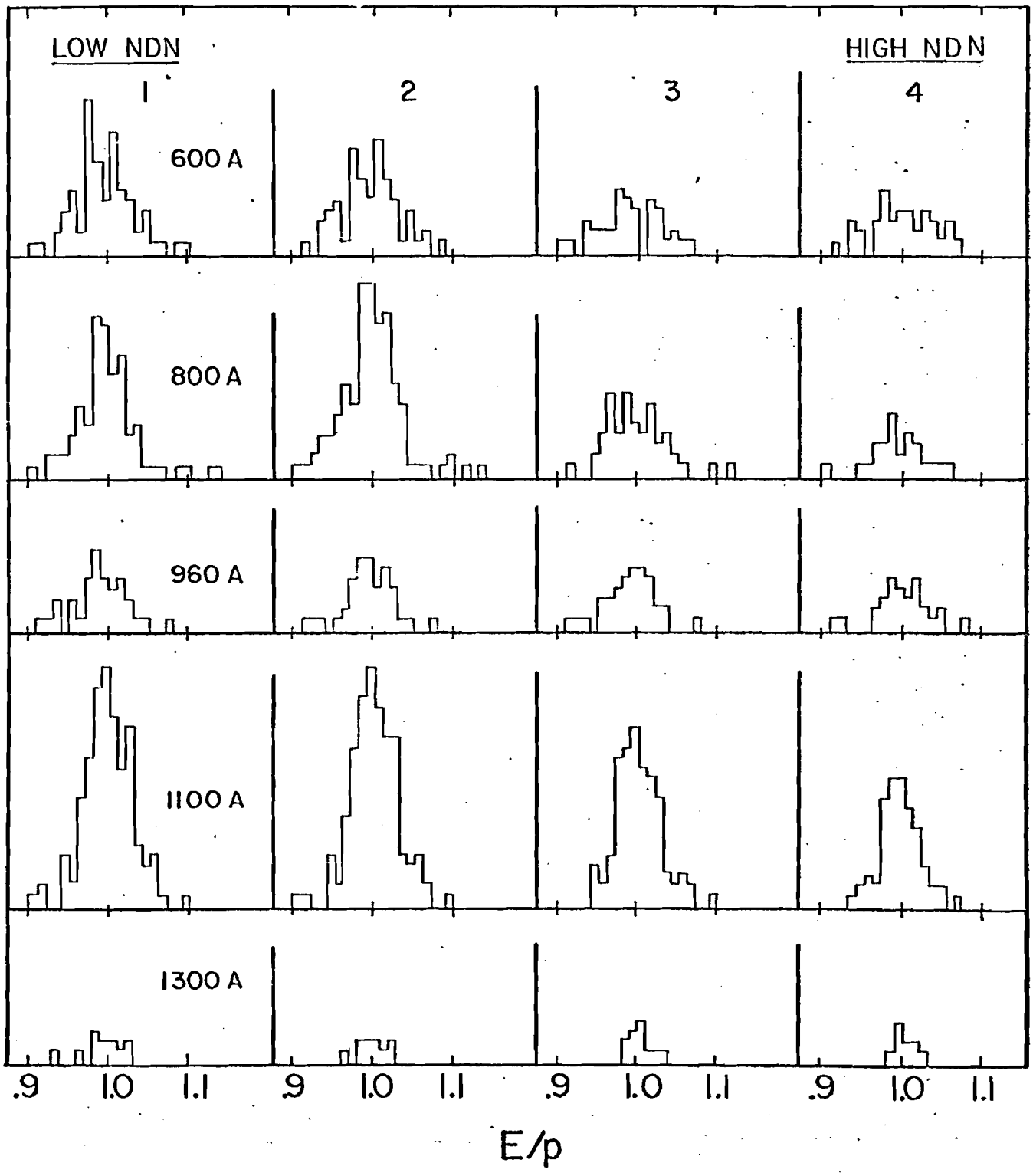

NOTE: EVENTS BELOW E/p=0.9 AND ABOVE E/p=1.15 ARE NOT SHOWN

Figure 36

DIELECTRON E/p PLOTS

a.) EVENTS OF E/p ≥ 0.9 (PAIRS ONLY)

b.) PASSING MEDIUM LEAD GLASS LONGITUDINAL SHOWER CUTS

c.) 400 GeV DATA

d.) DIVIDED INTO 4 BINS OF INDUTY × NDN(=I×N)

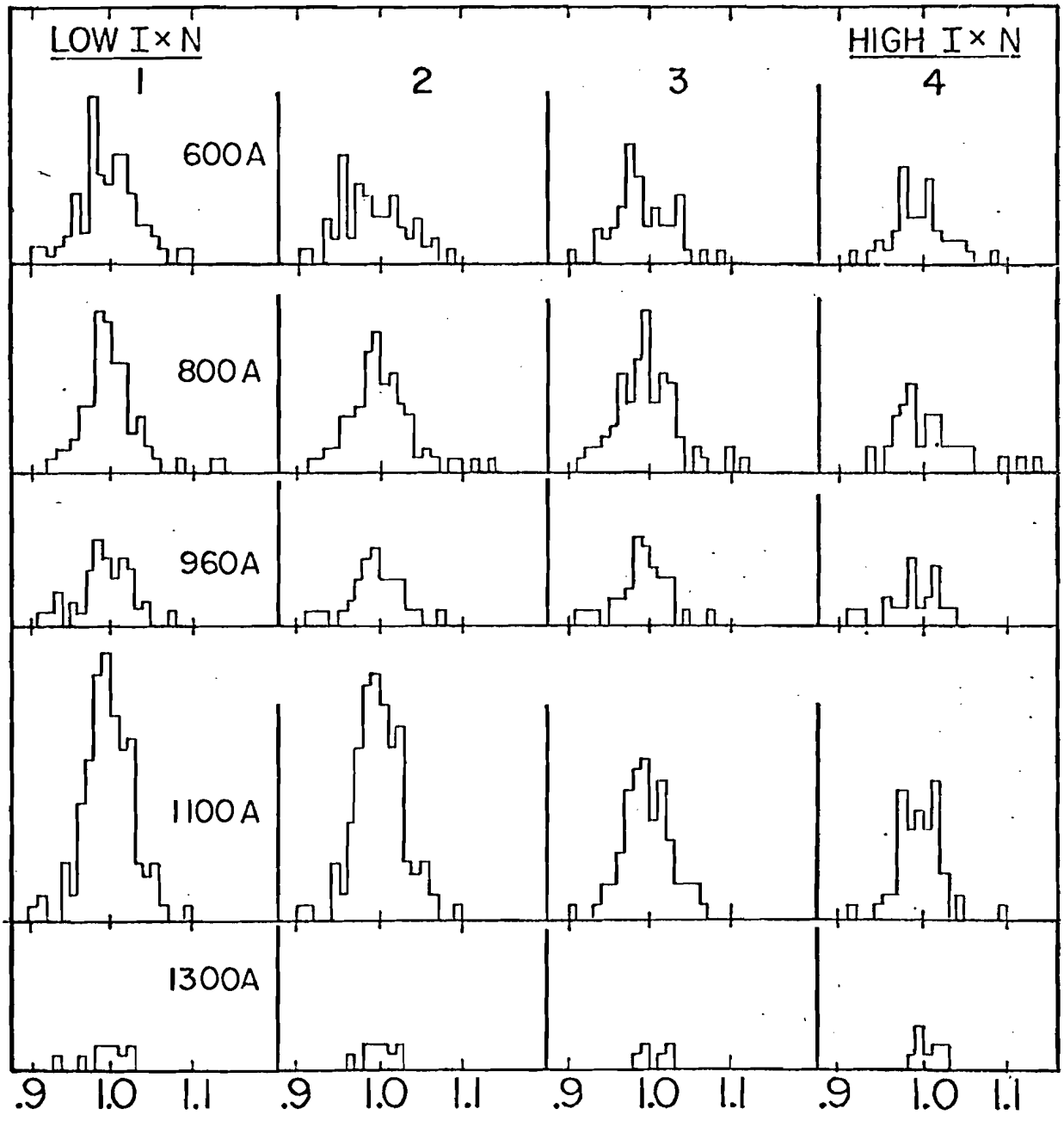

NOTE: EVENTS BELOW E/p=0.9 AND ABOVE E/p=1.15 ARE NOT SHOWN

Figure 37

EXCESS LEAD GLASS ENERGY PLOTS

400 GeV DIELECTRONS

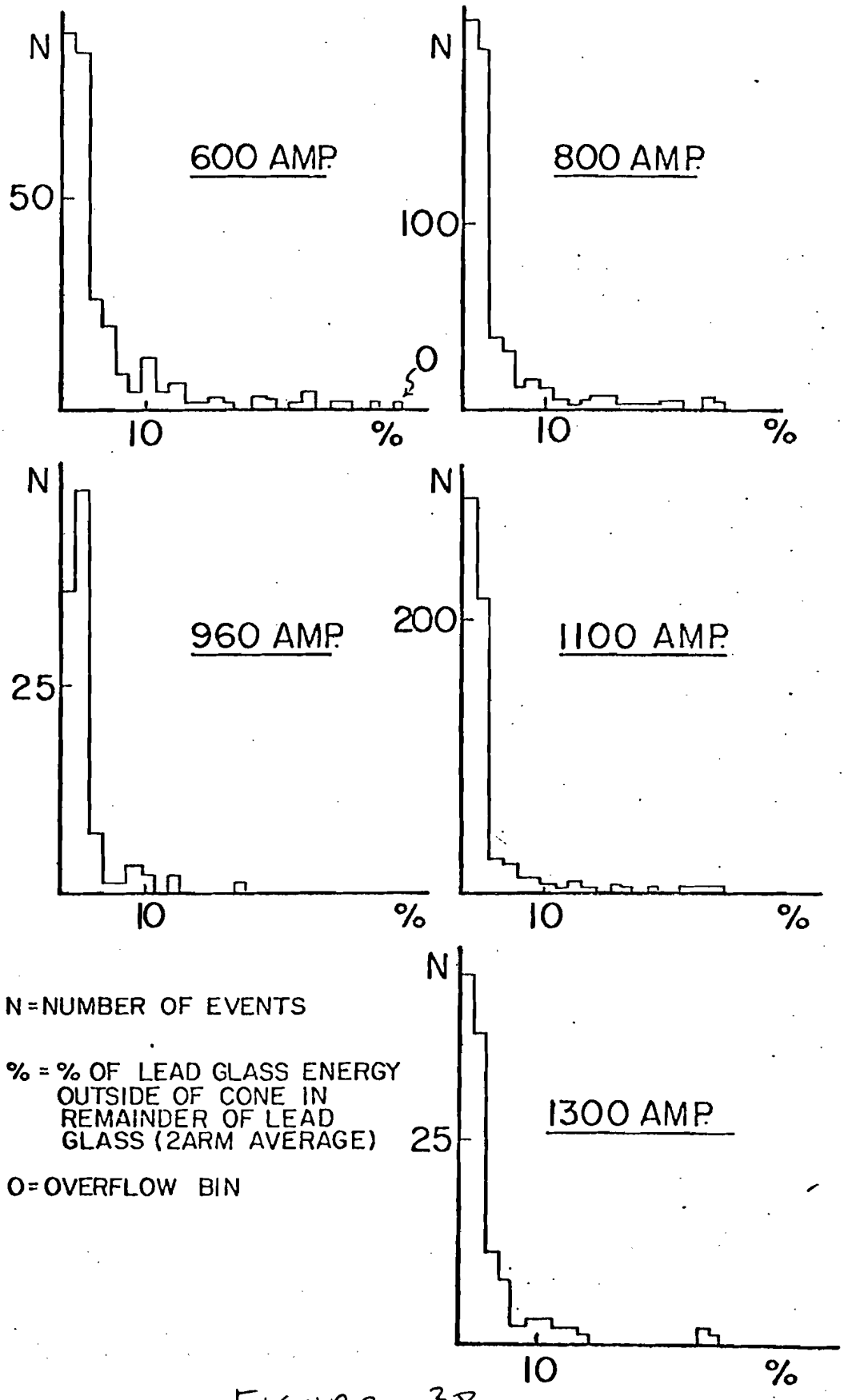

N = NUMBER OF EVENTS

% = % OF LEAD GLASS ENERGY OUTSIDE OF CONE IN REMAINDER OF LEAD GLASS (2ARM AVERAGE)

O = OVERFLOW BIN

Figure 38

FRACTIONAL ENERGY DEPOSIT IN LEAD GLASS LAYERS

(P= 18–25 GeV, 802 AMP.)

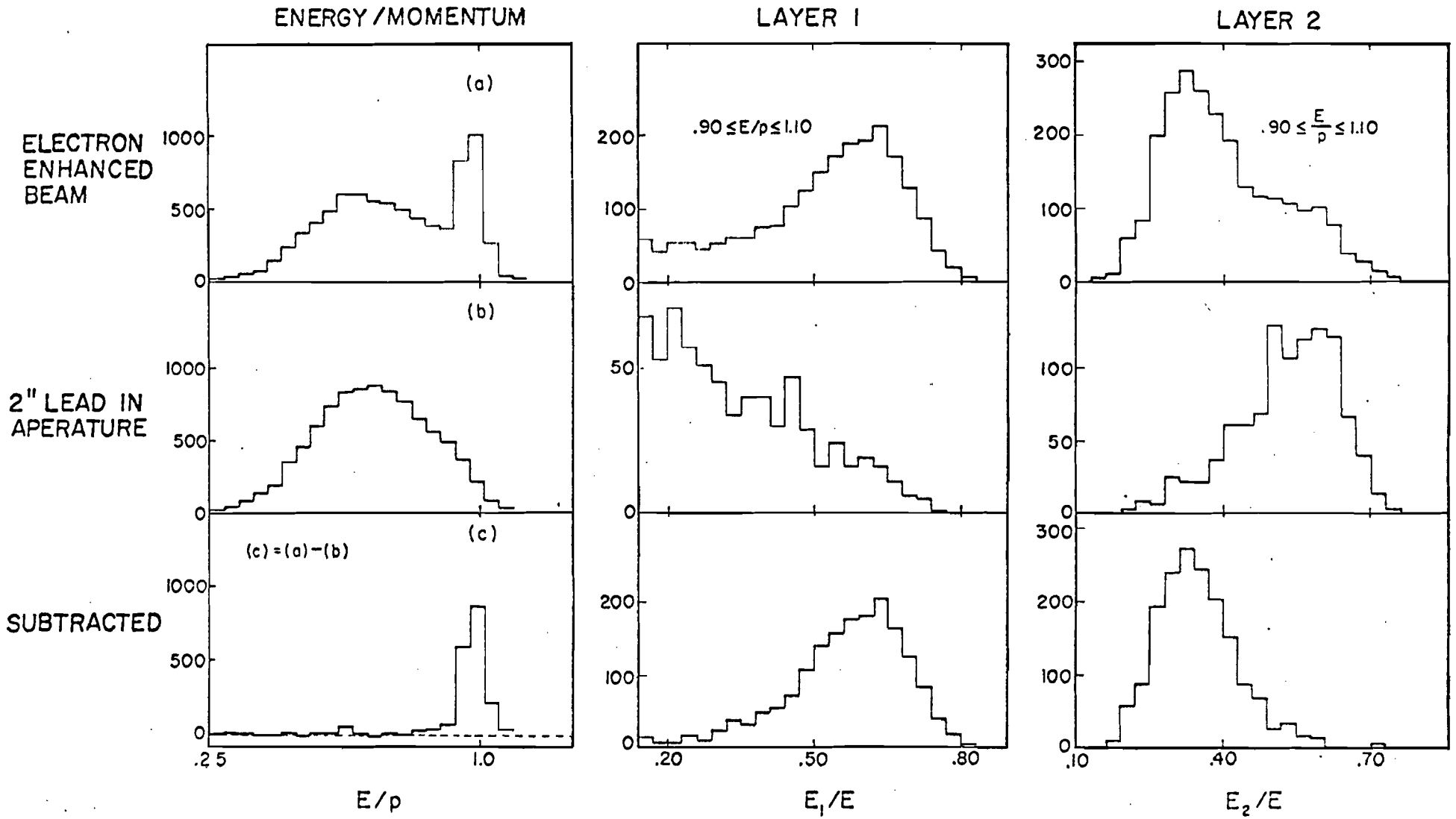

Figure 39

FRACTIONAL ENERGY DEPOSIT IN LEAD GLASS LAYERS
(P=18—25 GeV, 802 AMP.)

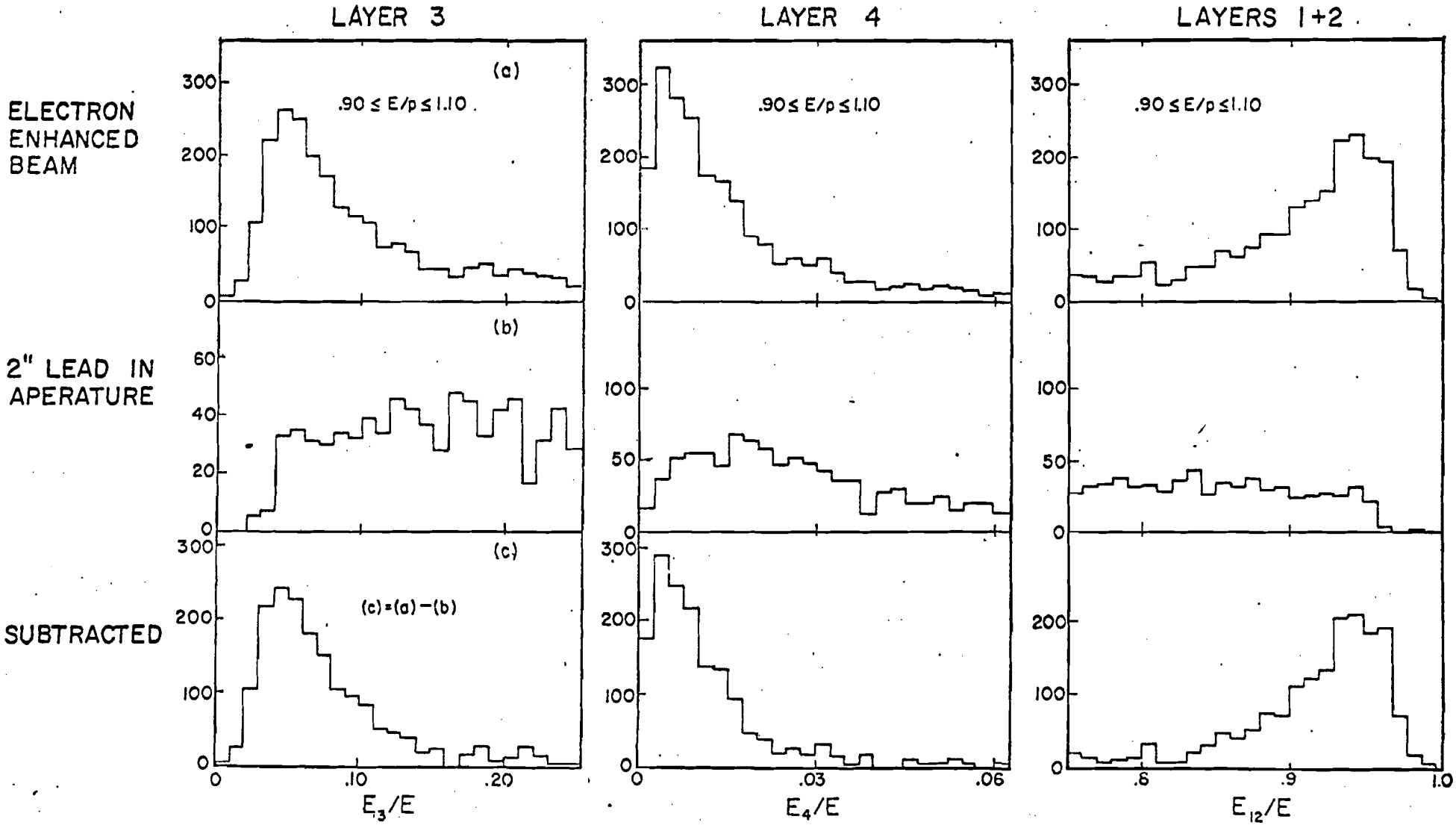

Figure 40

J/ψ YIELD VS BEAM MONITORS

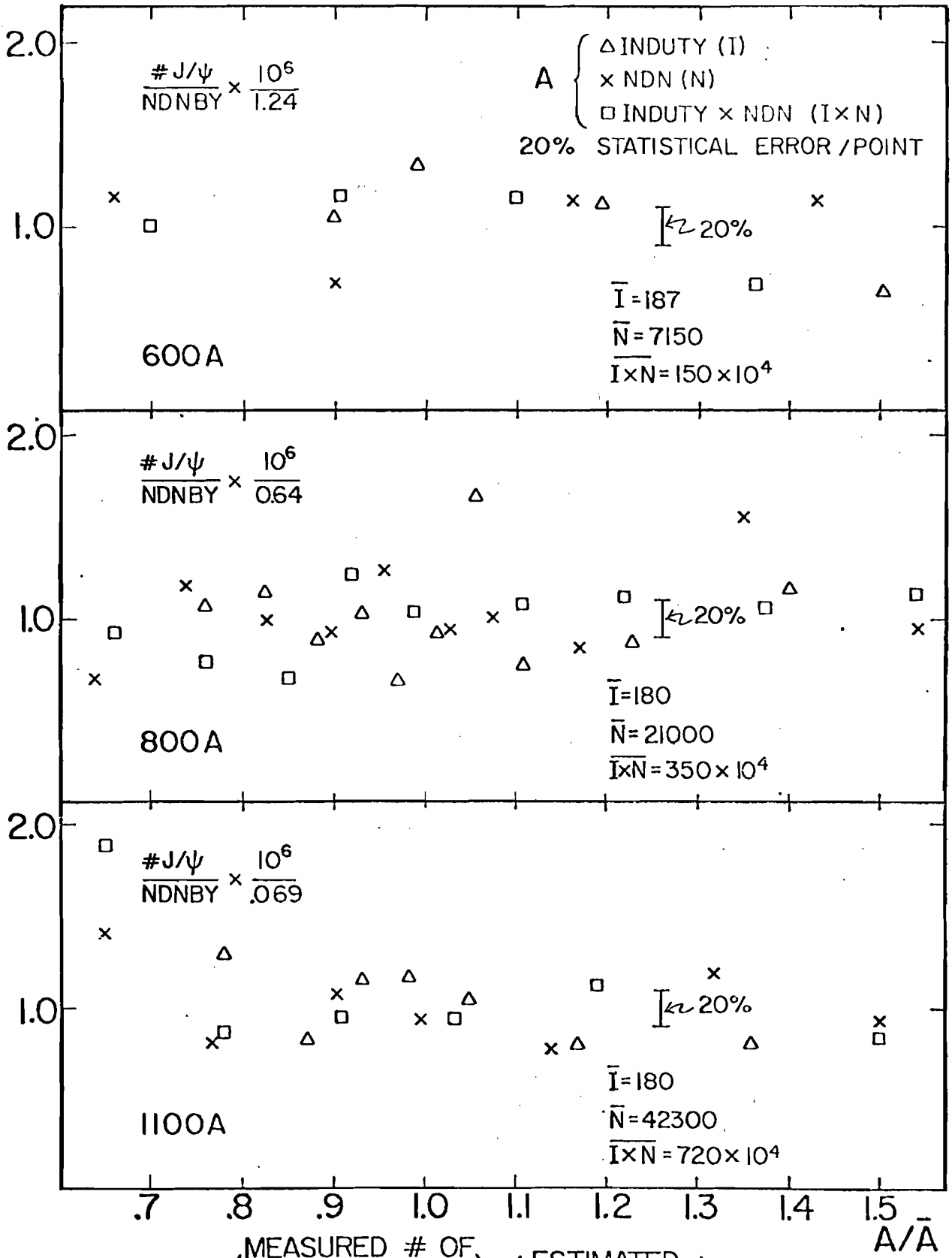

$$\#J/\psi = \left(\begin{array}{c}\text{MEASURED \# OF}\\ \text{EVENTS IN } J/\psi\\ \text{MASS REGION}\end{array}\right) - \left(\begin{array}{c}\text{ESTIMATED}\\ \text{BACKGROUND}\end{array}\right)$$

NDNBY = NDN CORRECTED FOR SYSTEM DEADTIMES

FIGURE 41

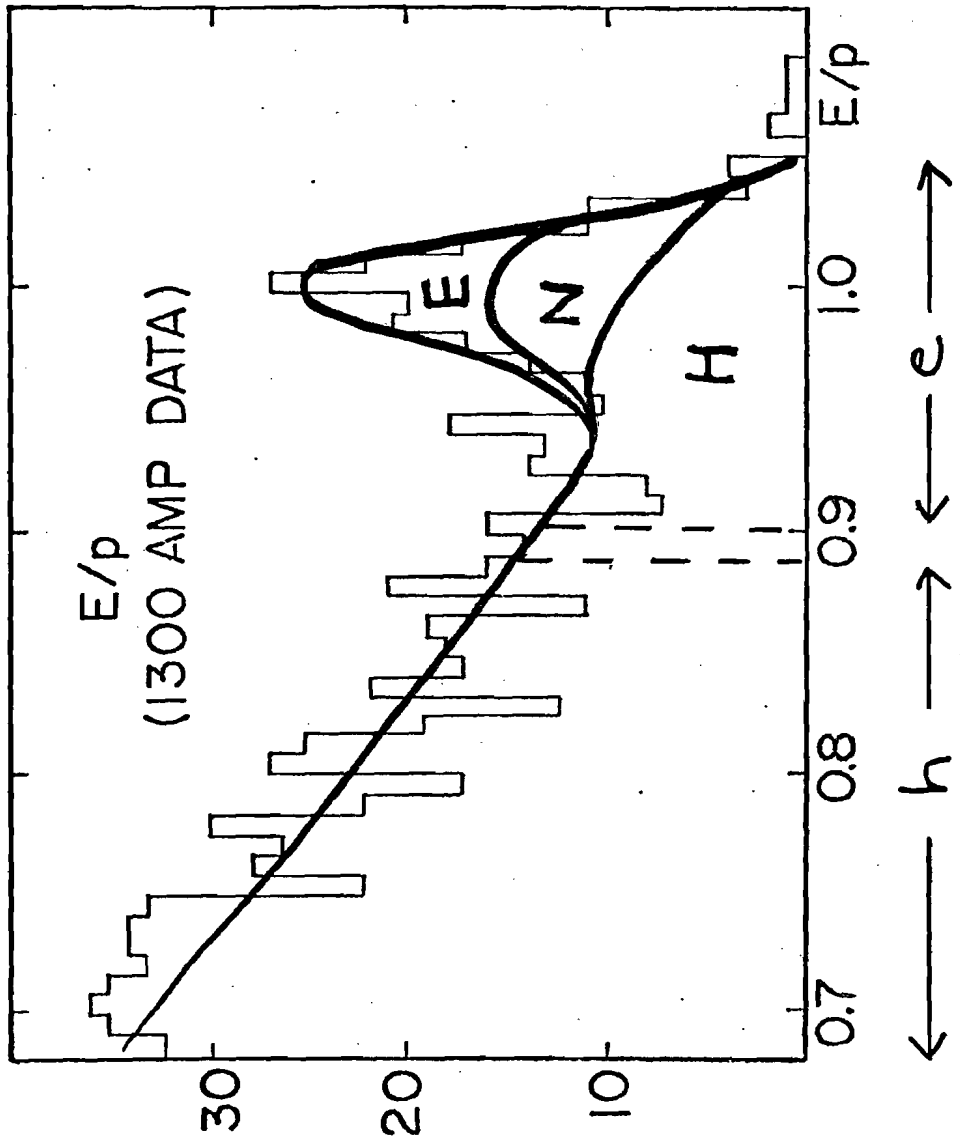

FIGURE 42

$\pi - K - p$ E/p COMPARISON

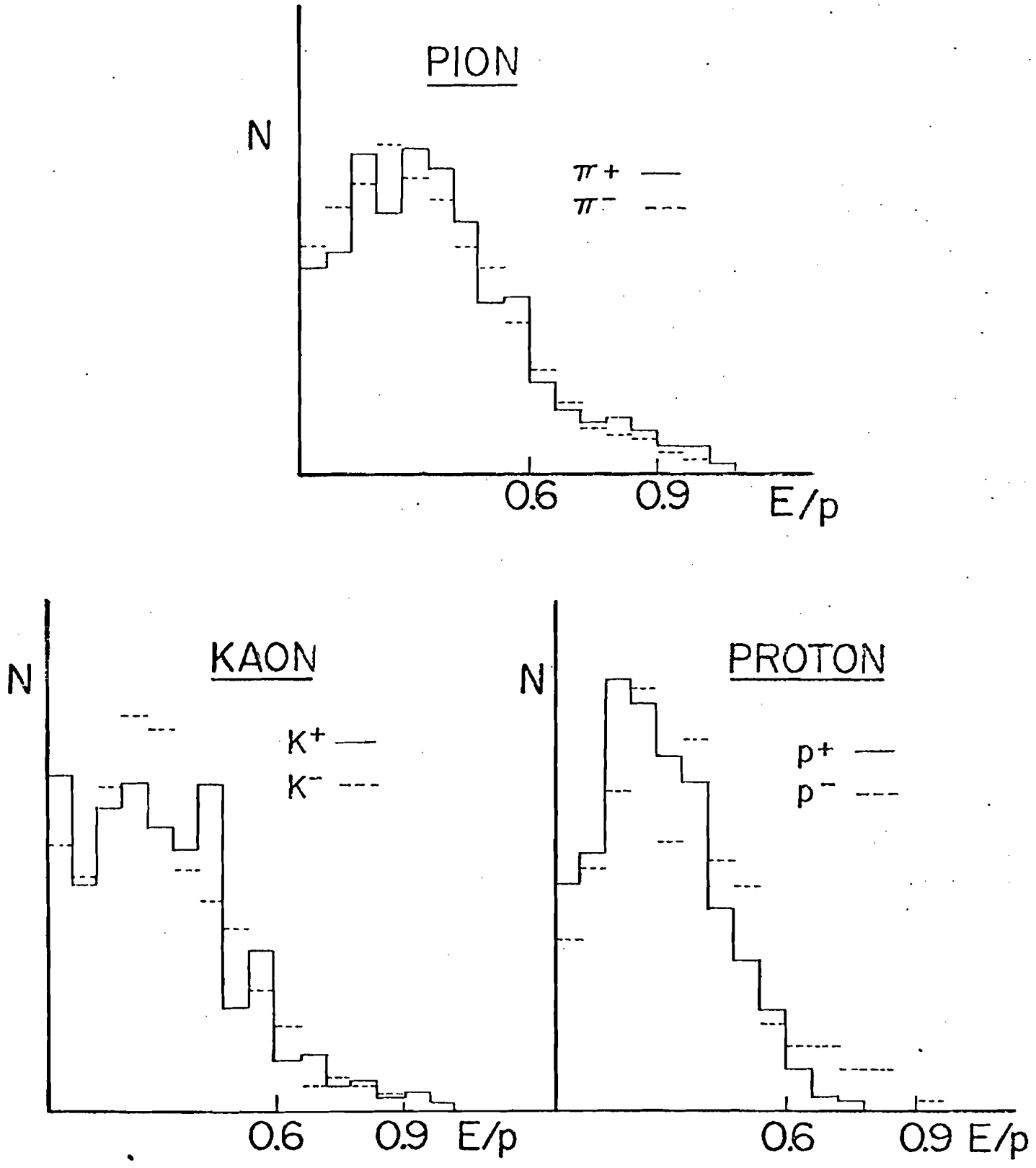

N = # OF EVENTS
PLOTS RENORMALIZED TO EQUALIZE AREAS

Figure 43

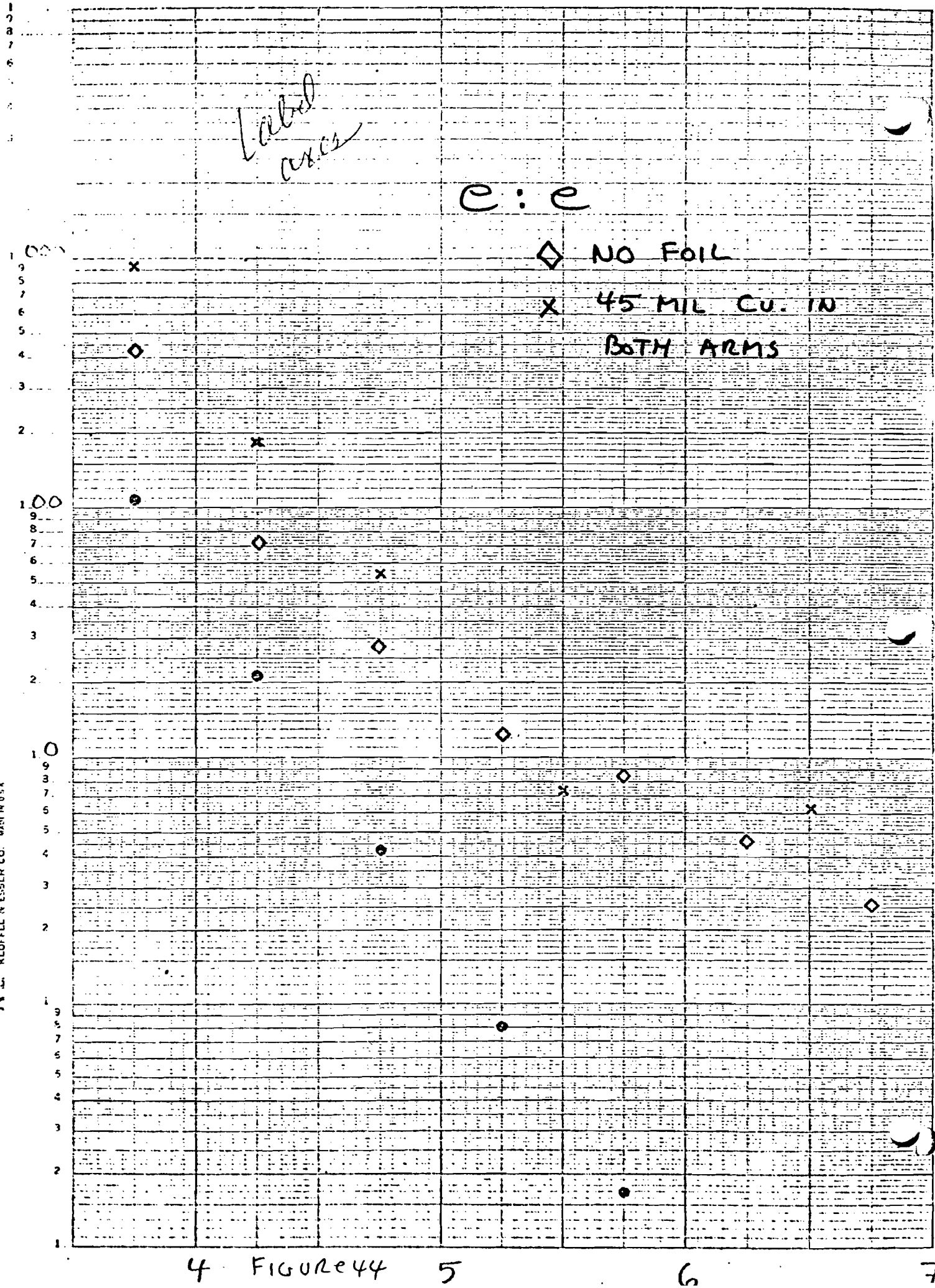
Label axes
e : e
◇ NO FOIL
× 45 MIL CU. IN BOTH ARMS
46 6210
SEMI-LOGARITHMIC 5 CYCLES X 70 DIVISIONS
KEUFFEL & ESSER CO. MADE IN U.S.A.
4
5
6
7

FIGURE 44

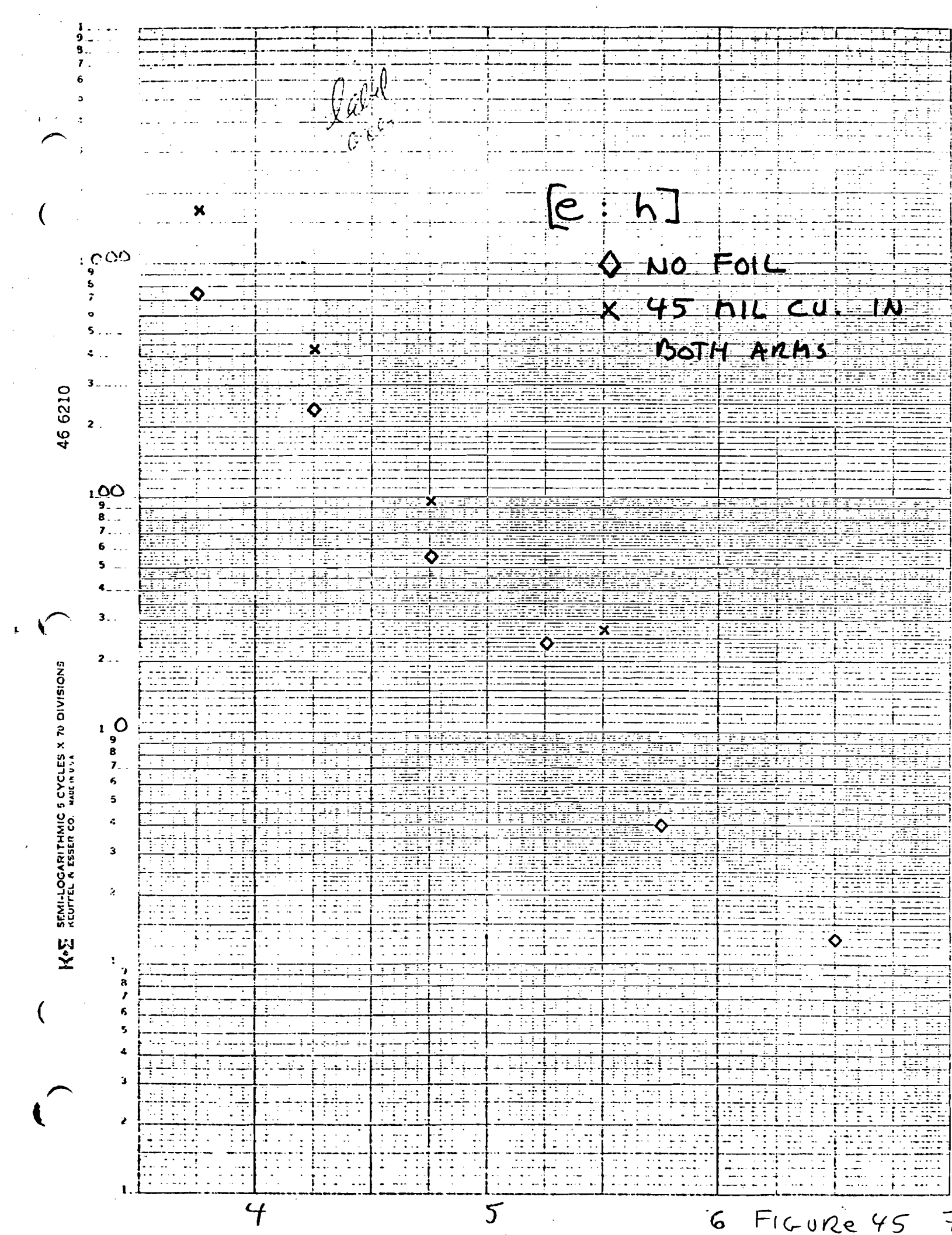
[e : h]
◇ NO FOIL
× 45 MIL CU. IN BOTH ARMS
46 6210
K+E SEMI-LOGARITHMIC 5 CYCLES X 70 DIVISIONS
KEUFFEL & ESSER CO. MADE IN U.S.A.
4
5
6

FIGURE 45

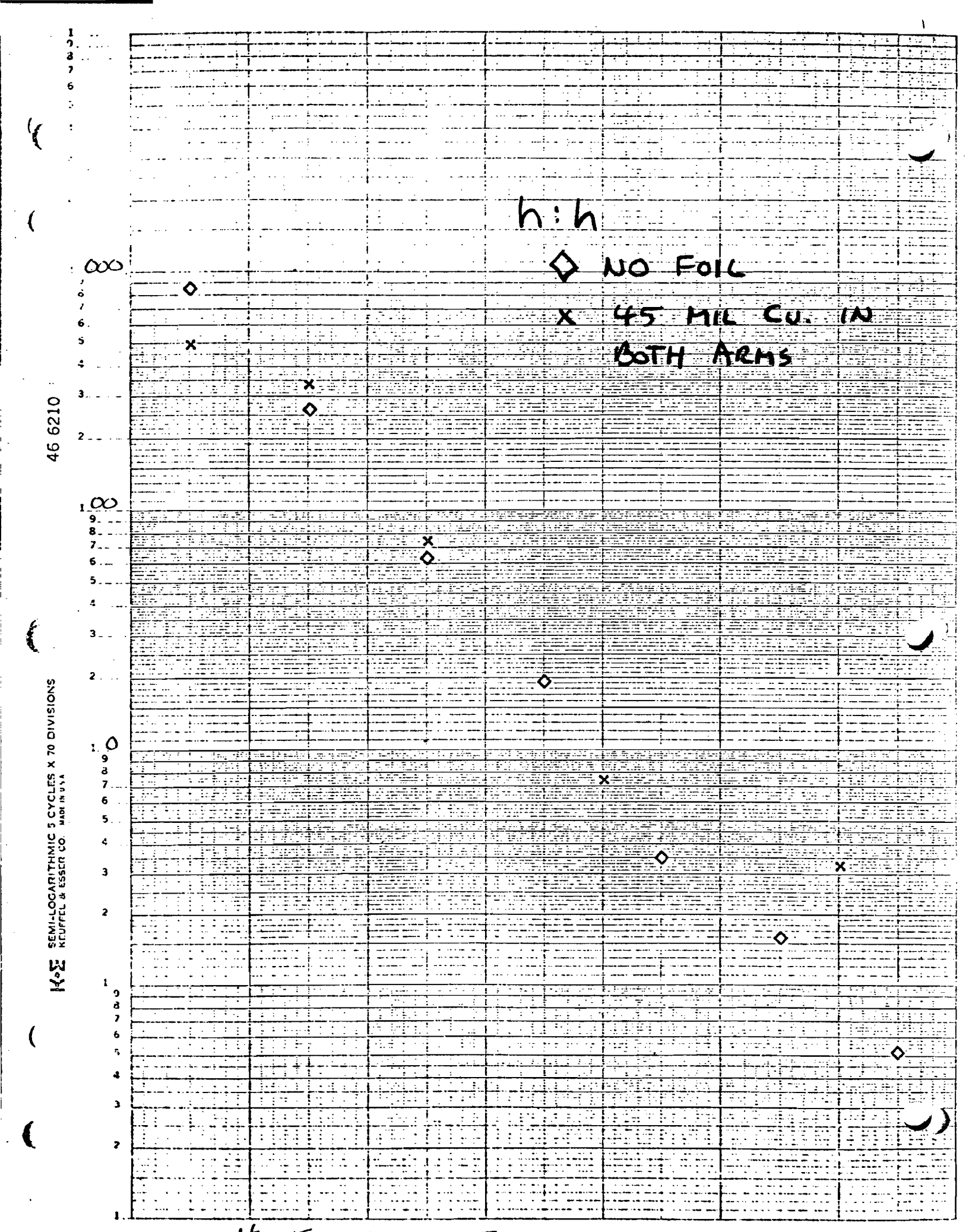
h:h
◇ NO FOIL
x 45 MIL Cu. IN BOTH ARMS
46 6210
K+E SEMI-LOGARITHMIC 5 CYCLES X 70 DIVISIONS
KEUFFEL & ESSER CO. MADE IN U.S.A.
4
5
6

FIGURE 46

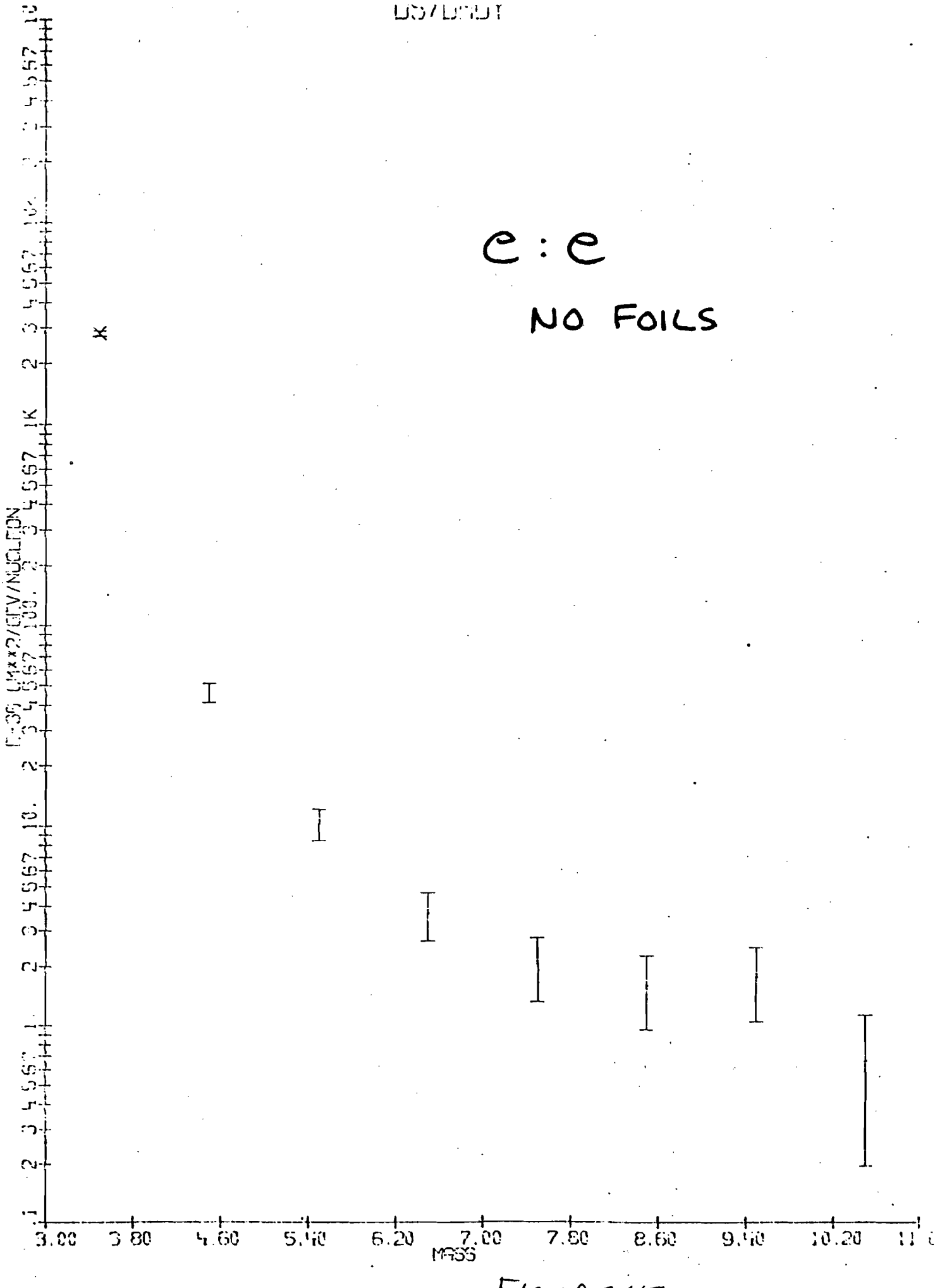

FIGURE 47

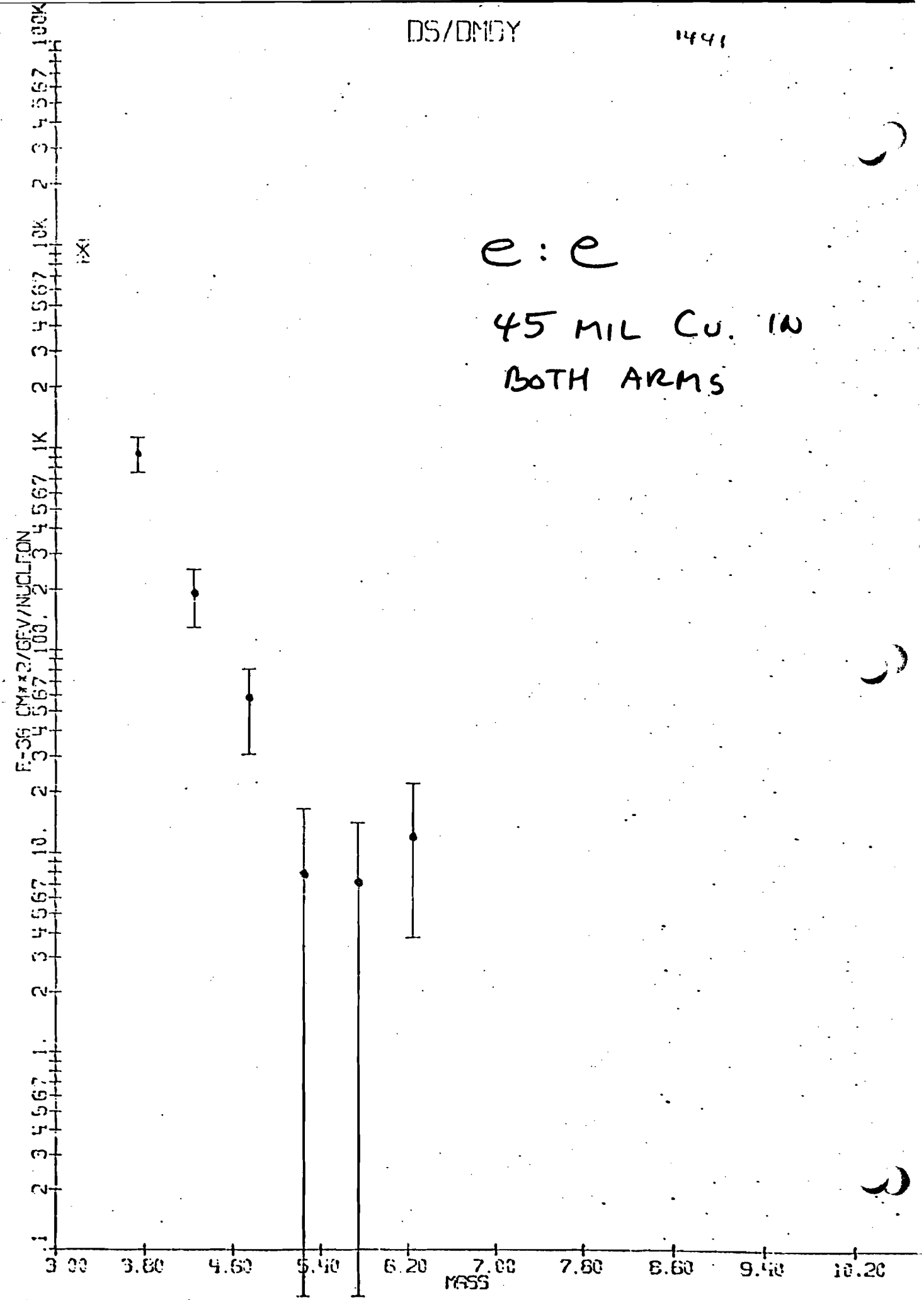
e:e
45 MIL Cu. IN
BOTH ARMS
E-36 CM**2/GEV/NUCLEON
MASS
3.00
3.80
4.60
5.40
6.20
7.00
7.80
8.60
9.40
10.20

Figure 48

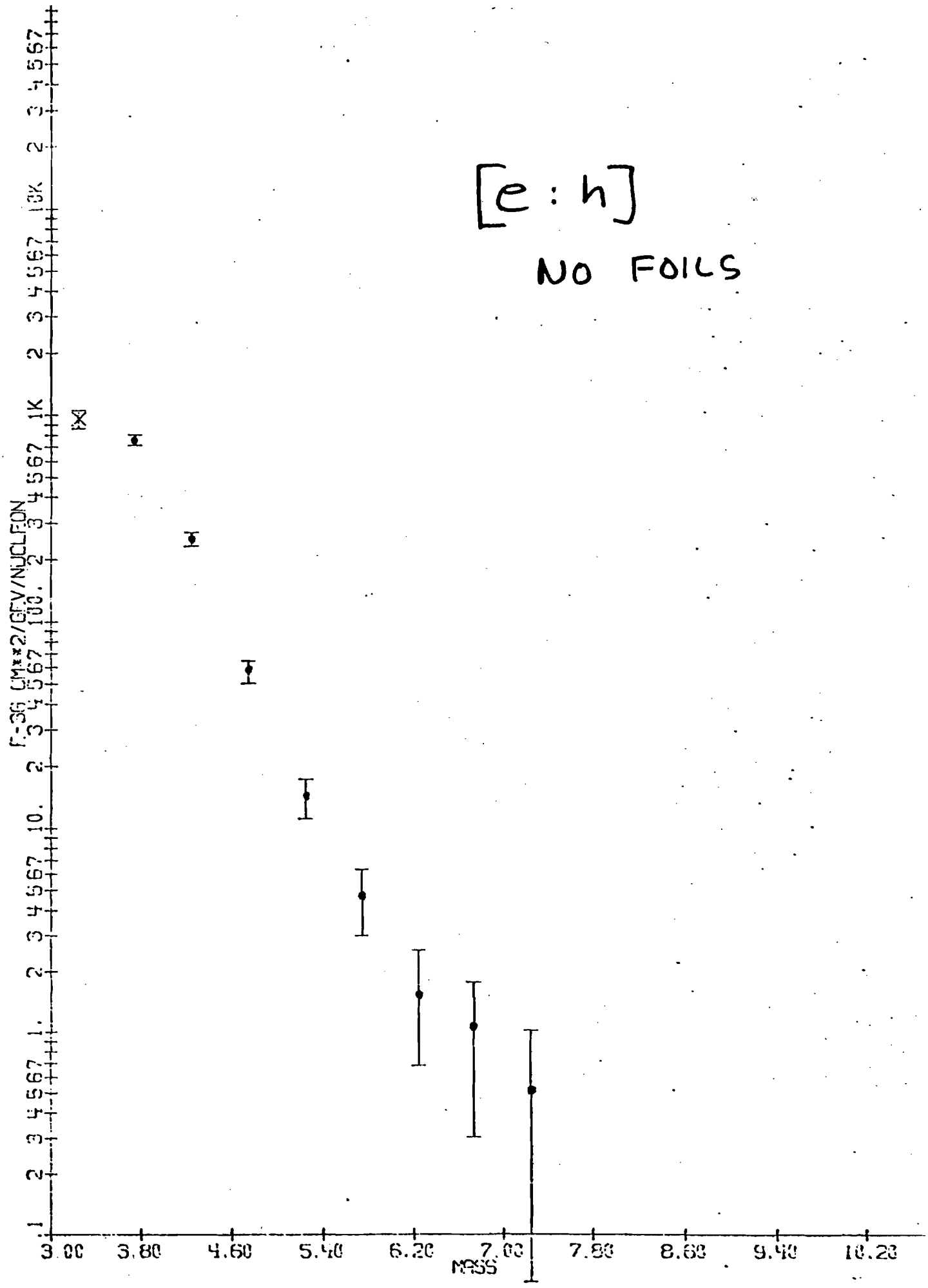
[e : h]
NO FOILS
E-36 CM**2/GEV/NUCLEON
MASS
3.00
3.80
4.60
5.40
6.20
7.00
7.80
8.60
9.40
10.20

FIGURE 49

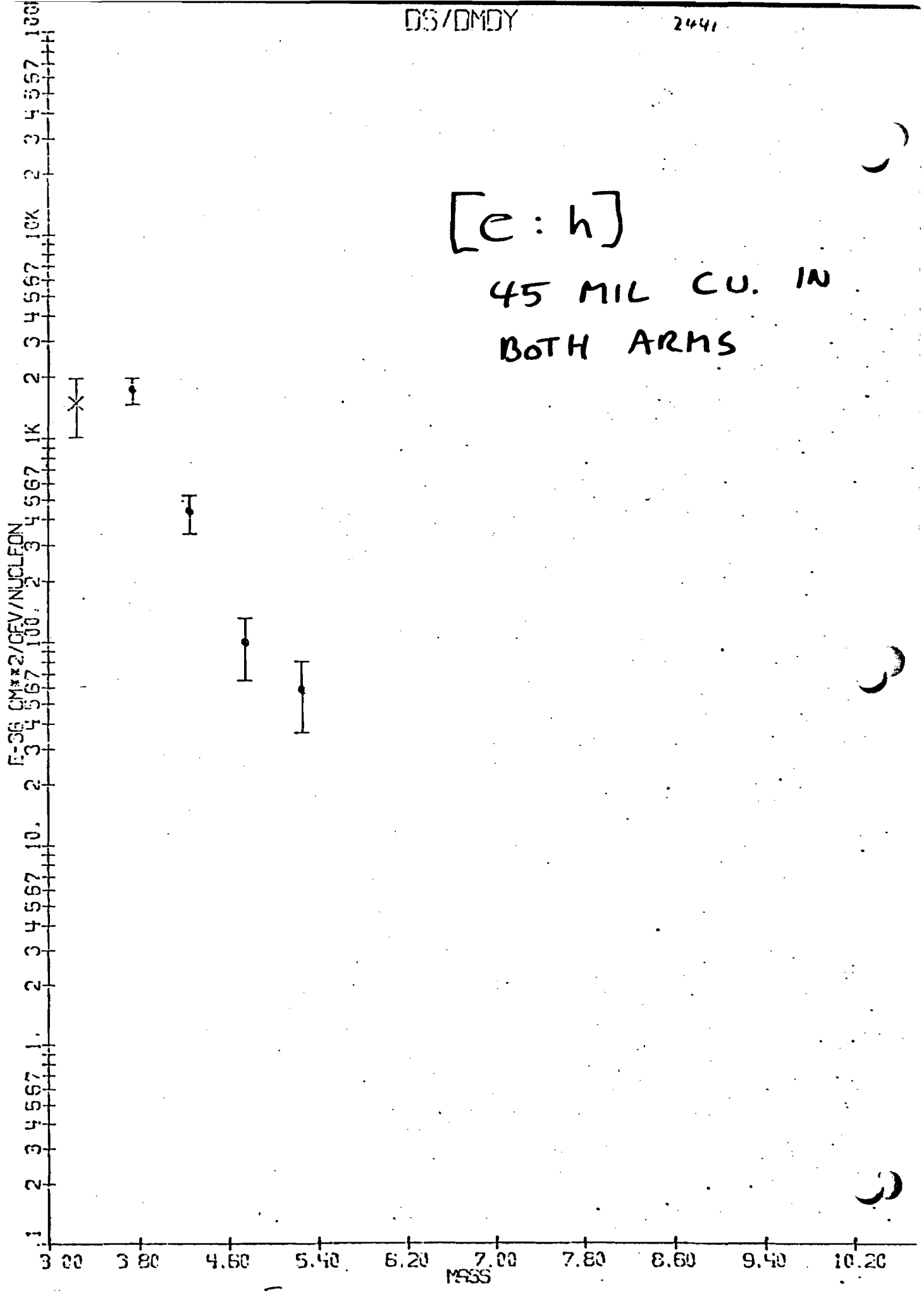
[e:h]
45 MIL CU. IN
BOTH ARMS
E-36 CM**2/GEV/NUCLEON
MASS
3.00
3.80
4.60
5.40
6.20
7.00
7.80
8.60
9.40
10.20

Figure 50

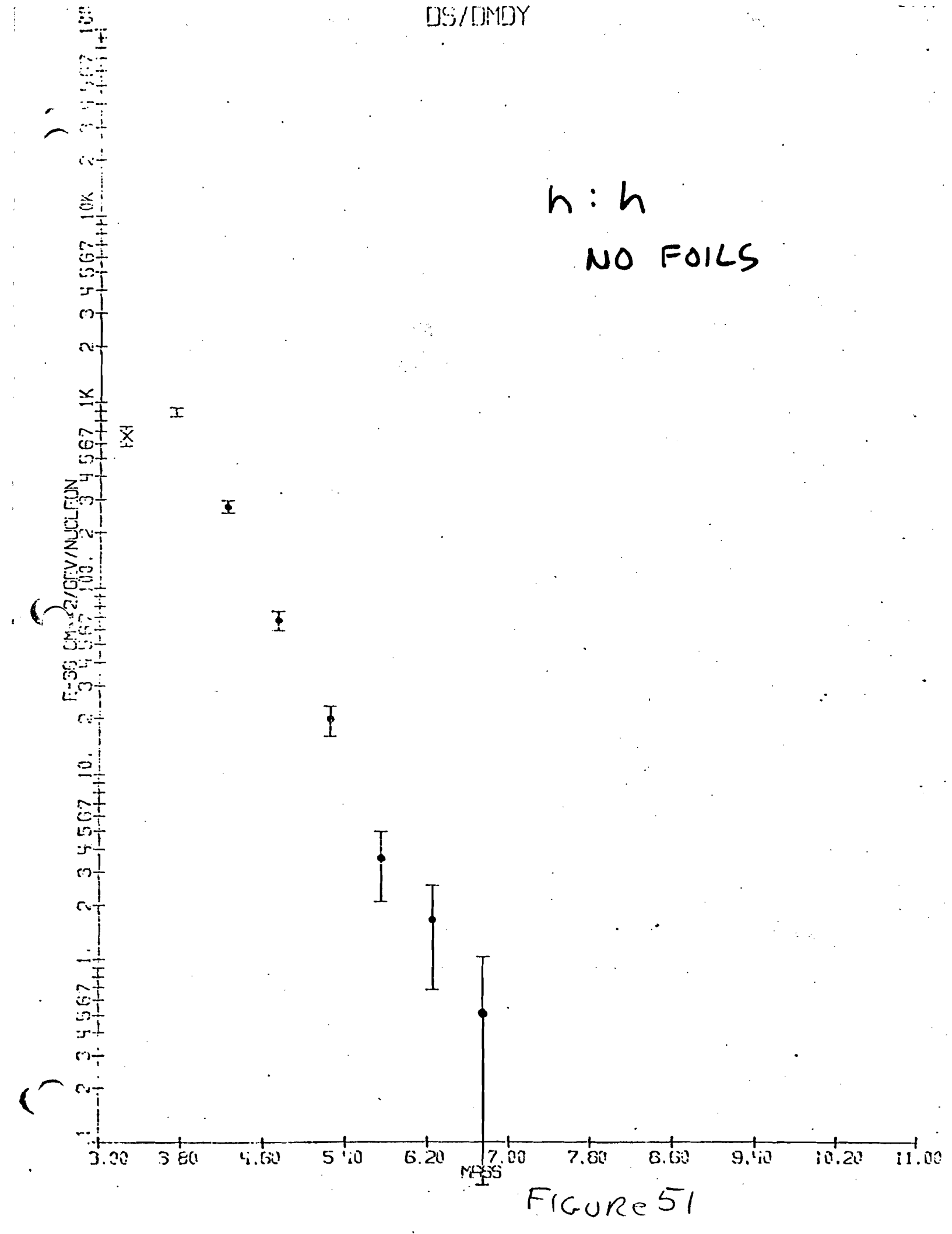
DS/DMDY
h : h
NO FOILS
E-36 CM**2/GEV/NUCLEON
INV
H
3.00
3.80
4.60
5.40
6.20
7.00
7.80
8.60
9.40
10.20
11.00
MASS

FIGURE 51

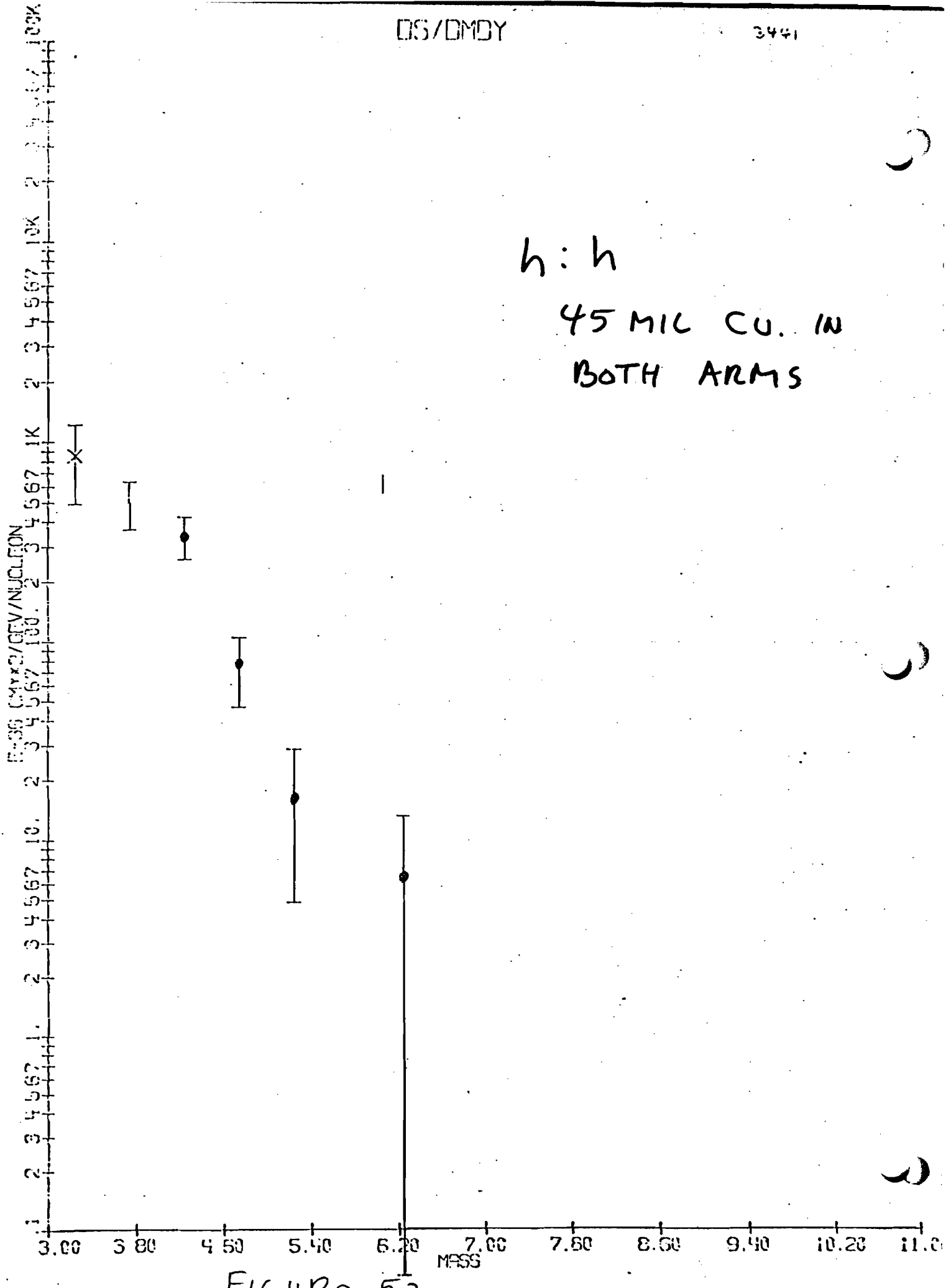
h:h
45 MIC CU. IN
BOTH ARMS
MASS
3.00
3.80
4.50
5.40
6.20
7.00
7.80
8.50
9.40
10.20

FIGURE 52

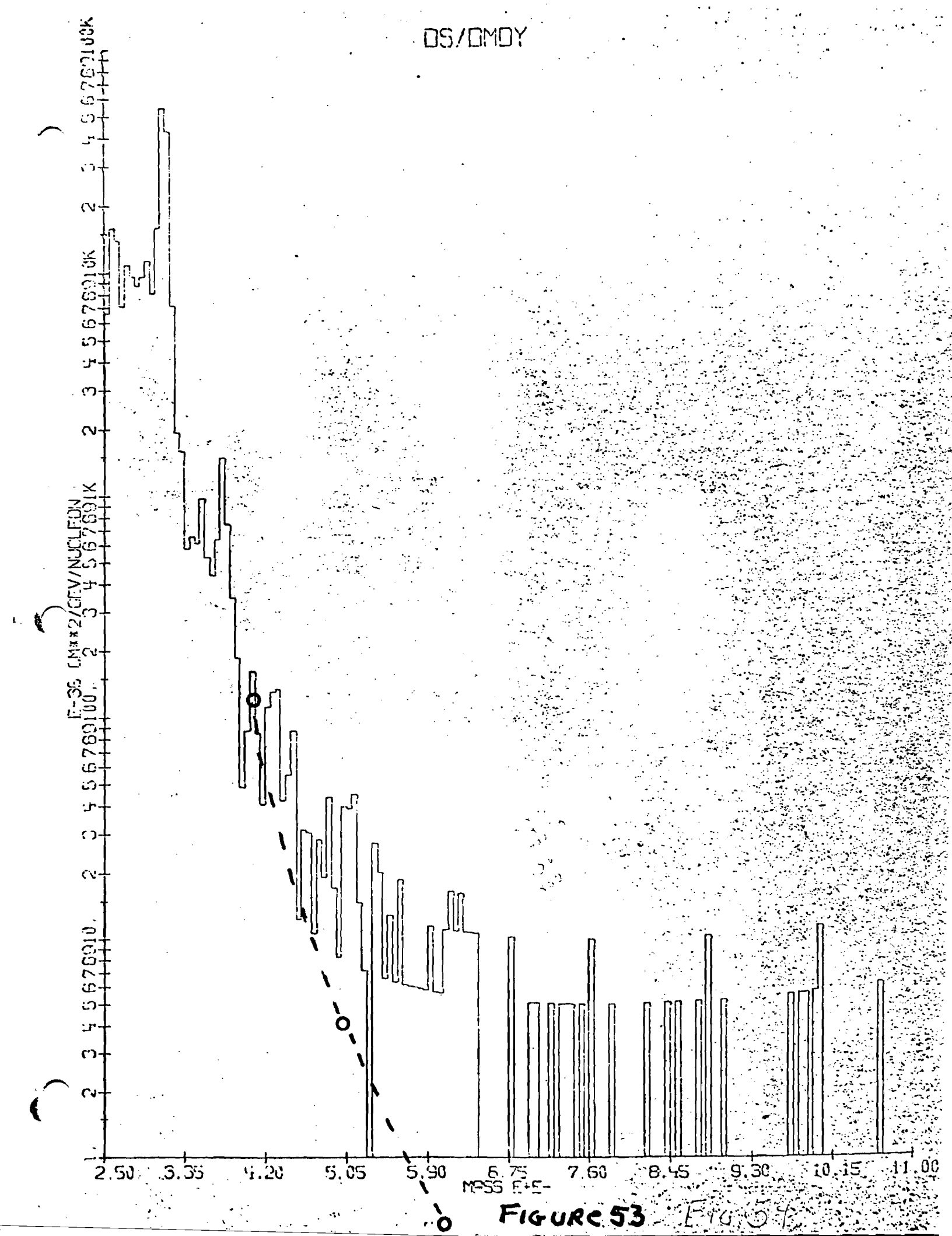

FIGURE 53 - EVENTS

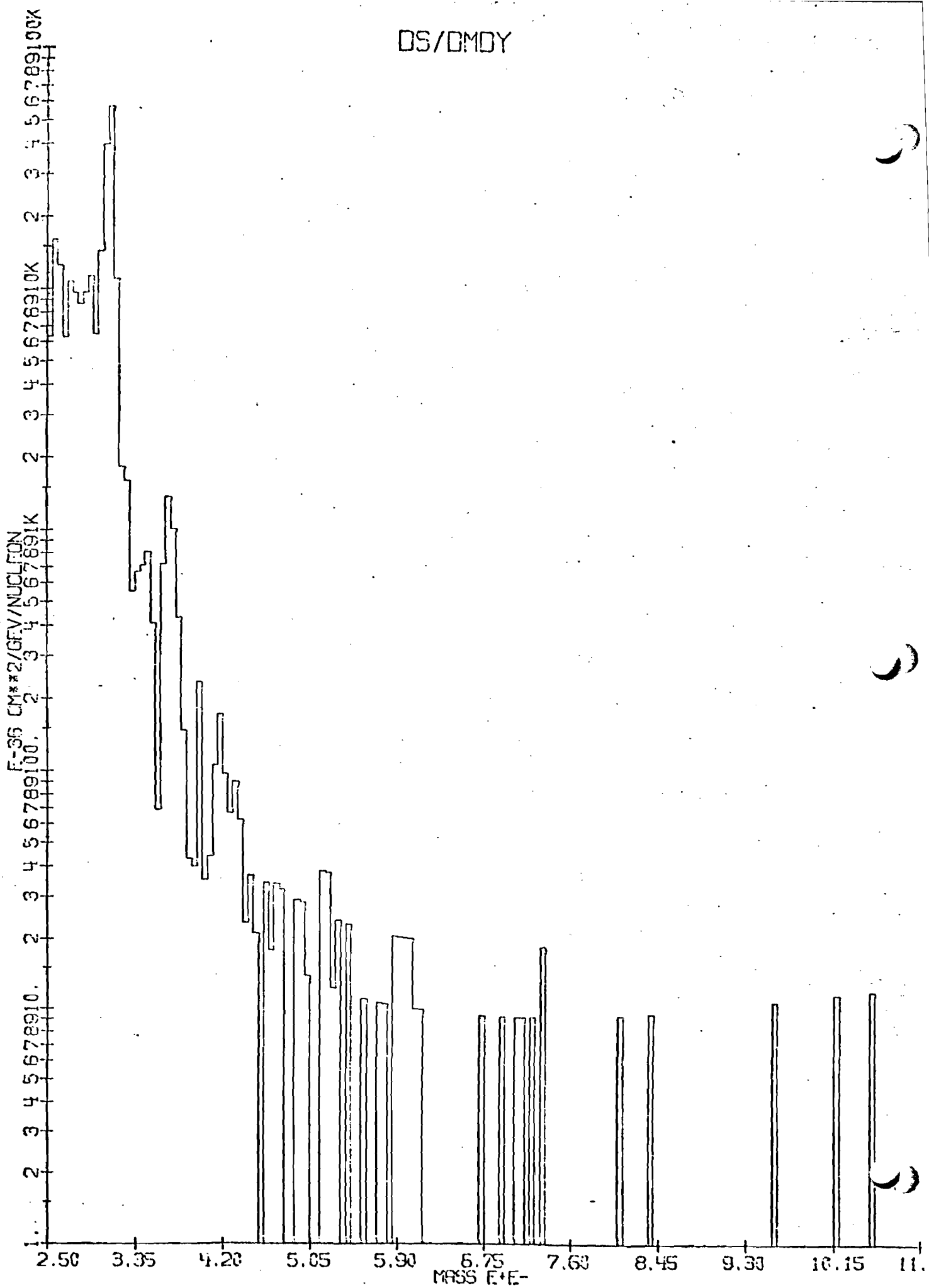
DS/DMDY
F-35 CM**2/GEV/NUCLEON
MASS E+E-
2.50
3.35
4.20
5.05
5.90
6.75
7.60
8.45
9.30
10.15

FIGURE 54

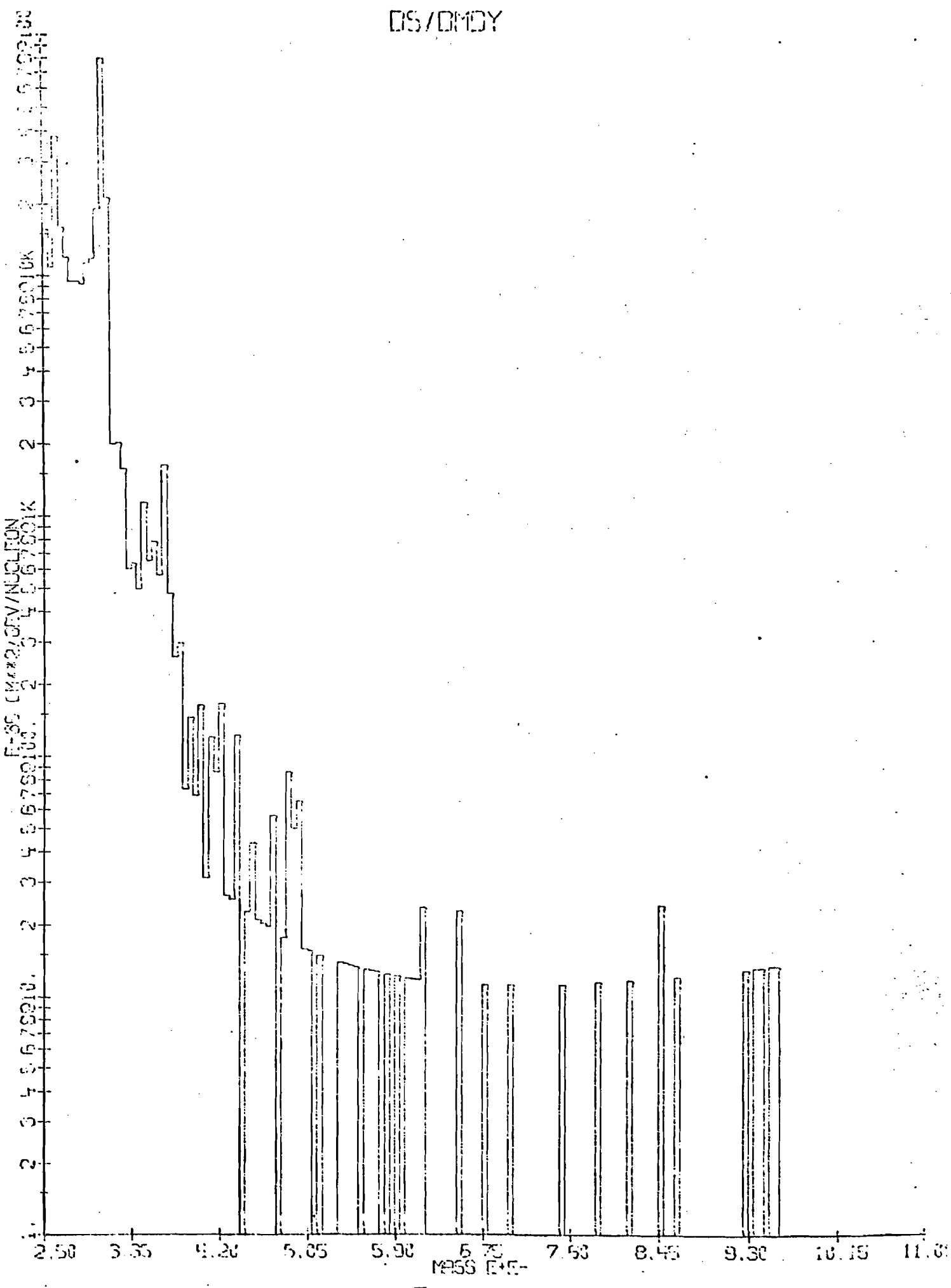

FIGURE 55

FIGURE 56

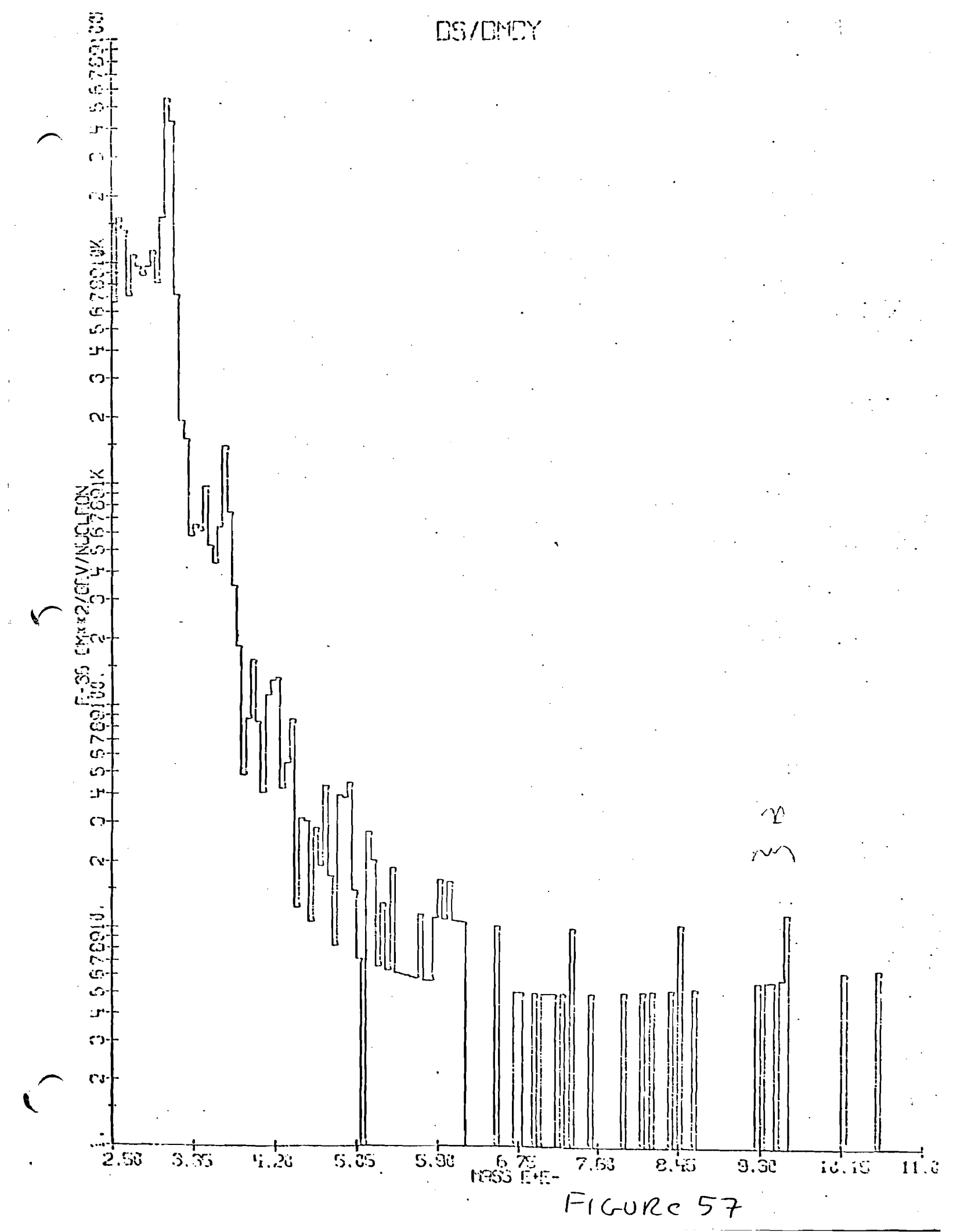
DS/DMDY
F-35 DMx*2/GEV/NUCLEON
2.58
3.35
4.20
5.05
5.90
6.75
7.60
8.45
9.30
10.15
MASS GEV-

FIGURE 57

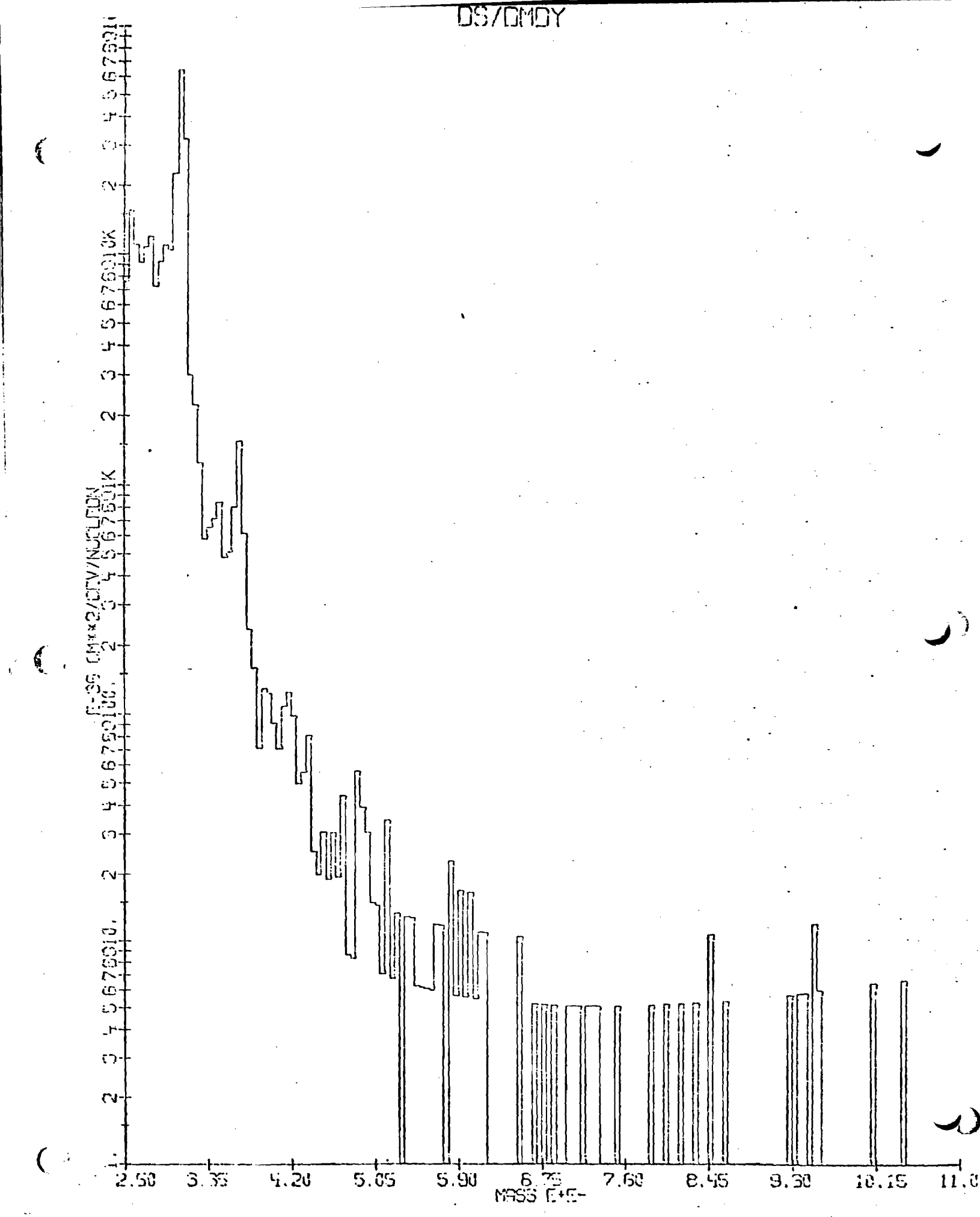

FIGURE 58

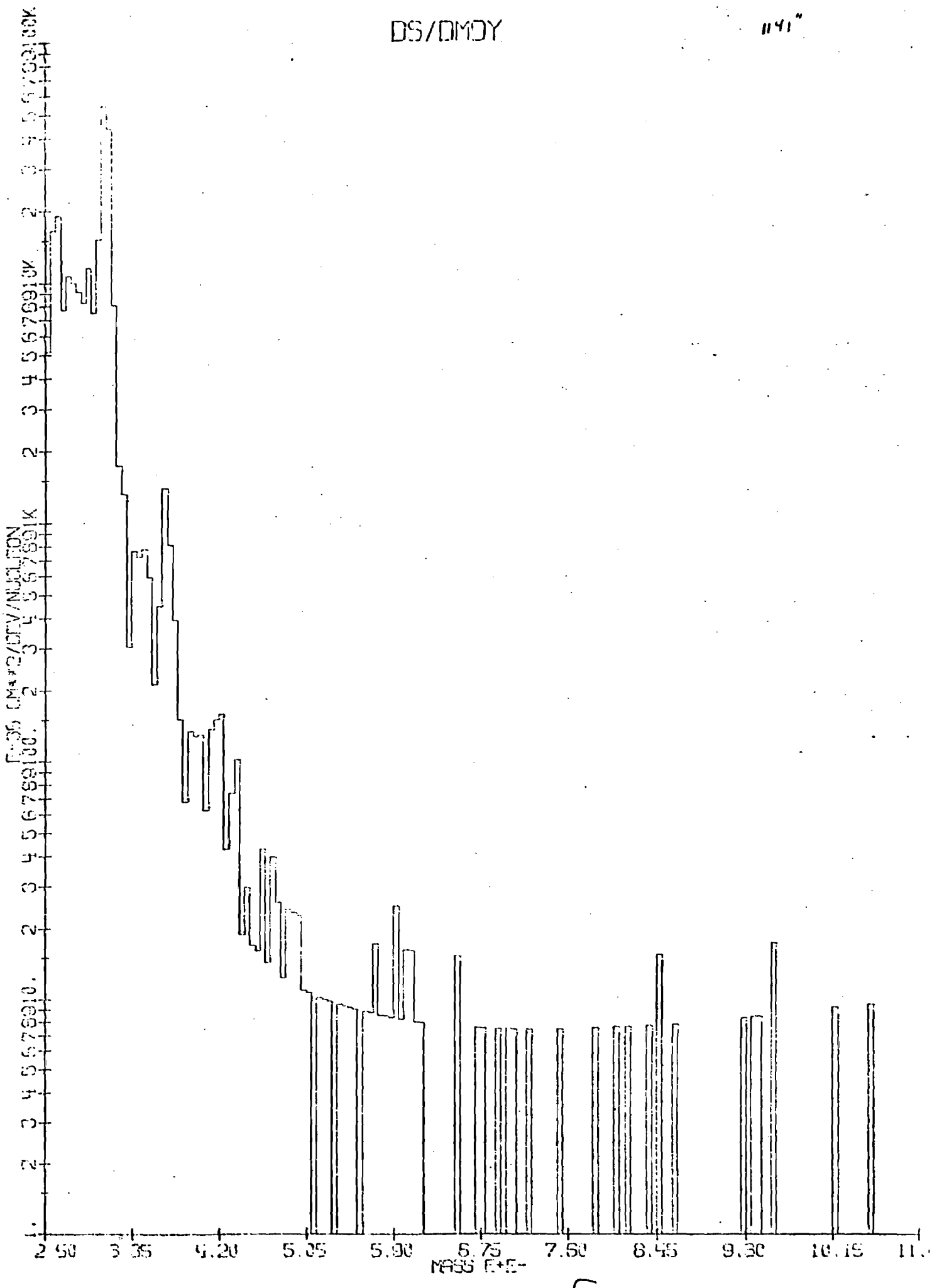
F.35 CM**2/STR/NJOULTON
1.
2
3
4
5
6
7
8
9
10.
2
3
4
5
6
7
8
9
100.
2
3
4
5
6
7
8
9
1K
2
3
4
5
6
7
8
9
10K
2.50
3.35
4.20
5.05
5.90
6.75
7.60
8.45
9.30
10.15
11.
MASS E+E-

Figure 59

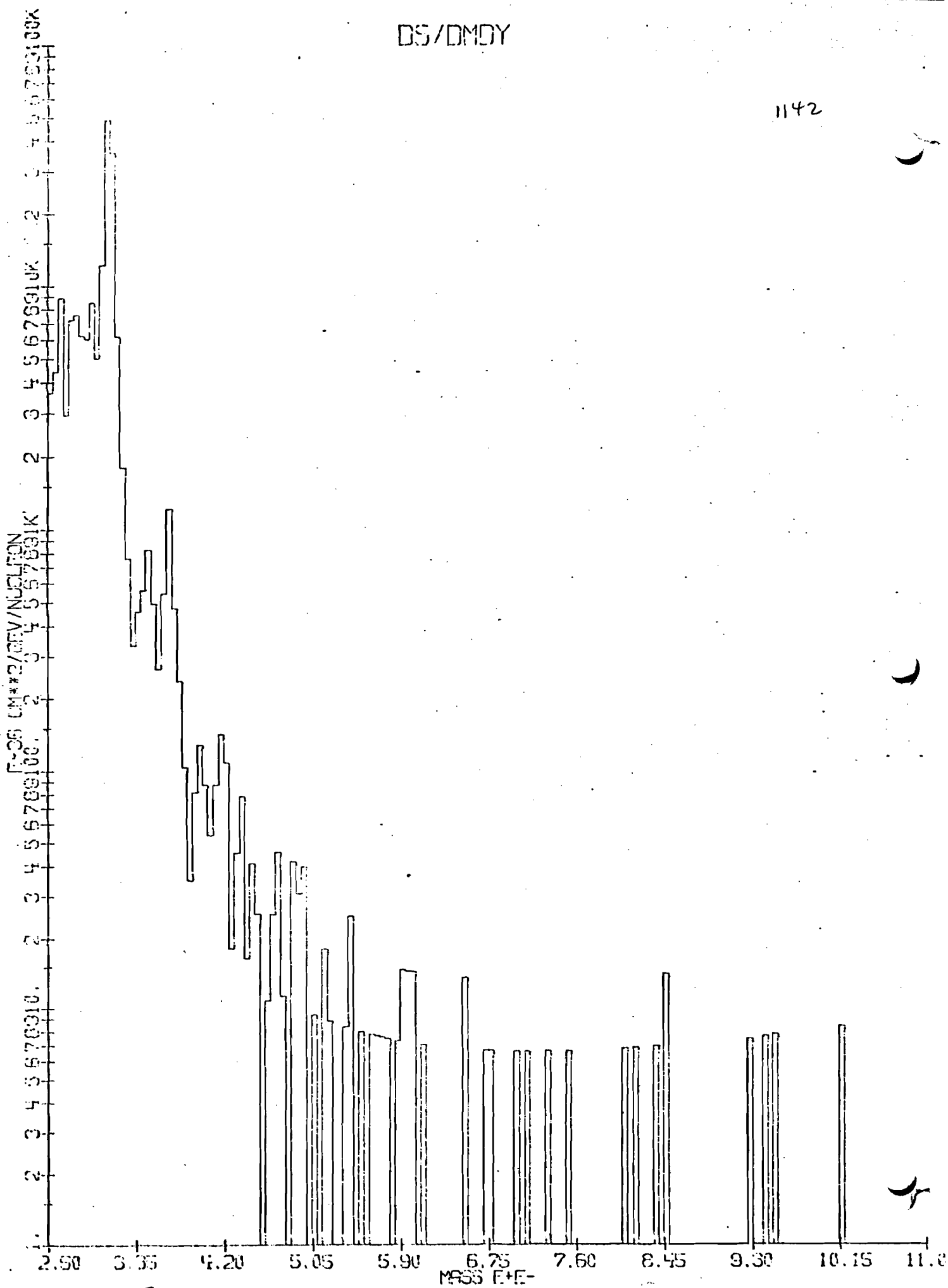
DS/DMDY
F-35 DM**2/DEV/NUCLEON
MASS E+E-
2.50
3.35
4.20
5.05
5.90
6.75
7.60
8.45
9.30
10.15

FIGURE 60

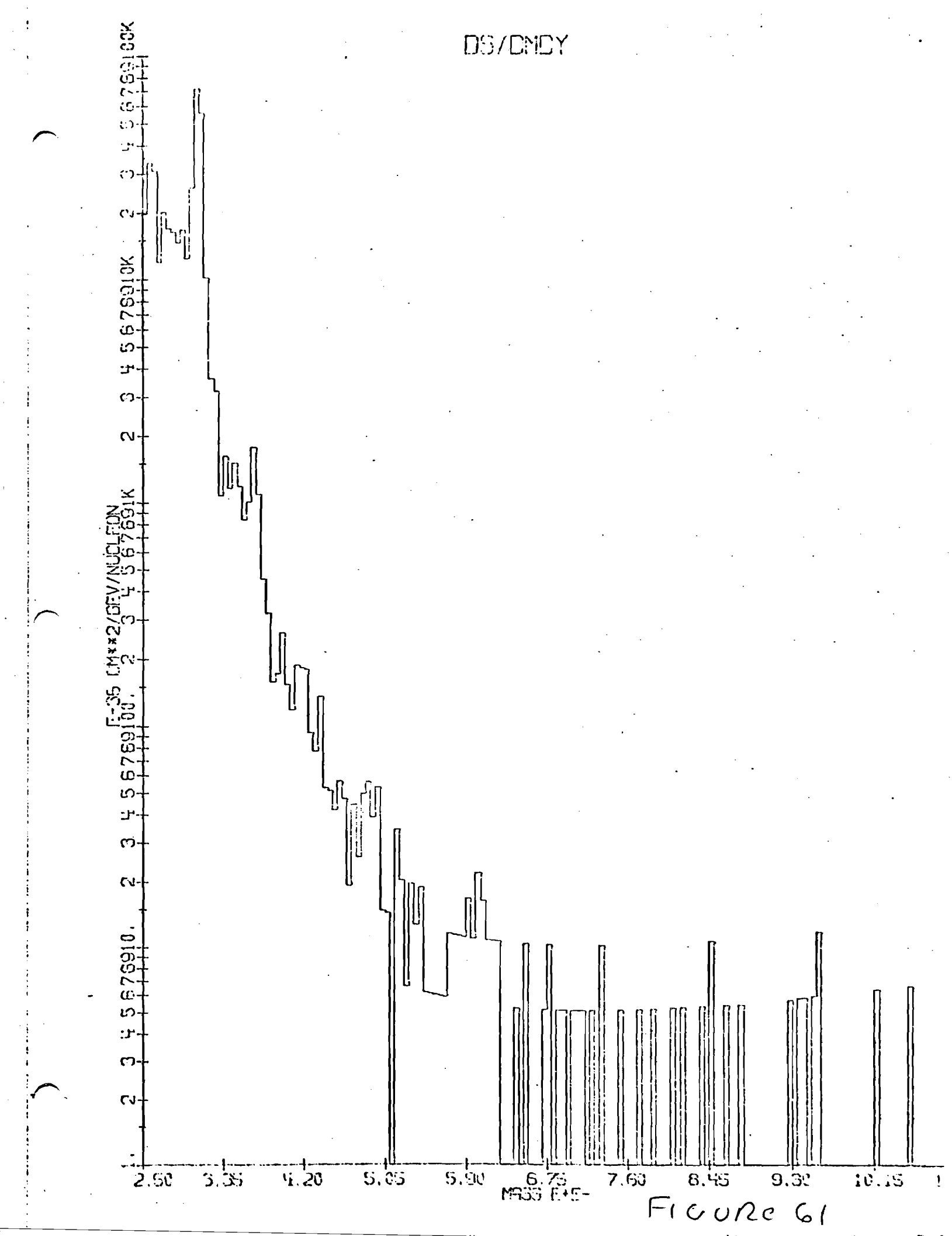
DS/DMDY
F-35 DM**2/DEV/NUCLEON
100.
10.
1.
2.50
3.35
4.20
5.05
5.90
6.75
7.60
8.45
9.30
10.15
MASS E+5-

Figure 61

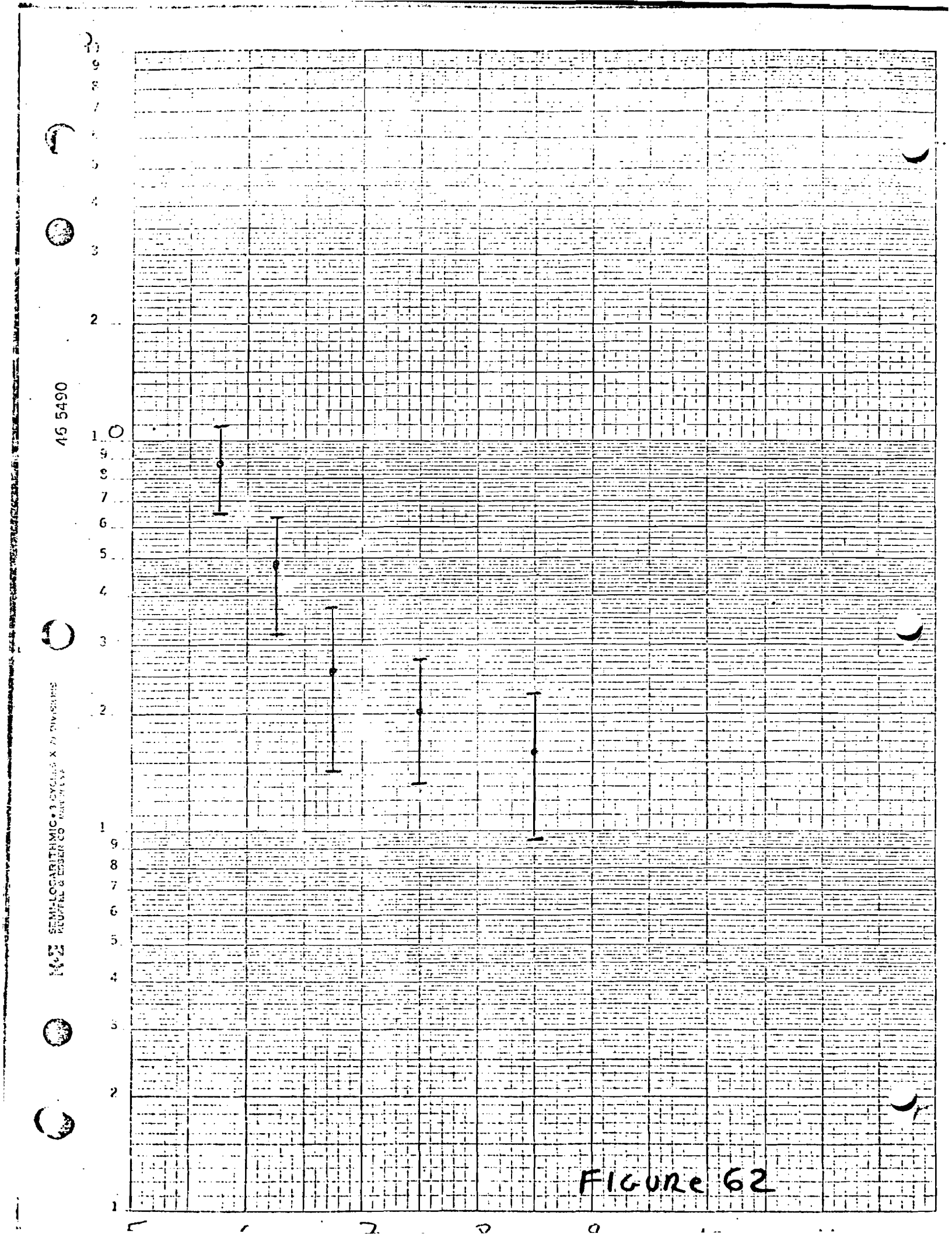
46 5490
SEMI-LOGARITHMIC • 3 CYCLES X 70 DIVISIONS
KEUFFEL & ESSER CO.

FIGURE 62

Pb = ?

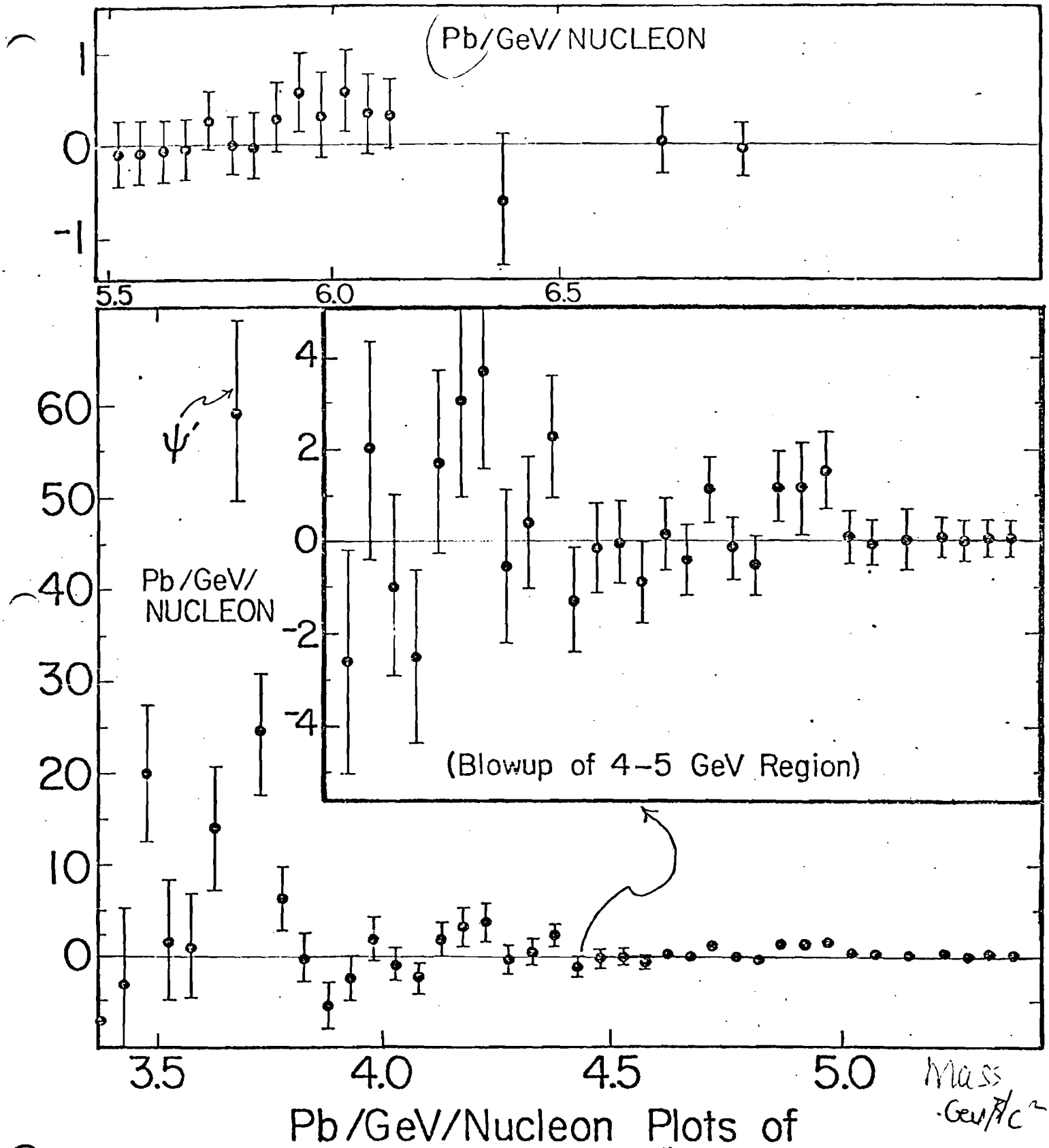

Pb/GeV/Nucleon Plots of
"Fit Subtracted" Data

FIGURE 63

Figure 69

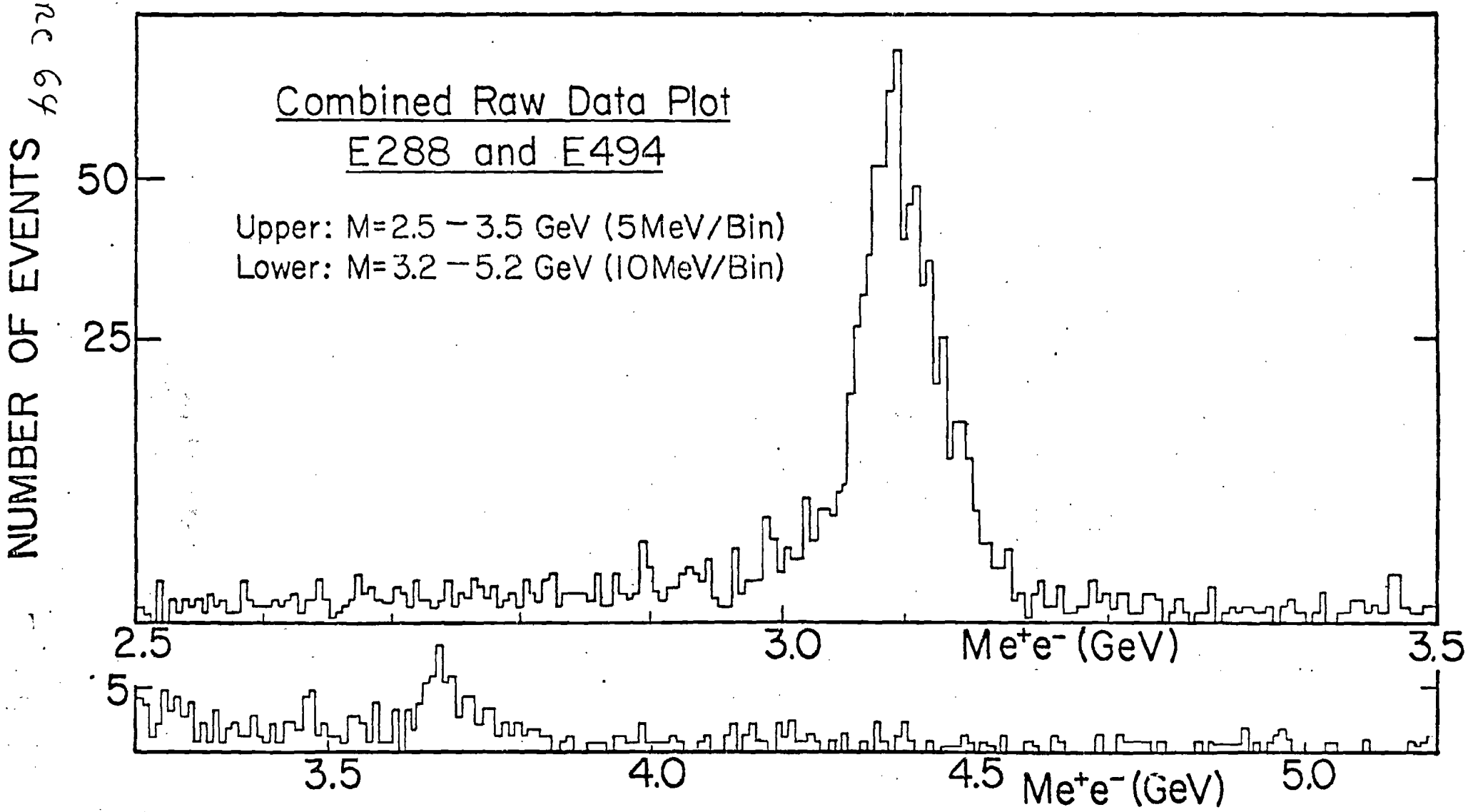
Combined Raw Data Plot
E288 and E494
Upper: M=2.5 – 3.5 GeV (5MeV/Bin)
Lower: M=3.2 – 5.2 GeV (10MeV/Bin)
NUMBER OF EVENTS
50
25
2.5
3.0
3.5
Me+e- (GeV)
5
3.5
4.0
4.5
5.0
Me+e- (GeV)

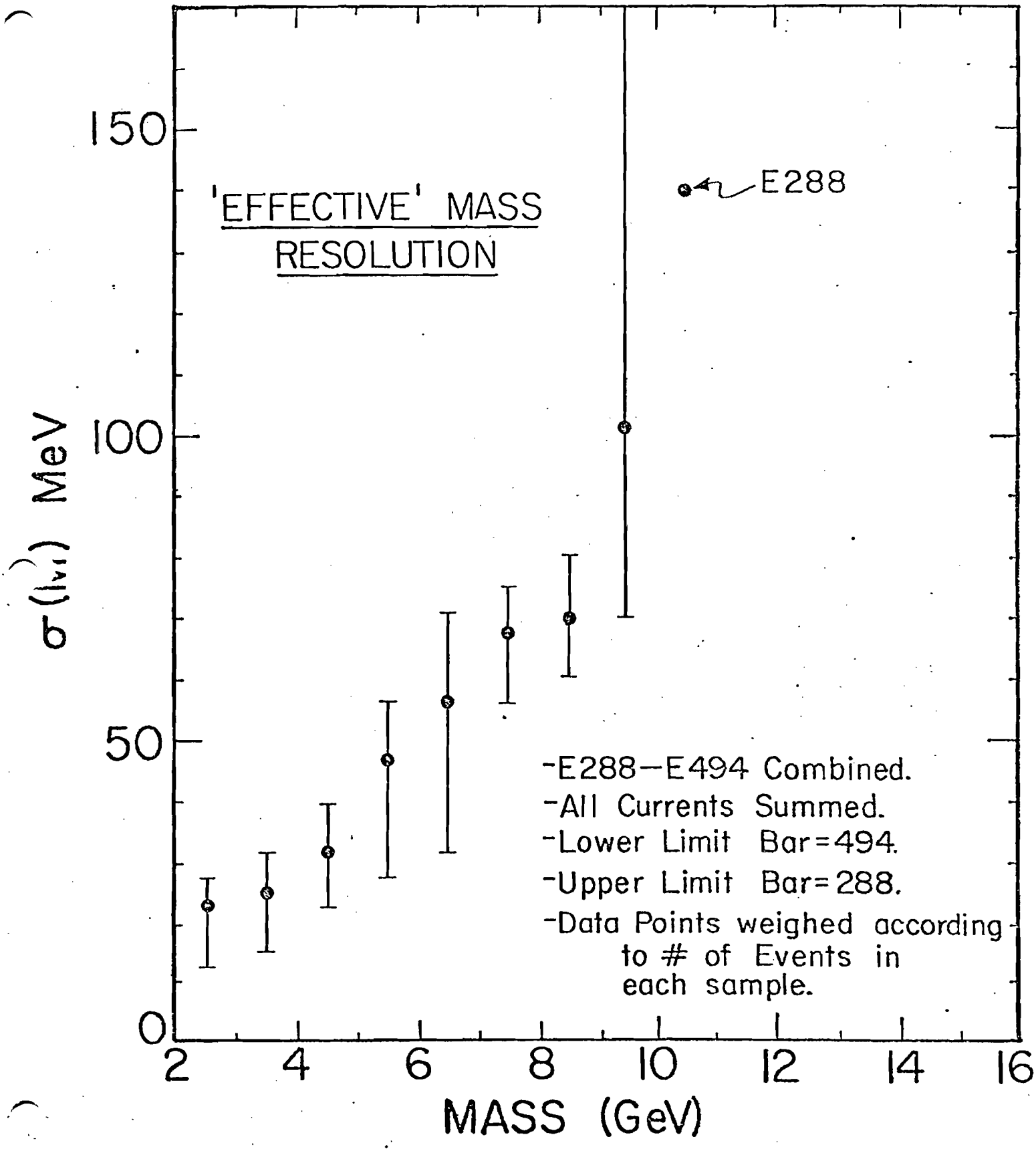
'EFFECTIVE' MASS RESOLUTION
E288
-E288—E494 Combined.
-All Currents Summed.
-Lower Limit Bar=494.
-Upper Limit Bar=288.
-Data Points weighed according to # of Events in each sample.
σ(M²) MeV
MASS (GeV)
0
50
100
150
2
4
6
8
10
12
14
16

Figure 65

TABLE 1

QUANTITY	PREDICTION	OBSERVATION	COMMENT
BJORKEN SCALING	$W_1(q^2,\nu) \to F_1\left(\frac{q^2}{2M\nu}\right)$ $\frac{\nu}{M} W_2(q^2,\nu) \to F_2\left(\frac{q^2}{2M\nu}\right)$ as $\nu, q^2 \to \infty$ $x = q^2/2M\nu$ FIXED SIMPLE PARTON THEORY PREDICTS A CROSS SECTION WITH UNVIOLATED 'SCALING'.	SCALING VIOLATED BY 20-30 % a) $x \geq 0.15$ F_2 FALLS AS q^2 INCREASES b) $x \sim 0.1, 0.2$ F_2 CONSTANT IN q^2 TO 100 GeV c) $x \ll 0.1$ F_2 RISES AS q^2 INCREASES	NON-SCALING EFFECTS MAY BE DUE TO: - FINITE QUARK SIZE - GLUON BREMSSTRAHLUNG - GLUON PAIR PRODUCTION - THRESHOLD EFFECTS DUE TO NUCLEAR CONSTITUENT MASSES - EXCITATION OF NEW DEGREES OF FREEDOM - CREATION OF BOUND STATES ETC. NO VERDICT SO FAR
$R = \frac{\sigma_L}{\sigma_T}$	SPIN 0 PARTONS: $R \neq 0$ SPIN 1/2 PARTONS: $R = 0$ SPIN 1 PARTON: ADDS A SCALING VIOLATING q^2 DEPENDENCE TO CROSS SECTION R MAY BE RELATED TO QUARK TRANSVERSE MOMENTA: $R = 4\,\frac{(\langle k_1^2 \rangle + m_q^2 + \delta)}{Q^2}$ THIS IS DUE TO THE FACT THAT QUARK TRANSVERSE MOMENTUM MAKES QUARK AND PHOTON NON-COLLINEAR.	'R' VALUES HAVE BEEN FIT TO SEVERAL FUNCTIONAL FORMS. TAKEN AS A CONSTANT: $R = 0.25 \pm 0.10$ COMBINING SLAC AND MIT-SLAC DATA.	THE SMALL VALUE OF R IMPLIES THAT PARTONS ARE DOMINANTLY SPIN 1/2. VALUE AND FUNCTIONAL FORM OF 'R' MAY HAVE IMPLICATIONS FOR QUARK $k_\perp$ and QCD PREDICTIONS IN GENERAL, ONE NEEDS BETTER R DATA TO LEARN HOW IT FALLS OFF WITH Q^2.

TABLE 2

QUANTITY	PREDICTION	OBSERVATION	COMMENT
$F_2(x) = 2x F_1(x)$	PREDICTED FOR SPIN 1/2 PARTONS	$F_2(x) = 2x F_1(x)(1+A)$ $A(\text{PROTON}) = 0.14 \pm 0.06$	
$\int dx\, F_2(x)$	$= \sum P(N) \sum \frac{Q_i^2}{N}$ $P(N)$ = PROB. OF OBSERVING N PARTONS IN NUCLEUS Q_i = QUARK CHARGE FOR THE QUARK MODEL: $\frac{\sum Q_i^2}{N} = \frac{5}{18}$ (PROTON) $= \frac{2}{9}$ (NEUTRON)	$\int_{0.1}^{1} dx\, F_{2p}(x) = 0.14$ $\int_{0.1}^{1} dx\, F_{2n}(x) = 0.10$	QUARK MODEL PREDICTIO ARE HIGH. KUTI AND WEISSKOPF ACHIEVED A FIT TO THE DATA ASSUMING 3 'VALENCE' QUARKS, A SEA OF QUARK-ANTIQUARK PAI AND NEUTRAL GLUONS. PROVIDED THESE ADDED PARTICLES POSSESS ZERO STRANGENESS, ISOSPIN AN BARYON NUMBER. THEY WILL NOT AFFECT QUAR MESON AND BARYON PREDICTIONS. QUARKS AN ANTIQUARKS INTERACT BY EXCHANGING NEUTRAL GLUONS, WHICH SERVE T BIND QUARKS BUT AR INACTIVE IN LEPTON SCATTERING.

TABLE 3

	QUANTITY	PREDICTION	OBSERVATION	COMMENT
	$R = \frac{\sigma(\bar{\nu})}{\sigma(\nu)}$	SPIN ½ : $R = \frac{1}{3}$ SPIN 0, 1, 3/2 : $R \sim 1$	$R = 0.38 \pm 0.02$	
	$\frac{d^2\sigma}{dx\,dy} = \frac{G^2 M E_\nu}{\pi} F(x,y)$	SCALING AND PARTON MODEL PREDICT: $\sigma \propto E_\nu$	TRUE OVER A WIDE ENERGY RANGE - 1-200 GeV. HARD TO RULE OUT SCALING AT HIGH ENERGY END OF SCALE WHERE STATISTICS BECOME A PROBLEM	
	$\frac{3}{2}\frac{\pi}{G^2 M E}\int\left(\frac{d\sigma^{\nu N}}{dx} - \frac{d\sigma^{\bar{\nu}N}}{dx}\right)\frac{dx}{x}$	$= \int(n + p - \bar{n} - \bar{p})\,dx$ $= N_q - N_{\bar{q}}$ = NET NUMBER OF NUCLEAR QUARKS = 3 IN QUARK MODEL	3.2 ± 0.35	IMPORTANT EVIDENCE SUGGESTING THAT PARTONS BE IDENTIFIED WITH QUARKS

TABLE 4

QUANTITY	PREDICTION	OBSERVATION	COMMENT
FRACTION OF PROTON MOMENTUM HELD BY		$\bar{\sigma}(\nu) = 0.50 \pm 0.05$ $\sigma(\bar{\nu}) = 0.19 \pm 0.02$	VALENCE QUARKS CARRY 50% OF THE NUCLEON MOMENTUM, THE STRANGE QUARKS CARRY VERY LITTLE AND 50% OF THE MOMENTUM IS UNACCOUNTED FOR. THIS REMAINING FRACTION TO THE NEUTRAL NUCLEON CONSTITUENTS - THE GLUON
a) $U+d$ QUARKS	$= \frac{3}{8}(3\bar{\sigma}(\nu) - \bar{\sigma}(\bar{\nu}))$	$= 0.49 \pm 0.06$	
b) $\bar{U}+\bar{d}$ QUARKS	$= \frac{3}{8}(3\bar{\sigma}(\bar{\nu}) - \bar{\sigma}(\nu))$	$= 0.02 \pm 0.03$	
c) $S+\bar{S}$ QUARKS	$= \frac{9}{2}\left[\int (F_2^{ep} + F_2^{en})\,dx - \frac{5}{12}(\sigma(\nu) - \sigma(\bar{\nu}))\right]$	$= \frac{9}{2}(0.01 \pm 0.04)$	
AVERAGE CHARGE SQUARED OF THE NUCLEAR CONSTITUENTS.	$\frac{1}{2}(\sigma(\nu,p) + \sigma(\nu,n) + \sigma(\bar{\nu},p) + \sigma(\bar{\nu},n)) = \frac{4GME}{3\pi} J_V$ $J_V = \int_0^1 x(u+d+\bar{u}+\bar{d})\,dx$ $J_L = \frac{1}{2}\int_0^1 (F_2^{ep}(x) + F_2^{en}(x))\,dx$ $= \frac{5}{18} J_V + \int_0^1 x(\frac{4}{9}(s+\bar{s}) + \frac{4}{9}(c+\bar{c}))\,dx$ $\langle Q^2 \rangle = \frac{J_L}{J_V} \geq \frac{5}{18}$ IGNORING S AND C CONTRIBUTIONS $\langle Q^2 \rangle = .278$	$\frac{J_L}{J_V} = 0.29 \pm 0.03$	

TABLE 5

QUANTITY	PREDICTION	OBSERVATION	COMMENT
RELATION BETWEEN $F_2^{\nu N}(x)$ AND $F_2^{eN}(x)$	$F_2^{\nu N} \cong 3.6\, F_2^{eN}(x)$	VERY GOOD AGREEMENT BETWEEN THE FUCTIONS IN SHAPE AND NORMALIZATION.	THE NUMBER 3.6 IS PROVIDED BOTH BY CVC ARGUMENTS AND THE QPM. THIS RELATION PROVIDES A CONSISTENCY CHECK THAT SHOWS THAT CHARGED LEPTON AND NEUTRINO EXPERIMENTS SEE THE SAME STRUCTURE.

TABLE 6

INTEGRATED INTENSITIES IN FINAL DATA SAMPLE

	SEM	NON	PULSES
E288			
600A	512K	67.0M	12.1K
800A	2.48M	375M	23.9K
960A	917K	148M	6.48K
1100A	12.1M	2239M	65.1K
1300A	13.7M	2424M	53.9K
E494			
960A	22.5M	2601M	114K
1300A	18.7M	2216M	76.3K

TABLE I

Mass Range (GeV)	Analyzing Magnet Current (Amps)	Running Modes ~# incident protons per 1 sec pulse	C_1 Gas (n - 1)	C_2 Gas (n - 1)	Momentum Bands for Particle Identification (GeV/c) π min	π max	K min	K max	p min	p max
4.0 - 5.5	980	3×10^8	He (3.95×10^{-5})	N_2 (2.65×10^{-4})	19	59	23	41	23	41
5.0 - 6.5	980	5×10^9	He "	N_2-Ne (1.76×10^{-4})	19	59	29	50	29	50
6.0 - 10.5	980, 1300	3×10^{10}	He "	N_2-Ne (1.3×10^{-4})	23	59	36	58	36	58

Table 2

TABLE 8.

SEM CALIBRATION DATA

NUMBER OF PROTONS = (SEM COUNTS) × C × 10^8

DATE	C	ENERGY (GeV)
1/26/74	1.04	300
4/30/74	1.07	300
6/25/74	1.08	300
4/17/75	.985	300
4/18/75	.943	300
9/16/75	1.00	400
4/27/76	1.03	400
6/6/76	.997	400
12/6/76	1.01	400

$\sigma(Cu \rightarrow {}^{24}Na) = 3.5$ mb

SPILL STRUCTURE CALIBRATION DEPENDENCE

	C
100 GeV (SLOW SPILL)	1.17
400 GeV (FAST SPILL)	1.30
400 GeV (SLOW SPILL	1.05

NOTE: These DATA ARE NOT TAKEN WITH THIS EXPERIMENT'S SEM.

STATISTICAL ERRORS ~ 1%

SYSTEMATIC ERRORS ~ 5%

TABLE 9

NUMBER OF [illegible] DILEPTON EVENTS CUT BY SCALER, TOF AND RAPIDITY CUTS

MAGNET CURRENT	TOTAL # OF EVENTS	FAIL SCALER	FAIL TOF	FAIL RAPIDITY
600 A	326	50	1	13
800 A	754	21	10	9
960 A	107	1	1	1
1100 A	757	32	2	5
1300 A	184	22	1	1

INTEGRATED NDN VALUES FOR VARIOUS FOIL STATES (E288)

1) NO FOIL IN EITHER ARM
2) 15 MIL Cu × 15 MIL Cu
3) 30 MIL Cu × 30 MIL Cu
4) 45 MIL Cu × 45 MIL Cu
5) 2" LEAD × 2" LEAD

MAGNET	1	2	3	4	5
600A	76.7M	368K	403K	3.32M	88.9K
800A	381M	827K	802K	34.7M	142K
960A	150M	—	—	—	—
1100A	2.29B	5.88M	5.73M	295M	482K
1300A	2.56B	19.3M	47.6M	272M	273M

TABLE 10

E 288 J/ψ MASS VALUES USING

A) E288 MAGNET CALIBRATION

B) E494 MAGNET CALIBRATION

MAGNET CURRENT	A		B	
	MASS (Gev)	S.D. (Gev)	MASS (Gev)	S.D. (Gev)
600	3.091	.043	3.075	.043
800	3.105	.035	3.086	.034
960	3.107	.037	3.090	.033
1100	3.121	.030	3.095	.028

COUNTER PLANE	STATION	COUNTER NUMBERS *	WIDTH PER COUNTER	NUMBER OF COUNTERS	SCINTIL. THICKNESS	LENGTH	SCINTIL. DIRECTION
V1	1	1-16 17-34 35-38	.75 1.4 2.0	16 18 4	.125 .25 .25	16.0 16.0 16.0	V
TØ	1	1 2-4 5	2.0 4.0 2.0	1 3 1	.25 .25 .25	48.0 48.0 48.0	H
T1	2	1-8	6.0	8	.25	30.0	H
V2	3	1-24 25-48 49-55	.85 1.4 2.0	24 24 7	.25 .25 .25	33.0 33.0 33.0	V
S2	3	1-12	5.75	12	.25	33.0	V
T2	3	1-13	5.5	13	.25	33.0	V

TABLE II

* COUNTING CONVENTION : COUNTERS CLOSEST TO 50 MR HAVE THE LOWEST COUNTER NUMBERS. VERTICAL COUNTING STARTS AT COUNTER CLOSEST TO NEUTRAL BEAM.

600 MP

TABLE 12

INTENSITY REGION	(1)	(2)	(3)	(4)	(5)	(6)	(7)	(8)
CCI data Sample Totals:								
Pulses	1721	2600	4500	3252	720	126	24	105
% NOGY	2	13	36	36	9	2	.3	2
Typical per pulse rates								
SCM	27	34	46	47	55	66	66	900
NDN	1226	3533	5664	7862	9967	11.3K	11.7K	20.7K
TU	152K	354K	615K	840K	1.08M	1.13M	1.11M	1.13M
TUD	3214	10.0K	19.5K	30.7K	46.0K	62.0K	76.0K	93.0K
TUDX	1497	6020	12.6K	21.8K	33.0K	41.7K	49.0K	70.0K
TGO	12	30	50	65	91	117	132	181
Track finding information								
ERT/EIZ								
ALL	.79	.79	.81	.86	.80	.75	.52	.71
CLEAN MPNC	.59	.55	.86	.91	.89	.86	.90	.93
00	.04	.06	.08	.03	.05	.07	.05	.08
01	.14	.12	.09	.09	.12	.15	.14	.17
11	.34	.39	.41	.41	.34	.30	.35	.20
12	.12	.14	.14	.17	.14	.12	.12	.05
MM	.36	.30	.27	.30	.34	.36	.34	.46

600 MP.

800

INTENSITY REGION	(1)	(2)	(3)	(4)	(5)	(6)	(7)	(8)
CCI data Sample Total:								
Pulses	1856	3187	9880	6159	948	334	220	222
% NOGY	2	10	43	33	6	2	2	2
Typical per pulse rates								
SCM	54	81	98	122	147	179	214	242
NON	5389	11.9K	16.6K	20.9K	25.7K	31.0K	38.8K	46.2K
TU	364K	687K	933K	1.23M	1.57M	1.88M	2.32M	2.72M
TUD	5548	18.7K	32.7K	47.2K	63.0K	87.2K	125K	173K
TUDX	4115	14.1K	25.2K	37.9K	52.6K	74.5K	[illegible]	[illegible]
TGO	16	37	58	78	110	139	[illegible]	[illegible]
Track finding information								
EIRT/EIR								
ALL	.61	.83	.86	.83	.77	.76	.75	.75
CLEAN MPNC	.75	.89	.89	.89	.87	.86	.87	.86
00	.23	.05	.02	.04	.05	.04	.04	.07
01	.12	.13	.16	.17	.19	.20	.21	.23
11	.37	.52	.53	.46	.31	.26	.17	.19
12	.13	.13	.14	.14	.14	.12	.14	.10
MM	.15	.16	.15	.19	.30	.38	.45	.40

TABLE 13

800 AMP

960 AMP A

Table 14

INTENSITY REGION	(1)	(2)	(3)	(4)	(5)	(6)	(7)	(8)
CCI data Sample Table:								
Pulses	459	1356	2288	1899	393	139	146	65
% NOGY	1	14	34	34	8	3	4	2
Typical per pulse rates								
SCM	58	106	132	160	191	227	252	351
NON	5.9K	16.1K	23.4K	29.6K	35.9K	41.5K	43.1K	52.9K
TU	215K	517K	875K	1.15M	1.35M	1.53M	1.52M	1.52M
TUD	3.8K	14.7K	26K	34.4K	30.5K	80.9K	[illegible]	[illegible]
TUDX	2.4K	11.0K	20.6K	31.1K	[illegible]	59.0K	[illegible]	[illegible]
TGO	4	10	15	[illegible]	31	[illegible]	[illegible]	[illegible]
Track finding information								
ERT/EIR								
ALL	.82	.85	.86	.86	.86	.83	.86	.75
CLEAN MPNC	.96	.88	.89	.90	.89	.71	.84	.83
00	.04	.03	.02	.01	.01	—	.08	—
01	.17	.20	.18	.19	.21	.21	.13	.21
11	.65	.63	.64	.61	.56	.52	.56	.47
12	.13	.08	.10	.11	.12	.13	.15	.11
MM	—	.07	.07	.07	.11	.14	.15	.13

INTENSITY REGION	(1)	(2)	(3)	(4)	(5)	(6)	(7)	(8)
CCI data Sample Totals:								
Pulses	3765	10243	25482	20679	4842	1447	647	772
% NOBY	1	10	35	36	10	3	2	3
Typical pr pulse rates								
SCM	70	133	173	206	246	298	341	809
NON	8295	23.0K	35.0K	44.3K	52.8K	61.0K	675K	944K
TU	242K	660K	1.02M	1.31M	1.58M	1.82M	2.00M	2.47M
TUD	4123	17.4K	35.7K	58.2K	78.3K	102K	132K	251K
TUDX	2800	12.8K	26.3K	41.9K	62.3K	80.2K	102K	175K
TGO	3	10	18	23	31	38	44	440
Track finding information								
ERT/E12								
ALL	.86	.84	.83	.81	.77	.74	.71	.60
CLEAN MPNC	.89	.88	.86	.85	.83	.85	.82	.75
00	.04	.03	.04	.05	.08	.08	.08	.17
01	.24	.21	.22	.25	.26	.26	.26	.31
11	.55	.60	.55	.51	.47	.46	.47	.31
12	.09	.10	.10	.10	.09	.10	.12	.17
MM	.08	.07	.08	.09	.09	.09	.07	.16

TABLE 15

1100 AMP

1300 AMP.

TABLE 16

INTENSITY REGION	(1)	(2)	(3)	(4)	(5)	(6)	(7)	(8)
CCI data Sample Totals:								
Pulses	3558	12946	20658	10307	2999	864	292	55
% NOBY	.2	14	38	28	10	3	1	4
Typical per pulse rates								
SCM	69	195	228	312	391	468	534	1455
NON	3119	26K	14.7K	74K	100K	125K	144K	254K
TU	94K	586K	1.06M	1.69M	2.31M	2.84M	3.08M	4.81M
TUD	1061	14.5K	45.6K	118K	190K	276K	36[illegible]K	5[illegible]K
TUDX	739	11.4K	37.6K	95.7K	161K	240K	315K	[illegible]K
TGO	1	12	15	23	30	38	45	24
Track finding information								
EKT/EIR								
ALL	.61	.78	.68	.59	.61	.61	.54	.54
CLEAN MPNC	.80	.88	.82	.75	.78	.77	.73	.74
00	.25	.08	.15	.23	.18	.16	.19	.22
01	—	.17	.22	.24	.28	.30	.34	.34
11	.42	.21	.22	.16	.13	.10	.10	.06
12	.17	.16	.12	.10	.10	.11	.09	.07
MM	.17	.38	.29	.27	.30	.33	.28	31

TABLE 17

Trigger Counter Efficiencies

	Up	Down
T_0	98.2±1.1	99.8±0.8
T_1	96.3±0.6	97.1±0.5
S_2	98.9±0.3	99.6±0.2
T	93.7±0.7	96.5±0.6
T_2	99.8±0.7	99.7±0.6

NOTE

The T_0 efficiencies are in fact an upper limit as the T_1 bit efficiency cannot be taken out.

V_1 and V_2 Efficiencies

	Up	Down
V_1	97.5±0.2	97.3±0.2
V_2	98.4±0.1	98.7±0.1

Table 12

CHAMBER	STATION	ACTIVE AREA H	ACTIVE AREA V	WS	NUM. WIRES	WIRE DIRECTION	SIGNAL WIRE DIAMETER	NUM. AMP. CARDS.	STRIPLINE CABLES
1Y	1	48	15.441	.08042	192	H	.0008	24	6
1P(Q)	1	48	15.874	.07980	272	7.125° WRT H	.0008	34	8.5
2Y	2	70	22.675	.11810	192	H	.0012	24	6
3Y	3	70	33.067	.11810	280	H	.0012	35	9
3P(Q)	3	70	32.820	.11719	352	7.125° WRT H	.0012	44	11

TABLE 19

PROPORTIONAL WIRE CHAMBER X AND Y RESOLUTION

FOR A RECTANGULAR DISTRIBUTION 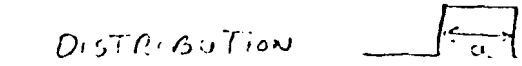

$$S.D. = a/\sqrt{12}$$

a = WIRE SPACING (WS)

Y CHAMBER	S.D. (η) = .289 * (WS)
P, Q CHAMBERS (IN COMBINATION)	$u = Y\cos\theta + X\sin\theta$ $v = Y\cos\theta - X\sin\theta$ $\theta = 7.125°$ $x = (u-v)/2\sin\theta$ $y = (u+v)/2\cos\theta$ S.D. (η) = S.D. (u) / $\sqrt{2}\sin(\theta)$ S.D. (η) = S.D. (u) / $\sqrt{2}\cos(\theta)$ S.D. (u) = (WS) / $\sqrt{12}$ S.D. (η) = 1.65 * (WS) S.D. (η) = .206 * (WS)

1) CHAMBER SURVEYED POSITIONS FLUCTUATED BY 10 - 20 MILS.

2) OFF-LINE POSITION CHECK OF CHAMBERS COULD DETECT .005" MISALIGNMENTS OF 1,2,3 Y AND .02 MISALIGNMENT IN X.

3) SURVEY AND OFF LINE CHECK AGREED WITHIN .015".

TABLE OF RESOLUTION VALUES

	WIRE SPACING	SURVEY	COMBINED
STATION 1			
x	.132	.1	
y	.013	.015	
STATION 3			
x	.193	.1	
y	.020	.015	

TABLE 20

TRIGGER INFORMATION

$T\emptyset(1) \cdot T1(1,5) \cdot S2$

$T\emptyset(2) \cdot T1(1,2,5,6) \cdot S2$

$T\emptyset(3) \cdot T1(2,3,6,7) \cdot S2$

$T\emptyset(4) \cdot T1(3,4,7,8) \cdot S2$

$T\emptyset(5) \cdot T1(4,8) \cdot S2$

— T TRIGGER

$(E_U \cdot \varepsilon_U) \cdot (E_D \cdot \varepsilon_D)$ MAIN TRIGGER

$T2(HIGH)_{UD} \cdot T1_{UD}$ MONITOR OF MAIN TRIGGER EFFICIENCY

$E_U(PS) \cdot \varepsilon_U$

$E_D(PS) \cdot \varepsilon_D$

— SAMPLED SINGLE ARM DATA. NORMALLY THE PRESCALERS WERE SET at 1-2K.

TFI	SLOW LOGIC
E_{UD}	$(E_U \cdot \varepsilon_U) \cdot (E_D \cdot \varepsilon_D)$
$E_U(PS)$	$E_U(PS) \cdot \varepsilon_U$
$E_D(PS)$	$E_D(PS) \cdot \varepsilon_D$
F_{UD}	$F_{UD} \cdot \varepsilon_U \cdot \varepsilon_D$

$F_{UD} = T2(HIGH)_{UD} \cdot T1_{UD}$

TABLE 21

DATA COMPRESSION CUTS

FIRST LEVEL:

CUTS WERE MADE ON THE PARTICLE'S LEAD GLASS SHOWER DEPOSIT IN THE FIRST (E1) AND FIRST + SECOND (E12) LAYERS OF LEAD GLASS. BOTH ARMS WERE REQUIRED TO EXCEED THE LOWER ENERGY AND AT LEAST ONE ARM HAD TO EXCEED THE HIGH:

	600	800	960	1100	1300
E1	4.5, 7.8	5.0 8.4	5.5, 9.6	6.0, 10.2	6.5, 10.8
E12	9.0, 13.0	10.0 14.0	11.0, 16.0	12.0 17.0	13.0, 18.0

SECOND LEVEL:

THX ≡ PAIR OPENING ANGLE AS MEASURED BY LEAD GLASS SHOWER DEVELOPMENT

REQUIREMENTS

a) $\sqrt{E_U E_D} \times THX > M\phi$

$M\phi$ = 2.0 (600A), 2.4 (800A), 2.5 (960A), 2.7 (1100A), 2.8 (1300A)

b) $\sqrt{E1_U E1_D} \times THX > 0.42\ M\phi$

c) $\sqrt{E12_U E12_D} \times THX > 0.78\ M\phi$

d) $\frac{E1_U\ (\text{ENERGY CLUSTER})}{E1_U} \times \frac{E1_D\ (EC)}{E1_D} > 0.3$

e) $\frac{E_U(EC)}{E_U} \times \frac{E_D(EC)}{E_D} > 0.3$

DATA CUTS

TABLE 22

	STANDARD	MEDIUM	TIGHT
LEAD GLASS LONGITUDINAL SHOWER DEVELOPMENT	$E1/E \geq 0.52 - .0046P$ $E12/E \geq 0.92 - .0024P$ $E4/E \leq 0.03 + .0002P$ (83% EFF.)	$0.59 - .005P$ $0.947 - .0022P$ $0.01 + .0001P$ (73% EFF.)	$0.622 - .0047P$ $0.961 - .0019P$ $.0075 + .0018P$ (62% EFF.)
E/P	$0.9 \leq E/P \leq 1.12$	$0.93 \leq E/P < 1.07$	$0.95 \leq E/P \leq 1.05$
TOF	EVENT MUST HAVE TOF CORRESPONDING TO CORRECT RF BUCKET	—	—
SCALERS	$A \leq$ AVG + 6.5 S.D.	$A \leq$ AVG + 3.75 S.D.	$A \leq$ AVG + 1.0 S.D.

TABLE 23

FIDUCIALS

CUTS WERE MADE ON:

1	X, Y	AT THE LEAD GLASS (PARTICLE TRACK MUST BE 2.5" FROM LEAD GLASS EDGE AT SHOWER MAXIMUM)
2	Y	AT CHAMBER Y1
3	X, Y	AT MAGNET EXIT
4	X	AT 2 FOOT PRECISION COLLIMATOR
5	Y	AT 2 INCH PRECISION COLLIMATOR
6, 7	THX, THY	PARTICLE PRODUCTION ANGLES
8	X	AT TARGET
9	P	PARTICLE MINIMUM MOMENTUM

THE PERCENTAGE OF TRACKS PASSING THESE CUTS A GIVEN BELOW FOR EVENTS PASSING THE 2ND LEVEL OF DATA COMPRESSION:

	600	800	960	1100	1300
1	.91	.87	.87	.83	.77
2	.99	.99	.98	.98	.97
3	.64	.65	.80	.76	.47
4	.93	.94	.95	.94	.88
5	.81	.75	.82	.78	.61
6	.995	.997	.999	.999	.994
7	.82	.75	.83	.79	.61
8	.66	.71	.82	.78	.56
9	.87	.85	.97	.95	.76
OVERALL	.54	.55	.67	.60	.34

TABLE 24

TERMS FOR DESCRIBING TRACK RECONSTRUCTION EFFICIENCY STUDY

RECONSTRUCTION TYPE

RØ SIMPLE RECONSTRUCTION (HITS IN 2 OF 3 'Y' CHAMBERS WERE USED TO DEFINE A TRACK)

R STANDARD TRACK RECONSTRUCTION

TRACK CATAGORIES

XX EVENT WITH NO 'R' TRACKS FOUND ON EITHER ARM

XT EVENT WITH ONE 'R' TRACK FOUND ON AN ARM

TT EVENT WITH 'R' TRACKS FOUND ON BOTH ARMS

MOMENTUM AND MASS CATAGORIES

PØ RØ CALCULATED MOMENTUM

P R CALCULATED MOMENTUM

MEE = $\sqrt{E_U E_D}$ THX (MASS CALCULATED USING LEAD GLASS ENERGY DEPOSITS ON BOTH ARMS AND LEAD GLASS ESTIMATE OF OPENING ANGLE)

MPØ PØ = $\sqrt{P_{\emptyset_U} P_{\emptyset_D}}$ THX

MPP = MASS CALCULATED BY STANDARD RECONSTRUCT ROUTINE

MEP = $\sqrt{E \cdot P}$ (THX)

CUT CATAGORIES

CØ CUTS BASED ON RØ RECONSTRUCTION
a) $|Y_\emptyset$ (MIDDLE OF MAGNET)$| < 2.5$"
b) $0.9 < E/P_\emptyset < 1.12$
c) STANDARD LONGITUDINAL SHOWER CUTS

C SAME CUTS AS CØ USING STANDARD RECONSTRUCTION

Event Track Multiplicity for 400 GeV Data

	m(GeV)	Number Events	Extra Tracks	Extra Electrons
600A	all	193	5	5
	ψ	92	3	3
	>5	2	0	0
800A	all	440	1	1
	ψ	253	0	0
	>5	1	0	0
960A	all	79	1	0
	ψ	47	1	0
	>5	1	0	0
1100A	all	345	2	2
	ψ	184	2	2
	>5	18	0	0
1300A	all	65	1	1
	ψ	15	0	0
	>5	16	0	0

NOTE

Multiple tracks which are identical to 100 MeV momentum and 1 mrad. opening angle are considered one track.

TABLE 26

Table XV

Material in Secondary Beam

	Material	Comment	Length	RL	%RL	z(in.)
1	Be	Tgt 4x.0088x1"	.154	35.3	.436	.154
2	He+.01Air	Target box	585.3	444×10^3	.1318	585.5
3	Kapton	5mil window	.0127	28.7	.04425	585.5
4	Air	Between tgt box and filter	71.10	30050	.2366	656.6
5		Filter				
6	Air	Bet filter/pile	17.46	30050	.0581	674.1
7	Mylar	Pile window	.0254	28.70	.0885	674.2
8	Airx3/760	Vac in shield	295.9	761×10^4	.0039	970.1
9	Airx3/760	Magnet vac	353.1	761×10^4	.0046	1323
10	Mylar	Mag window	.0254	28.7	.0885	1323
11	Polyeth	He Bag face	.0127	48.0	.0265	1323
12	He	He in bag	1057	477×10^3	.2215	2380
13	Polyeth	He bag face	.0127	48.0	.0265	2380
14	Air	Air gap to station 1	41.91	30050	.1395	2422
15	Al	Al screen	.00678	8.9	.0762	2422
16	Aclar	PWC windows	.00635	38	.0167	2422
17	Cu	HV planes	.00031	1.43	.0218	2422
18	W	Signal plane	.000016	.35	.00457	2422
19		Hodo light tight mat.	.0127	38	.0334	2422
20	Al	Al foil for	.00254	8.9	.0285	2422

		hodo wrapping				
21	Scint	V1 1/8 and 1/4"	.420	42.9	.979	2422
22		T0 light	.0127	38.0	.0334	2422
		tighting				
23	Al	Al for T0	.00254	8.9	.0285	2422
24	Scint	T0 1/4"	.635	42.9	1.480	2423
25	Air	Sta.1 to T0	41.91	30050	.1395	2465
26	Air	T0 to Y2	508.0	30050	1.691	2973
27		see 1Y,P,Q				
28	Air	Y2 to T1	60.96	30050	.2029	3034
29		see T0				
30	Air	T1 to Sta. 3	495.3	30050	1.648	3530

TABLE 27

Average Dielectron E/p Versus Beam Quality

x=NDN or INDUTY×NDN (I×N)

$\bar{x}$=median value of x for 400 GeV data

Regions: 1) $x<\bar{x}$

2) $\bar{x}<x<\bar{x}+\sigma$

3) $\bar{x}+\sigma<x<\bar{x}+2\sigma$

4) $\bar{x}+2\sigma<x$

E/p Averages (400 GeV)

Current:		600A	800A	960A	1100A	1300A
Low NDN	1	.992	.995	.990	.999	.994
	2	.994	.994	.996	1.000	1.0000
	3	.992	.994	.992	.999	1.004
	4	.998	.995	1.000	.994	1.004
Low I×N	1	.996	.994	.994	.999	.994
	2	.990	.995	.996	1.000	1.000
	3	.990	.994	.994	.997	1.008
	4	.994	.995	.994	.996	1.006

Table of Median Values (400 GeV)

	NDN	σ	INDUTY	σ	$N\times I\times 10^{-4}$	σ
600A	7150	2400	1.87	.30	1.5	.64
800A	21000	6400	1.80	.30	3.5	1.6
960A	29000	8600	1.8	.33	5.7	2.0
1100A	42300	13000	1.80	.31	7.2	3.7
1300A	66000	29000	1.80	.38	14.3	8.3

Incident protons=$5.6\times 10^{5}\times$NDN

LEAD GLASS CALIBRATION CHECK WITH J/ψ

		E/p AVERAGE	STANDARD DEVIATION	NUMBER OF EVENTS	MASS	STANDARD DEVIATION	NUMBER OF EVENTS
600 AMP.	1	1.001	.038	170	3.067	.102	168
	2	1.000	.035				
800 AMP.	1	.994	.037	528	3.052	.118	516
	2	.994	.040				
960 AMP.	1	.996	.040	58	3.070	.118	56
	2	.997	.031				
1100 AMP.	1	1.000	.035	406	3.100	.113	400
	2	.996	.034				

1 AND 2 ARE INDICES FOR RESPECTIVE SPECTROMETER ARMS

TABLE 28

LEAD GLASS ENERGY RESOLUTION				
	16 GeV	20 GeV	30 GeV	40 GeV
FORMULA	.0400	.0374	.0333	.0308
PREDICTED	.047	.045	.041	.039
ACTUAL	.063	.055	.045	.040

(FWHM)

TABLE 29

TABLE 30

Accidental Normalization and Rate Constants

400 GeV	e_U/NDNBY	e_D/NDNBY	E_{UD}
600A	.0584±.008	.0555±.0101	60.1
800A	.0206±.0075	.0196±.0074	111.5
1100A	.00634±.00152	.00648±.00254	162.2
1300A	.00104±.00035	.00133±.00038	10.0
300 GeV			
600A	.0886±.0120	.0743±.0043	122.9
800A	.0202±.0035	.0257±.0059	94.0
1100A	.00395±.00127	.00553±.00131	67.7

Table XI

Accidental Background Under ψ/ψ'

400 GeV

	Total Accid. Events	Expected Accidental Events	ψ	Expected Accidental ψ	ψ'	Expected ψ'
600A	1.76×10^{6}	60.1	3.22×10^{4}	1.1	4930	.17
800A	1.50×10^{6}	111.5	1.00×10^{5}	7.43	1.62×10^{4}	1.20
1100A	4.61×10^{5}	162.2	8.65×10^{4}	30.4	4.49×10^{4}	15.8

If we now normalize away from resonance region

	Acc.Evts $3.3<m<3.5$	Data Evts $3.3<m<3.5$	Expected Acc ψ	Expected Acc ψ'
600A	1.25×10^{4}	2	5	0.8
800A	4.16×10^{4}	6	14	2.3
1100A	7.34×10^{4}	15	18	9.2

VERTICAL ACCEPTANCE

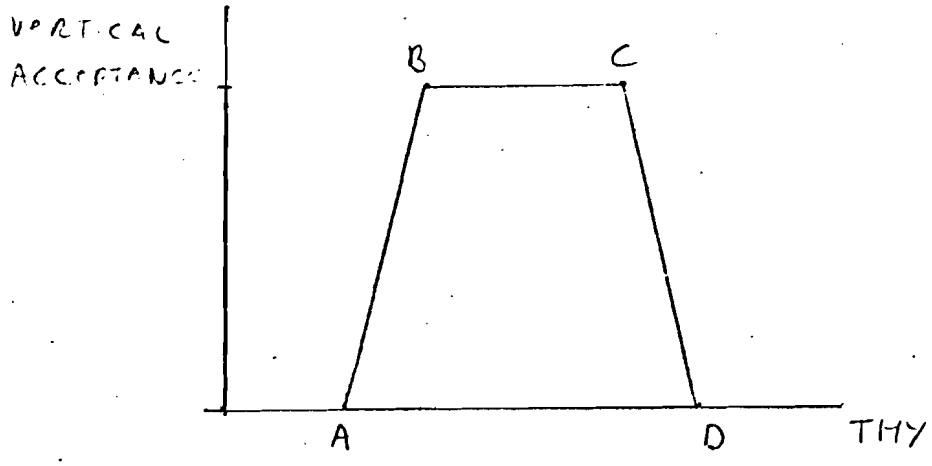

THY = PARTICLE VERTICAL PRODUCTION ANGLE

$$\text{MOMENTUM} = \frac{\text{MAGNET CURRENT (AMPS)}}{F}$$

TABLE OF F VALUES

APERATURE LIMITS DUE TO	A	B	C	D
Y1	55.47	39.38	18.32	2.232
LARGE LEAD GLASS BLOCKS	55.45	43.00	17.75	5.30
SHORT LEAD GLASS BLOCKS	50.81	38.36	17.75	5.30

TABLE 33

	H/h	E/P Lower Bound = 0.68	E/P Lower Bound = 0.66
$P = 35$ GeV	π^+	.24	.21
	π^-	.27	.23
	K^+	.29	.20
	K^-	.17	.13
	p	.09	.075
	$\bar{p}$	.08	.061
$35 < P < 40$ GeV	π^+	.27	.24
	π^-	.25	.22
	K^+	.17	.15
	K^-	.10	.078
	p	.02	.016
	$\bar{p}$	.03	.025
$P > 40$ GeV	π^+	.28	.24
	π^-	.29	.26
	K^+	.13	.12
	K^-	.13	.12
	p	—	—
	$\bar{p}$	.06	.05

TABLE 34

MATERIAL IN APERATURE BEFORE MAGNET BEND

Material	R.L. (cm)	d (cm)	$t = (d/R.L.) \times 100$
Target (50MR)	35.3	.2235	.6332
(95MR)		.1176	.3333
Target Box			
He	521000	585.3cm	.1123
He+.01 AIR	247700		.2363
He+.1 AIR	66262		.8833
AIR	30050		1.9478
He + .002 AIR (BY WEIGHT)	503575		.1162
KAPTON WINDOW	28.7	.0127	.04425
AIR GAP	30050	88.56cm	.2947
KAPTON WINDOW	28.7	.0254	.0885
SHIELDING PILE VACCUUM	7.61×10^6	295.9	.003887
1/2 MAGNET LENGTH	7.61×10^6	353.1	.004638

TABLE 35

BREMSSTRAHLUNG CORRECTION STUDY

EVENTS THROWN ACCORDING TO e^{-kM}

M = MASS , 8% of a R.L. assumed

$$\left(\begin{matrix}\text{Bremsstrahlung} \\ \text{Correction}\end{matrix}\right) = \frac{\text{Bremsstrahlled spectrum}}{\text{unbremsstrahled spectrum}} = e^{-2bt}$$

TABLE OF BREMSSTRAHLUNG CORRECTIONS

k	CASE 1	CASE 2	CASE 3	CASE 4	b
0.5	.83 ± .04	.83 ± .03	.83 ± .04	.84 ± .03	1.13
1.0	.77 ± .03	.77 ± .03	.77 ± .03	.77 ± .03	1.63
2.0	.69 ± .03	.68 ± .02	.69 ± .03	.68 ± .02	4.
4.0	—	.61 ± .02	.62 ± .02	.61 ± .02	6.05

For definition of cases, see page —.

TABLE 36

SPECTRUM LABEL	SPECTRUM EXPANDED IN TERMS OF CONSTITUENT PARTICLES
S1	$a_1[h(c):e(c)] = 2H:H + B[H:E] + G[H:N]$
S2	$a_1[h(0):e(0)] = 2H:H + [H:E] + [H:N]$
S3	$a_2^2\ h(0):h(0) = H:H$
S4	$S2 - S3 = H:H + [H:E] + [H:N]$
S5	$S1 - S3 = H:H + B[H:E] + G[H:N]$
S6	$e(0):e(0) = E:E + H:H + N:N + [E:H] + [E:N] + [N:H]$
S7	$e(c):e(c) = B^2E:E + H:H + G^2N:N + B[N:H] + BG[N:E] + B[H:E]$

$a_1 \sim .24$

$a_2 \sim .27$

$B \sim .86$

$G \sim 4.5$

TABLE 37 NUMERICAL DETAILS OF THE BACKGROUND CALCULATION

SPECTRUM LABEL	SPECTRUM	SPECTRUM SCALING FACTOR	CROSS SECTION M= 4.0 Gev	5.0 Gev	6.0 Gev
	[h(c):e(c)]	1.0	900	60	14
S1	"	.24	216	14.4	3.36
	[h(o):e(o)]	1.0	450	28	3
S2	"	.24	108	6.72	.72
	h(o):h(o)	1.0	560	37	3
S3	"	$(.27)^2$	40.8	2.7	.22
S4	S2 - S3	1.0	67.2	4.02	0,5
S5	S1 - S3	1.0	175.2	11.7	3.14
S6	e(o):e(o)	1.0	120	19	6
S7	e(c):e(c)	1.0	375	25	6.5
	BACKGROUND UPPER LIMIT	1.0	119.4	4.35	0.5

$$\text{BACKGROUND} \leq \frac{(S7 - S5) - B^2(S6 - S3)}{B(G-B)} + S4$$

WHERE FOR NUMERICAL CALCULATIONS, THE FOLLOWING VALUES HAVE BEEN EMPLOYED:

$$B^2 = (.86)^2$$

$$B(G-B) = 3$$

MASS ENHANCEMENT REGION (GeV)	MEASURED MASS (GeV)	MEASURED WIDTH (σ) (GeV)	CROSS SECTION (PB)	ENHANCEMENT SIGNIFICANCE	CLUSTER PROBABILITY WITHIN 4×σ(RESOL)	CLUSTER PROBABILITY WITHIN 5×σ(RES
3.583 - 3.781	3.681 ± .006	.030 ± .005	98.5 ± 14.0	15σ	—	—
4.097 - 4.292	4.22 ± .07	.068 ± .041	13.0 ± 15.0	3.4σ	15.3% (20EV/2BINS)	11.4% (2GEV/3B
4.750 - 5.150	4.94 ± .02	.042 ± .014	3.7 ± 1.6	3.9σ	12.0% (16/3)	15.2% (18/4)
5.611 - 6.373	6.01 ± .07	.107 ± .06	2.7 ± 1.2	3.9σ	2.9% (10/4)	2.3% (12/5)
9.064 - 9.844	—	—	—	—	0.1% (6/8)	0.3% (6/9)

TABLE 38

TABLE 39

ENHANCEMENT REGION	MASS CLUSTER CENTER (GEV)	# EVENTS / # 50 MEV BINS	CLUSTER PROBABILITY
4.2			
E288	4.20	15/3	9.4%
E494	4.21	9/2	18.8%
COMBINED	4.22	20/2	15.3%
4.9			
E288	4.97	5/4	55.5%
E494	4.89	8/2	1.6%
COMBINED	4.94	16/3	12.0%
6.0			
E288	5.96	9/5	.04%
E494	6.14	4/3	2.8%
COMBINED	6.01	10/4	2.9%
9.4			
E288	9.57	1/9	21.3%
E494	9.48	4/5	.03%
COMBINED	—	6/8	.14%

DEEP INELASTIC SCATTERING: CHARGED LEPTONS (67)

$$e(k) + N \rightarrow e(k') + X$$

Proceeding as before:

$$\frac{d^2\sigma}{dE' d\Omega} = \left(\frac{d\sigma}{d\Omega}\right)_{MOTT} \left(W_2(q^2, \nu) + 2 W_1(q^2, \nu) \tan^2 \tfrac{1}{2}\theta \right)$$

$$\left(\frac{d\sigma}{d\Omega}\right)_{MOTT} = \frac{\alpha^2 \cos^2 \frac{1}{2}\theta}{4E^2 \sin^4 \frac{1}{2}\theta}$$

where

$$\nu \equiv \frac{P \cdot q}{M} = E - E'$$

$$q \equiv k - k'$$

$$Q^2 = -q^2 = 4EE' \sin^2 \tfrac{1}{2}\theta$$

$$S = W^2 = 2M\nu + M^2 - q^2$$

= invariant mass of hadrons in final state

This cross section can be related to the probability of inducing a transition by transverse (T) or longitudinal (L) photons:

$$W_1(q^2, \nu) = \frac{W^2 - M^2}{2M} \frac{\sigma_T(q^2, \nu)}{4\pi\alpha}$$

$$W_2(q^2, \nu) = \frac{-q^2}{\nu^2 - q^2} \frac{W^2 - M^2}{2M} \left(\frac{\sigma_T(q^2, \nu) + \sigma_L(q^2, \nu)}{4\pi^2 \alpha} \right)$$

One can write:

$$W_1(q^2, \nu) = G_1\left(x, \frac{q^2}{M^2}\right)$$

$$\frac{\nu}{M} W_2(q^2, \nu) = G_2\left(x, \frac{q^2}{M^2}\right)$$

$$x \equiv Q^2/2M\nu$$

$$y \equiv \frac{\nu}{E}$$

Bjorken scaling: in the limit, ν, q^2 large, x constant

$$G_1\left(x, \frac{q^2}{M^2}\right) \rightarrow F_1(x)$$

$$G_2\left(x, \frac{q^2}{M^2}\right) \rightarrow F_2(x)$$

$$\frac{d^2\sigma}{dx\,dy} = \frac{8\pi^2\alpha^2}{q^4} \frac{ME}{\pi} \left(2xy F_1(x) + (1-y) F_2(x) \right)$$

APPENDIX 2

DEEP INELASTIC SCATTERING: NEUTRINOS (68)

$$\nu(\bar{\nu}) + N \rightarrow \mu^-(\mu^+) + X$$

Referring to figure:

$$\frac{d^2\sigma^{\nu\bar{\nu}}}{dQ^2 d\nu} = \frac{G^2}{2\pi M}\frac{E_M}{E}\left(\cos^2\frac{\theta}{2}\, W_2^{\nu\bar{\nu}} + 2\sin^2\frac{\theta}{2}\, W_1^{\nu,\bar{\nu}} \mp \frac{E+E_M}{M}\sin^2\frac{\theta}{2}\right.$$

$$W_1(q^2,\nu) = G_1\left(x, \frac{q^2}{M^2}\right)$$

$$\frac{\nu}{M} W_2(q^2,\nu) = G_2\left(x, \frac{q^2}{M^2}\right)$$

$$\frac{\nu}{M} W_3(q^2,\nu) = G_3\left(x, \frac{q^2}{M^2}\right)$$

In the Bjorken limit (Appendix):

$$G_i\left(x, \frac{q^2}{M^2}\right) \rightarrow F_i(x)$$

and

$$\frac{d\sigma^{\nu\bar{\nu}}}{dx\,dy} = \frac{G^2 M E}{\pi}\left((1-y)F_2^{\nu\bar{\nu}}(x) + \frac{1}{2}y^2(2xF_1^{\nu\bar{\nu}}(x)) \mp \right.$$

$$\left. y\left(1-\frac{1}{2}y\right)(xF_3^{\nu\bar{\nu}}(x))\right)$$

MAGNETS

RESISTANCE = .105Ω / COIL
MAGNET CENTER LINE AT 443" FROM TARGET
MAGNETIC FIELD AT 1430 AMP BIAS 11.7 KG.
FRACTION OF FIELD UPSTREAM OF CENTER LINE = 0.53
FRACTION OF FIELD DOWNSTREAM OF CENTER LINE = 0.47

COORDINATES

$x = 0$ AT 72.5MR HORIZONTAL ANGLE
$y = 0$ AT INCIDENT BEAM HEIGHT
$+y$ IN DIRECTION OF MAGNET BEND
$+x$ TOWARDS INCREASING OPENING ANGLE
z IN DIRECTION OF BEAM

FIELD SHAPE

$$B_\theta(z) = \frac{466.6}{\rho} \times B_0 \quad ,,$$

ρ = radial distance to target

THE SOLUTION TO A RECTANGULARLY SYMMETRIC MAGNETIC FIELD WAS USED TO APPROXIMATE THE FIELD SHAPE:

$$\Phi = \sum_{lm} a_{lm} x^l y^m$$

$$\nabla^2 \Phi = 0$$

$$-\vec{\nabla} \Phi = \vec{B}$$

WHERE ONE ASSUMES:

$$B_x(x,y) = B_x(-x,y) = B_x(-x,-y) = B_x(x,-y)$$

$$B_y(x,y) = B_y(-x,y) = -B_y(x,-y) = -B_y(-x,y)$$

THE SOLUTION IS:

$$B_x(x,y) = B_x(0,0)\left[a_1 + a_2(x^2 - y^2) + a_3(x^4 - 6x^2y^2 + y^4) + a_4(x^6 - 15x^4y^2 + 15x^2y^4 - y^6) + a_5(x^8 - 28x^6y^2 + 70x^4y^4 - 28x^2y^6 + y^8)\right]$$

$$B_y(x,y) = B_y(0,0)\left[-2a_2xy + 4a_3(xy^3 - x^3y) - a_4(6x^5y - 20x^3y^3 + 6xy^5) + a_5(8xy^7 - 56x^3y^5 + 56x^5y^3 - 8x^7y)\right]$$

$$a_1 = 1.0$$
$$a_2 = 3.522 \times 10^{-4}$$
$$a_3 = -1.6901 \times 10^{-6}$$
$$a_4 = 4.545 \times 10^{-9}$$

MOMENTUM × BEND ANGLE = $A \times 10^{-4} \times I$ (AMPS)

$$A = A\emptyset \left(1 - \left(\frac{I}{5000}\right)^{**3.5}\right)$$

$A\emptyset$

ARM \ POLARITY	+	−
UP	8.19	8.12
DOWN	8.10	8.05

APPENDIX 4

SCIENTISTS + ENGINEERS
STUART L. MEYER
P388

LINEAR LEAST SQUARES WITH CORRELATIONS

$$\varepsilon = Y - Ca$$

Y = a position measurement x, y, r, ϕ.

a = a track parameter to be determined by the least squares fit

We define also: $S \equiv \varepsilon^T W \varepsilon$

$$W \equiv (\mathrm{cov}(Y))^{-1} = E^{-1}$$

= INVERSE ERROR MATRIX

We wish to find the best fit values for 'a', so we minimize S:

$$\frac{dS}{da_i} = \emptyset \qquad (1)$$

This equation yields the following relation for a:

$$a = (C^T W C)^{-1}(C^T W y) \qquad (2)$$

To learn the $\mathrm{cov}(a)$ one can use a result from propagation of errors:

if $V = D z$ Then $\mathrm{cov}(V) = D\,\mathrm{cov}(z)\,D^T$

or applying this explicitly to equation (2) we have:

$$\mathrm{cov}(a) = (C^T W C)^{-1} C^T W \,\mathrm{cov}(y)\,[(C^T W C)^{-1} C^T W]^T$$

$$= (C^T W C)^{-1} \qquad (3)$$

APPENDIX 5

INDUTY

P_i = number of particles in the ith bucket

N = effective number of buckets / spill

X = number of X counts / spill

X_i = number of X counts in the ith bucket

$\sigma(X)$ = cross section of process X

$A(X)$ = corrects to cross section for targets, apparatus acceptance, deadtime effects etc effects

If all buckets are equally populated then

Prob. of an X count in a bucket = X/N

~~If~~ If processes X and Y are uncorrelated and all buckets are ~~equally populated~~ then we can predict the pair rate $X:Y$

$$\frac{X:Y}{N} = \frac{X}{N} \times \frac{Y}{N}$$

$$\text{INDUTY} \equiv \frac{X:Y}{X\,Y} N = 1$$

If all buckets are not equally populated (but processes X & Y remain uncorrelated)

$$X_i = P_i\, \sigma(x) A(x)$$

$$X{:}Y_i = P_i^2\, \sigma(x)\sigma(y) A(x) A(y)$$

$$\frac{X:Y}{X\,Y} N = \frac{\langle P^2 \rangle}{\langle P \rangle^2}$$

This is not 1 if all P_i's are not the same. The greater the fluctuations in bucket contents, the larger the value of 'induty'.

Derivation of $b = \frac{4}{3} \ln\left(\ln\left(\frac{E_c}{E}\right)\right)$

The energy loss to radiation increases rapidly with increasing energy while the average energy loss by collision remains constant. At the electron energies of this experiment only the radiation losses of electrons need be considered.

Bothe + Hütter computed the probability density $W(E_0\ E\ t)$ that an electron starting with E_0 will have an energy E after t radiation lengths:

$$W(E_0, E, t) = \frac{1}{E_0} \frac{\ln\left(\frac{E_0}{E}\right)^{\left(\frac{t}{\ln 2}-1\right)}}{\Gamma\left(\frac{t}{\ln 2}\right)}$$

Let us set:

$$\eta \equiv \frac{4}{3} t$$

$$e^u \equiv \frac{E_0}{E}$$

$$\therefore \quad dE = -E_0 e^{-u} du$$

$$W_1(u)\, du \equiv W(E_0, E, t)\, dE$$

$$\therefore \quad W_1(u, \eta) = -\frac{e^{-u} u^{\eta-1}}{\Gamma(\eta)}$$

$$\text{I}\quad W_1(u) \equiv \int_0^u W_1(u', \eta)\, du'$$

$$\Gamma(n+1) = n\,\Gamma(n)$$

$$\log \Gamma(1+x) = -Cx + \frac{S_2 x^2}{2} - \dots$$

$$x\,\Gamma(x) = e^{-Cx + \frac{S_2 x^2}{2} - \dots} = 1 - Cx + \frac{S_1 x^2}{2} - \dots,$$

$$\Gamma(x) = \frac{1}{x} - C + \frac{S_1 x}{2} - \dots$$

So assuming x small

$$\therefore \quad 1/\Gamma(x) \equiv x

If $W_1(u,n)$ represents the probability of coming out with an energy greater than E after a thickness n.

One can use the fact that

$$\frac{1}{\Gamma(n)} \simeq n$$

and for $u < 1$ $(E/E_I < e)$ one obtains:

$$I W_1(u,n) = \int_0^u W_1(u',n)\,du' = \left(\sum_{i=1}^{\infty} A_i\, u^{n+i-1}\right) e^{-u}$$

By sorting out terms we see

$$A_i = A_1 / (n+1)(n+2)\ldots(n+i-1)$$
$$A_1 = 1$$

$$I W_1(u,n) = e^{-u} e^{n \ln u}\left(1 + u\left(1 - n + \frac{n^2}{2} + \ldots\right) + \right.$$

$$\left. \frac{u^2}{2}\left(1 - n + \frac{n^2}{2} + \ldots\right)\left(1 - \frac{n}{2} + \frac{n^2}{3} + \ldots\right)\right)$$

$$= e^{-u}\left(1 + n\left(\ln u - u - \frac{3u^2}{4}\right) + \right.$$

$$\left. n^2\left(\frac{u}{2} + \frac{9u^2}{16} + \frac{1}{2}\ln^2 u - \ln u\left(u - \frac{3u^2}{4}\right)\right) + \ldots\right.$$

For $(E_I - E) \ll E_I \Rightarrow |\ln u| \gg u$ so we neglect u in comparison with $\ln u$:

$$I W_1(u,n) = e^{-u}\left(1 + n\ln u + \frac{1}{2}(n \ln u)^2 + \ldots\right)$$

$$= e^{-u} e^{n \ln u}$$

$$= e^{-u} e^{bl}$$

$$b = \frac{4}{3}\ln u = \frac{4}{3}\ln\left(\ln \frac{E_I}{E}\right)$$

$\frac{E}{E_I}$	b
1.2	2.1
1.1	3.1
1.05	4.0
1.03	4.5
1.01	6.1
1.001	9.2

1) J.H. CHRISTENSON, G.S. HICKS, L.M. LEDERMAN, P.J. LIMON, B.G. POPE
PRL 25, 1523 (1970)
J.H. CHRISTENSON, G.S. HICKS, L.M. LEDERMAN, P.J. LIMON, B.G. POPE,
E. PAVATTINI PRD X, 2016 (1973)

2) G.B. WEST PHYS. REPORTS 18, 263 (1975)

3) M.L. PERL PHYS. TODAY 24, No.7, 34 (1971)

4) E. RUTHERFORD PHIL. MAG. V21 669 (1911)

5) R.P. FEYNMAN PHOTON-HADRON INTERACTIONS, W.A. BENJAMIN (1972)
R.P. FEYNMAN PRL 23 1415 (1969)
S.D. DRELL, TUNG-MOW YAN ANN. OF PHYS. 66, 578 (1971)
R.P. FEYNMAN 3RD INTERN. CONF. ON HIGH ENERGY COLLISIONS
SUNY, STONY BROOK, SEPT. 1969
J. KOGUT, L. SUSSKIND PHYS. REPORTS 8 75 (1973)
J.D. BJORKEN, E.A. PASCHOS PR 185 1975 (1969)

6) G. RUTHERGLEN PROC. OF THE 4TH INTERN. SYMP. ON ELECTRON
AND PHOTON INTERACTIONS AT HIGH ENERGY P163
DARESBURY, 1969
M. GOURDIN PHYS. REPORTS 11 29 (1974)

7) G. PREPARATA BNL 16173 SEPT. 1971
G. PREPARATA CORAL GABLES CONF. ON FUNDAMENTAL INTERACTIN
AT HIGH ENERGY JAN. 1972
R.L. JAFFE PRD 5 2622 (1972)
R.L. JAFFE SEMINAR ON QUARK AND PARTON PROBLEMS
MOSCOW, JUNE 1974
Y. FRISHMAN PHYS. REPORTS 13C 1 (1974)

8)

9) M. GELL-MANN CAL-TECH REPT CT SL-20 (1961)
M. GELL MANN PL 8 214 (1964)

10) G. ZWEIG CERN REPT #8182/TH-401 JAN 1964

11 H.D. POLITZER PHYS. REPORTS 14C 129 (1974)
G. ALTARELLI, G. PARISI LPTENS 77/6 MARCH 1977

12 T.D. Lee PHYS. TODAY 25 23 (1972)
T.D. Lee NEUTRINO 1972 CONF. BALATONFÜRED, HUNGARY JUNE 1972 (CO-3067(2)-11)

13 F.J. GILMAN PHYS. REPORTS 4, 95 (1972)
L.W. MO MEETING OF THE DIVISION OF PARTICLES AND FIELDS APS BNL OCT 1976

14 E.D. BLOOM, D.H. COWARD, H. DESTABLER, J. DREES, G. MILLER, L.W. MO, R.E. TAYLOR, M. BREIDENBACH, J.I. FRIEDMAN, G.C. HARTMA H.W. KENDALL PRL 23 930 (1969)

15 Y. WATANABE, L.N. HAND, S. HERB, A. RUSSEL, C. CHANG, K.W. CHEN, D.J. FOX, A. KOTLEWSKI, P.F. KUNZ, S.C. LOKEN, M. STROVINK, W. VERNON PRL 35 898 (1975)
C. CHANG, K.W. CHEN, D.J. FOX, A. KOTLEWSKI, P.F. KUNZ, L.N. HAND, S. HERB, A. RUSSEL, Y. WATANABE, S.C. LOKEN, M. STROVINK, W. VERNON. PRL 35, 901 (1975)
H.L. ANDERSON, V.K. BHARADWAJ, N.E. BOOTH, R.M. FINE, W.R. FRANCIS, B.A. GORDON, R.H. HEISTERBERG, R.G. HICKS, T.B.W. KIRK, G.I. KIRKBRID W.A. LOOMIS, H.S. MATIS, L.W. MO, L.C. MYRIANTHOPOULOS, F.M. PIPKIN, S.H. PODRES, T.W. QUIRK, W.D. SHAMBROOM, A. SKUJA, M.A. STATON, W.S.C. WILLIAMS, L.J. VERHEY, RICHARD WILSON, S.C. WRIGHT PRL 36 1450 1977
H.L. ANDERSON, V.K. BHARADWAJ, N.E. BOOTH, R.M. FINE, W.R. FRANCIS, B.A. GORDON, R.H. HEISTERBERG, R.G. HICKS, T.B.W. KIRK, G.I. KIRKBRIDE W.A. LOOMIS, H.S. MATIS, L.W. MO, L.C. MYRIANTHOPOULOS, F.M. PIPKIN, S.H. PODRES, T.W. QUIRK, W.D. SHAMBROOM, A. SKUJA, L.J. VERHEY, W.S.C. WILLIAMS, RICHARD WILSON, S.C. WRIGHT PRL 36 1422 (1976), PRL 37, 4 (1976)

16) S.D. DRELL AMSTERDAM INTERNATIONAL CONFRENCE ON ELEMENTARY PARTICLES P301, AMSTERDAM 1971

17) F.E. CLOSE FUNDAMENTALS OF QUARK MODELS 17TH SUMMER SCHOOL, ST. ANDREWS UNIVERSITY 1 (1976)

18 L.M. SCHGAL ANL-HEP-PR-75-45 AUG. 1975
D.H. PERKINS CONTEMP. PHYS. V16 173 (1975)
B.C. BARISH CALT 68-507 AUG. 1973
H. WACHSMUTH CERN/EP/PHYS 77-40 AUG 1977
C.H. LLEWELLYN SMITH PHYS. REPORTS 3C 261 (1972)
S.L. ADLER PR 143 1144 (1966)

19 L.M. SCHGAL REF 17 P.

20 V. BARGER, R.J.N. PHILLIPS NP B73 (1974)
P.V. LANSHOFF, J.C. POLKINGHORN NP B 33 221 (1971)
R. McECHANEY, S.F. TUAN PRD8 2267 (1973)
G. FARRAR NP B77 429 (1974)
G. ALTARELLI, N. CABIBBO, L. MAIANI, R. PETRONZIO NP B92 413 (1975)

21 L.M. SCHGAL ANL-HEP-PR 75 45 P 59 AUG 1975

22 H. FRITZCH CALT-68-415 INTERN. MEETING ON e^+e^- ANNIHILATION BIELEFELD, GERMANY SEPT 1973
G.J. FELDMAN, MARTIN L. PERL PHYS. REPORTS 19 233 (1975)
C.H. LLEWELLYN SMITH INTERN. SCHOOL OF SUBNUCLEAR PHYSICS ERICE JULY 1974 ACADEMIC PRESS V12.
J. ELLIS, M.K. GAILLARD CERN 76-18 NOV 1976

23 J.-E. AUGUSTIN, A.M. BOYARSKI, M. BREIDENBACH, F. BULOS, J.T. DAKIN, G.J. FELDMAN, G.E. FISCHER, D. FRYBERGER, G. HANSON, B. JEAN-MARIE, R.R. LARSEN, V. LÜTH, H.L. LYNCH, D. LYON, C.C. MORE HOUSE, J.M. PATERSON, M.L. PERL, B. RICHTER, P. RAPIDIS, R.F. SCHWITTERS, W.M. TANENBAUM, F. VANNUCCI, G.S. ABRAMS, D. BRIGGS, W. CHINOWSKY C.E. FRIEDBERG, G. GOLDHABER, R.J. HOLLEBEEK, J.A. KADYK, B. LULU, F. PIERRE, G.H. TRILLING, J.S. WHITAKER, J. WISS, J.E. ZIPSE PRL 33 1406 (1974)

24 J.J. AUBERT, U. BECKER, P.J. BIGGS, J. BURGER, M. CHEN, G. EVERHART, P. GOLDHAGEN, J. LEONG, T. MCCORRISTON, T.G. RHOADES, M. ROHDE, SAMUEL C.C. TING, SAU LAN WU, Y.Y. LEE PRL 33 1404 (1974)

25 N. CABIBBO, G. PARISI, M. TESTA NC 4 35 (1970)

26 J.D. BJORKEN 6TH INTERN. SYMPOS. ON ELECTRON AND PHOTON INTERACTIONS AT HIGH ENERGY NORTH HOLLAND 1974
J. CLEYMANS, G.J. KOMEN NP B78 396 (1974)

27 M. BREIDENBACH PROC. OF THE SLAC INSTITUTE ON PARTICLE PHYSICS STANFORD CALIF. AUG 1976

28 M.L. PERL, G.J. FELDMAN, G.S. ABRAMS, M.S. ALAM, A.M. BOYARSKI, M. BREIDENBACH, J. DORFAN, W. CHINOWSKY, G. GOLDHABER, G. HANSON, J.A. JAROS, J.A. KADYK, D. LUKE, V. LÜTH, R.J. MADARAS, H.K. NGUYEN, J.M. PATERSON, I. PERUZZI, M. PICCOLO, T.P. PUN, P.A. RAPIDIS, B. RICHTER, W. TANNENBAUM, J.E. WISS SLAC PUB 1997 AUG 1977

29 T. APPELQUIST, H. GEORGI PRD8 4000 (1973)
A. ZEE PRD8 4038 (1973)

30 C.H. LLEWELLYN SMITH REF 22 P248

31 J.W. CRONIN REVIEW OF MASSIVE DILEPTON PRODUCTION IN PROTON - NUCLEUS COLLISIONS INTERN. SCHOOL OF SUBNUCLEAR PHYSICS ERICE JULY 1976

TUNG-MOW YAN MASSIVE LEPTON PAIR PRODUCTION IN HADRONIC COLLISIONS CLNS 369 AUG 1977

32 M. DUONG-VAN PL 60B 287 (1976)
F. RAUNDAL NORDITA 76/13 MAY 1976

33 J. KUTI, V. WEISSKOPF PRD4 3418 (1971)

35 S.D. DRELL, T.M. YAN PRL 25 316 (1970)

36 THE DRELL-YAN CROSS SECTION IS CONSIDERED IN MANY PAPERS & IS EVALUATED FOR QUARK-ANTIQUARK ANNIHILATION (DRELL-YAN MECHANISM) AS WELL AS OTHER MECHANISMS (GLUON-GLUON ANNIHILATION, FOR EXAMPLE). SEVERAL SAMPLE REFERENCES ARE GIVEN BELOW:

M. DUONG-VAN, K.V. VASAVADA, R. BLANKENBECLER PRD 16 137 (1977)
G.R. FARRAR NP B77 429 (1974)
M. DUONG-VAN PL 60B 287 (1976)
H.D POLITZER HUTP-77/A029
J. KUTI, V.F. WEISSKOPF PRD 4 3418 (1971)
S. PAKVASA, D. PARASHAR, S.F. TUAN PRD 10 2124 (1974)
A. SONI UCSB-TH-2 1977
C.K. CHEN ANL-HEP-PR-77-24 MARCH 1977
C.M. DEBEAU, D. SILVERMAN TR-77-28 UCI, IRVINE

36 J.G. BRANSON, G.H. SANDERS, A.J.S. SMITH, J.J. THALER, K.J. ANDERSON, G.G. HENRY, K.T. MCDONALD, J.E. PILCHER, E.I. ROSENBERG. PRL 38 1334 (1977)

37 D. ANTREASYAN, J.W. CRONIN, H.J. FRISCH, M.J. SHOCHET, L. KLUBER J.J. MUELLER, P.A. PINOUE', R.C. SUMNER, TEST OF SCALING IN MUON PAIR PRODUCTION BY HADRONS CP-7C-6
L.M. LEDERMAN, B.G. POPE PL 66B 486 (1977)

38 R.F. PEIERLS, T.L. TRUEMAN; LING-LIE WANG PRD 16 1397 (1977)

39 S.W. HERB, D.C. HOM, L.M. LEDERMAN, J.C. SENS, H.D. SNYDER, J.K. YOH, J.A. APPEL, B.C. BROWN, C.N. BROWN, W.R. INNES, K. UENO, T. YAMANOUCHI, A.S. ITO, H. JÖSTLEIN, D.M. KAPLAN, R.D. KEHART PRL 39 252 (1977)

40) Y. YAMAGUCHI NC 43 2577 (1966)
L.M. LEDERMAN, B.G. POPE PRL 27 765 (1971)

41 C. QUIGG. REV. MOD PHYS 49 297 (1977)
L.L. WANG, BNL 22661 APRIL 1977
R.B. PALMER, E.A. PASCHOS, N.P. SAMIOS, CING-LIE WANG BNL 20634 (1976)
R.F. PEIERLS ET AL, REFERENCE 37

42 G. CHU, J.F. GUNION PRD 10 3672 (1974)

43) F.T. DAO, E. FERMINIO, KWAN-WU LAI, W. METCALF, CING-LIE WANG, A STUDY OF QUARK STRUCTURE FUNCTION BNL PREPRINT
V. BARGER, R.J.N. PHILLIPS COO-881-5 Oct 1977

44 M. FONTANNAZ, D. SCHIFF LPTHE 77/23 JUNE 1977
R.D. FIELD, R.P. FEYNMAN PRD 15 2590 (1977)
E.L. BERGER, T. DONOHUE, S. WOLFRAM ANL-HEP-PR-77-63 AUG 1977
J. KOGUT, J. SHIGEMITSU CLNS-364 AUG 1977
S.D. DRELL, D.J. LEVY, T.M. YAN PR 187 2159 (1969)
H.D. POLITZER HUTP-77/A029
F.E. CLOSE, F. HALZEN, D.M. SCOTT PL 68B 447 (1977)
J.F. GUNION PRD14 1400 1976
J. D, KOGUT PL 65B 377 (1976)

45 REFERENCE 24

46 H.D. SNYDER, D.C. HOM, C.M. LEDERMAN, H.P. PAAR, J.M. WEISS, J.K. YOH, J.A. APPEL, B.C. BROWN, C.N. BROWN, W.R. INNES, T. YAMANOUCHI, D.M. KAPLAN PRL 36 1415 (1976)

47 REFERENCES

48 A. DONNACHIE, P.V. LANDSHOFF NP B112 233 (1976)
J.F. GUNION PRD12 1345 (1975)
F. HALZEN, S. MATSUDA, QUARK PARTON RELATIONS FOR THE HADRONIC PRODUCTION OF MASSIVE LEPTON PAIRS AND J/ψ WITH DIFFERENT BEAM PARTICLES RUTHERFORD LAB JUNE 1977
M.B. EINHORN, S.D. ELLIS PRD12 2007 (1975)
C.E. CARLSON, R. SUAYA WM-PP-12 March 1976
M.B. GREEN, M. JACOB, P.V. LANDSHOFF NC 29 123 (1975)
T.K. GAISSER, F. HALZEN, E.A. PASCHOS PRD 15 2572 (1977)
H. FRITZCH PL 67B 217 (1977)

49 R.D. KEPHART, R.J. ENGLEMANN, R.J. FISK, M.L. GOOD, A.S. ITO, H. JÖSTLEIN, D.M. KARAN, R.C. McCARTHY, H. WAHL, C.W. HERB, D.C. HOM, L.M. LEDERMAN, J.C. SENS, H.D. SNYDER, J.K. YOH, J.A APPEL, B.C. BROWN, G.N. BROWN, W.R. INNES, K, UENO PRL: TO BE PUBLISHED

50 G.W. TAUFEST, H.R. FECHTER RSI 26 229 1955
V.J. VAN HUYSE, E.D. WATTECAMPS, R.E. VAN de VIJVER, G.S. VAN PRAET NIM 15 59 (1962)
V.J. VANHUYSE, R.E. VAN de VIJVER NIM 15 63 (1962)
D.B. ISABELLE, P.H. ROY NIM 20 17 (1963)

51 J. HUDIS I. DOSTROVSKY, G. FRIEDLANDER, J.R. GROVER, N.T. PORILE, L.R. REMSBERG, R.W. STOENNER, S. TANAKA PR 129 434 (1963)
N.T. PORILE, S. TANAKA PR 135 B122 1964

52 B. ROSSI K. GREISEN REV. MOD. PHYS. 13 240 1941
B. ROSSI HIGH ENERGY PARTICLES (PRENTICE HALL) CHAPTER 5 (1952)

53 H. MESSEL, D. CRAWFORD ELECTRON-PHOTON SHOWER DISTRIBUTION FUNCTION TABLES, PERGAMON PRESS, 1970
U. VOLKEL DESY 65/6 (JULY 1965); DESY 67/16 (MAY 1967)
E. LONGO, I. SESTILI NIM 128 283 (1975)

54 W. Heitler THE QUANTUM THEORY OF RADIATION (3rd ED.) CLARENDON 35 (1954)

55 J.A. APPEL, F.H. BURKHARD, E. GAINES, D.C. HOM, L.B. LEDERMAN, P. LOCH, J.R. ORR, J.K. PARRY, L.C. STONEHILL, J.M. WEISS, J.K. YOH, B.C. BROWN, C.N. BROWN, J.H. GALLARDO, J.R. SAUER, T. YAMANOUCHI, NIM 127 495 (1975)

56 W.B. ATWOOD SLAC REPORT 185 APPENDIX B (JUNE 1975)

57 (CRONIN-EUA4)

58 G. MILLER INELASTIC ELECTRON SCATTERING AT LARGE ANGLES
APPEN A. III SLAC REPT 129, JAN 1971

59 YUNG-SU TSAI RMP 46 4 833 (1974)

60 B. ROSSI HIGH ENERGY PARTICLES (PRENTICE HALL) 1952

61 J.H. GALLARDO 'ELECTRONS AND GAMMA RAYS THROUGH FILTERS'
FERMILAB EXPERIMENT 70 INTERNAL MEMO
D.H. SAXON 'COMMENT ON ELECTRONS AND GAMMA RAYS THROUGH FILTERS' FERMILAB EXPERIMENT 70 INTERNAL MEMO

62 I. GAINES Thesis COLUMBIA UNIV. R-1069, CU321, NEVIS 215
H.P. PAAR Thesis COLUMBIA UNIV. R-957, CU 314, NEVIS 208

63 K. KINOSHITA, H. SATZ, D. SCHILDKNECHT BI-TP-77/14

64 D.M. KAPLAN, R.J. FISK, A.S. ITO, H JÖSTLEIN, R.O. KERMODE, J.A. APPEL, B.C. BROWN, C.D. BROWN, W.R. INGRAM, K. UENO, T. YAMANOUCHI, W. HESS, D.C. HUM, C.D. LEDERMAN, J.C. SENS, H.D. SNYDER, J.K. YOH, PRL TO BE PUBLISHED

65 L. GUTTINGER ET AL. PR 57 782 (1940)

66 J. ORCHARD NOTES ON STATISTICS FOR PHYSICISTS UCRL-8417 BERKELY, CALIF AUG 1958

67 T. de FOREST J.D. WALECKA ADV. IN PHYS 57 1 (1966)
M GOURDIN NC 21 3662 (1961)
S.D. DRELL ANN. OF PHYS. 28 18 (1964)

68 S.J. ADLER PR 143 1144 (1966)
C.M. SEHGAL ANL-HEP-PR-75-45 AUG 1975